# Characteristics and Formation of Precipitation over the Kananaskis Emergency Site during March and April 2015

by

Ida Hung

A Thesis submitted to the Faculty of Graduate Studies of

The University of Manitoba

in partial fulfilment of the requirements of the degree of

MASTER OF SCIENCE

Department of Environment and Geography

University of Manitoba

Winnipeg

## Abstract

A field campaign was conducted in March and April 2015 in the Kananaskis Valley of Alberta to investigate the formation and characteristics of ice crystals and solid precipitation particles in the lee of the Rocky Mountains. This thesis examines data from 11 storms producing mainly light precipitation within generally sub-saturated surface and near-surface conditions. Instruments utilized include soundings, radar images, and surface observations, but the focus is on the analysis of 1,183 microphotographic images of precipitation particles. The particles (diameters up to 24 mm) were placed into 12 categories with rimed irregular snow particles being most common. Unrimed and rimed particles were commonly (14% of images) observed simultaneously and 62% of particles were rimed. Rimed, dense particles were less likely to sublimate before reaching the surface in the dry sub-cloud region that was at least partially a result of the air aloft being directed mainly towards the east and ‘downslope’.

**Acknowledgements**

First of all, I would like to express my deepest gratitude to my advisor, Dr. Ronald Stewart for his knowledge, guidance, and encouragement. Without his wisdom and advice, my thesis would not have been possible. I would also like to thank my committee members, Dr. John Hanesiak, Dr. Julie Theriault, and Bob Kochtubajda. Their suggestions, questions, and comments were greatly valued.

I would like to thank all the researchers, students, and contributors who were involved in the Alberta field campaign including Dr. Julie Theriault, Dr. Ronald Stewart, Dr. John Pomeroy, Juris Almonte, Paul Vaquer, Emilie Poirier, May Guan, Angus Duncan, Bruce Cole, Stephen Berg, Emilie Bresson, Al Jachik, Housseyni Sankare, Dominic Matte, Melissa Cholette, Craig Smith, Scott Landlot, and Lucia Scaff. I would not have been able to write my thesis without their hard work and commitment.

Much appreciation goes towards Université du Québec à Montréal students Paul Vaquer and Emilie Poirier. They took the time out of their busy schedules to answer my many emails and questions about the data and Python! In addition, I would like to thank Craig Smith for taking the time to "clean up" the Geonor data. I would also like to thank Michelle Curry and Stephen Berg for their support and advice. Your thoughts and suggestions were greatly appreciated.

Thank you to James Cummine and Robyn Dyck for providing surface analysis maps. Acknowledgements to Alberta Agriculture and Forestry, Alberta Climate Information Service (ACIS) for providing the Kananaskis Boundary Auto station data, found at http://agriculture.alberta.ca/acis/. Thank you to Dr. John Pomeroy for providing data for the Hay Meadow station at the Marmot Creek Research Basin.

Last but not least, I would like to thank my parents, siblings, Fiancé, and friends for their unconditional love and support during my study. I would not have been able to complete this thesis without their continuous love and their constant reminder to not give up.

# Table of Contents

# List of Tables

# List of Figures

# Chapter 1 – Introduction

Cold season precipitation occurs frequently in the lee of the Rocky Mountains, yet no study has examined the formation and characteristics of the associated ice crystals and solid precipitation particles on the eastern side of the Alberta Rockies. The formation of precipitation particles are influenced by many factors in the atmosphere and understanding those factors can be improved through detailed observations of precipitation at and near the surface.

## 1.1 Related Studies

A number of studies have been conducted on the characteristics of ice crystals and solid precipitation particles in various areas (Nakaya, 1954; Magono and Lee, 1966; Gibson and Stewart, 2007; Kikuchi et al., 2013; Stewart et al., 2015).

For example, Nakaya (1954) developed the first classification of snow crystals by creating crystals in a laboratory. Magono and Lee (1966) continued Nakaya's (1954) work using five surface observation points at Mt. Teine, Hokkaido, Japan. Their results increased the classification from 36 to 80 categories. More recently, Kikuchi et al. (2013) expanded on Magono and Lee's (1966) classification of ice crystals by identifying particles from the mid-latitudes to the polar regions including regions in Canada, such as Inuvik and Yellowknife. Kikuchi et al. (2013) identified new types of ice crystals and increased the classification to 121 categories.

Gibson and Stewart (2007) and Gibson et al. (2009) studied the formation of ice pellets at Mirabel, Quebec in November 2003. Photographs were utilized to categorize ice pellets based on their shape and form. Gibson and Stewart were able to identify several different classes of ice pellets occurring simultaneously.

A recent study by Stewart et al. (2015) summarized some of our understanding of cold season precipitation. Stewart stated that there are no official terms to classify some types of precipitation. For example, an almost melted particle is when the original particle is not apparent and the precipitation is composed mainly of liquid. A particle with an ice shell and liquid water contained within it is only colloquially known as a liquid core pellet. Other precipitation, such as wet snow, is officially defined but the relative amount of liquid within it varies dramatically.

Other studies have also been conducted on accreted particles and sublimation, particularly over Northern Canada. For example, Burford and Stewart (1998) studied sublimation of falling snow over the Mackenzie River Basin as part of the 1994 Beaufort and Arctic Storms Experiment (BASE). Burford and Stewart found unrimed particles to sublimate rapidly due to their lower density and terminal velocity. This process created a negative effect on the amount of precipitation recorded at the surface. A two-part study was carried out by Stewart et al. (2004) and Hudak et al. (2004) during the Canadian Global Energy and Water Cycle Experiment (GEWEX) during the autumn and winter of 1998 and spring of 1999. Stewart and Hudak found the process of sublimation to negatively influence unrimed and rimed precipitation at Fort Simpson, Northwest Territories. Henson et al. (2011) photographed precipitation particles in Iqaluit during the 2007 Storm Studies in the Arctic (STAR) field campaign (Hanesiak et al., 2010). Henson identified rimed dendrites and many aggregates at the surface. However, sublimation was also found to negatively influence the amount of precipitation received at the surface. Similar results were found by Fargey et al. (2013) in southern Baffin Island, Nunavut of rimed particles at the surface. Results suggested that small particles are easily sublimated due to their lower density and fall velocity.

## 1.2 Thesis Motivation

Because of the importance of precipitation, research networks have been established to improve our understanding of its occurrence. For example, the Changing Cold Regions Network (CCRN) was formed to better address, diagnose, and predict interactions of the cryospheric, ecological, hydrological, and climatic components of the Earth system at multiple scales (DeBeer et al. 2014). The focus region of CCRN is on the rapidly changing cold interior of western and northern Canada of the Mackenzie and Saskatchewan River Basins. The network is funded from 2013 to 2018 through the Climate Change and Atmospheric Research (CCAR) Initiative of the Natural Sciences and Engineering Research Council of Canada (NSERC) (DeBeer et al., 2014). One of the primary concerns for CCRN is future changes in precipitation. DeBeer et al. stated that projections for the southern regions of western Canada show a substantial decrease in cold season precipitation. This claim contradicts the Intergovernmental Panel on Climate Change (IPCC) findings of a trend in heavier precipitation in central North America (DeBeer et al., 2014).

## 1.3 Alberta Field Campaign

To better understand precipitation in the CCRN domain, an Alberta field campaign was carried out during March and April 2015 in the foothills of the Rocky Mountains in southern Alberta. The project focused on precipitation events in the Kananaskis Valley at the Kananaskis Emergency Site (KES). The goals of the study were to: (1) gain a better understanding of rain, snow, and transition regions, (2) relate the atmospheric conditions to precipitation events for a better understanding of its development, and (3) to examine the weather systems associated with these precipitation events.

## 1.4 Thesis Objective

Given the research gap on precipitation and the opportunity afforded by this field campaign, the objective of this thesis is to study the characteristics and formation of cold season precipitation at KES during March and April 2015. The thesis utilizes information obtained during the Alberta field campaign with emphasis placed on precipitation events having specialized ice crystal and solid precipitation particle observations.

# Chapter 2 - Background

## 2.1 Fundamentals of Precipitation Formation

Precipitation can be formed by two possible mechanisms: growth by collision and coalescence in warm clouds and growth of ice crystals in cold clouds. This section provides a brief overview of the formation of precipitation.

## 2.2 Cloud Droplet Formation

Cloud droplets may form by heterogeneous nucleation. Heterogeneous nucleation requires aerosols or cloud condensation nuclei (CCN). CCN are often abundant with concentrations being of order several 100 per $cm^3$ over land areas. In the atmosphere, as the relative humidity approaches 100%, water begins to condense onto a CCN, creating a cloud droplet (Rogers, 1978).

Cloud droplets that exist when temperatures are below 0˚C are referred to as supercooled droplets. When the air is free of aerosols, droplets can freeze instantaneously at temperatures of approximately -40˚C, a process known as homogeneous freezing (Rogers, 1978).

## 2.3 Ice Nucleation Process

The ice nucleation process is similar to cloud droplet formation although, ice crystals form under temperatures between 0 and -40˚C on ice forming nuclei (IN), known as heterogeneous nucleation (Rogers, 1978). Nucleation occurs effortlessly if the particle contains a lattice structure similar to ice. Unlike CCN, IN is found at temperatures below 0°C and typically have a low concentration. For example, at about -20˚C, concentrations are of order 1 nucleus per

litre of air (Rogers, 1978) although concentrations increase dramatically with decreasing temperatures.

### 2.4 Growth of Ice Crystals: Diffusion

Stoelinga et al. (2012) stated that the coexistence of water droplets and ice crystals in a cloud causes the water vapour to diffuse from the water droplet to the ice crystal. This is due to the greater saturation vapour pressure over water than over ice at any given temperature. Figure 2.1 illustrates the difference of saturation vapour pressure over water and ice using the Clausius-Clapeyron equation. The growth of ice crystals by diffusion in a cold cloud follows the Bergeron-Findeisen process. The graph indicates that the largest difference is between -10 to -20˚C, where the difference between the saturation vapor pressure over water and ice is greatest (Stoelinga et al., 2012).

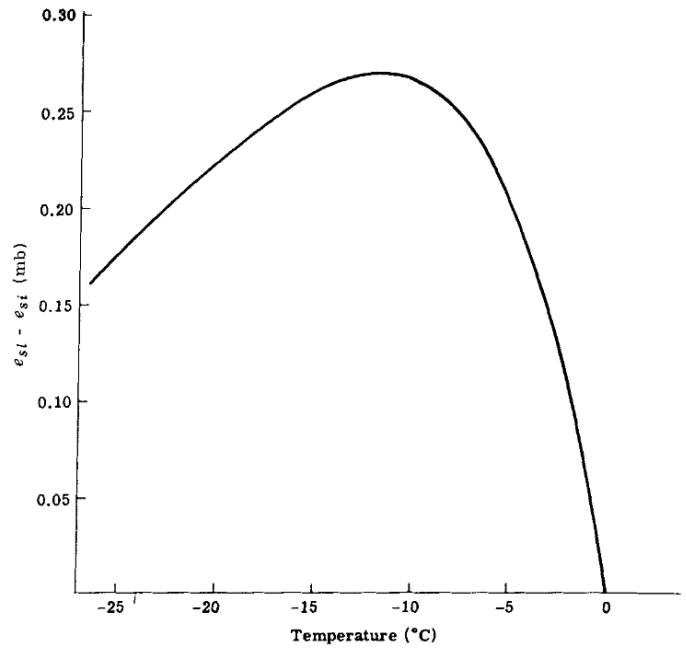


Figure 2.1: Difference in the saturation vapour pressure over water and over ice as a function of temperature. The image was adapted from Fleagle and Businger (1980).

Morphology diagrams (Figures 2.2 and 2.3) illustrate the various crystal and particle types that form at different temperature and vapour conditions. Furukawa and Wettlaufer (2007) describe the morphology diagram as a summary of the results found by Ukirchiro Nakaya, a physicist that developed snow crystals in a laboratory in 1954, along with the results by his students, and many others.

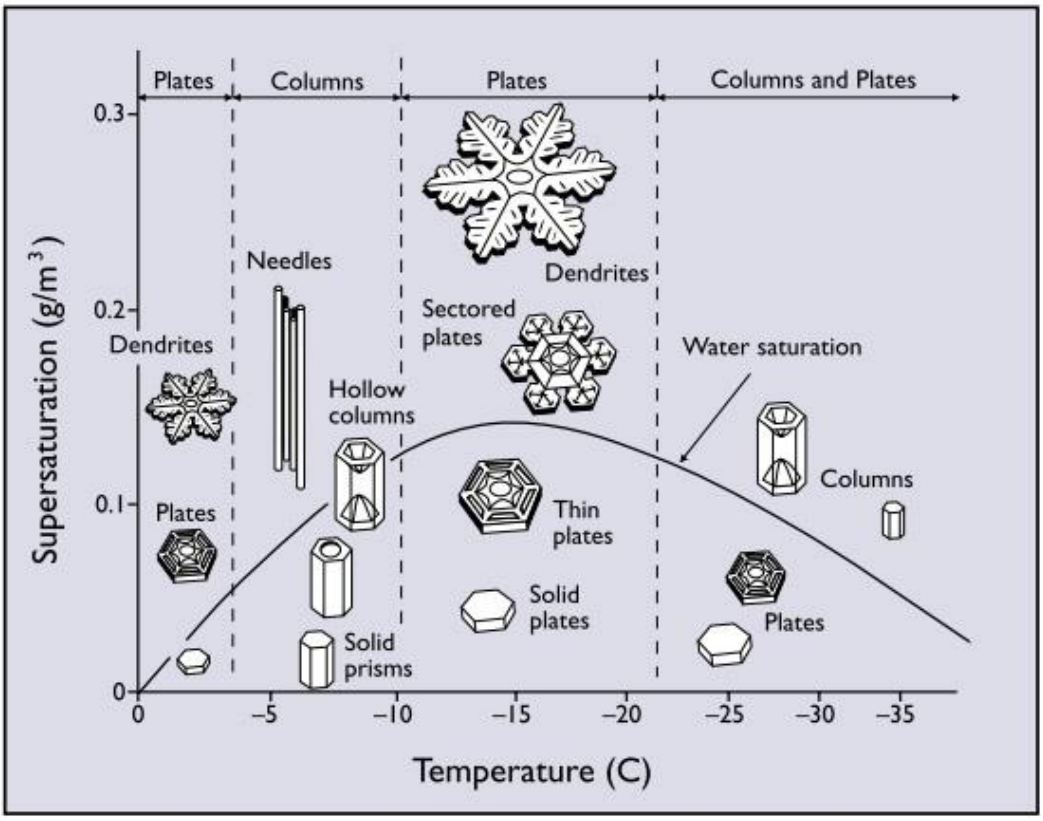


Figure 2.2: Morphology diagram of ice crystals at different temperature and supersaturation ranges. The vertical axis of the diagram is of the supersaturation and the curved line is the saturation with respect to water as a function of temperature. The image was adapted from Libbrecht (2001).

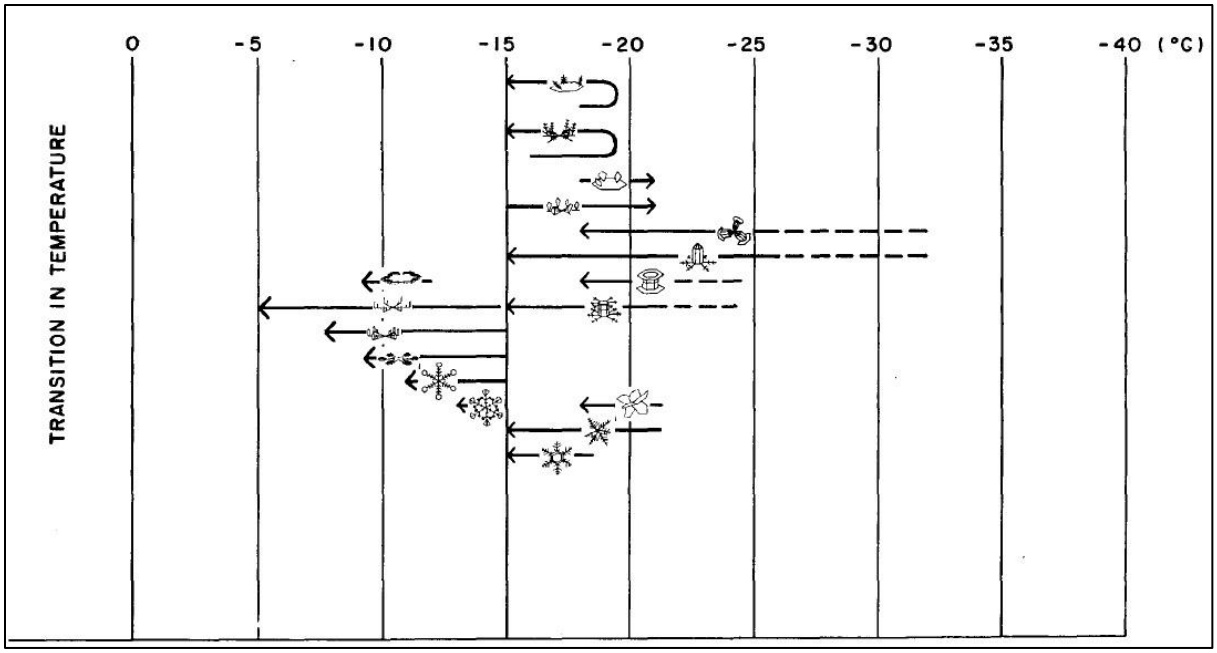


Figure 2.3: Transition of ice crystals as it moves through different temperature layers. The image was adapted from Magono and Lee (1966).

The diagram indicates that, when supersaturation is high, columns grow into needle crystals and hexagonal plates grow into stellar dendrites (Libbrecht, 2001). The diagram also displays abrupt changes in the structure of a crystal from plates to columns as the temperature changes (Figure 2.3). Although not all crystal types are shown in the diagram, we can see the complexity of how ice crystals are formed. As well, the diagram demonstrates how one can find ice crystals with different habits at the surface.

### 2.5 Growth of Ice Crystals: Accretion (Riming)

Another growth mechanism includes accretion. Accretion or riming occurs through the collision of supercooled droplets with ice crystals where they adhere to the ice surface and freeze (Fleagle and Businger, 1980). Also, the process of accretion is responsible for the formation of

graupel. The intensity of riming first begins as light, proceeding to moderate, heavily rimed, and finally to snow pellets (Stoelinga et al, 2012).

### 2.6 Growth of Ice Crystals: Aggregation

Aggregation is another form of ice crystal growth. Stoelinga et al. (2012) stated that aggregation occurs when ice crystals collide and stick together. This is possible due to mechanical linking or to the liquid molecules on the outer surface acting as glue. The adhesive-like surface allows the crystals to stick once they come in contact. Aggregation is therefore generally enhanced in cloud layers near 0˚C. Aggregation forms snowflakes which can grow several cm in diameter (Stoelinga et al., 2012) and can be made up of 10 – 100 or more ice crystals (Fleagle and Businger, 1980).

# Chapter 3 - Data and Methodology

## 3.1 Study Area

The Kananaskis Valley is located within Kananaskis Country 70 km west of Calgary, Alberta, Canada (Whitefield, 2014) as seen in Figure 3.1. Kananaskis Country is a park system that covers 4,257 km² and is a recreation area at the foothills of the Rocky Mountains (Travel Alberta, 2016).

The Kananaskis River flows northwards through the Kananaskis Valley where it connects with the Bow River (Whitefield, 2014). Other major water bodies in the Kananaskis Valley include Kananaskis Lakes and Barrier Lake.


Figure 3.1: Map of Kananaskis Country. The location of KES is represented by the red star. The image was adapted from Kananaskis Trails (2016).

The location of Kananaskis Emergency Site (KES) with respect to Calgary, Alberta can be seen in Figure 3.2. KES is located at 50°55’42” N and -115°07’31” W with a MSL elevation of 1447 m and is situated within the lee of the Rocky Mountains. Observations and analyses of precipitation events were undertaken at this site.

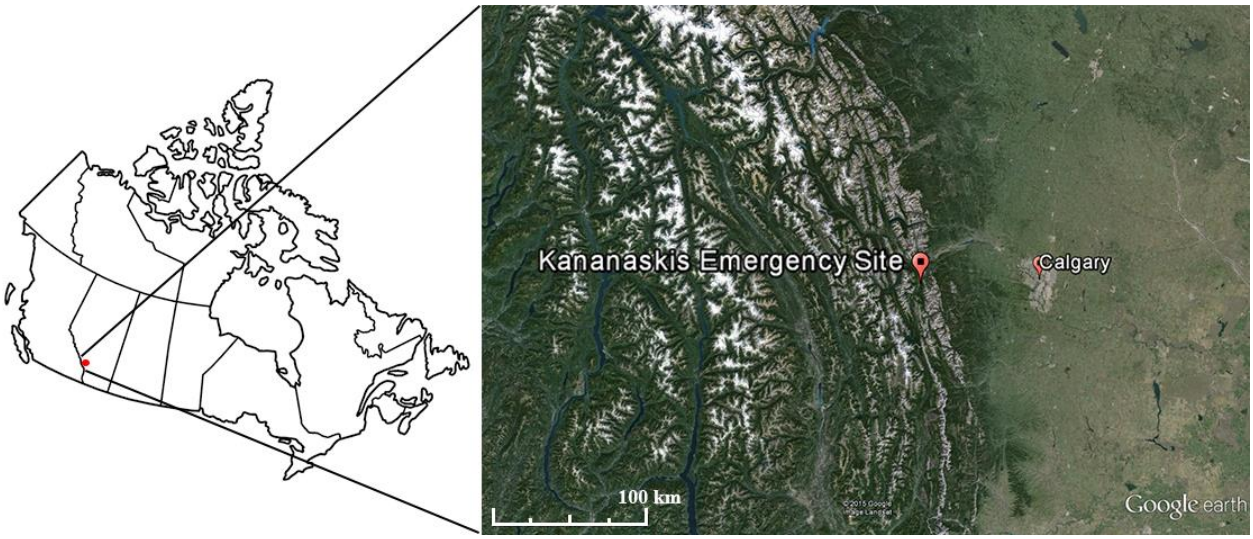


Figure 3.2: The Kananaskis Emergency Site is located in Alberta at the lee of the Rocky Mountains. 50.928421, -115.125276. Google Earth. September 23, 2012. Retrieved on September 12, 2015.

### 3.1.2 Climatology

The climate of Kananaskis Valley is considered to be humid continental (Harder, 2008). Humid continental regions experience long cold winters with cool wet summers. The warmest month is July, with an average temperature of 14.1°C, whereas the coldest month is January, with an average temperature of -7.5°C (Harder, 2008). Temperatures during the winter months vary between cold, dry, and warm, due to the influence of Chinooks. In winter, Chinooks occur about 30 times in the Kananaskis Valley (Whitefield, 2014).

The average temperature and relative humidity during the months of March and April at KES were not known. Therefore, values were calculated from the on-site Kananaskis Boundary

Auto (KBA) weather station. Archived data are available from April 2005 from the Alberta Agriculture and Forestry (AAF), Alberta Climate Information Service (ACIS) website (see http://agriculture.alberta.ca/acis/). Temperature data were available for the KBA station from 2005 – 2016, while relative humidity data were available from 2012 to 2016. The average temperature for March and April 2005 to 2014 and 2016 was -1.1°C. The relative humidity from 2012 to 2014 and 2016 was 69%.

Kananaskis Valley receives, on average, 105 days of precipitation a year, with 350 mm of rain and 270 mm of snow (Whitfield, 2014). Snowfall is most prominent in May and June where precipitation accounts for 40% of the annual precipitation (Whitfield, 2014). Studies have found that at higher elevations, 70 to 75% of the annual precipitation occurred as snow or a mixture of rain and snow. The maximum depth of the region varied from 0.6 to 1.4 m on lower slopes while on higher slopes, the depth varied from 2.0 to 2.6 m (Whitfield, 2014).

Precipitation accumulation is available during the summer months from the KBA station using a tipping bucket rain gauge. Therefore, historical data from the Marmot Creek Research Basin, CCRN were used (J. Theriault, personal communication, April 14, 2014). In total, 7 hydrometeorological stations have collected data between 2005 and 2013 at 15 min intervals. Of the 7 stations in the Marmot Creek Research Basin, Hay Meadow station is located closest to KES (2.1 km) and likely records similar accumulation results, therefore, its precipitation data were utilized. An example of the location with respect to KES will be shown in a later subsection. Analysis of the annual precipitation accumulation (March and April) can be viewed in Figure 3.3. The results indicated an average precipitation accumulation of 108 mm.

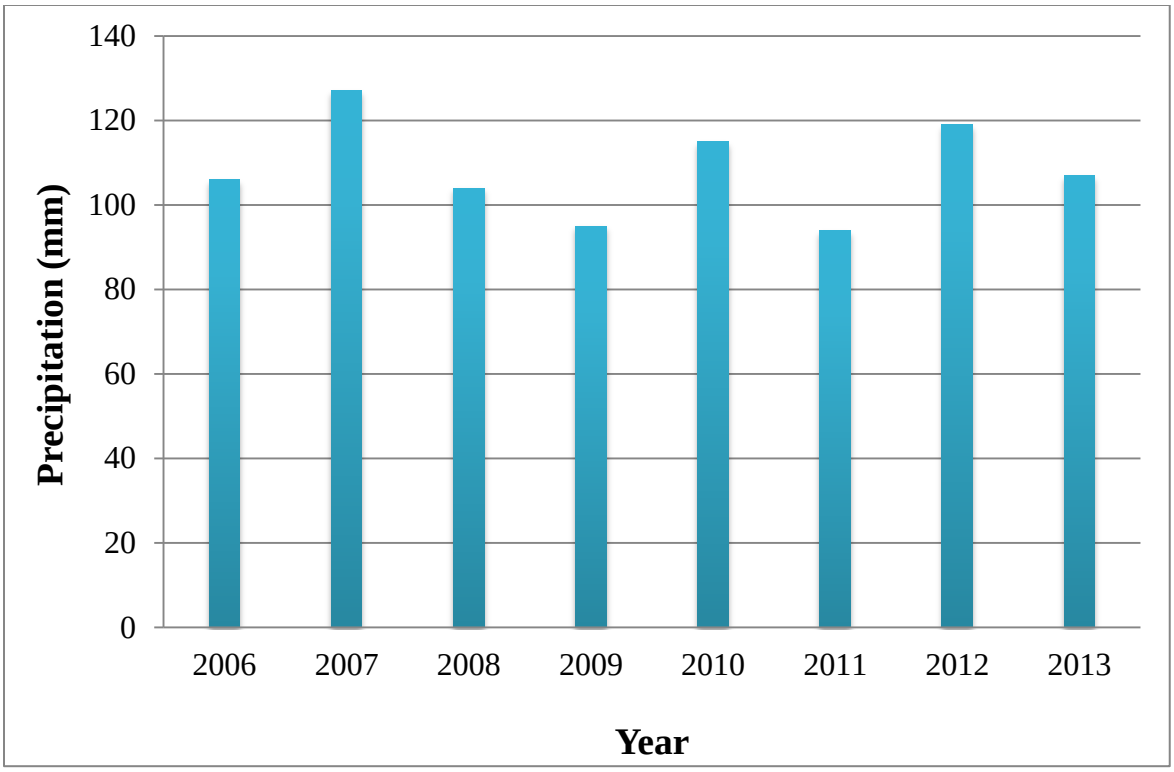


Figure 3.3: Annual precipitation accumulation for the months of March and April (2006 to 2013) at the Hay Meadow station.

The location of KES is known to local residents as often being subjected to reduced precipitation due to topographic influences. During the study, no major precipitation event occurred, so results were limited to events producing modest precipitation. In comparison to archived temperature and precipitation data, the year 2015 was warm and dry, with March – April 2015 having above normal temperatures and substantially low precipitation amounts. Results will be further discussed in a subsequent section.

### 3.2 Upper Analysis Data

Upper analysis maps were retrieved from the University Corporation for Atmospheric Research (UCAR) website (see http://www2.ucar.edu/). Maps are available at 0000 UTC and 1200 UTC from 850 to 300 mb. The operational surface pressure analysis maps were retrieved

from the National Oceanic and Atmospheric Administration (NOAA) – Weather Prediction Center (WPC) website (see http://www.wpc.ncep.noaa.gov). The maps are archived every 3 h and are available from 2005.

### 3.3 Radiosonde System

The radiosonde system began operating on March 28 and observations were made when precipitation was present at KES. To obtain measurements of the vertical atmospheric profile, radiosondes were released every 3 – 6 h during precipitation events from the field site. However, several launches did not record wind data due to a technical issue.

Radiosonde data were analyzed using the Universal Rawinsonde Observation program (RAOB). The program was used to analyze the 1000 – 500 m thickness of the profiles as well as the surface based convective available potential energy (CAPE) of the total atmosphere. Cloud layers were determined with the RAOB Integrated Cloud and Precipitation System (RICAPS). RICAPS calculates the location of clouds using a series of scans and a combination of temperature, dew point, relative humidity, wet-bulb temperatures, frost point temperatures, and lapse rates (RAOB, 2008).

### 3.4 Radar Data

Archived radar images were retrieved from the historical climate data portion of the Environment and Climate Change Canada (ECCC) website, producing images at 10 min intervals (see http://climate.weather.gc.ca/radar/index_e.html). The Strathmore radar provides complete coverage of the KES location with images available from 2007.

### 3.5 Weather Station Data

A surface weather station provided by ECCC was operated at KES. The weather station was installed at an elevation of 1447 m MSL and began recording data on March 17 at 2140 UTC to March 23 at 1705 UTC at 5 min intervals. The frequency was increased to 1 min intervals from March 24 at 2057 UTC to April 30 at 1621 UTC. Observations included temperature, relative humidity, wind speed, wind direction, sea level and surface pressure, and precipitation accumulation. Wind speed and direction sensors were mounted at 3 m AGL and temperature and humidity sensors at 0.9 m AGL.

As previously mentioned, a surface weather station operated by KBA has been recording data at KES since 2005. During the field campaign, the station was 41.2 m from the ECCC station at an elevation of 1446 m MSL. The KBA wind speed and direction sensors are mounted at 10 m AGL and temperature and relative humidity at 2 m AGL. The observations include temperature, relative humidity, wind speed, wind direction, and precipitation at either yearly, monthly, daily, or hourly periods. The hourly data are a calculation of the average values recorded from the previous 59 min, prior to the top of the hour (B. Kochtubajda, personal communication, June 6, 2016). The KBA station does not automatically adjust for Daylight Savings Time (occurred on March 8, 2015); therefore the data were adjusted forward 1 h for precise measurements and results (P. Vaquer, personal communication, June 27, 2016). Precipitation is measured using the tipping bucket type rain gauge. However, precipitation data are only available during the summer months.

### 3.6 Microphotography Data

Photographing precipitation particles followed the same technique as described by Gibson and Stewart (2007) and Theriault et al. (2014), utilizing a collection pad covered with black velvet to collect frozen particles. High-resolution images were produced using a 10.2 megapixel Nikon D80 digital SLR camera equipped with a 60 mm macro lens set at its shortest focus and a mounted portable flash.

### 3.7 Manual Observation Data

Manual weather observations were also made at KES. Observations of precipitation conditions, cloud cover, temperature, relative humidity, wind speed, wind direction, and surface pressure were generally recorded at 10 min intervals. Comments regarding conditions at the site and particles observed on the vehicle or surface prior to melting were also noted.

### 3.8 Instrument Location

This section provides the coordinates of the instruments utilized in this thesis (Table 3.1). The precipitation instrument is not listed due to an error in the recorded coordinates. The Magellan Explorist 110 GPS device was used to determine the instrument coordinates and Google Earth was used to determine the coordinates of the KBA station. The placement of the stations and instruments with respect to the buildings and forest can be viewed in Figure 3.4 (a – b). Images of the instruments can be viewed in Appendix A.

Table 3.1: List of the instruments, coordinates, and elevation.

| Instrument | Latitude (North) | Longitude (West) | Elevation AGL (m) |
|---|---|---|---|
| **Sounding instrument 1** | 50.927849 | -115.124590 | 1446 |
| **Sounding instrument 2** | 50.927848 | -115.124599 | 1446 |
| **Hay Meadow station** | 50.944101 | -115.138903 | 1430 |
| **KBA station** | 50.927787 | -115.124313 | 1447 |
| **ECCC station** | 50.927940 | -115.124449 | 1447 |


Figure 3.4: a) Location of the weather stations and b) placement of the instruments at KES. 50.928421, -115.125276. Google Earth. September 23, 2012. Retrieved on October 4, 2016.

### 3.9 Methodology

In total, 17 precipitation events of snow, rain, and mixed precipitation were recorded at KES during the field campaign (Table 3.2). For optimal results, the focus is placed on 11 events. The 11 events contain microphotography observations (7 events) and manual observations that do not contain photos when winter precipitation was observed at the surface above 0°C (4 events). From this point on in the thesis, only the bolded and italicized precipitation events will be discussed.

Table 3.2: List of the 17 precipitation events. Bolded events contain microphotography observations; Italicized events include manual observations that do not contain photos.

| Date | Precipitation Type |
|---|---|
| **Mar 15 - 16** | **Snow** |
| **Mar 21 - 22** | **Rain/Snow** |
| *Mar 23* | *Snow* |
| Mar 28 | Rain |
| Mar 29 - 30 | Rain |
| Mar 31 | Rain/Snow |
| Apr 1 - 2 | Snow |
| **Apr 4 - 5** | **Snow** |
| *Apr 6* | *Snow* |
| **Apr 11 - 12** | **Snow** |
| **Apr 14 - 15** | **Snow** |
| Apr 17 | Rain |
| **Apr 18** | **Snow** |
| *Apr 22 - 23* | *Rain/Snow* |
| *Apr 24 - 25* | *Snow* |
| **Apr 25 - 26** | **Snow** |
| Apr 29 | Rain |

### 3.9.1 Microphotography Observations

Operating the microphotography equipment was shared among 9 researchers during the two-month campaign. Particles were photographed approximately every 10 min during precipitation events using a collection pad covered with black velvet, producing up to 9 images during each collection. The collection interval ranged from 10 s up to several minutes based on the intensity of the event. After each collection interval, the pad was then taken into a ventilated tent to be photographed. Similar to Theriault et al. (2014) description, the camera was attached to a vertical mount that was attached to a metal base. An adjustable elevated stand, attached to the metal base was used for focusing, as seen in Figure 3.5 (a) to achieve a clear image. The metal base contains markings that act as a guide to consistently photograph the center of the pad to

produce a set of images that are a centimeter apart as shown in Figure 3.5 (b). A crank attached to the metal base was used to move the elevated stand from left to right (Theriault et al., 2014). For example, the instrument would be set to ‘1 start’ and the collection pad would move to each point on the ruler to be photographed. After a set of 3 images have been photographed, the collection pad would then move to position ‘2’ and the same steps would be repeated until the final positions are at ‘3 stop’.

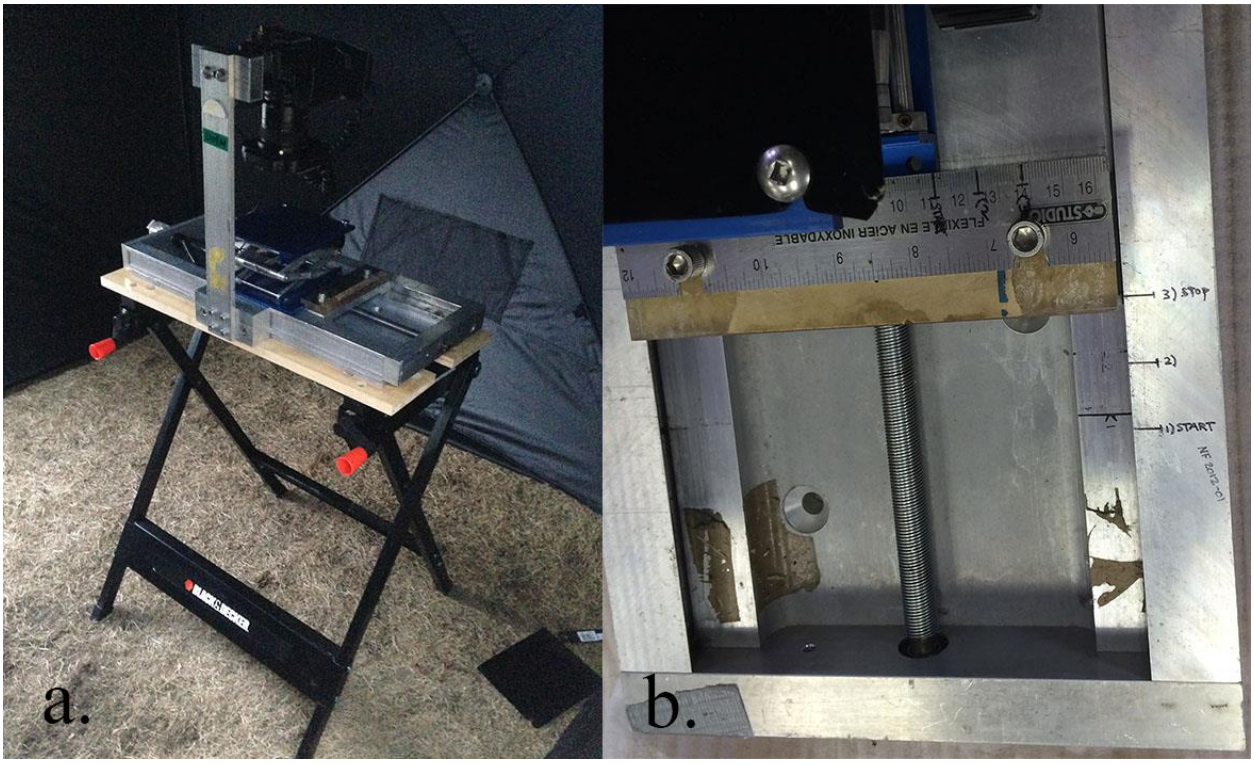


Figure 3.5: Microphotography observation set up of: (a) a stand used to photograph detailed characteristics of precipitation particles and (b) measurements on the stand were used as a guide.

As a reference for scale, a ruler was photographed during each event or a prescribed setting on the camera mount was used. However, the exceptions were the events on March 21 – 22 and April 18 where a ruler was not photographed, seen in Table 3.3. Rulers photographed from events closest to these dates were used for analysis which assumes that the adjustable

elevated stand was left in the same state. Therefore, the rulers photographed on March 15 – 16 and April 4 – 5 was used when analyzing the March 21 – 22 event. The rulers photographed on April 14 – 15 and April 25 – 26 was used to analyze the April 18 event.

Table 3.3: Summary of the photographed rulers used in the precipitation events containing microphotography observations.

| Event | Photographed Ruler | Pixels per 1 mm (px) | Photographed Ruler Used | Number of Pixels used (px) |
|---|---|---|---|---|
| **Mar 15 - 16** | Yes | 135 | Mar 15 - 16 | 135 |
| **Mar 21 - 22** | No | -- | Mar 15 - 16 & Apr 4 - 5 | 135 & 98 |
| **Apr 4 - 5** | Yes | 98 | Apr 4 - 5 | 98 |
| **Apr 11 - 12** | Yes | 158 | Apr 11 - 12 | 158 |
| **Apr 14 - 15** | Yes | 151 | Apr 14 - 15 | 151 |
| **Apr 18** | No | -- | Apr 14 - 15 & Apr 25 - 26 | 151 & 140 |
| **Apr 25 - 26** | Yes | 140 | Apr 25 - 26 | 140 |

#### 3.9.1.1 Melting Particles

Several events contained precipitation particles that melted rapidly once in contact with the velvet pad, the surface of the ground, or the window of the vehicle. Such conditions were not ideal for microphotography images as the particles melted before being photographed. As a result, microphotography observations were insufficient and researchers used manual observations to describe the characteristics of the particles. Manual observations will be further discussed in later subsections.

### 3.9.2 Ice Crystal and Solid Precipitation Particle Categories

A researcher analyzed each image by eye using the Adobe Photoshop CS6 software. A point was placed on each ice crystal and solid precipitation particle using the Pen Tool to avoid duplication when tallied and categorized.

Precipitation particles were organized into general categories adapted from the Kikuchi et al. (2013) classification of ice crystals and solid precipitation particles (see Appendix B). For organizational purposes for this study, the particle, ‘irregular particles’ was placed into the irregular snow particle category, originally in the germ of ice crystals (Kikuchi et al., 2013). Graupel particles in the rimed snow crystals category (Kikuchi et al., 2013) were placed into the snow pellets category; created for organizational and simplification purposes.

This study only discusses the ice crystals and solid precipitation particles from Kikuchi et al. (2013) that were observed at KES. Table 3.4 lists the categories and particles that have been examined as well as the elementary names. The complete list of categories and their elementary names can be found in Appendix C which was adapted from Kikuchi et al. (2013).

For this study, twelve categories were slightly adapted from Kikuchi et al. (2013) to organize the particles. Six of the categories were of rimed particles and the other six were unrimed particles. Figure 3.6 illustrates the categories into which the particles may be placed.

Table 3.4: A list of the unrimed and rimed ice crystal and solid precipitation particle categories slightly adapted from Kikuchi et al. (2013). The bolded names are the changes made for this study.

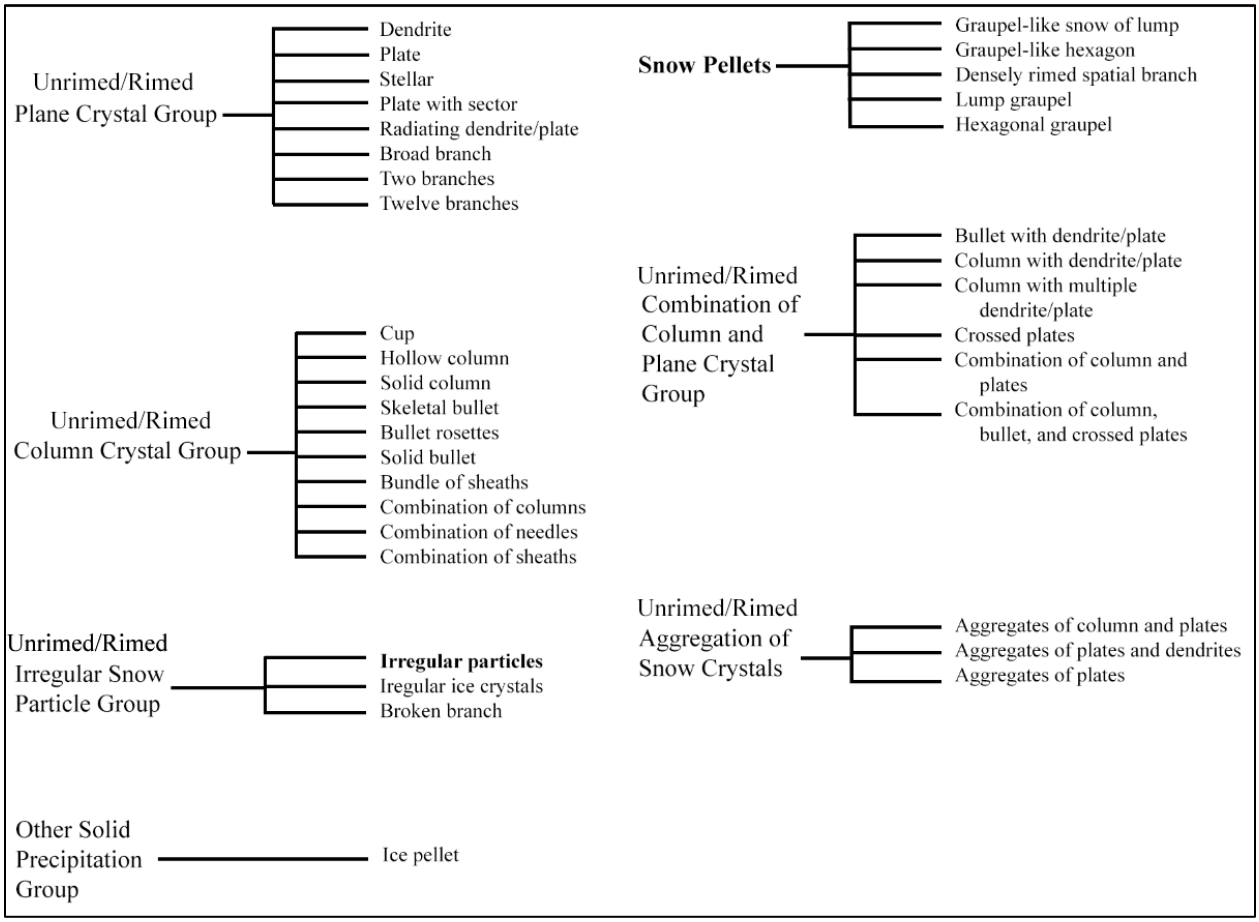

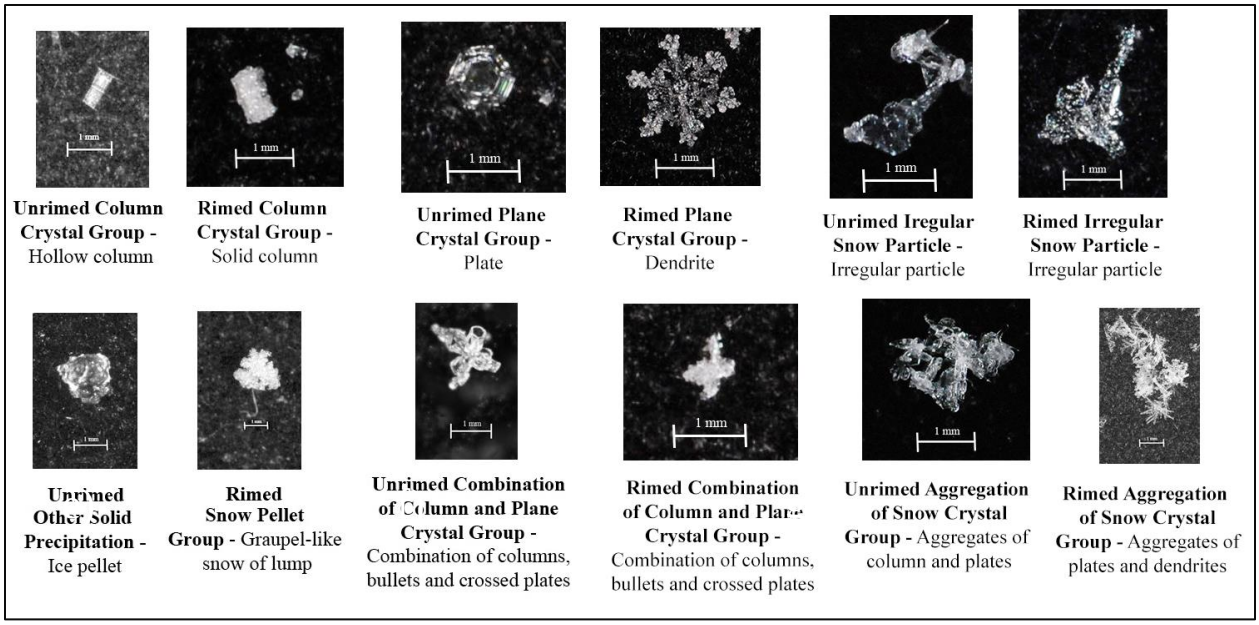


Figure 3.6: Unrimed (left) and rimed (right) categories of the ice crystals and solid precipitation particles. The general category name (bold) and the type of particle are described under each image.

### 3.9.3 Temperature and Humidity Data

The ECCC station 5 min data (March 17 at 2140 UTC to March 23 at 1705 UTC) and 1 min data intervals (March 24 at 2057 UTC to April 30 at 1621 UTC) were utilized to determine the average hourly data from the previous 59 min. The average hourly ECCC station data were then compared to the hourly KBA station data. However, no comparison was made for the missing data on the March 15 – 16 and March 23 events.

For example purposes, the April 11 – 12 event was used to compare the station data. Figure 3.7 (a – b) compares the ECCC and KBA station data from 0000 to 2300 LST. 'ACIS' represents the KBA station and 'DataLogger' represents the ECCC station. To examine specifically when precipitation events occurred, additional plots were made to compare the station data in UTC (Figure 3.8 a – b). Comparison of all precipitation events can be found in Appendix D.

Overall, the ECCC station and the KBA station temperature were in close agreement during cloudy conditions on site (J. Theriault, personal communication, May 16, 2016). At times significant differences in data were observed when the two stations were compared. This may be due to the sensors being installed at different height levels as well as the ECCC station being installed in close proximity to buildings and a trailer. For optimal results, data collected from both stations were listed in this thesis (Table 3.5).

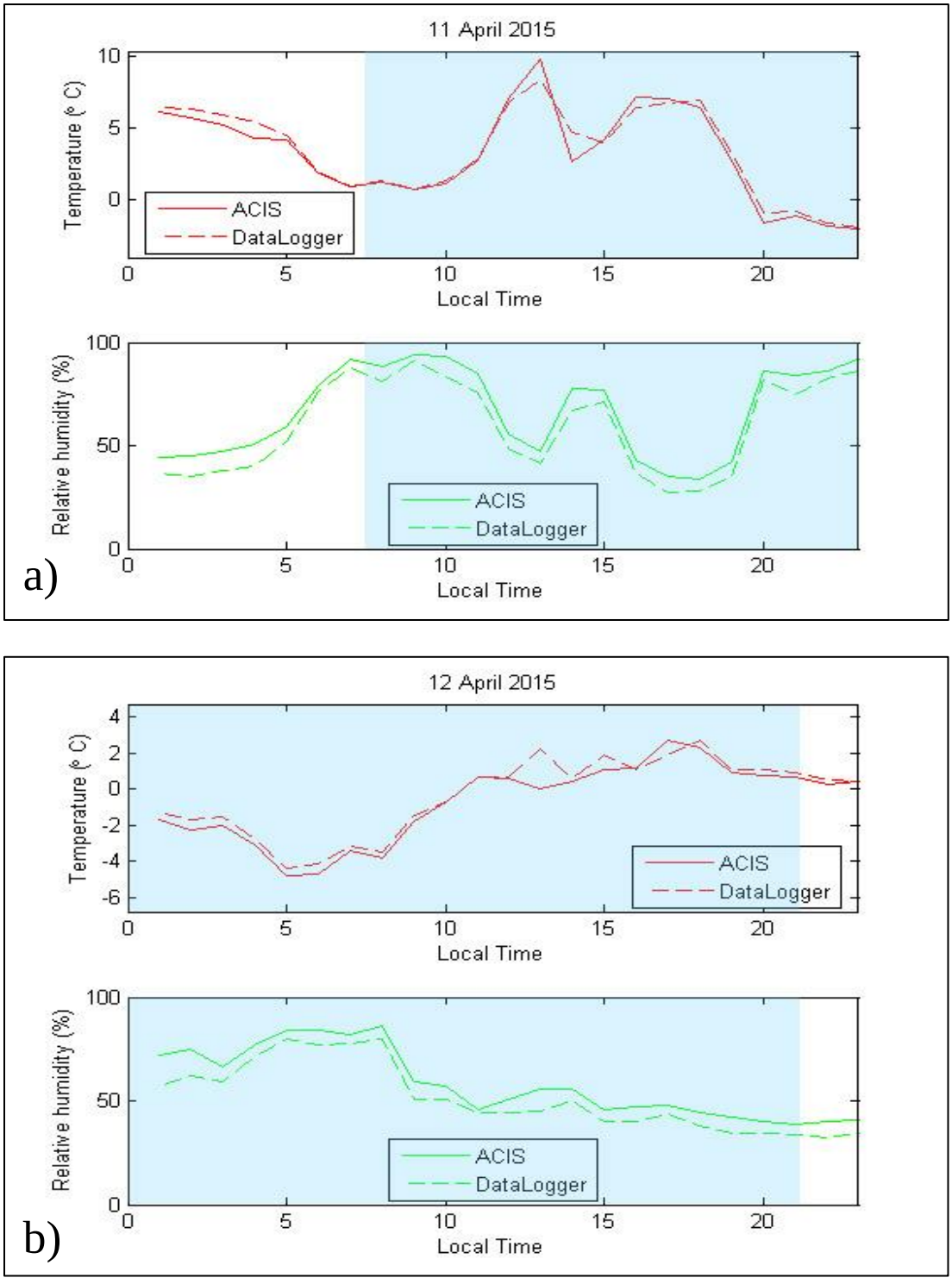


Figure 3.7: Temperature (red) and relative humidity (green) difference on a) April 11 and b) April 12 between the ECCC station (datalogger) and KBA station (ACIS). Observation periods are shown in blue shading. (P. Vaquer, personal communication, June 27, 2016).

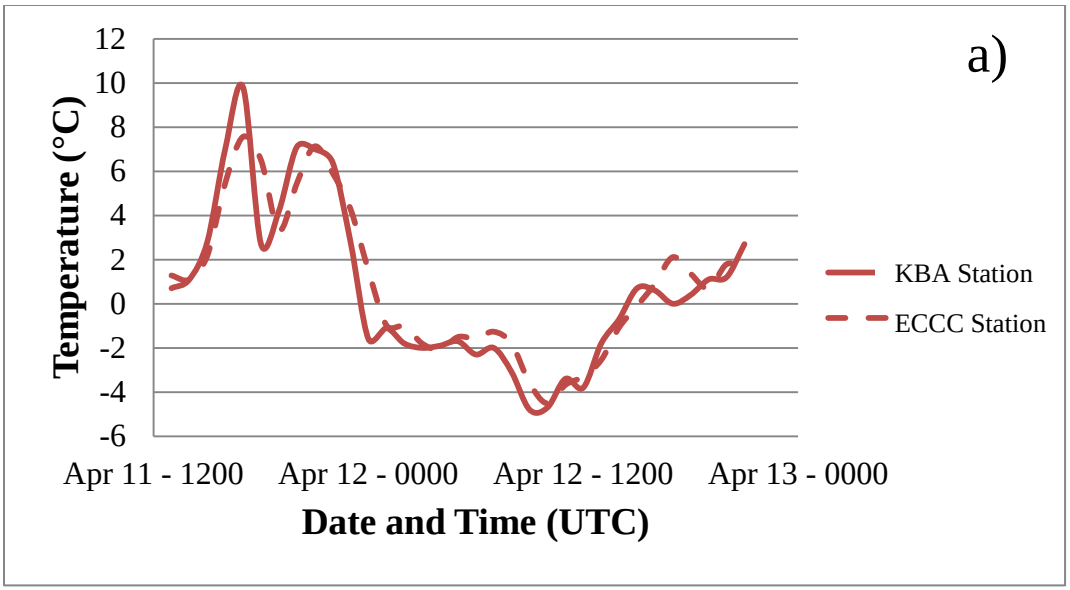


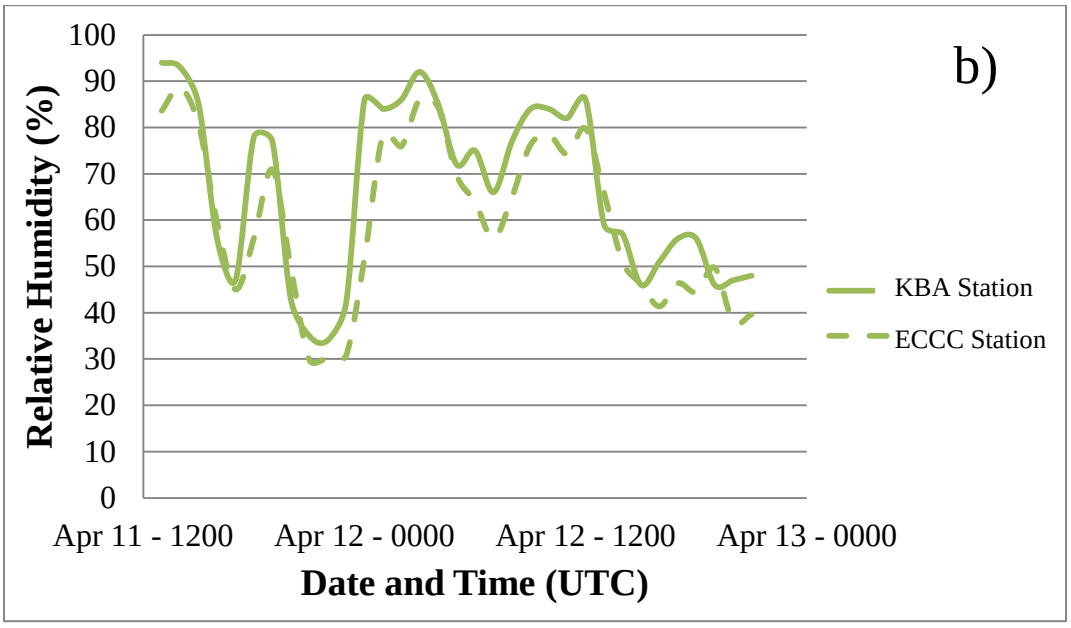


Figure 3.8: a) Temperature (red) and b) relative humidity (green) difference on April 11 – 12 between the ECCC station and KBA station when observations commenced on site.

Table 3.5: A list of the average temperature and relative humidity during observation periods for the ECCC station data (first) and the KBA station data (second). Bolded events include microphotography observations; italicized events included manual observations that do not contain photos.

| Event | Average Temperature (°C) | Average Relative Humidity (%) |
|---|---|---|
| **Mar 15 - 16** | **--/-1.2** | **--/90** |
| **Mar 21 - 22** | **--/2.7** | **--/85** |
| *23-Mar* | *--/0.3* | *--/83* |
| **Apr 4 - 5** | **-0.5/-1.3** | **83/90** |
| *6-Apr* | *-0.5/-2.3* | *62/75* |
| **Apr 11 - 12** | **2.0/1.9** | **63/71** |
| **Apr 14 - 15** | **3.2/2.9** | **76/83** |
| **Apr 18** | **1.6/2.4** | **79/85** |
| *Apr 22 - 23* | *9.9/10.4* | *42/48* |
| *Apr 24 - 25* | *6.3/5.5* | *49/58* |
| **Apr 25 - 26** | **3.4/3.4** | **65/69** |

### 3.9.4. Wind Speed and Direction

This section compares the wind data during precipitation events. A summary of the average wind speed and wind direction of the ECCC station and KBA station can be viewed in Table 3.6. As previously mentioned, ECCC wind data were unavailable for the March 15 – 16 and March 23 events as the station was not recording data when these events occurred.

The examined wind speeds varied per precipitation event. Of the events examined, the average wind speed was 7.0 km/h. The average wind direction was 155° (southeasterly). The event with the highest average wind speed was 11.2 km/h on April 25 – 26 as seen in Table 3.6.

The KBA average wind speeds during precipitation events are much higher than the average ECCC station. This may be due to the KBA station wind sensor being mounted higher

than the ECCC station wind sensor (10 m AGL at the KBA station, 3 m AGL at the ECCC station, respectively).

Table 3.6: A list of the average wind speed and wind direction during observation periods for the ECCC station data at 3 m AGL (first entry), and the KBA station data at 10 m AGL (second entry). Bolded events include microphotography observations; Italicized events included manual observations that do not contain photos.

| **ECCC – 3 m AGL / KBA – 10 m AGL** | | |
|---|---|---|
| **Date** | **Wind Speed (km/h)** | **Wind Direction (°)** |
| **Mar 15 - 16** | --/5.5 | --/145 |
| **Mar 21 - 22** | 4.3/6.1 | 208/201 |
| *23-Mar* | *--/6.1* | *--/160* |
| **Apr 4 - 5** | 1.9/6.2 | 155/98 |
| *6-Apr* | *2.8/4.7* | *165/197* |
| **Apr 11 - 12** | 5.7/7.9 | 179/210 |
| **Apr 14 - 15** | 2.5/6.6 | 137/104 |
| **Apr 18** | 2.7/5.5 | 184/161 |
| *Apr 22 - 23* | *7.3/7.8* | *112/212* |
| *Apr 24 - 25* | *5.1/8.7* | *179/174* |
| **Apr 25 - 26** | 5.1/11.2 | 198/41 |

The wind direction and wind speed data were utilized from the ECCC station and KBA station. Wind rose graphs were produced using the Lakes Environmental Wind Rose Plots software. For example purposes, Figure 3.9 are the wind rose plots from the April 4 – 5 event. Additional wind rose plots comparing the 2 stations can be found in Appendix E.

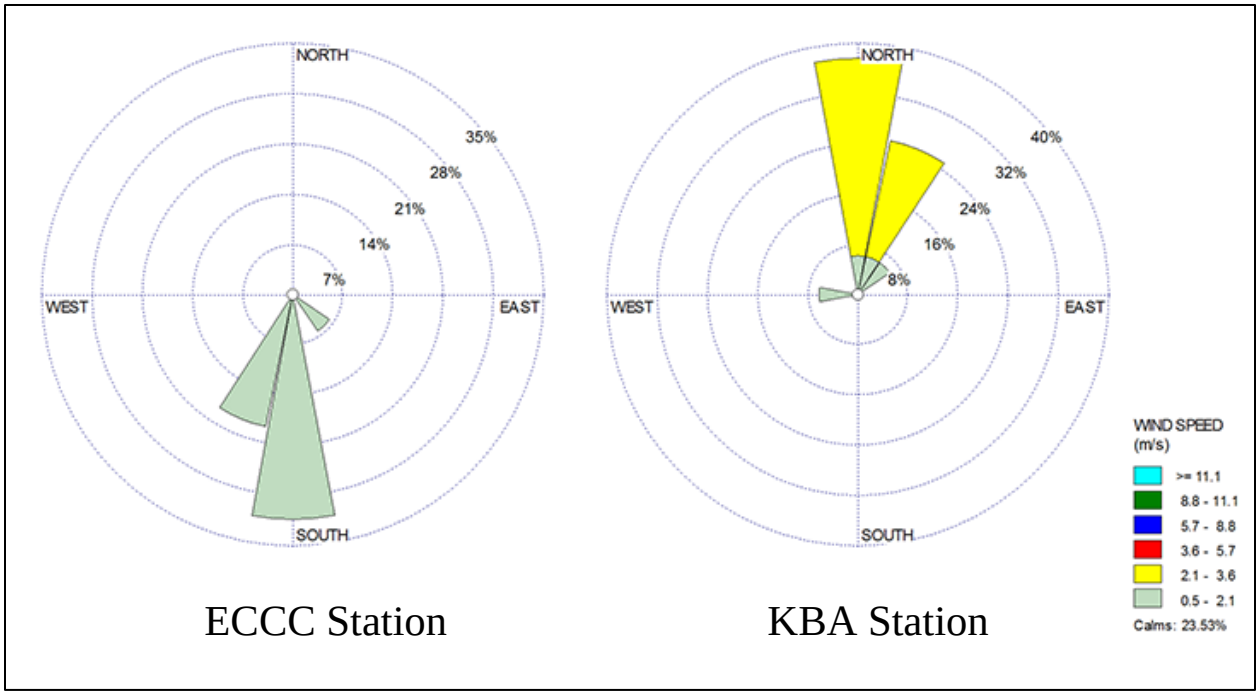


Figure 3.9: A wind rose plot during the precipitation event on April 4 – 5. The left plot is the ECCC Station and the right is the KBA station.

This study will utilize the KBA wind data to achieve optimal results. The KBA wind data are ideal due to the installation of the instrument at a standard exposure height and is not obstructed by buildings.

### 3.9.5 Manual Observation Data

Manual observations were usually recorded at 10 min intervals during precipitation events. The task of manual observations was interchanged between 9 researchers throughout the campaign. It should be noted that not all of the manual observations included the type and/or size of the ice particles observed at the surface, or other notable details.

One of the variables included documenting precipitation conditions of the precipitation intensity using one's own judgement. A scale was made to differentiate the precipitation intensity as seen in Table 3.7. The precipitation intensity is an approximate measurement where

it was based on visibility. For example, light precipitation (1) was considered if the distance of visibility was high. In contrast, heavy precipitation (3) was considered if the distance of visibility was low.

Table 3.7: Summary of the precipitation intensity scale.

| Scale | Precipitation Scale |
|---|---|
| **0** | No precipitation |
| **1** | Light precipitation |
| **2** | Moderate precipitation |
| **3** | Heavy Precipitation |

# Chapter 4 – Precipitation Observations and Interpretations

## 4.1 Overview

Ambient meteorological conditions were recorded at KES during the field campaign. Temperature data obtained from the KBA station indicated an average of 2.6°C during March and April 2015, 3.7°C warmer than the average. The average relative humidity was 63%, 6% lower than the average. The warmest temperature recorded during the field campaign was 23.7°C on April 28 at 2000 UTC and the coldest temperature was on March 17 of -11.8°C at 1300 UTC.

Precipitation accumulation at KES (ECCC station data) was a total of 18 mm from March 24 to April 30, significantly lower than the climate data from Hay Meadow station (108 mm). Particular events on April 6, April 24 – 25, and April 25 – 26 indicated 0 mm of precipitation accumulation, however, winter precipitation particles were observed at the surface and microphotography observations were recorded on April 25 – 26. It should be noted that the precipitation intensity during these 3 events was ‘light’. Therefore precipitation accumulation may not have been detected by the precipitation sensor.

A summary of the maximum, minimum, and average temperature from the beginning to end of observations for each event is provided in Table 4.1. The warmest event of 9.9°C (10.2°C at the KBA station) occurred on April 22 – 23, and the coldest event of -0.5°C (-2.3°C at the KBA station) was on April 6. The duration of each event varied, with the longest occurring on March 15 - 16 for 21 h, and the shortest event on March 23 for 3 h.

Table 4.1: A summary of the 11 precipitation events using the ECCC station data and the KBA station data. The first entry is the ECCC station data and the second entry after the forward slash is the KBA station data. The bolded events represent the 7 precipitation events containing microphotography observations. The events in italics represent the 4 precipitation events examined using manual observations.

| Event | Duration of event (h) | Maximum Temperature (°C) | Minimum Temperature (°C) | Average Temperature (°C) | Average Precipitation Accumulation (mm) |
|---|---|---|---|---|---|
| **Mar 15 - 16** | **21** | **--/4.7** | **--/-3.6** | **--/-1.2** | **--/--** |
| **Mar 21 - 22** | **11** | **--/10.0** | **--/-1.8** | **--/2.7** | **--/--** |
| *Mar 23* | *3* | *--/2.8* | *--/-1.3* | *--/0.3* | *--/--* |
| **Apr 4 - 5** | **15** | **5.5/2.1** | **-3/-3.1** | **-0.5/-1.3** | **2.4/--** |
| *Apr 6* | *6* | *3.9/2.0* | *-5.7/-6.8* | *-0.5/-2.3* | *0/--* |
| **Apr 11 - 12** | **20** | **8.7/9.8** | **-2.5/-2.3** | **2/1.9** | **1/--** |
| **Apr 14 - 15** | **11** | **9.5/8.1** | **0.5/-0.9** | **3.2/2.9** | **3.2/--** |
| **Apr 18** | **16.75** | **9/7.9** | **0.5/-0.7** | **1.6/2.4** | **2.7/--** |
| *Apr 22 - 23* | *7* | *16.4/16* | *5.2/6.4* | *9.9/10.4* | *0.2/--* |
| *Apr 24 - 25* | *11* | *11.3/10.8* | *-0.1/-0.4* | *6.3/5.5* | *0/--* |
| **Apr 25 - 26** | **6** | **10.2/8.6** | **0.1/-0.3** | **3.4/3.4** | **0/--** |

A total of 1,183 images were collected and analyzed, with 17,504 ice crystals and solid precipitation particles. The April 4 – 5 event contained the largest number of ice crystals and solid precipitation particles as well as the most images collected (Table 4.2). The least number of images and particles collected was during the March 21 – 22 event. The March 15 – 16 event contained the greatest average number of particles per image (22 particles) and the March 21 – 22 event contained the least (2 particles).

Table 4.2: A summary of the 7 precipitation events containing microphotography images.

| Event | Number of Images | Number of Particles | Average Number of Particles per Image |
|---|---|---|---|
| **Mar 15 - 16** | 258 | 5760 | 22 |
| **Mar 21 - 22** | 16 | 36 | 2 |
| **Apr 4 - 5** | 503 | 8289 | 16 |
| **Apr 11 - 12** | 162 | 1242 | 9 |
| **Apr 14 - 15** | 184 | 1894 | 10 |
| **Apr 18** | 25 | 118 | 5 |
| **Apr 25 - 26** | 50 | 154 | 3 |

## 4.2 Ice Crystals and Solid Precipitation Particles

The following subsections will examine the unrimed and rimed ice crystals and solid precipitation particle categories photographed during the study. Of the total ice crystals and solid precipitation particles examined (17,504), 63% were rimed.

### 4.2.1 Unrimed Ice Crystals and Solid Precipitation Particles

Unrimed ice crystals and solid precipitation particles occurred less frequently in comparison to rimed particles. However, a large number of unrimed particles occurred during the March 15 – 16 event, producing a variety of ice crystal and solid precipitation particles. Figure 4.1 illustrates the distribution of the unrimed ice crystals and solid precipitation particles.

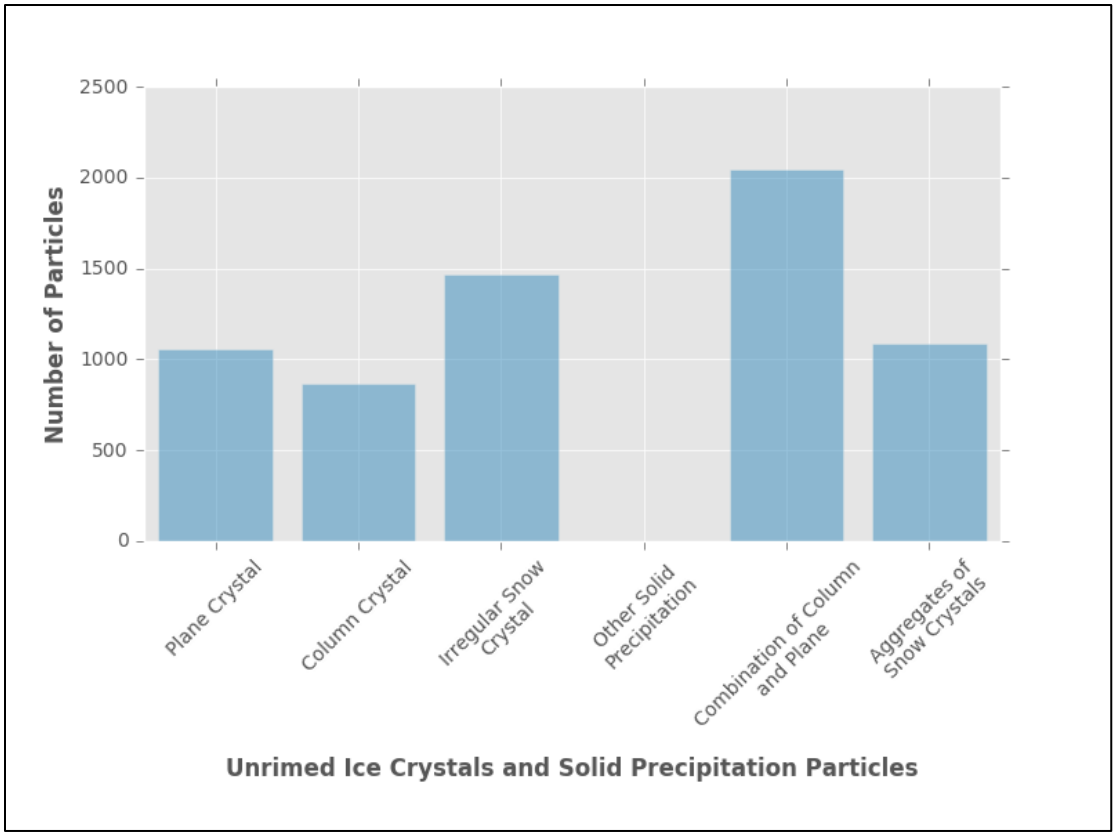


Figure 4.1: Number of unrimed ice crystals and solid precipitation particles photographed from March to April 2015.

The unrimed combination of column and plate particles were the most common (2,043 particles), with 98% of the particles occurring during the March 15 – 16 event. The second most common category was the unrimed irregular snow particles (1,470 particles), with the majority of particles also occurring on the March 15 – 16 event. The other solid precipitation category occurred least frequently where only 1 particle was examined during the April 14 – 15 event.

Graphs were created to illustrate the types of unrimed particles within the categories. These graphs can be found in Appendix F.

### 4.2.2 Rimed Ice Crystals and Solid Precipitation Particles

Rimed ice crystals and solid precipitation particles were a common occurrence during precipitation events. A large number of rimed particles were observed during the April 4 – 5 event. Figure 4.2 shows the distribution of the rimed ice crystals and solid precipitation particles.

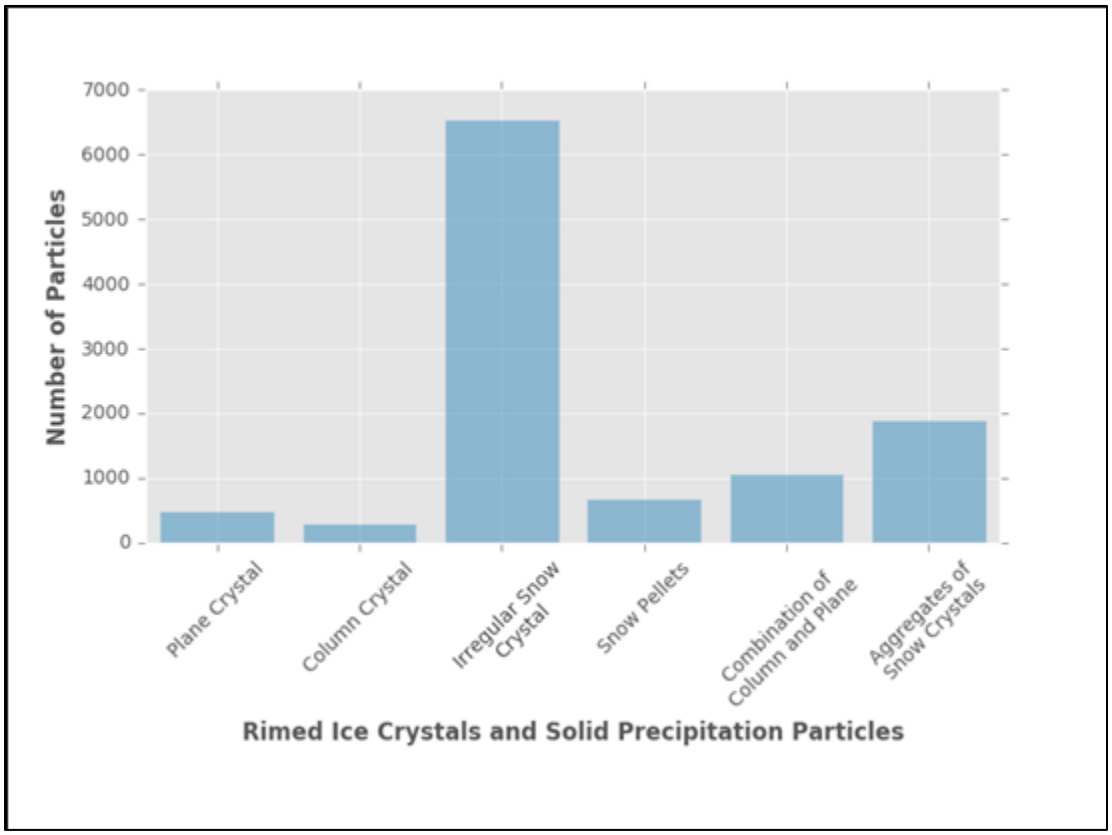


Figure 4.2: Number of rimed ice crystals and solid precipitation particles photographed from March to April 2015.

Rimed irregular snow particles category occurred most frequently (6,529 particles), with 74% of the particles occurring on the April 4 – 5 event. The second most common rimed category was the rimed aggregates of snow crystals (1,884 particles), with the majority of particles also occurring on the April 4 – 5 event. The rimed column crystals occurred least frequently throughout the study (300 particles).

Additional graphs were created to illustrate the types of rimed particles within the categories. These graphs can be found in Appendix G.

### 4.3 Unusual Particles

An unusual particle type referred to as a twelve-branched dendrite was examined in some images. Nakaya (1954) believed twelve-branched dendrites were formed by two overlapped dendrites. Kobayashi and Furukawa (1974) continued the study and found that there are two types of these snow crystals. The first being centred twelve-branched dendrites when each point develops from the centre and the angle between each branch is equal. The second type is an off-centred twelve-branched dendrite when the two centres are located a distance apart. Kobayashi and Furukawa (1974) suggest a twelve-branched dendrite forms through the collision of a "primary" dendrite crystal and a supercooled droplet that develops into a "secondary" dendrite. They state that a centred twelve-branched dendrite forms during the early growth stages of the "primary" dendrite through the overlapping of two dendrite crystals by the process of aggregation.

Among the 17,504 particles examined, only 4 twelve-branched dendrites were identified over the two-month study. Twelve-branched dendrites were photographed on April 4 at 2323 UTC and on April 5 at 0334 UTC, 0341 UTC, and 0512 UTC as seen in Figure 4.3. The dendrite at 0512 UTC of Figure 4.3 (d) had only 11 branches, possibly due to overlapping. The average temperature when the twelve-branched dendrites were photographed at the surface was -1.7°C (-2.5°C at the KBA station) with an average relative humidity of 92% (99% at the KBA station). The crystals photographed at 2323 UTC and 0512 UTC are unclear whether they are centred or

off-centred dendrites. The crystals at 0334 UTC and 0341 UTC were photographed 7 min apart and appeared as though the branches developed from the centre of the crystal.

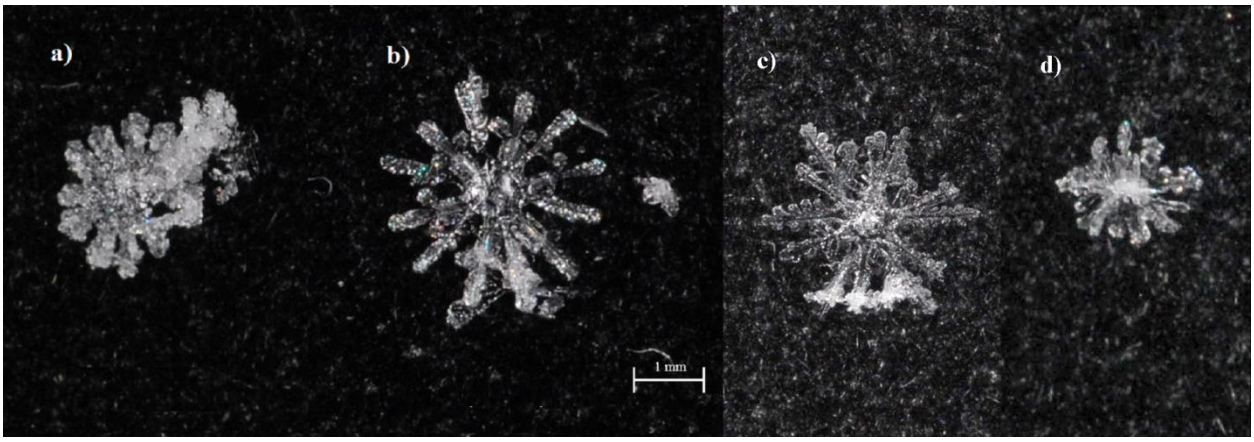


Figure 4.3: Twelve-branched dendrites photographed on April 4 at (a) 2323 UTC and April 5, 2015 at (b) 0334 UTC, (c) 0341 UTC, and (d) 0512 UTC.

### 4.4 Large Ice Crystals and Solid Precipitation Particles

Microphotography images were analyzed to identify the longest axis of a particle photographed during each precipitation event. The largest particles visible in the images were selected to be examined. The photographed rulers were used to measure these particles as described in Table 3.2. As previously mentioned, March 21 – 22 and April 18 do not contain a photographed ruler. The photographed rulers on March 15 – 16 and April 4 – 5 were used to measure the March 21 – 22 particle and the April 14 – 15 and April 25 – 26 rulers were used to measure the April 18 particle. However, due to the uncertainty of the magnification, the particles measured during the March 21 – 22 and April 18 events is an approximate measurement. The particles were measured with the photographed ruler on the Adobe Photoshop CS6 software by placing the ruler alongside the particle being examined.

Particles examined in the images were of a variety of types and sizes. The largest particles analyzed for each event are listed in Table 4.3. The average length of the particles measured was 12 mm. The largest particle was photographed on April 14 at 2220 UTC and measured 24 mm in length. The particle was of a rimed aggregate of plates and dendrites in the aggregation of snow crystals category as seen in Figure 4.4. The temperature at the surface when the particle was photographed was 1.2°C (2.2°C at the KBA station) with a relative humidity of 87% (81% at the KBA station). In a similar study, the largest particle recorded by Stewart et al. (1984) was > 11 mm across near 0°C in the California Valley.

Table 4.3: Largest particles photographed for each event. The first entry is the ECCC station data and the second entry after the forward slash is the KBA station data. The italicized events represent an approximate measurement of size.

| Event | Time (UTC) | Image (#) | Size (mm) | Temperature (°C) | Relative Humidity (%) | Particle Type |
|---|---|---|---|---|---|---|
| **Mar 15** | 2335 | 214 | 10 | --/-0.9 | --/93 | Unrimed aggregate of snow crystal - Aggregates of column and plates |
| ***Mar 22*** | *0806* | *26* | *3* | *--/-1.8* | *--/95* | *Rimed Plane Crystal – Radiating dendrite* |
| **Apr 05** | 0441 | 185 | 15 | -2.1/-2.4 | 93/98 | Rimed aggregate of snow crystal - Rimed aggregates of column and plates/dendrites |
| **Apr 11** | 1341 | 14 | 22 | 1.2/1.2 | 86/88 | Rimed aggregate of snow crystal - Rimed aggregates of plates and dendrites |
| **Apr 14** | 2220 | 42 & 47 | 24 | 1.2/2.2 | 87/81 | Rimed aggregate of snow crystal - Rimed aggregates of plates and dendrites |
| ***Apr 18*** | *1202* | *50* | *15 - 18* | *0.0/-0.4* | *95/100* | *Rimed aggregate of snow crystal - Rimed aggregates of column and plates/dendrites* |
| **Apr 25** | 0200 | 83 | 2 | 0.1/-0.3 | 78/83 | Rimed plane crystal - Heavily rimed plates |

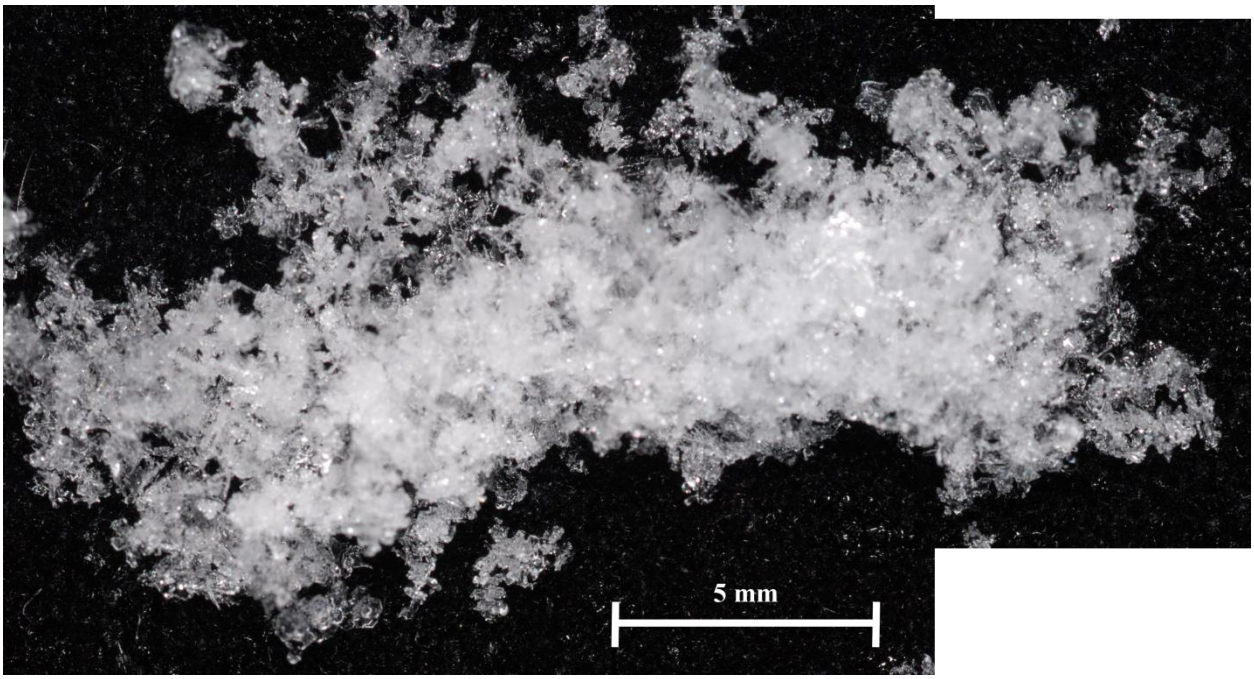


Figure 4.4: An image of a rimed aggregate of snow crystal - rimed aggregate of plates and dendrites photographed on April 14 – 15 at 2220 UTC.

The largest plane crystal was selected from each event, with the exception of the March 21 – 22 event when the particles were mainly snow pellets (73%). The average diameter of the plane crystals was 3 mm. The largest plane crystals were examined when temperatures were mainly above 0°C at the surface, ranging up to 9.6°C (7.5°C at the KBA station) as seen in Table 4.4.

The largest plane crystal was examined on April 4 at 2101 UTC. The particle type was a rimed dendrite and was 5 mm in diameter as seen in Figure 4.5. The temperature at the surface was 0.4°C (-0.6°C at the KBA station) with a relative humidity of 85% (91% at the KBA station).

Table 4.4: Largest dendrite or plate photographed during each event. The first entry is the ECCC station data and the second entry after the forward slash is the KBA station data. The italicized events represent an approximate measurement of size.

| Event | Time (UTC) | Image (#) | Size (mm) | Temperature (°C) | Relative Humidity (%) | Particle Type |
|---|---|---|---|---|---|---|
| **Mar 15** | 1956 | 125 | 3 | --/0.8 | --/80 | Plate |
| **Apr 04** | 2101 | 165 | 5 | 0.4/-0.6 | 85/91 | Rimed dendrite |
| **Apr 11** | 1402 | 37 | 2 | 0.8/0.7 | 91/94 | Rimed dendrite |
| **Apr 14** | 2100 | 97 | 3 | 0/5.5 | 92/67 | Rimed dendrite |
| ***Apr 18*** | *1110* | *32* | *3-4* | *0.3/0.0* | *95/100* | *Rimed dendrite* |
| **Apr 25** | 2000 | 60 | 3 | 9.6/7.5 | 37/50 | Rimed dendrite |

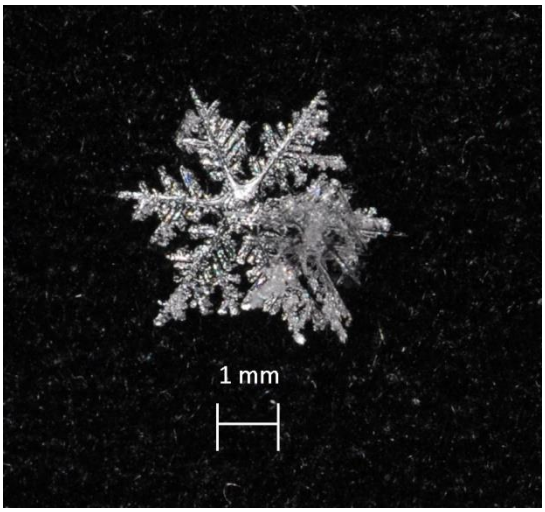


Figure 4.5: Largest rimed plane crystal - dendrite photographed on April 4 – 5 at 2101 UTC.

### 4.5 Precipitation Intensity and the Particle Types

This section examines the precipitation intensity, determined through manual observations that ranged from no precipitation (0) to heavy (3), as previously mentioned in section 3.9.5. Of the varying intensities examined, light intensity contained the most number of

observations (327) and moderate intensity contained the most particles identified (8,398 particles).

Particle categories in relation to precipitation intensity were also examined. All 12 particle categories were observed with moderate intensity. Heavy precipitation was the least observed with only 7 manual observations and 896 particles were identified. During heavy precipitation, only 8 out of 12 categories were examined. The missing categories were unrimed particles with the exception of unrimed irregular snow particles and unrimed aggregates of snow crystals as seen in Table 4.5. This indicates that the majority of particles identified during heavy precipitation were rimed and of large particles.

Table 4.5: Summary of the number of particles and categories during varying precipitation intensities.

| **Precipitation Intensity** | **Number of manual observations** | **Number of Particles** | **Number of Categories** | **Categories Not Identified** |
|---|---|---|---|---|
| **Light (1)** | 327 | 2,407 | 11/12 | Other solid precipitation |
| **Moderate (2)** | 39 | 8,398 | 12/12 | -- |
| **Heavy (3)** | 7 | 896 | 8/12 | Plane crystal, column crystal, other solid precipitation, and combination of column and plane |

Figures 4.6 (a – f) demonstrates the evolution of precipitation intensity from the initial observation on site to the end of the event. The events examined illustrated a large variation in precipitation intensity and provided an indication of how weather can change drastically in a short period of time. This was seen in the April 11 – 12 event (Figure 4.6c) where the intensity consistently fluctuated from no precipitation to heavy.

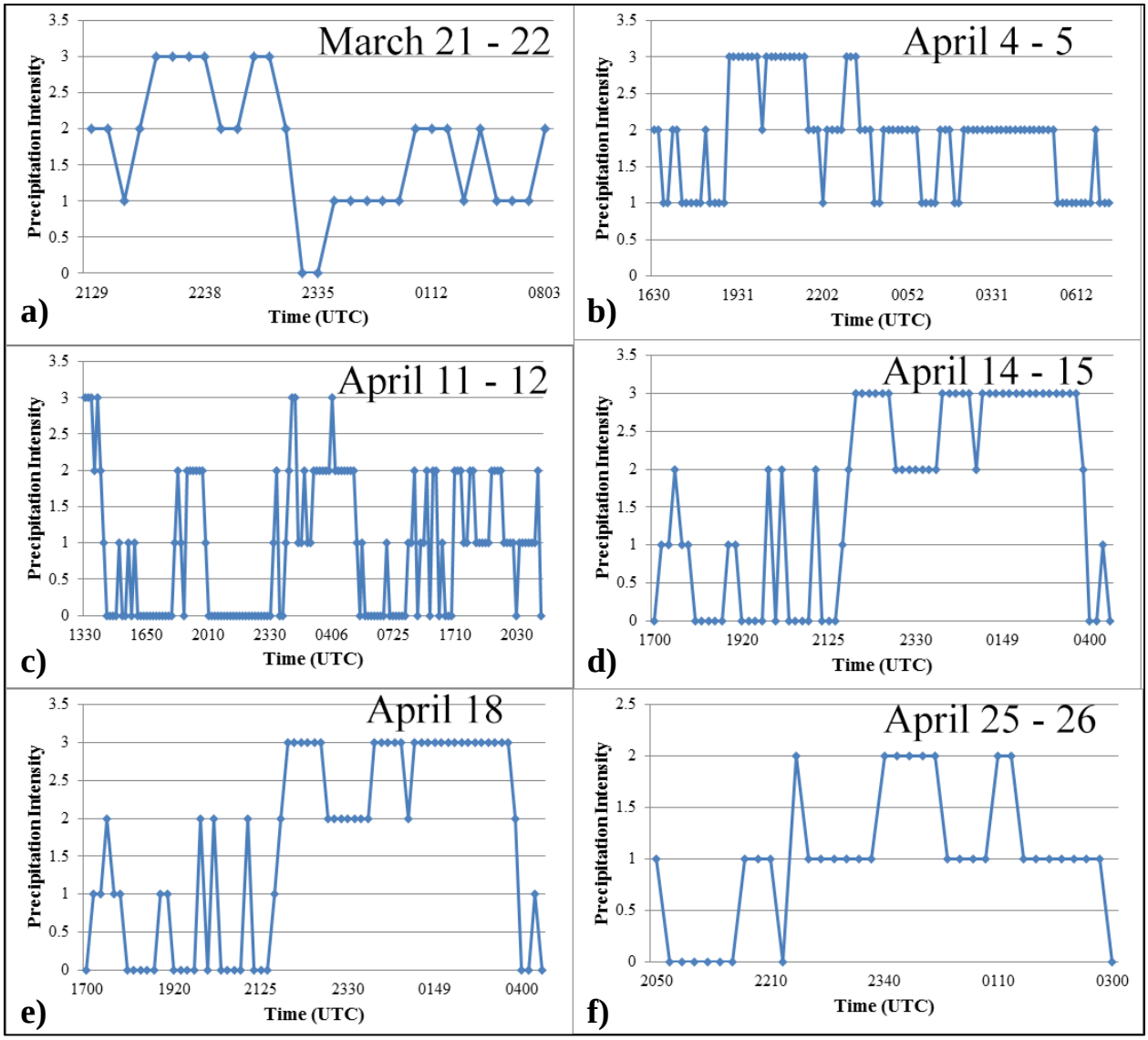


Figure 4.6: A qualitative assessment of the precipitation intensity examined during a) March 21 – 22, b) April 4 – 5, c) April 11 – 12, d) April 14 – 15, e) April 18, and f) April 25 – 26 using manual observations.

### 4.6 Rime Intensity

Rimed particles were examined in Adobe Photoshop and were placed into categories with respect to the riming degree. The riming degrees and riming descriptions were slightly adapted from the categories and descriptions of Barthazy and Schefold (2005, see also Table 4.6) of unrimed, lightly rimed, moderately rimed, and heavily rimed particles. A particle would be

considered moderately rimed if visible bumps appear on the surface from the frozen cloud droplets. An example of the various riming degrees is shown in Figure 4.7.

Table 4.6: Classification of the rime intensity on crystal surfaces.

| Riming Degree | Description |
|---|---|
| **Unrimed (0)** | No cloud droplet on the surface. |
| **Light Rimed (1)** | A few scattered cloud droplets on the surface. |
| **Moderate Rimed (2)** | The surface nearly or completely covered with droplets. |
| **Heavily Rimed (3)** | The original crystal shape is barely recognizable due to a heavy layer of droplets. |

The table was slightly adapted from Barthazy and Schefold (2005).

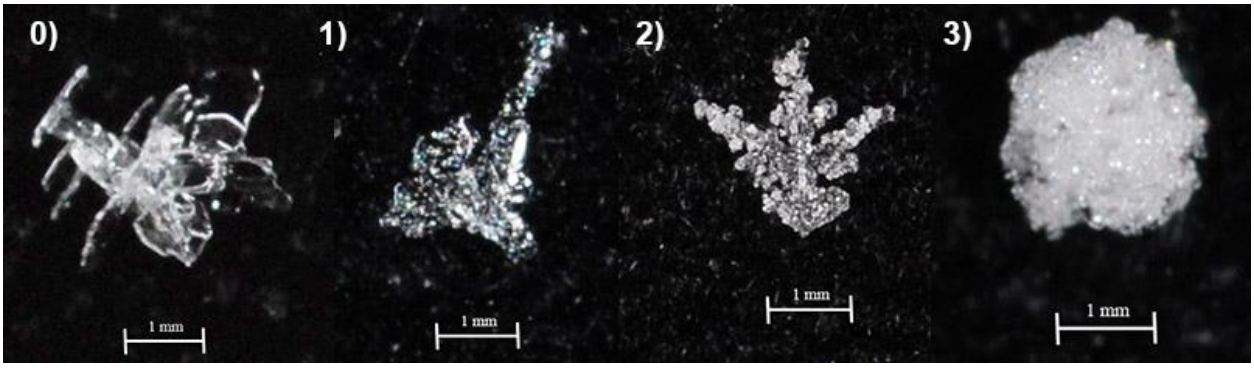


Figure 4.7: Examples of the rime intensities examined during the study. From the left: (0) unrimed photographed on March 15, 2015 at 2106 UTC, (1) light rime photographed on April 12, 2015 at 0829 UTC, (2) moderate rime photographed on April 5, 2015 at 0412 UTC, and (3) heavily rimed photographed on April 12, 2015 at 0910 UTC.

A summary of the unrimed and rimed particles during the two-month study is shown in Figure 4.8. Overall, the intensity of riming varied for each ice crystal and solid precipitation particle. Of the particles examined, 37% were unrimed. However, the event on March 15 – 16

contained a large number of unrimed particles, which comprises 86% of the unrimed category. Of the rimed particles examined, moderate rime was most identified (26%). The event on March 21 – 22 was entirely heavily rimed particles, though the April 4 – 5 event contained the greatest amount of heavily rimed particles. As a result, April 4 – 5 constitutes 52% of the heavily rimed category. The total number of unrimed and rimed particles can be viewed in Table 4.7.

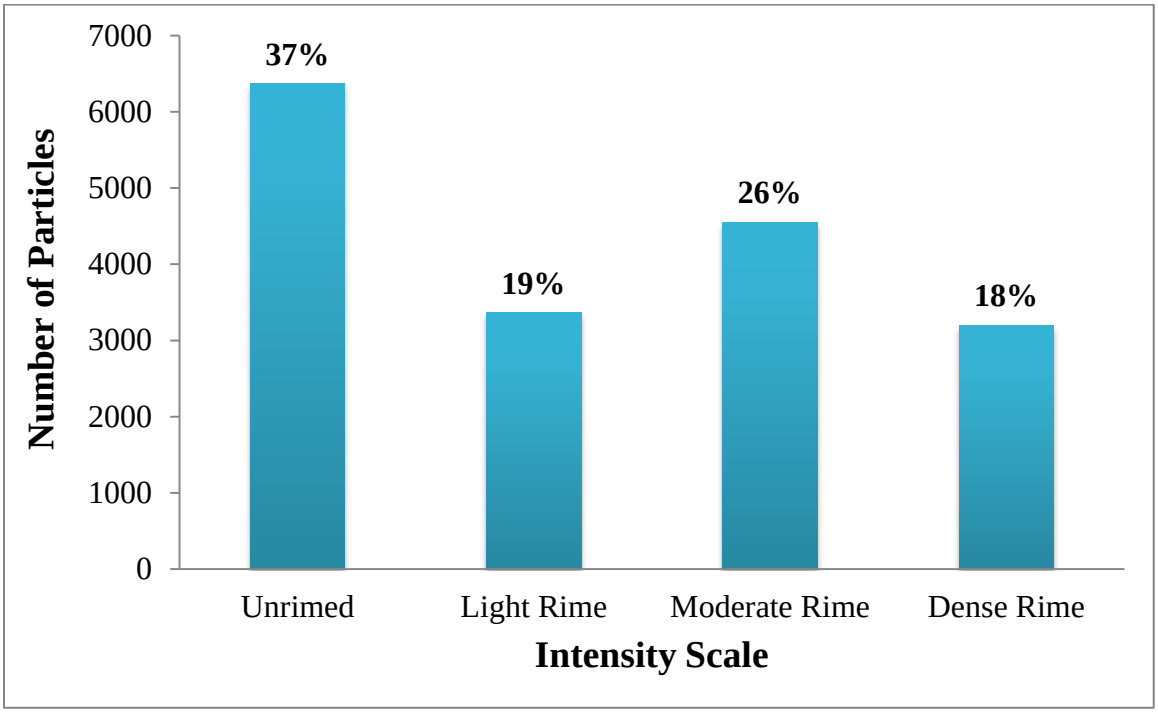


Figure 4.8: The intensity of riming on particles photographed during the study.

Table 4.7: Total numbers of unrimed and rimed ice crystals and solid precipitation particles examined for each event containing microphotography images.

| Event | Unrimed | Light Rime | Moderate Rime | Heavy Rime |
|---|---|---|---|---|
| **Mar 15 – 16** | 5697 | 54 | 9 | 0 |
| **Mar 21 – 22** | 0 | 0 | 0 | 35 |
| **Apr 4 – 5** | 772 | 2699 | 3188 | 1634 |
| **Apr 11 – 12** | 61 | 75 | 229 | 883 |
| **Apr 14 – 15** | 69 | 357 | 1036 | 434 |
| **Apr 18** | 5 | 6 | 66 | 41 |
| **Apr 25 – 26** | 3 | 0 | 0 | 151 |

### 4.7 Time of Occurrence of Precipitation Particles

Plots were created to better understand the evolution of particles falling to the surface under various temperature and relative humidity conditions. Microphotography observations of unrimed and rimed particles were examined. For optimal results, the ECCC station minute data (temperature and relative humidity) were utilized. In this section, the April 4 – 5 and April 11 – 12 events will be discussed. These events were chosen to illustrate significant features during the precipitation events. Plots of the other precipitation events can be viewed in Appendix H.

The April 4 – 5 event began with aggregates of snow crystals followed by column crystals, as seen in Figure 4.9. In the initial stage of the precipitation event, few particles were observed and the temperature and relative humidity fluctuated. As the temperature decreased and the relative humidity increased, the number of particles photographed on the collection pad increased. A variety of precipitation particles were observed throughout the event; however, a majority of the particles were rimed. Figure 4.9 displays many occurrences when rimed and unrimed particles occurred simultaneously in photos.

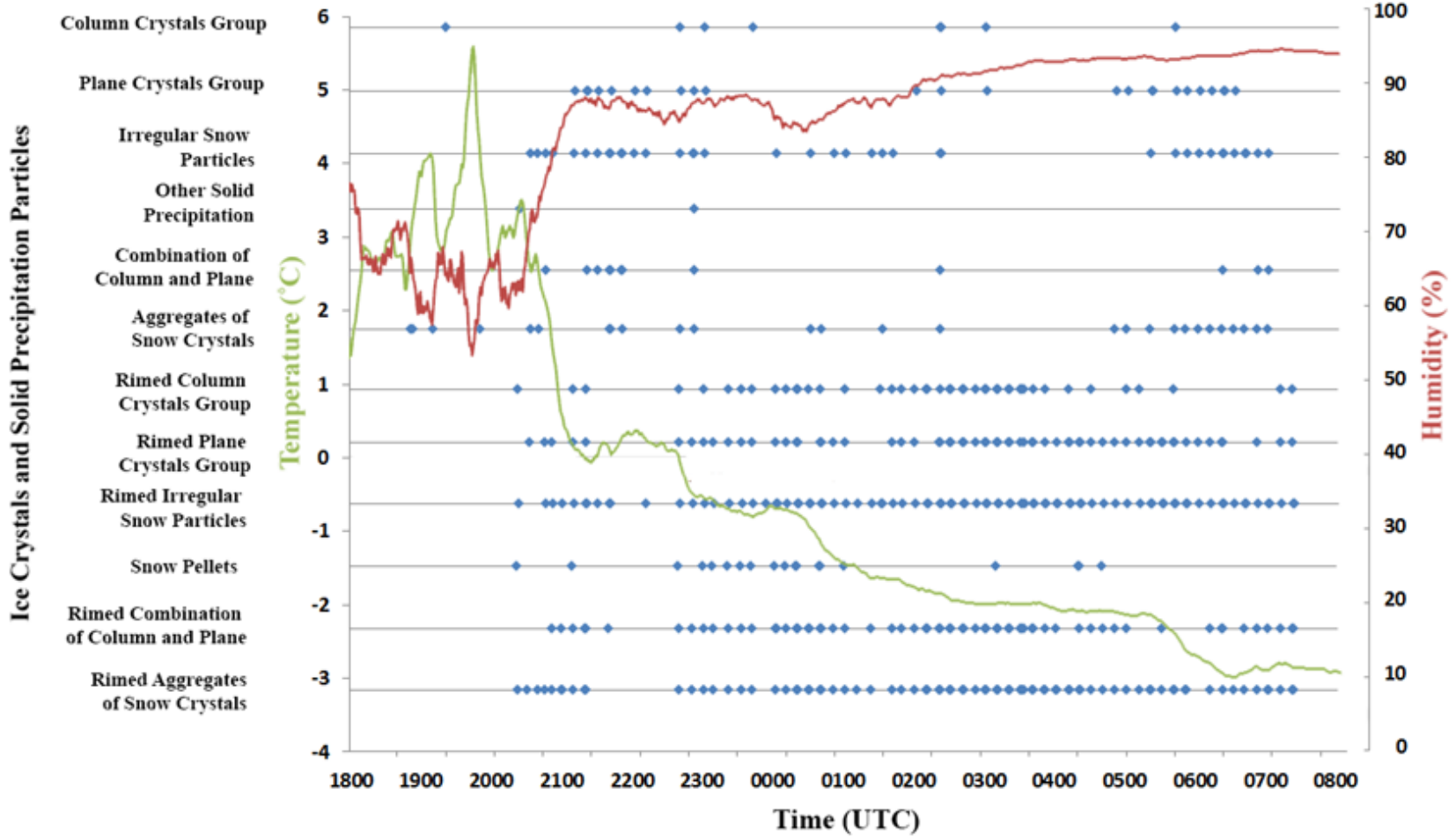


Figure 4.9: The evolution of ice crystals and solid precipitation particles on April 4 – 5. Each blue point indicates the occurrence of a particle from either a rimed or unrimed category listed on the left. The green line represents temperature and the red line represents relative humidity.

Figure 4.10 illustrates the evolution of the ice crystals and solid precipitation particles examined on April 11 – 12, which began with both rimed and unrimed particles occurring simultaneously on the same photo and several times after. From approximately 1500 UTC to 2330 UTC, surface conditions became warm and dry, though, around 1900 UTC, temperature and relative humidity values were nearly in equilibrium. During these conditions, no precipitation particles were photographed due to the particles melting rapidly. Conditions became favourable as temperatures decreased and relative humidity values increased from approximately 0100 UTC to 0900 UTC therefore, microphotography observations were possible.

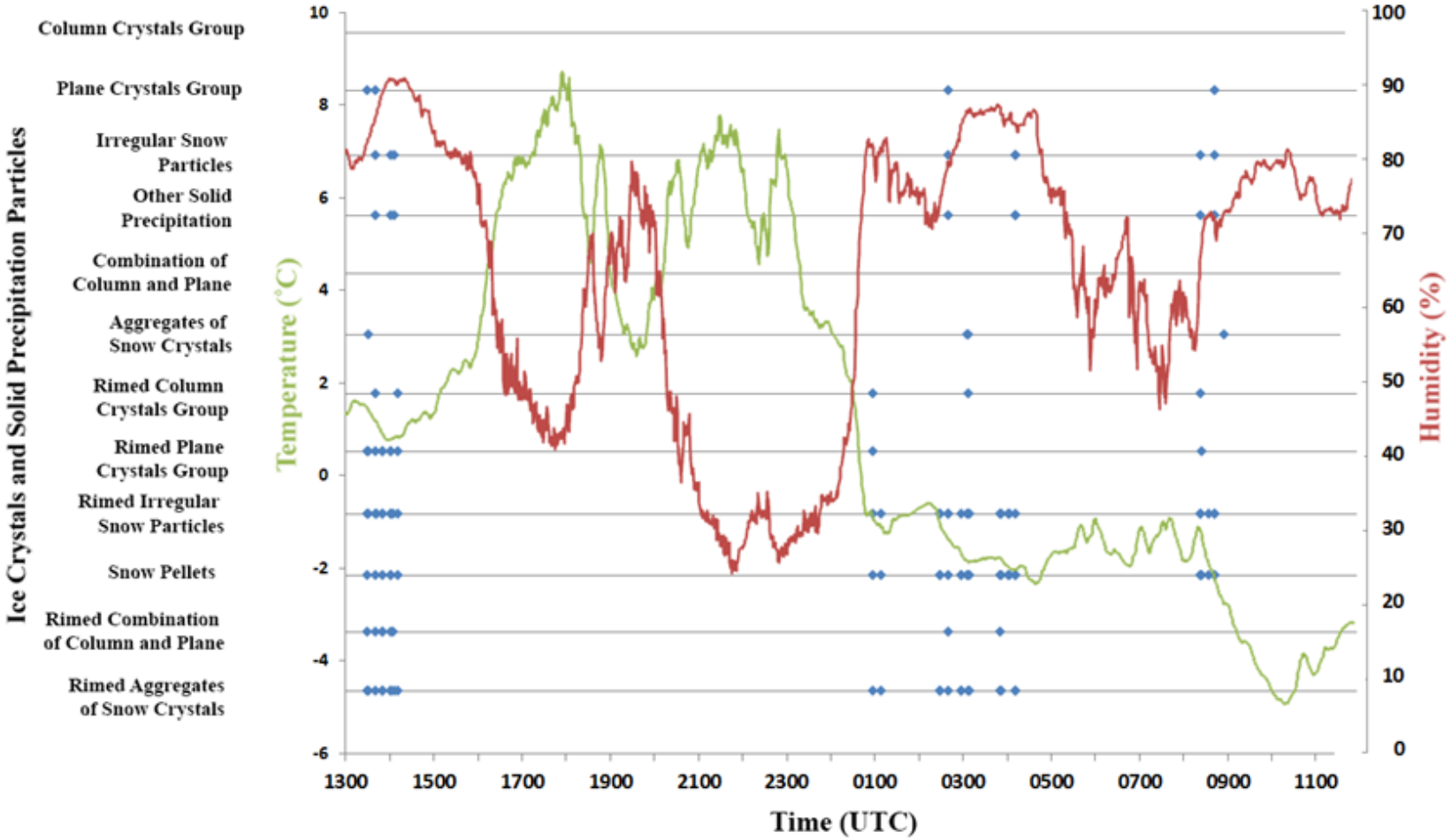


Figure 4.10: The evolution of ice crystals and solid precipitation particles on April 11 – 12. Each blue point indicates the occurrence of a particle from either a rimed or unrimed category listed on the left. The green line represents temperature and the red line represents relative humidity.

Of the cases examined when precipitation occurred on site, the seven plots indicated a similar pattern. Microphotography observations commenced when temperatures were < 3.5°C and the relative humidity was > 50%. The majority of particles identified were rimed with several cases of unrimed. Microphotography observations were not possible when temperatures were ≥ 3.5°C with relative humidities ≤ 50% due to the particles melting rapidly.

The plots indicated that the evolution of precipitation particles occurred at random without any major pattern. There was no indication that one specific type of particle occurred at the beginning or at the end of events.

### 4.8 Images Containing Rimed and Unrimed Particles Occurring Simultaneously

Analysis of unrimed and rimed ice crystals and solid precipitation particles occurring simultaneously was examined. Of the total number of images examined, 14% contained unrimed and rimed particles occurring simultaneously. The average temperature during microphotography observations of unrimed and rimed particles was -1.4°C (0.4°C at the KBA station) with an average relative humidity of 89% (82% at the KBA station).

Of the cases examined, 6 of the 7 events contained unrimed and rimed particles occurring simultaneously with the exception of the March 21 – 22 event that contained only heavily rimed particles photographed at the surface.

The fraction of images for each event was also examined (Figure 4.11). The April 4 - 5 event contained the most number (21%) of images with unrimed and rimed particles occurring simultaneously as well as the April 18 event (20%). The particles identified during the March 21 – 22 event were entirely rimed, therefore, the particles did not occur simultaneously.

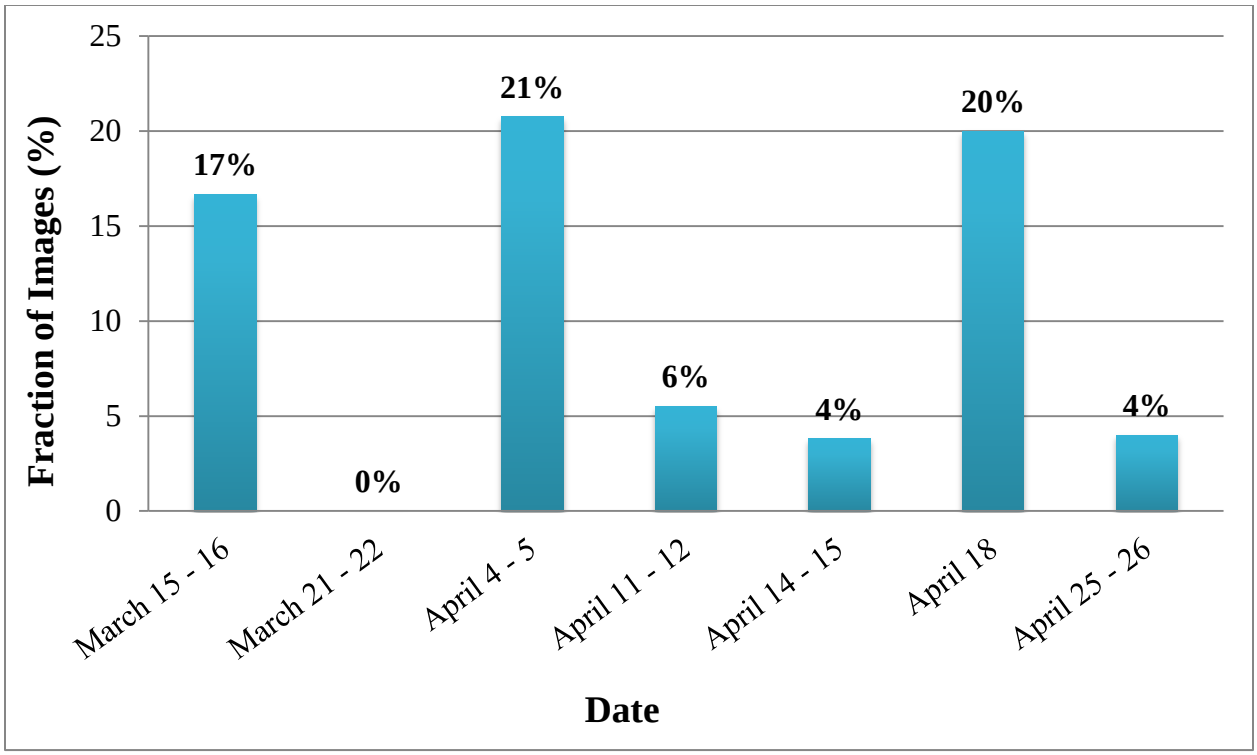


Figure 4.11: The percentage of images containing unrimed and rimed particles occurring simultaneously for each precipitation event containing microphotography observations.

### 4.9 Cloud Droplets on Precipitation Particles

The growth of ice crystals can be enhanced by accretion when the crystal falls through a cloud of supercooled water droplets with temperatures below 0°C (Rogers, 1978). Accretion leads to snow pellets and riming of particles with varying intensity from light to heavy riming. Riming was observed throughout the Alberta field campaign with cloud droplets varying in sizes.

Images were examined for precipitation particles containing visible cloud droplets. Cloud droplets were selected at random, though, the clarity was also considered. The droplets were selected if the droplets were clearly visible on the particle and not obstructed by the glare of the flash or overlapped by other cloud droplets. Therefore, light to moderately rimed particles were ideal for this analysis. Precipitation particles were magnified on Adobe Photoshop CS6 to view

the cloud droplet; however, the droplets were too small to be measured using a ruler alone as seen in Figure 4.12. Therefore, a liquid equivalent radius calculation was used to determine the size. The cloud droplets examined may be an overestimate in size given that on impact, cloud droplets would undoubtedly spread outwards before freezing and they may also expand on freezing. Also, as previously mentioned in Table 3.2, the rulers photographed on April 14 – 15 and April 25 – 26 were used to measure the cloud droplets on April 18. Due to the uncertainty in magnification, the April 18 cloud droplets are an approximate measurement in size.

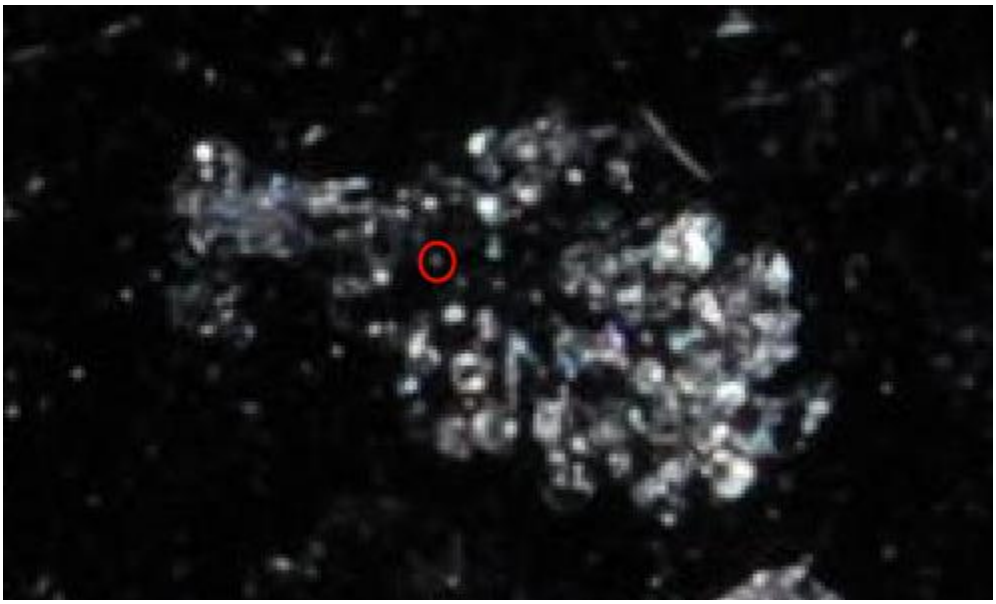

Figure 4.12: Cloud droplet on a particle on April 15 at 0041 UTC. The analyzed droplet is outlined in red.

The Magnetic Lasso Tool within Adobe Photoshop CS6 is a freehand selection tool that automatically selects the edges of an object that has a high color contrast with the background. The tool was used to outline the cloud droplets to determine the total number of pixels selected. The photographed rulers were then used to determine the area of a pixel in mm.

$$P_a = (1/P_w)^2 \tag{5.1}$$

where $P_a$ is the area of one pixel in mm² and $P_w$ is the number of pixels in 1 mm.

The area of one pixel was then used to determine the area of the frozen cloud droplet

$$A_i = P_a * PD_t \tag{5.2}$$

where $A_i$ is the area of the frozen cloud droplet in $mm^2$ and $PD_t$ is the total number of pixels.

The area of the frozen cloud droplet was then used to determine the liquid equivalent radius. The frozen cloud droplets are assumed to be spheres. The equivalent radius of a frozen droplet $r_i$ is related to $A_i$ through:

$$A_i = \pi {r_i}^2 \tag{5.3}$$

$$r_i = \sqrt{\frac{A_i}{\pi}} \tag{5.4}$$

To find the equivalent radius $r_i$ of a liquid droplet, one considers that the mass of the particle does not change from ice to liquid. Therefore,

$${r_i}^3 \cdot \rho_i = {r_l}^3 \cdot \rho_l \tag{5.5}$$

Where $\rho_i$ is the density of ice and $\rho_l$ is the density of liquid water. Rearranging terms to solve for $r_l$:

$$r_l = r_i \cdot \sqrt[3]{\frac{\rho_i}{\rho_l}} \tag{5.6}$$

Substituting in Equation 5.4 for $r_i$ and converting from mm to microns leads to:

$$r_l = \sqrt{\frac{A_i}{\pi}} \cdot \sqrt[3]{\frac{\rho_i}{\rho_l}} \cdot 1000 \tag{5.7}$$

In total, 29 ice crystals and solid precipitation particles, ranging from light to moderate rime were selected to be examined. From these 29 particles, 29 cloud droplets were measured. Table 4.8 summarizes the characteristics of these particles. The table identifies the maximum, minimum, and mean liquid equivalent radius for the frozen cloud droplets.

Table 4.8: Summary of the minimum, maximum and mean liquid equivalent radii of the 29 cloud droplets on 29 ice crystals and solid precipitation particles. The italicized event represents a range of the approximate measurement of size.

| Event | Number of Cloud Droplets | Maximum Radius (μm) | Minimum Radius (μm) | Mean Radius (μm) |
|---|---|---|---|---|
| **Mar 15 – 16** | 2 | 17 | 15 | 16 |
| **Apr 4 – 5** | 5 | 25 | 19 | 23 |
| **Apr 11 – 12** | 3 | 16 | 14 | 14 |
| **Apr 14 – 15** | 15 | 17 | 11 | 14 |
| ***Apr 18*** | *2* | *16-15* | *15-14* | *15* |
| **Apr 25 – 26** | 2 | 15 | 13 | 14 |

Figure 4.13 is an overview of the 29 cloud droplets examined in this study. Of the cloud droplets examined, the average liquid equivalent radius was 16 μm. The largest cloud droplet had a liquid equivalent radius of 25 μm on April 4. The smallest cloud droplet was identified on an irregular snow particle on April 14 with a liquid equivalent radius of 11 μm.

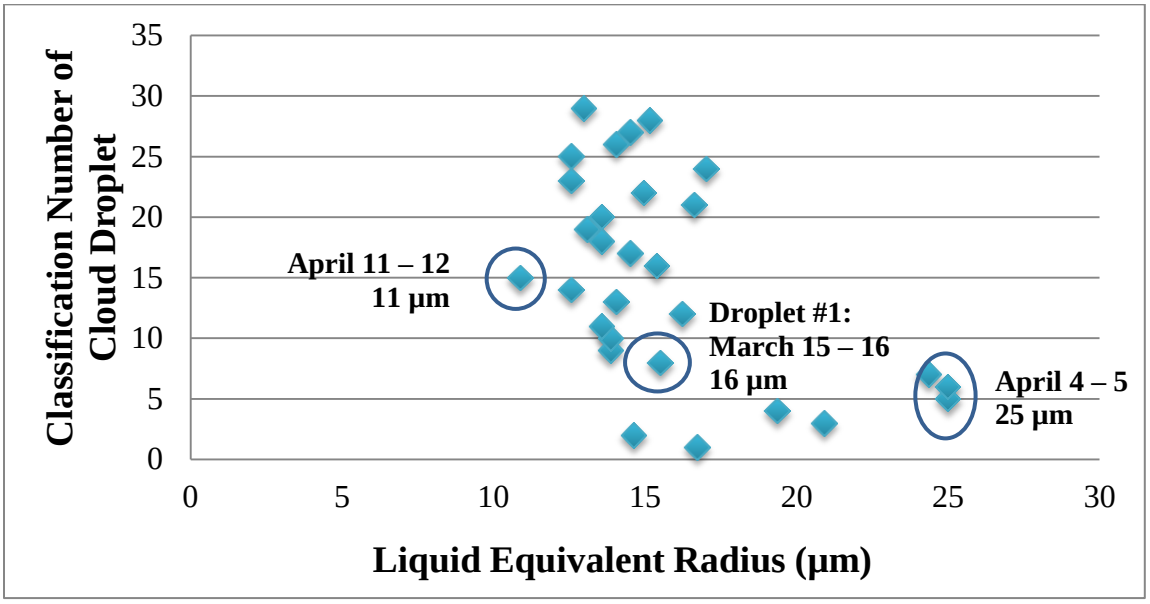


Figure 4.13: The classification number of cloud droplets and the size distribution of the liquid equivalent radius of cloud droplets on photographed rimed particles. For example, cloud droplet 1 was identified on March 15 – 16 with a liquid equivalent radius of 16 μm.

The location of KES suggests that the frozen cloud droplets in the microphotography images are droplets formed within continental conditions. If the location was more marine, one would expect to find larger droplets. Caution is needed in interpreting these results, however, as heavily rimed particles were not examined since it was not possible to discern individual droplets.

### 4.10 Ice Crystals and Solid Precipitation Particles above 0°C at the Surface

There were several instances when ice crystals and solid precipitation particles were observed at the surface when temperatures were above 0°C at the ECCC station. The particles were noted in both manual observations and microphotography. However, there were many cases when the particles instantly melted once in contact with the surface or with an object, making it difficult to determine the particle type. A description of the particles characteristic and size was made in these cases.

#### 4.10.1 Manual Observations of Ice Crystals and Solid Precipitation Particles above 0°C at the Surface

In total, 18 periods were examined when temperatures were above 0°C. Overall, 10 of the periods contained more than 1 observation as seen in Table 4.9. Observations of the ice crystals and solid precipitation particles above 0°C were based on the ECCC station temperature and relative humidity minute data. Data from the KBA station were noted as well for each case.

The average temperature during the observed cases was 3.8°C (3.5°C at the KBA station) with a relative humidity of 57% (64% at the KBA station). In comparison to the KBA station,

most temperature and relative humidity data were similar, though 4 cases showed temperatures below freezing.

The warmest temperature when particles were recorded at the surface was on April 25 at 9.1°C (7.5°C at the KBA station).The wet bulb temperatures were also calculated for both the ECCC and KBA stations to determine the amount of available water vapour in the atmosphere. These values ranged up to 5.3°C (5.1°C at the KBA station).

Table 4.9: Summary of the surface conditions when ice crystals and solid precipitation particles were recorded with manual observations above 0°C temperatures. The first entry is the ECCC station data and the second entry after the forward slash is the KBA station data.

| Date | Time (UTC) | Observations (#) | Temperature (°C) | Relative Humidity (%) | Wet Bulb Temperature (°C) | Particle Description /Size | Transition |
|---|---|---|---|---|---|---|---|
| **Mar 22** | 0605 | 1 | 2.8/2.0 | 67/79 | 1.0/0.9 | Heavily rimed. Very small | R→S |
| **Mar 23** | 2030 | 1 | --/2.8 | --/79 | --/1.7 | Large rimed particles | S→R |
| **Apr 4** | 1810 - 1850 | 5 | 2.7/0.0 | 68/83 | 0.9/-0.8 | Large particles | -- |
| **Apr 6** | 1840 - 2120 | 17 | 1.9/0.0 | 52/66 | -1.0/-1.9 | Small particles | -- |
| **Apr 11** | 1820 - 2000 | 15 | 4.4/5.6 | 67/67 | 2.5/3.6 | Small particles | -- |
| **Apr 11** | 2350 | 1 | 3.2/6.4 | 32/34 | -1.8/-1.5 | Snow pellets | -- |
| **Apr 12** | 0000 - 0030 | 4 | 2.7/2.8 | 37/42 | -1.6/-1.1 | Rimed. Very small particles | -- |
| **Apr 12** | 1710 - 1900 | 12 | 1.8/0.3 | 46/54 | -1.7/-2.4 | Small particles | -- |
| **Apr 12** | 2140 | 1 | 1.1/1.2 | 43/47 | /-2.1 | Rimed particles | -- |
| **Apr 12** | 2000 | 1 | 8.8/7.8 | 46/57 | 5.1/5.1 | Snow pellet | -- |
| **Apr 18** | 0920 - 1035 | 14 | 0.5/0.4 | 93/100 | 0.2/0.4 | Rimed. Large and small particles | R→S |
| **Apr 18** | 1500 - 1540 | 3 | 1.2/0.2 | 85/95 | 0.5/-0.0 | Large and small particles | R→S |
| **Apr 23** | 0205 - 0210 | 2 | 6.5/6.4 | 41/49 | 2.3/2.4 | Small particles | R→S |
| **Apr 24** | 2350 - 0030 | 6 | 4.9/7.4 | 60/47 | 2.4/3.7 | Small particles | R→S |
| **Apr 25** | 2050 | 1 | 9.1/7.5 | 40/50 | 5.3/4.2 | Small particles | R→S |
| **Apr 25** | 2230 | 1 | 5.3/5.3 | 59/57 | 2.8/2.7 | Rimed particles | R→S |
| **Apr 25** | 2300 | 1 | 4.1/3.3 | 67/73 | 2.3/1.8 | Rimed. Small particles | R→S |
| **Apr 25** | 2330 - 0000 | 4 | 3.4/2.8 | 68/75 | 1.6/1.4 | Small particles | R→S |

The table also lists the particle description and size. Large particles were observed in 4 of the periods and 9 of the periods contained rimed particles. Of the periods examined, 12 contained particles described as “small”. However, manual observations did not state whether the particles

were partially melted. It may be possible that a large number of "small particles" were observed due to the particles partly sublimating before reaching the surface.

### 4.10.2 Photographed Ice Crystals and Solid Precipitation Particles above 0°C at the Surface

Of cases examined when temperatures were above 0°C based on the ECCC station, 7 periods contained 243 images of ice crystals and solid precipitation particles. The KBA station temperature data were used to examine the March 15 – 16 event due to the missing ECCC station data. Cases occurred on March 15, March 22, April 4, April 11, April 14, April 18, and April 26 (Table 4.10). The average ECCC station temperature during above 0°C cases was 1.1°C (1.0°C at the KBA station) with a relative humidity of 80% (85% at the KBA station).

The warmest average temperature was recorded on March 21 – 22 of 1.7°C (2.0°C at the KBA station) with a relative humidity of 72% (79% at the KBA station). In comparison, the warmest temperature identified for the KBA station was 2.2°C (1.3°C at the ECCC station) with a relative humidity of 82% (87% at the ECCC station) during the April 14 – 15 case. The wet bulb temperature was also determined which ranged up to 0.7°C (1.3°C at the KBA station)

Table 4.10: A summary of the temperature and relative humidity data. Cases are of microphotography observations when temperatures were above 0°C. The first entry is the ECCC station data and the second entry after the forward slash is the KBA station data.

| Date | Time (UTC) | Images (#) | Temperature (°C) | Relative Humidity (%) | Wet Bulb Temperature (°C) | Transition |
|---|---|---|---|---|---|---|
| **Mar 15 - 16** | 1853-2005 | 40 | --/0.8 | --/82 | --/-0.1 | -- |
| **Mar 21 - 22** | 0612-0803 | 1 | 1.7/2.0 | 72/79 | 0.2/0.9 | R→S |
| **Apr 4 - 5** | 1852-2111 | 43 | 1.6/0.9 | 77/82 | 0.4/-0.0 | -- |
| **Apr 11 - 12** | 1330-1430 | 49 | 1.0/1.0 | 88/91 | 0.4/0.6 | -- |
| **Apr 14 - 15** | 2155-0011 | 75 | 1.3/2.2 | 87/82 | 0.7/1.3 | R→S |
| **Apr 18** | 1054-1126 | 16 | 0.3/0.0 | 95/100 | 0.1/0.0 | R→S |
| **Apr 25 - 26** | 0020-2000 | 19 | 0.9/0.3 | 60/81 | -1.4/-0.7 | R→S |

Plots were created for the 7 cases to illustrate the number of ice crystals and solid precipitation particles photographed when temperatures were above 0°C. The April 4 – 5 event will be discussed in this section for example purposes (Figure 4.14). The remaining plots can be viewed in Appendix I.

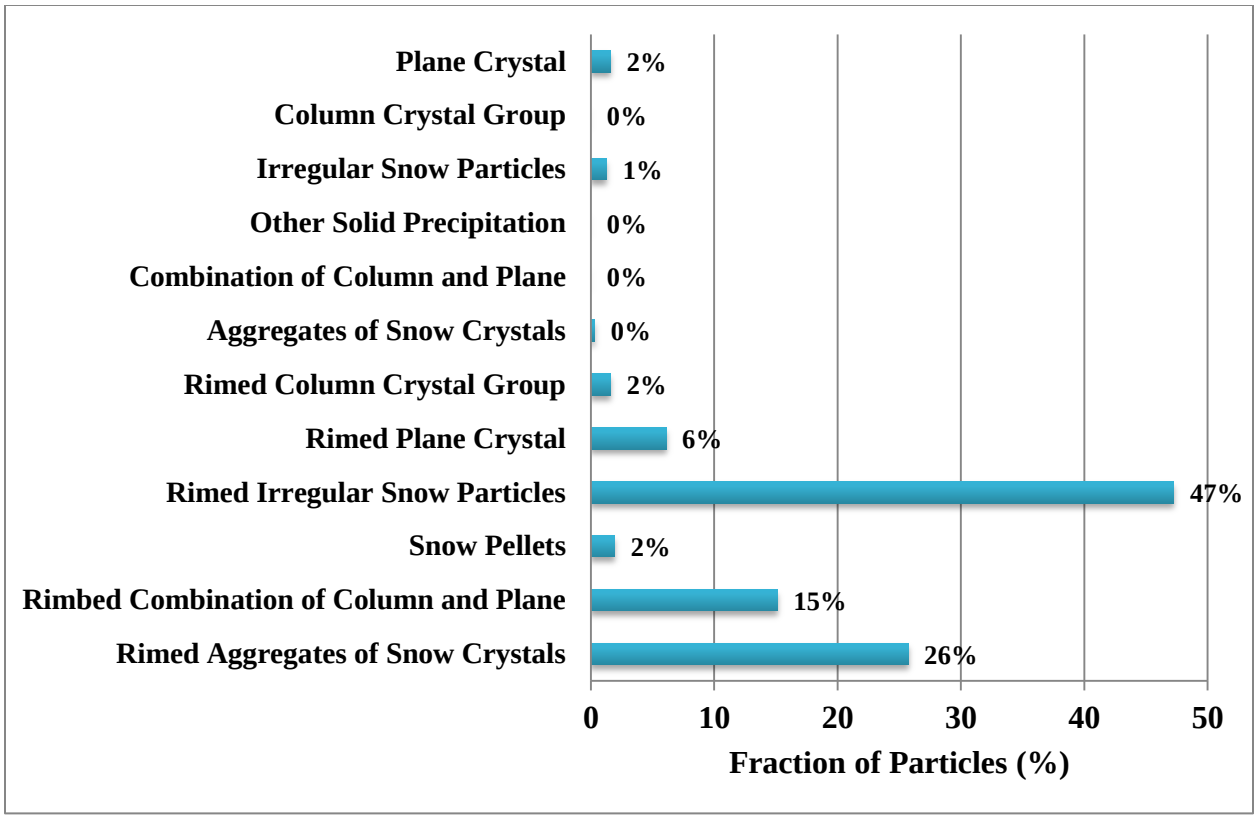


Figure 4.14: The fraction of ice crystals and solid precipitation particles photographed on April 4 at 1852 UTC – 2111 UTC when temperatures were above 0°C based on the ECCC station 1 min data.

Of the particles examined when temperatures were above 0°C, rimed irregular snow particles were most common. The April 4 – 5 plot (Figure 4.14) also indicates that unrimed and rimed particles occurred simultaneously. However, the amount of unrimed particles observed was less common in comparison to rimed particles. The results suggest that unrimed particles, typically with a lower density and terminal velocity, are able to maintain their frozen state during above 0°C conditions.

### 4.10.3 Comparison to Ice Crystals and Solid Precipitation Particles Observed below 0°C

The plot in Figure 4.15 is a summary of particles at the surface above 0°C temperatures in comparison to particles below 0°C. As seen in Table 4.9 and 4.10, the humidity was sub-saturated for all events. The results suggest many particles may have sublimated before reaching the surface, particularly when temperatures were above 0°C. As seen in Figure 4.15, as the months progressed, an increased number of frozen precipitation particles were at the surface when conditions were above 0°C.

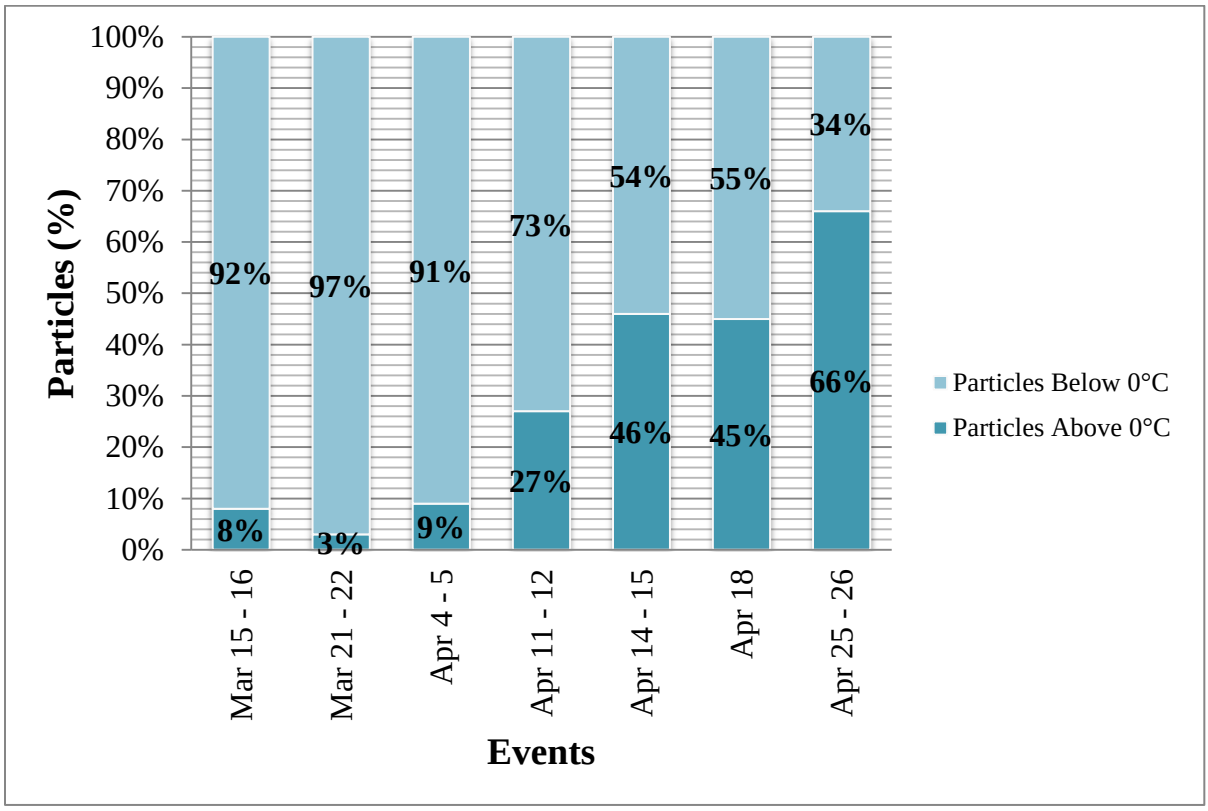


Figure 4.15: Percentage of the number of particles above 0°C using microphotography images. The dark blue shading represents particles above 0°C and the light blue shading represents particles below 0°C.

The average number of particles in each image during precipitation events is summarized in Table 4.11. Overall, a greater number of particles were identified in images when

temperatures were below 0°C. This may be due to many particles sublimating before reaching the surface as well as the particles melting on contact with the surface or an object. However, the average number of particles photographed during the April 25 – 26 event had the same low average number of particles for both conditions. The station data during the April 25 – 26 event had a consistently low average relative humidity (65% at the ECCC station and 69% at the KBA station) despite the fluctuating temperatures above and below 0°C.

Table 4.11: Summary of the average number of precipitation particles in an image above and below 0°C.

| Event | Average number of particles above 0°C | Average number of particles below 0°C |
|---|---|---|
| **Mar 15 - 16** | 8 | 27 |
| **Mar 21 - 22** | 1 | 2 |
| **Apr 4 - 5** | 7 | 18 |
| **Apr 11 - 12** | 7 | 10 |
| **Apr 14 - 15** | 9 | 11 |
| **Apr 18** | 3 | 7 |
| **Apr 25 - 26** | 3 | 3 |

A large number of the ice crystals and solid precipitation particles above 0°C ranged from light to heavy rime. Rimed irregular snow particles and rimed aggregates of snow crystals were most common. Overall, the majority of particle types were rimed suggesting that the particles were able to reach the surface before sublimating due to its greater density and fall velocity.

### 4.11 Mixed Rain and Snow Events

The occurrence of mixed rain and snow was examined at KES through manual observations. A comparison of the temperature and relative humidity with past studies of mixed precipitation was carried out.

A study completed by Maidment (1993) reported that the temperature layer of air in which a snowflake falls through determined whether the snowflake will arrive at the surface as either rain or snow. Maidment (1993) was able to determine the relationship between the occurrences of rain, snow, and mixed precipitation with the temperature at the surface (Figure 4.16).

The plot indicates that there is a greater chance of mixed rain and snow to occur when temperatures are between 1.0 to 3.5°C. At temperatures above 0°C, the probability of rain is greater. In contrast, the probability is greater for snow when temperatures are below 0°C.

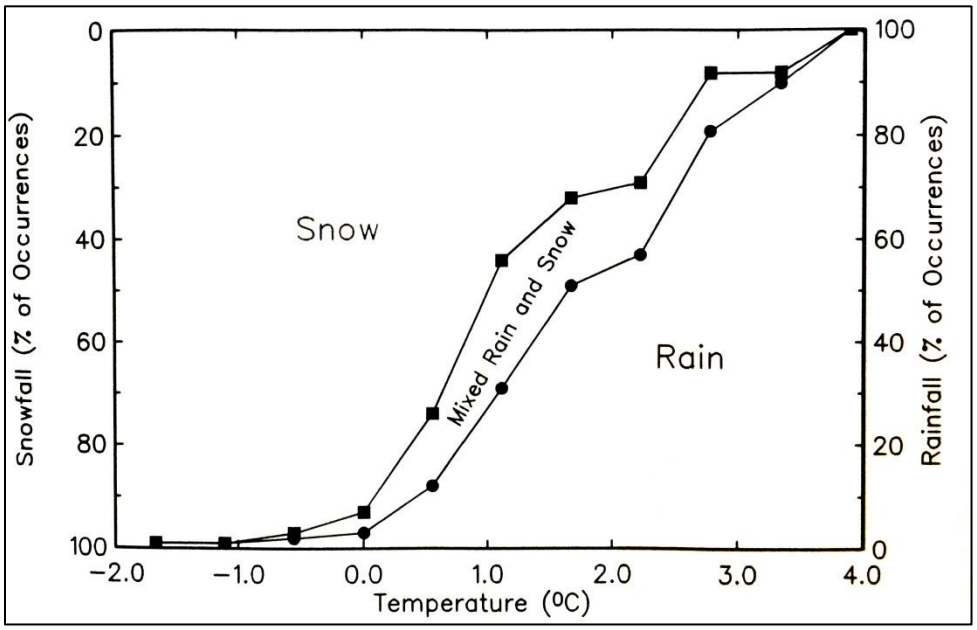


Figure 4.16: The image was adapted from Maidment (1993) displaying the occurrence of rain, snow, and mixed precipitation and temperature.

The occurrence of mixed rain and snow has also been discussed by Dingman (1994). He stated that the height of the 0°C surface temperature was critical for determining the type of

precipitation that will reach the surface. If the height was high, rain reached the surface due to the extended region conducive to melting.

Figure 4.17 is the relationship between the occurrence of rain, snow, and mixed precipitation with the surface temperature (Auer, 1974, as cited in Dingman, 1994). The probability of rain and snow at each temperature was calculated using over 1000 weather observations. It was found that rain did not occur when temperatures were below 0°C and snow did not occur when temperatures were above 6°C, though there was a near linear increase in the probability of rain with temperature. The plot in Figure 4.17 illustrates that there is a 50% probability of mixed rain and snow when the temperature is approximately 2.5°C, indicating that snow is capable of occurring when temperatures are above 0°C.

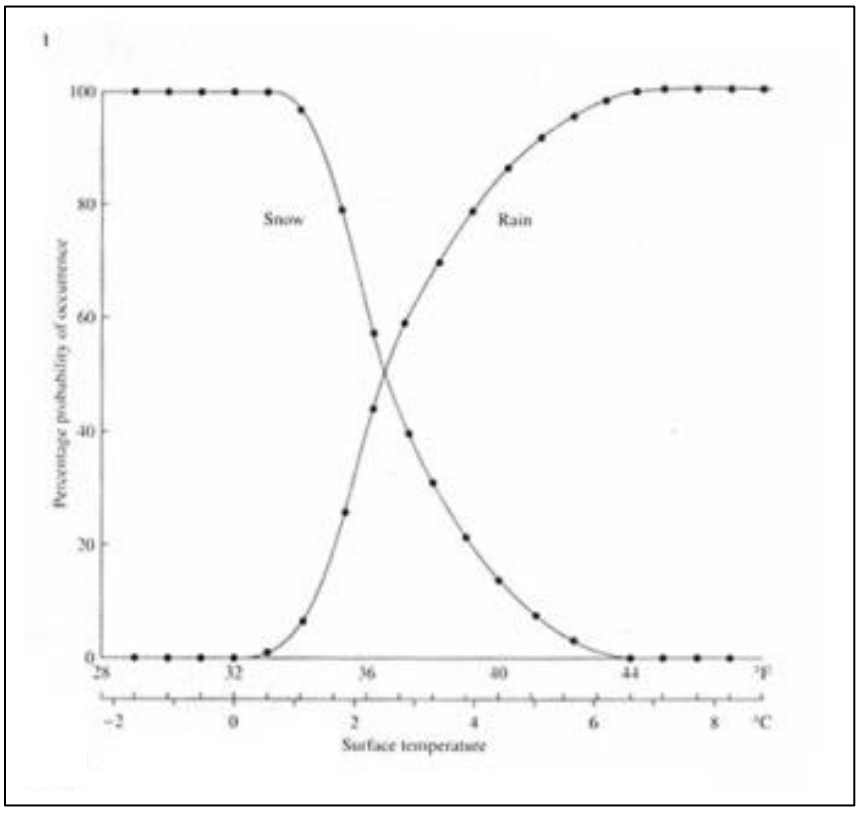


Figure 4.17: The probability of occurrence of rain and snow with surface temperature measured at 2 m AGL. The image was adapted from Auer (1974), as cited in Dingman (1994).

Similar to Maidment (1993) and Dingman (1994), a graph created by Matsuo et al. (1981) displayed the relationship between precipitation types to the surface temperature and surface relative humidity as seen in Figure 4.18 (a – b). The study was completed in Japan utilizing three weather stations in Wajima, Matsumoto, and Nikko. The lines were used to delineate regions of precipitation for mixed rain and snow, rain, and snow.

As relative humidity decreases, Matsuo et al. (1981) found that the width of the transition region decreases. The type of precipitation found within the transition region includes rain, snow, and ice pellets mixed with rain or snow. They found that at the same temperature, precipitation types varied due to differences in relative humidity. The results found by Matsuo et al. (1981) suggest precipitation types are dependent on the temperature and relative humidity.

The graphs discussed by Maidment (1993) and Matsuo et al. (1981) agree with Dingman's (1994) assessment that there is a 50% probability of mixed rain and snow occurring at approximately 2.5°C. It can be seen that the widths within the mixed rain and snow region are wide when temperatures are between 2.0 to 2.5°C.

Mixed rain and snow cases observed during the field campaign were plotted in Figure 4.18 using the a) ECCC station and b) KBA station. A total of 10 mixed precipitation cases were examined at KES (Table 4.12). The average temperature and relative humidity were determined based on when observations were made. As previously mentioned, the ECCC data are recorded at 1 min intervals (March 17 – 23 data are 5 min intervals) and the KBA station data are an hourly average of the previous 59 min data. Manual observations of the ratio between rain and snow were also estimated for several cases. For instance, if the mixed precipitation contained a greater amount of snow, the observer would specify a 30/70 ratio. For events containing more than 1 ratio, the average ratio was determined for these cases.

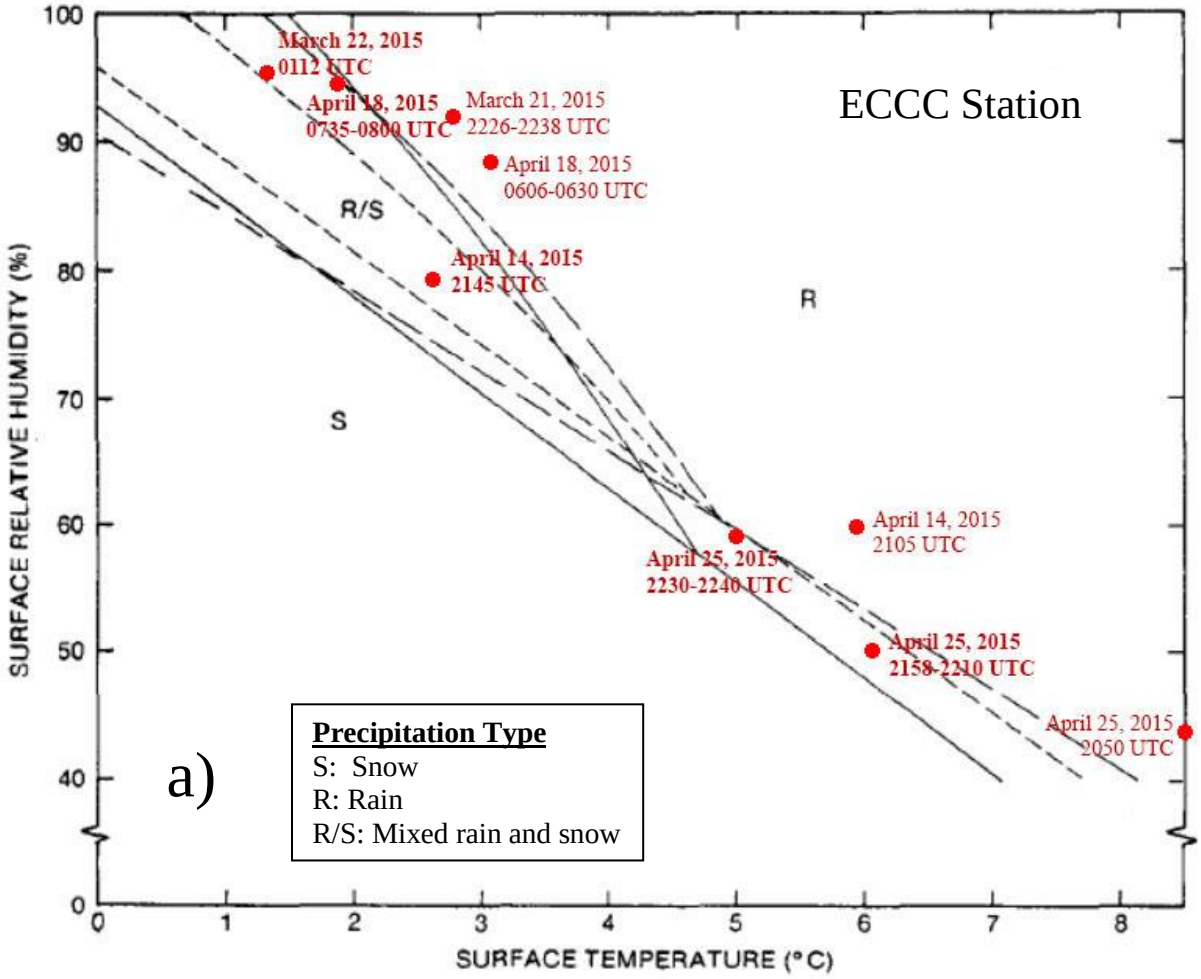
ECCC Station
March 22, 2015
0112 UTC
April 18, 2015
0735-0800 UTC
March 21, 2015
2226-2238 UTC
April 18, 2015
0606-0630 UTC
April 14, 2015
2145 UTC
April 14, 2015
2105 UTC
April 25, 2015
2230-2240 UTC
April 25, 2015
2158-2210 UTC
April 25, 2015
2050 UTC
R/S
R
S
a)
Precipitation Type
S: Snow
R: Rain
R/S: Mixed rain and snow
SURFACE RELATIVE HUMIDITY (%)
SURFACE TEMPERATURE (°C)
100
90
80
70
60
50
40
0
0
1
2
3
4
5
6
7
8

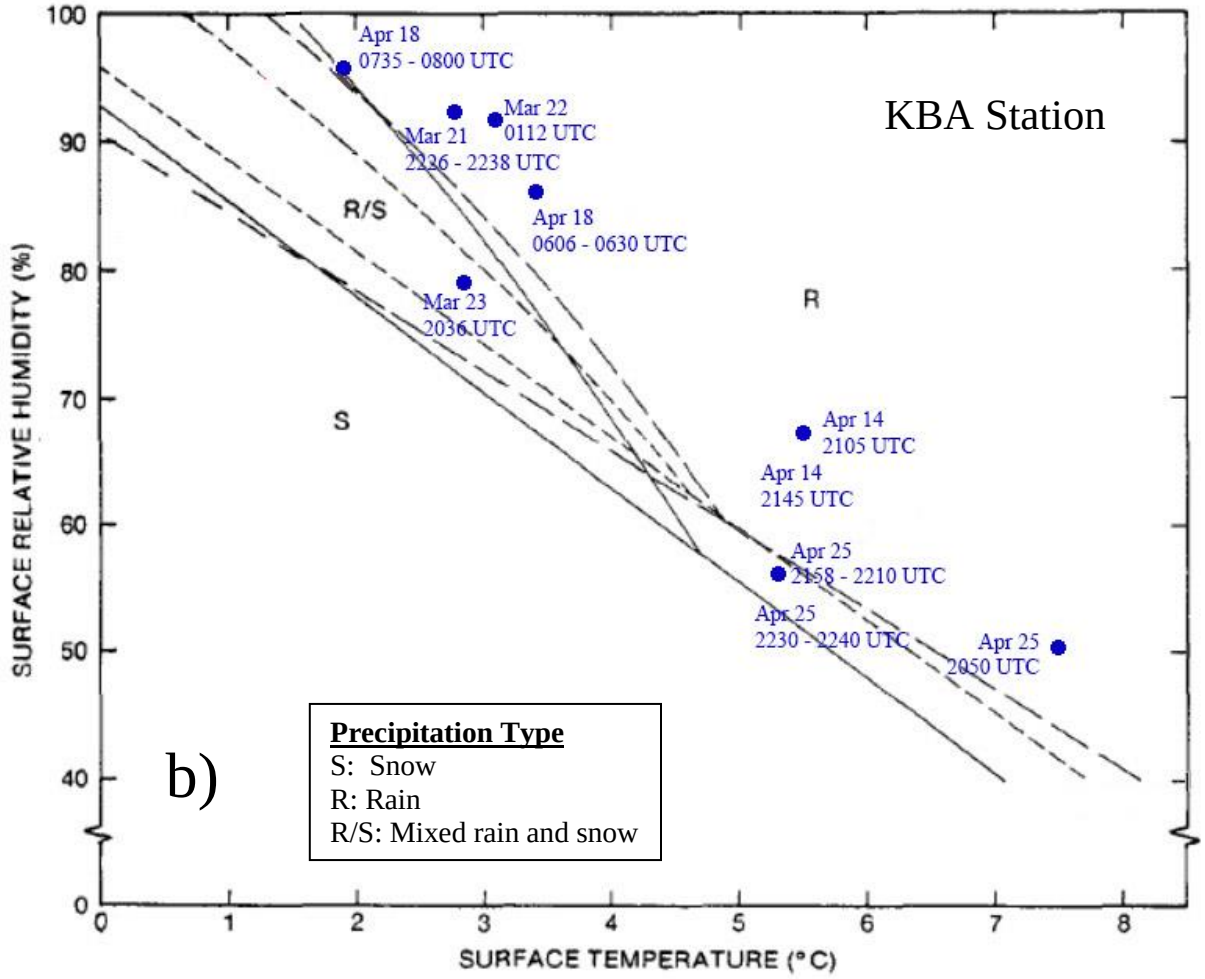


Figure 4.18: The relationship between precipitation type, surface temperature, and surface relative humidity. Precipitation types including rain (R), snow (S), and mixed rain and snow (R/S). The a) red marks represent the ECCC station temperature and relative humidity data when mixed rain and snow was observed. The b) blue marks represent the KBA station temperature and relative humidity data when mixed rain and snow was observed. The image was adapted from Matsuo et al. (1981).

Table 4.12: Summary of the occurrence of mixed rain and snow cases observed on site. The first entry is the ECCC station data and the second entry after the forward slash is the KBA station data.

| Event | Time (UTC) | Average Ratio (rain/snow) | Temperature (°C) | Relative Humidity (%) |
|---|---|---|---|---|
| **Mar 21** | 2226 – 2238 | | 4.3/2.8 | 77/92 |
| **Mar 22** | 0112 | | 3.6/3.1 | 82/91 |
| **Mar 23** | 2036 | | --/2.8 | --/79 |
| **Apr 14** | 2105 | | 5.9/5.5 | 60/67 |
| | 2145 | | 4.3/5.5 | 67/67 |
| **Apr 18** | 0606 – 0630 | 85/15 | 3.1/3.4 | 88/87 |
| | 0735 – 0800 | 62.5/37.5 | 1.9/1.9 | 94/96 |
| **Apr 25** | 2050 | 20/80 | 9.2/7.5 | 42/50 |
| | 2158 – 2210 | | 6.1/5.3 | 50/57 |
| | 2230 – 2240 | | 5.0/5.3 | 59/57 |

The average temperature when mixed precipitation occurred was 4.8°C (4.3°C at the KBA station) and the relative humidity was 69% (74% at the KBA station). Temperatures ranged from 1.9 to 9.2°C (1.9 to 7.5°C at the KBA station) and the humidity ranged from 42 to 94% (50 to 96% at the KBA station).

As mentioned in Table 4.12, an unusual case occurred on April 25 at 2050 UTC. Snow pellets and rain were observed at the surface when the temperature was 9.2°C (7.5°C at the KBA station) with a relative humidity of 42% (50% at the KBA station). Snow pellets were able to reach the surface in such warm conditions due to the low wet-bulb temperature decreasing the melting rate. The rain/snow ratio was reported as 20/80 with a short duration (< 10 min).

The rain/snow ratios on the April 18 event agreed with Matsuo et al. (1981) illustration (ECCC station and KBA station). However, the April 25 event at 2050 UTC indicated a higher snow ratio, though, the placement on the graph suggested the mixed precipitation case was more rain based.

The majority of events (ECCC station data) agreed with the illustration created by Matsuo et al. (1981) (Figure 4.18a). However, the April 18 case at 0606 - 0630 UTC (ECCC station data) did not agree with the plot. This may be due to the cases observed at KES occurring at warmer temperatures than Matsuo et al. (1981). The results may have also been influenced by the many rimed particles observed at KES which would undoubtedly decrease the melting rate.

Many cases, using the KBA station data also did not agree with the illustration by Matsuo et al. (1981) as previously seen in Figure 4.18b. This may be due to the temperature and relative humidity data being approximate measurements during mixed precipitation cases due to the station (KBA) recording data at 1 h intervals. Only 4 events agreed with the Matsuo et al. illustration. These cases include March 23 at 2036 UTC, April 18 at 0735 – 0800 UTC, April 25 at 2158 – 2240 UTC, and April 25 at 2230 – 2240 UTC.

# Chapter 5 – Atmospheric Observations of Precipitation at the Surface

## 5.1 Wind Speed and Wind Direction

As previously mentioned, the wind rose graphs were plotted to view the wind speed and direction for each precipitation event (KBA station). Of the cases examined, the plots indicated that the winds were primarily northerly and southerly during precipitation events. The frequent north and south wind flow may be due to the location of KES within a mountain valley where channelled winds are prone to occur (Figure 5.1).

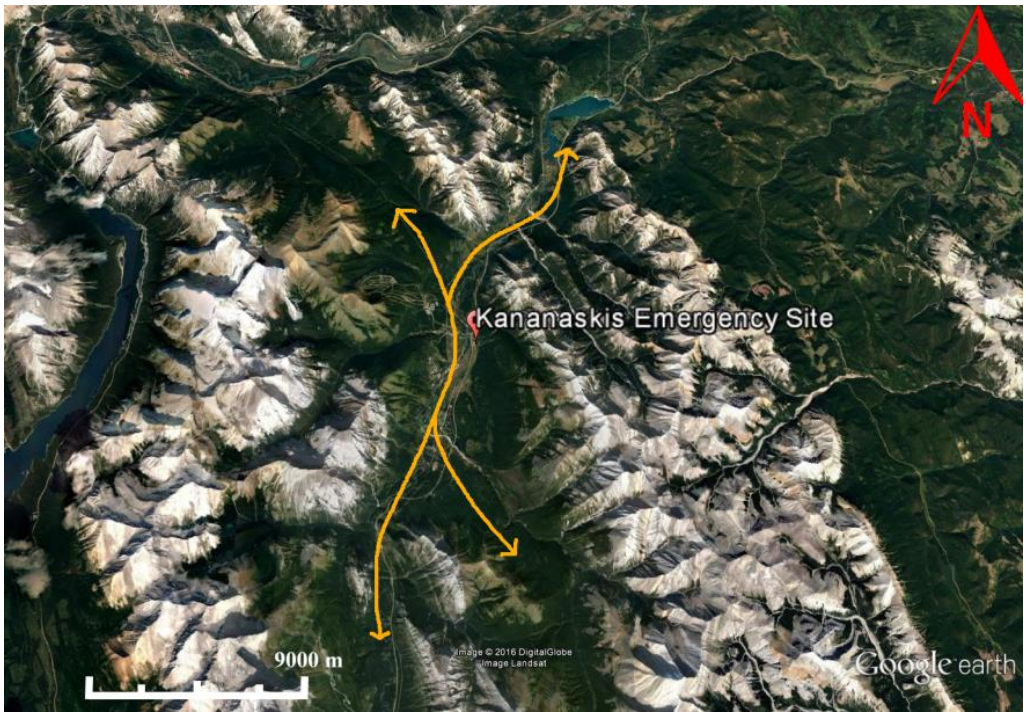


Figure 5.1: Example of the mountain topography surrounding KES. The orange arrows are examples of the possible air flow between the mountain barriers. Google Earth. September 23, 2012. Retrieved on October 18, 2016.

Figure 5.2 of the a) April 11 – 12 and b) April 25 – 26 events are examples of the wind rose plots. The example plots were chosen as they contained the greatest wind speeds recorded.

The plot of the April 11 – 12 event indicates that a southerly wind was commonly observed. In contrast, the April 25 – 26 event indicates that a northeasterly wind was most common.

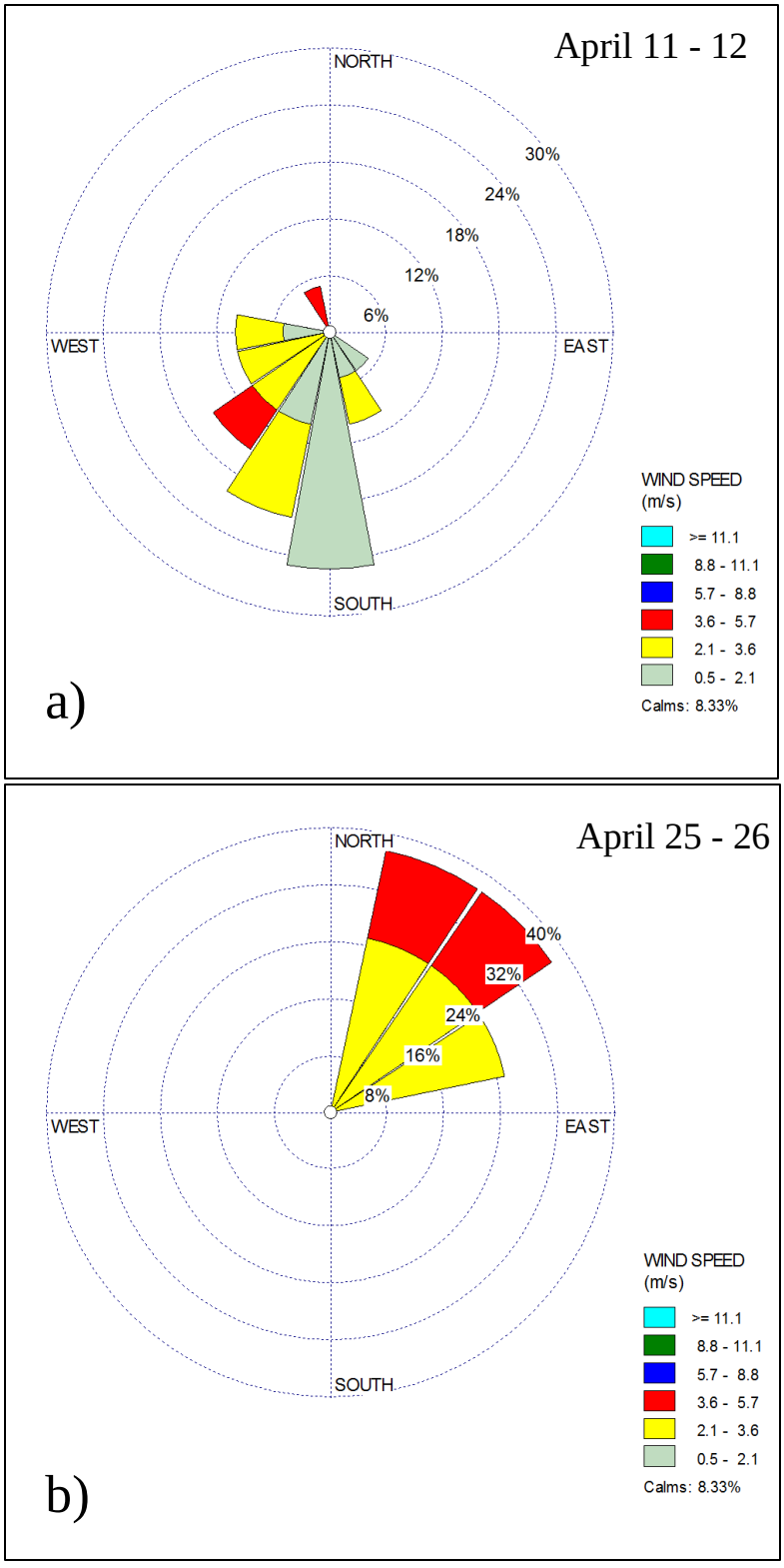


Figure 5.2: Hourly wind speed and direction during precipitation events on a) April 11 – 12 and b) April 25 – 26.

## 5.2 Ice Crystals and Solid Precipitation Particles during Different Wind Directions

Microphotography observations of precipitation particles were related to wind direction at the surface. As previously mentioned, for optimal results, the KBA wind data were utilized for this investigation.

The winds were divided into 8 quadrants (Figure 5.3). For example, northerly is considered to be between 337.5 and 22.5 degrees. It should be noted that the winds examined here were only during microphotography observations.

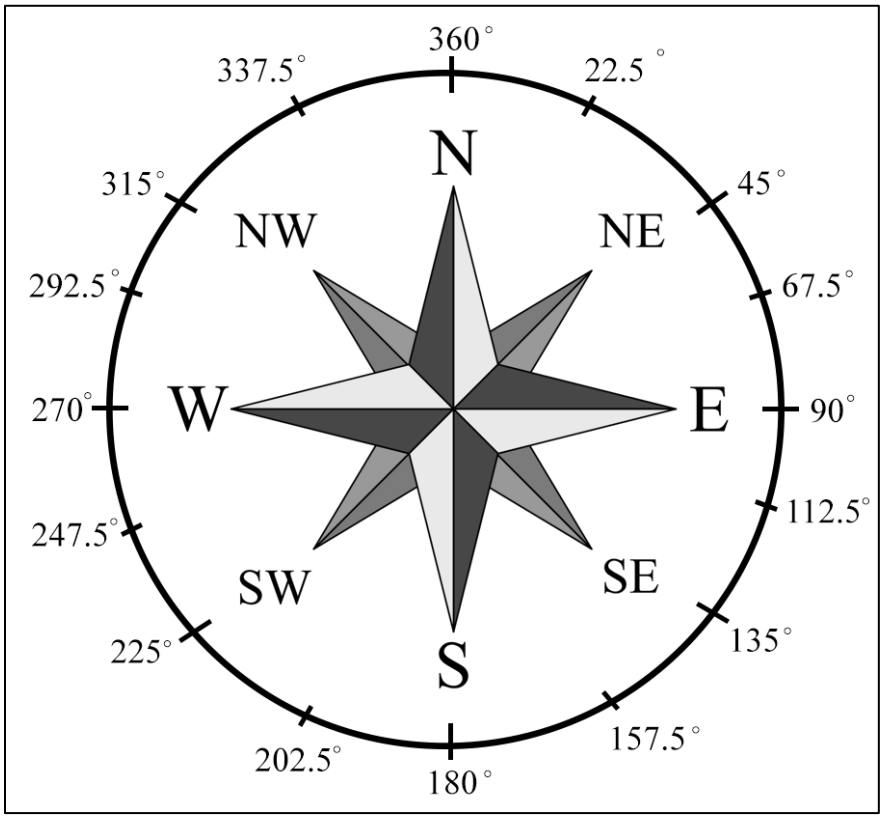


Figure 5.3: Example image of a compass and the 8 quadrants.

Atmospheric conditions may be influenced by the directional flow of the winds. For example, northerly winds may increase cold air advection as well as create sub-saturated

conditions, whereas a southerly flow may increase temperatures. The average temperature and relative humidity were also related to wind directions when particles were photographed (Table 5.1). The results indicate that temperatures ranged from -2.1 to 3.4°C. Relative humidity ranged from 74 to 95% where conditions were sub-saturated to near-saturated.

As previously mentioned, photographed precipitation particles were sorted into 12 categories of ice crystals and solid precipitation particles, 6 being accreted categories. The categories were examined to determine the wind direction at the time the particles were photographed. Of the quadrants examined, northerly, northeasterly, southwesterly, and westerly contained the most particle categories (11 out of 12) as listed in Table 5.1. The only exception was 'other solid precipitation'.

The easterly wind was associated with the least number of particle categories. Only 2 out of 12 categories were identified within the quadrant. These particle types were other solid precipitation and rimed irregular snow particles.

A majority of the number of accreted categories occurred in the 8 quadrants. However, only 1 accreted category (rimed irregular snow particles) occurred during an easterly wind. As well, not all accreted categories were recorded during a northwesterly wind. In particular, rimed column crystal, rimed plane crystal, and rimed combination of column and plane were not identified.

The degree of saturation was further investigated. The results indicated accreted particles were mainly observed when the relative humidity was $\geq 85\%$. However, not all accreted particle categories were identified during a southeasterly wind (95% relative humidity) and northwesterly wind (86% relative humidity). Accreted categories were less common when relative humidity values were approximately $< 75\%$, as observed with an easterly wind.

Table 5.1: Summary of the types of ice crystals and solid precipitation particles within the 8 quadrants. The average temperature, relative humidity, and the number of accreted categories were also determined.

| Quadrant | Temperature (°) | Relative Humidity (%) | Particle categories identified | Accreted categories identified | Particle categories not identified |
|---|---|---|---|---|---|
| **N (337.5° - 22.4°)** | -0.2 | 86 | 11/12 | 6/6 | Other solid precipitation |
| **NE (22.5° - 67.4°)** | 0.6 | 85 | 11/12 | 6/6 | Other solid precipitation |
| **E (67.5° - 112.4°)** | 3.4 | 74 | 2/12 | 1/6 | Plane crystals, column crystals, irregular snow particles, combination of column and plane, aggregates of snow crystals, rimed plane crystals, rimed column crystals, snow pellets, rimed combination of column and plane, and rimed aggregates of snow crystals |
| **SE (112.5° - 157.4°)** | 0.3 | 95 | 6/12 | 5/6 | Plane crystals, column crystals, irregular snow particles, other solid precipitation, combination of column and plane, and rimed column crystal |
| **S (157.5° - 202.4°)** | -0.7 | 85 | 10/12 | 6/6 | Other solid precipitation and combination of column and plane |
| **SW (202.5° - 247.4°)** | -1.9 | 90 | 11/12 | 6/6 | Other solid precipitation |
| **W (247.5° - 292.4°)** | -2.1 | 90 | 11/12 | 6/6 | Other solid precipitation |
| **NW (292.5° - 337.4°)** | -1.9 | 86 | 8/12 | 3/6 | Other solid precipitation, rimed column crystal, rimed plane crystal, and rimed combination of column and plane |

In summary, variations of ice crystals and solid precipitation particles were found with wind quadrants. The particle categories did not appear to show a general pattern or any notable association with the quadrants. Some quadrants were associated with almost all categories of

particles whereas the easterly wind only had 2 categories. Rimed particles were also examined in almost all 8 quadrants when conditions were mainly near saturation.

### 5.3 Large Scale Air Motion

This section examines the direction of air motion at different atmospheric levels. These include precipitation structures at a regional scale, operational surface pressure analyses, and upper air analyses of the 850 and 700 mb levels.

Precipitation events were classified as either being “upslope” or “downslope” events. An event was considered “upslope” when the air was directed towards the west, over the lee-side of the Rocky Mountains. A “downslope” event was recognized when the air was directed towards the east as seen in an example illustration in Figure 5.4.

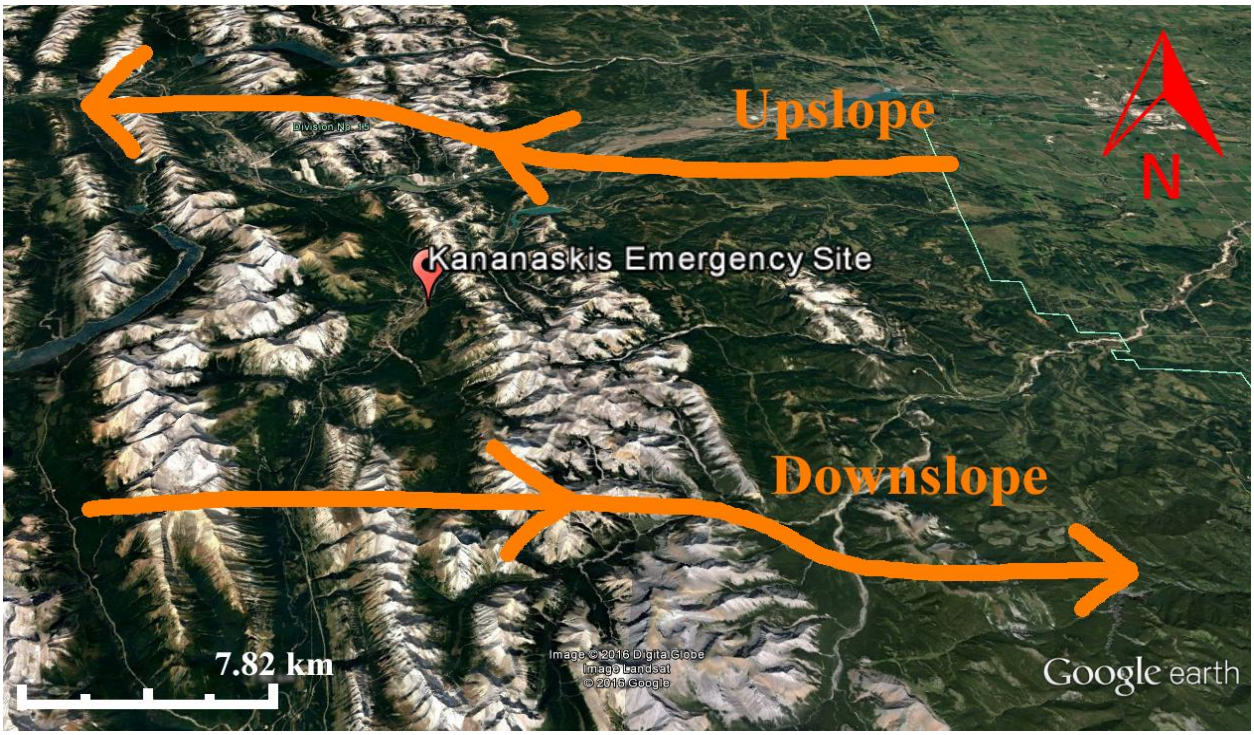


Figure 5.4: An illustration of ‘upslope’ and ‘downslope’ flow over mountain barriers. Google Earth. September 23, 2012. Retrieved on October 18, 2016.

### 5.3.1 Motion of Precipitation Structures

Radar images were retrieved from Environment Canada's website from the archived historical radar data to examine precipitation structures at a regional scale. Precipitation was detected over KES using the Strathmore, AB, radar. This section examines the precipitation structure pattern and features for the seven precipitation events containing microphotography observations.

#### 5.3.1.1 Precipitation Patterns

Common precipitation patterns observed in the radar images include widespread, scattered, and banded precipitation during observed events. An example of these structures can be viewed in Figure 5.5 (a – c).

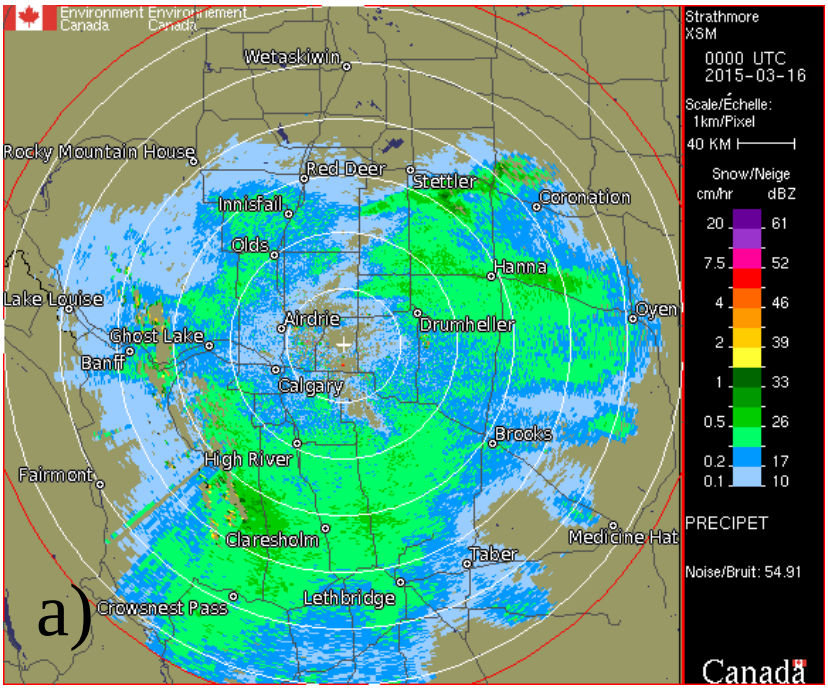

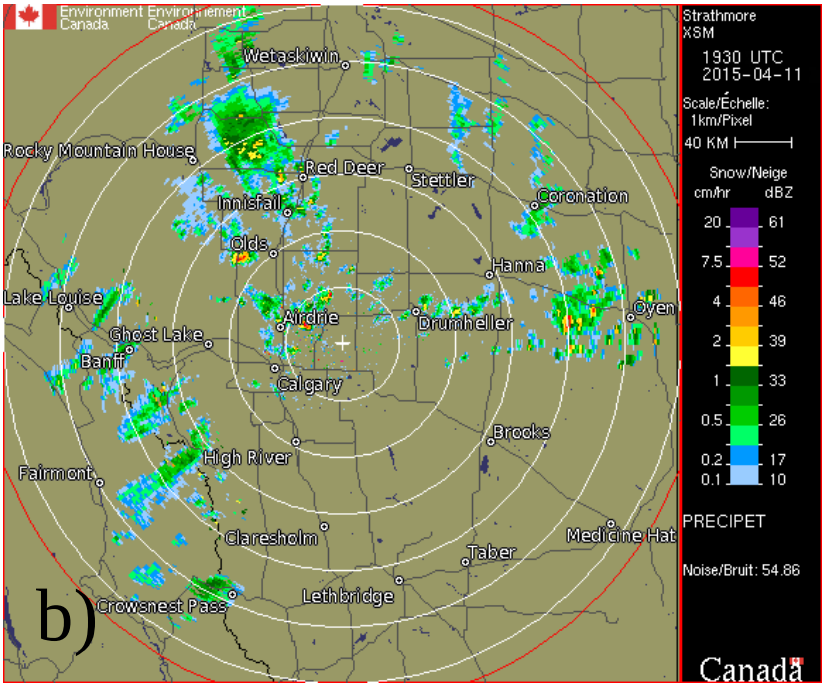


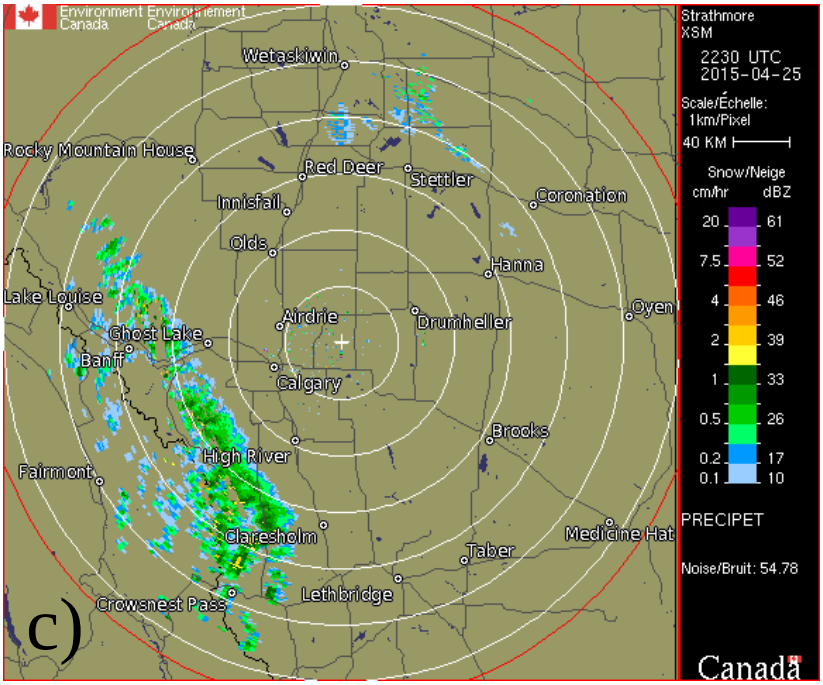


Figure 5.5: Example precipitation structures of a) widespread structures on March 16 at 0000 UTC, b) scattered structures on April 11 at 1930 UTC, c) banded structures on April 25 at 2230 UTC. [Strathmore Radar]. Retrieved March 8, 2016, from http://climate.weather.gc.ca/radar/index_e.html

#### 5.3.1.2 Precipitation Structures and their Features

The speed of the precipitation structures was determined by observing the amount of distance elapsed in 1 h. Each ring on the radar images are spaced 40 km apart and a ruler was used for a more accurate estimate allowing an approximate calculation of the speed. The ruler measured the distance from the location of the first position of the precipitation structure to the second location after an elapsed time of 1 h.

The average speed of the structures examined during precipitation events was 40 km/h. The precipitation structure with the highest speed was 60 km/h on the April 25 – 26 event and the structure with the lowest speed was 27 km/h on April 4 – 5 as summarized in Table 5.2.

Table 5.2: A summary of the precipitation structures and their direction of motion.

| Event | Precipitation Structure Evolution | Direction | Speed (km/h) |
|---|---|---|---|
| **Mar 15 – 16** | Widespread structure | NE → E → SE | 48 |
| **Mar 21 – 22** | Scattered of structures | NE → E | 34 |
| **Apr 4 – 5** | Light to moderate scattered structures → Banded structure → Scattered and banded structure → Scattered of light structures | NNE | 27 |
| **Apr 11 – 12** | Scattered of light structures | E | 40 |
| **Apr 14 – 15** | Banded structure → scattered structures | NE | 34 |
| **Apr 18** | Scattered structures | SE | 34 |
| **Apr 25 – 26** | Scattered structures | W | 60 |

Overall, the radar data provided a view of the precipitation structures at a regional scale. The results revealed that the events were primarily directed towards the east (downslope). However, the precipitation structure during the April 25 – 26 event was directed towards the west, indicating an upslope event as seen in Figure 5.6. Radar imagery of the precipitation events can be viewed in Appendix J.

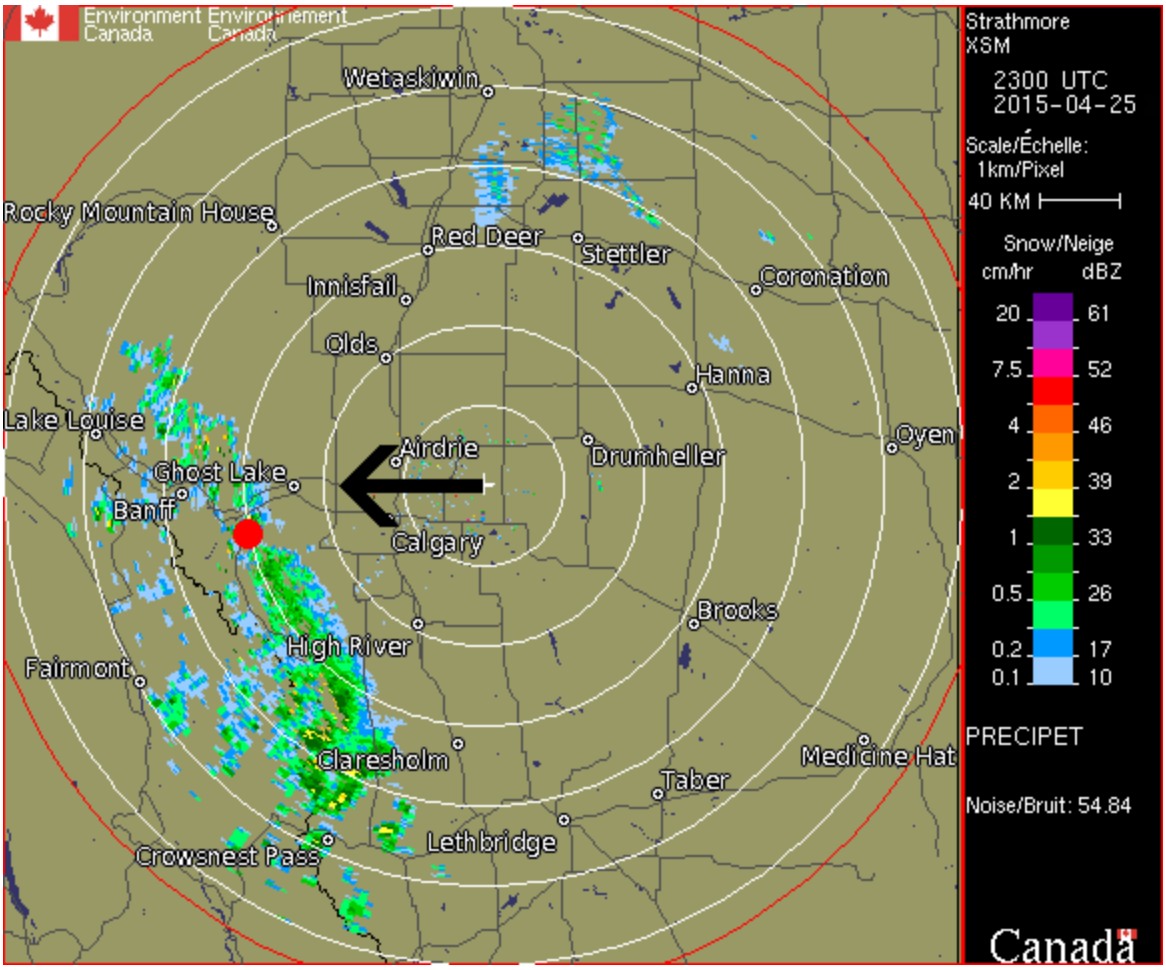


Figure 5.6: A regional view of the Strathmore, AB radar site. The precipitation structures are represented by an intensity scale located on the right of the image. The scale represents the snowfall rate in cm/h and the reflectivity in dBz. The rings act as a scale guide and are each equally spaced 40 km apart. The red mark indicates the location of KES and the black arrows represents the direction of motion of the radar echo. [Strathmore Radar]. (April 25, 2015). Retrieved March 9, 2016, from http://climate.weather.gc.ca/radar/index_e.html

### 5.3.2 Operational Surface Pressure Analysis

Analysis of the precipitation structure's direction of motion led to further examination of the operational surface pressure analysis maps using archived surface analyses from the National Weather Service. The surface analysis maps were chosen at times nearest to the timestamp displayed on the radar image.

An example of a surface analysis map on April 11 at 1500 UTC is shown in Figure 5.7. The air over KES was directed towards the east, indicating a ‘downslope’ event. Additional surface analysis maps of observed events can be viewed in Appendix K.

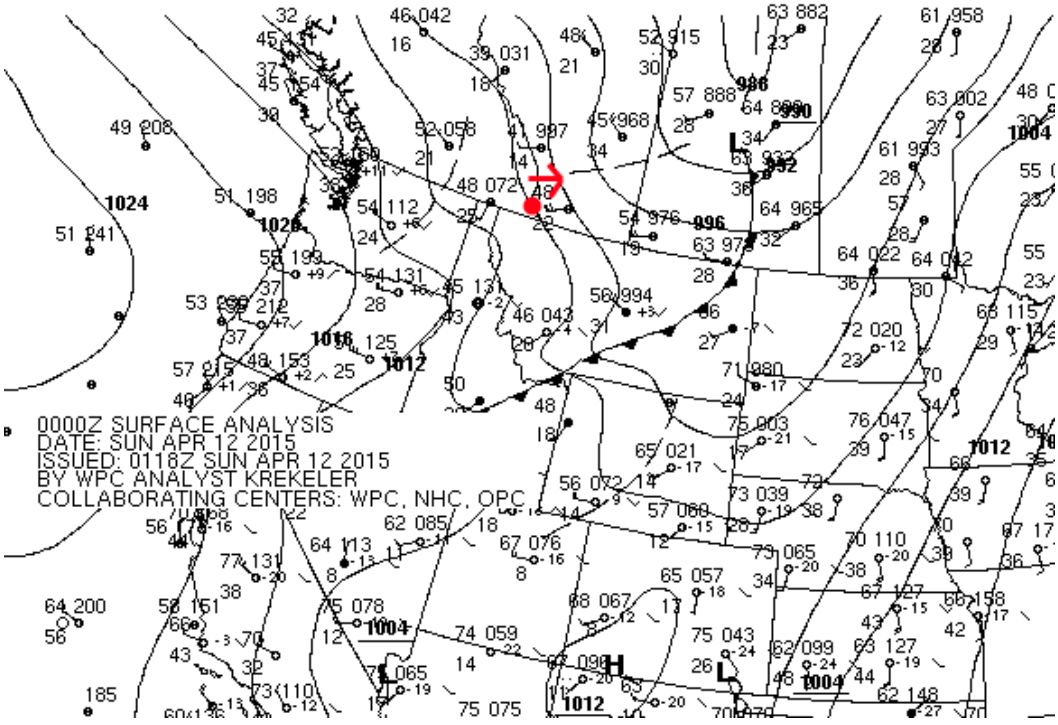


Figure 5.7: Operational surface pressure analysis map of the air direction on April 12 at 0000 UTC. The red mark represents the location of KES and the red arrow represents the wind flow. [Surface Analysis]. Retrieved May 16, 2016, from http://www.wpc.ncep.noaa.gov/archives/web_pages/sfc/sfc_archive.php

Overall, the surface analysis maps indicated 3 ‘downslope’ events and 3 ‘upslope’ events. The inferred surface air indicated a direction towards the west (upslope) during the March 15 – 16, April 4 - 5 events, and April 25 – 26 events. Of the inferred direction of motion examined, 2 events were in near agreement with the direction of the precipitation structure. These events include March 21 – 22 and April 18. The surface analysis maps indicated that 2 events were not

in agreement with the precipitation structures on radar images. These events were March 15 – 16 and April 4 – 5.

### 5.3.3 Upper Air Analysis Maps

Upper air analysis maps were examined using archived information retrieved from the UCAR website in 12 h intervals (0000 UTC and 1200 UTC). For this study, the focus was placed on the 850 and 700 mb levels to best illustrate the direction of motion. For a better observation of precipitation events, the time selected to be examined was based on when precipitation was observed on site.

Of the cases examined, the 850 and 700 mb levels were fairly similar, though the air during the April 25 – 26 event at 0000 UTC was directed towards the west at 850 mb and shifted towards the south at 700 mb.

### 5.3.4 Case Study

An overview of the air motion was examined for the March 15 – 16 and April 4 – 5 events. These events were selected based on a large number of unrimed particles during the March 15 – 16 as well as the April 4 – 5 event containing the most particles.

#### 5.3.4.1 Case Study: March 15 - 16

Figure 5.8 to Figure 5.11 are the operational surface pressure analysis map, radar image, and upper analysis 850 and 700 mb levels during the event on March 15 – 16. The surface analysis indicated the air was directed towards the west. However, the widespread precipitation

structure was directed towards the northeast. Similarly, the 850 and 700 mb level air were directed towards the east.

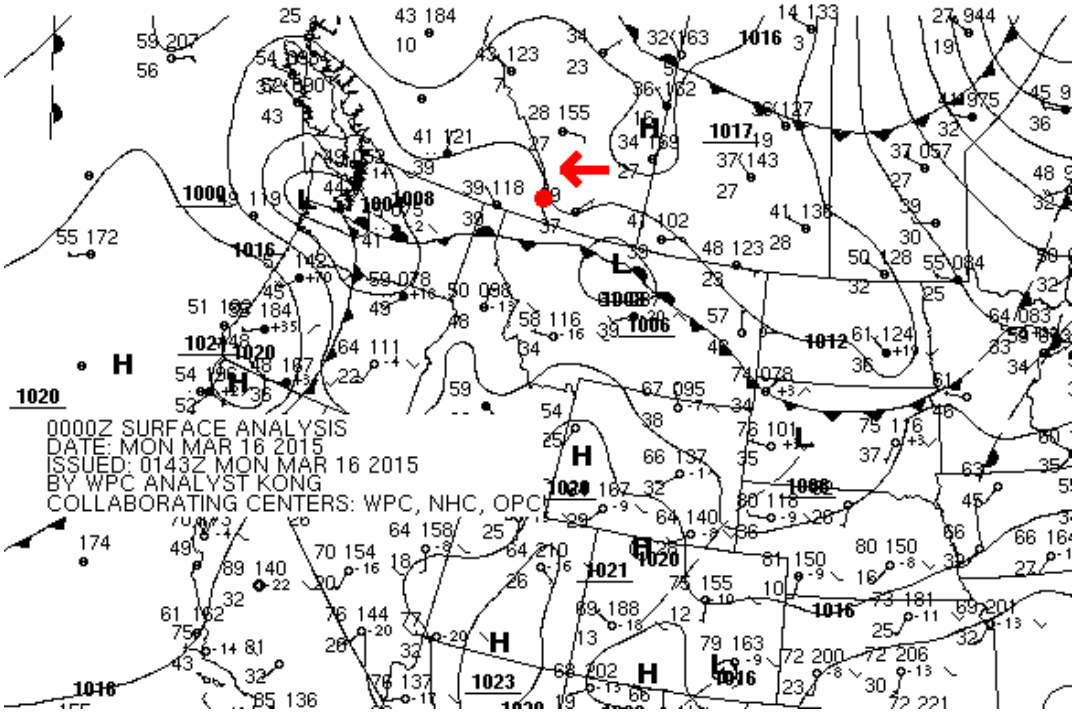


Figure 5.8: Operational surface pressure analysis map of the air direction on March 16 at 0000 UTC. The red mark represents the location of KES and the red arrow represents the wind flow. [Surface Analysis]. Retrieved May 16, 2016, from http://www.wpc.ncep.noaa.gov/archives/web_pages/sfc/sfc_archive.php

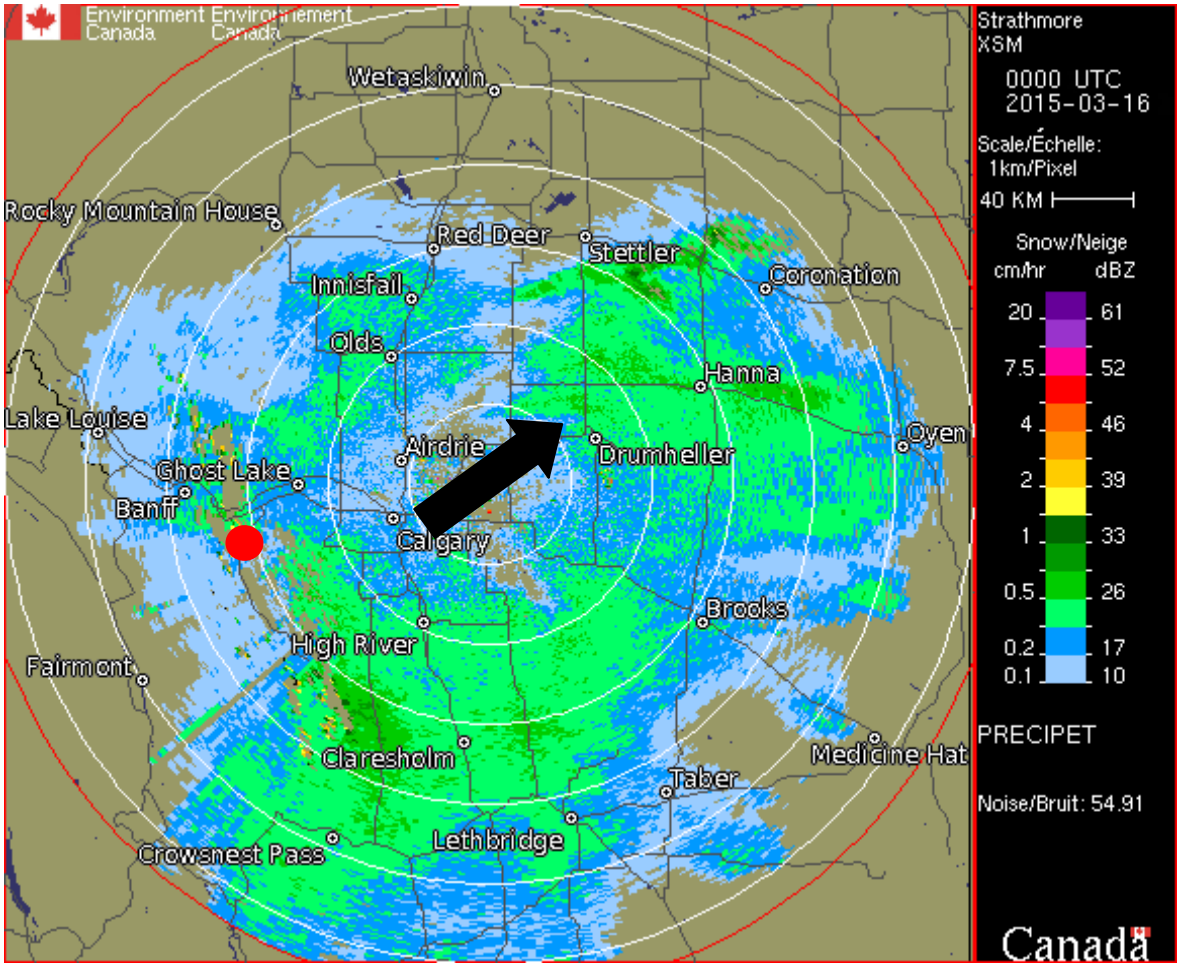


Figure 5.9: A regional view using the Strathmore, AB, radar site on March 16, 2015 at 0000 UTC. The precipitation structures are represented by an intensity scale located on the right of the image. The scale represents the snowfall rate in cm/h and the reflectivity in dBz. The rings act as a scale guide and are each equally spaced 40 km apart. The red mark indicates the location of KES and the black arrows represents the direction of motion of the radar echo. [Strathmore Radar]. Retrieved March 8, 2016, from http://climate.weather.gc.ca/radar/index_e.html

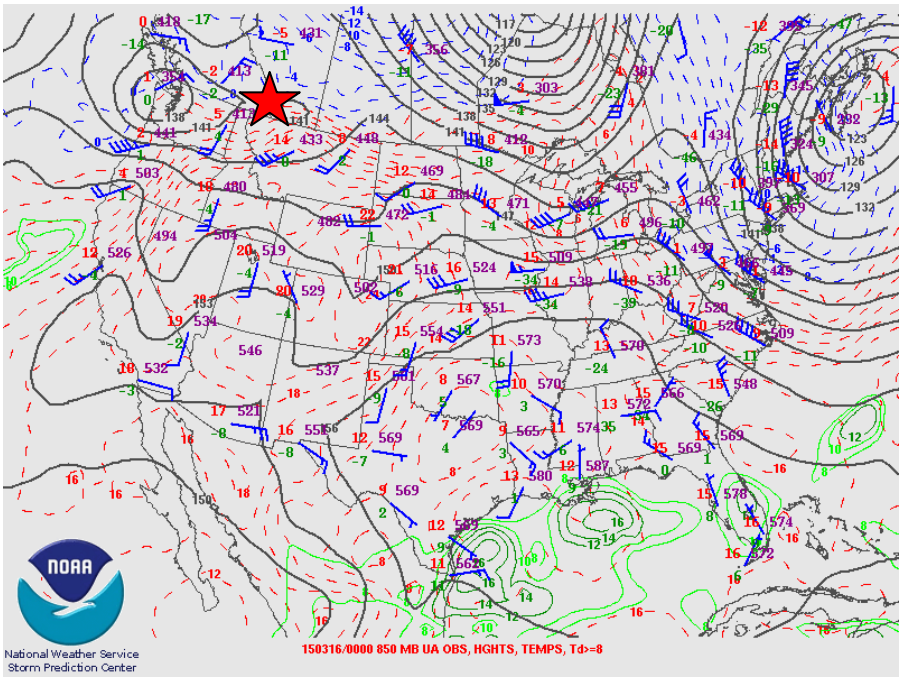


Figure 5.10: Upper analysis map of the 850 mb level on March 16, 2015 at 0000 UTC. The red star represents the location of KES. [Upper Analysis - 850 mb]. Retrieved April 26, 2016, from http://www.spc.noaa.gov/obswx/maps/

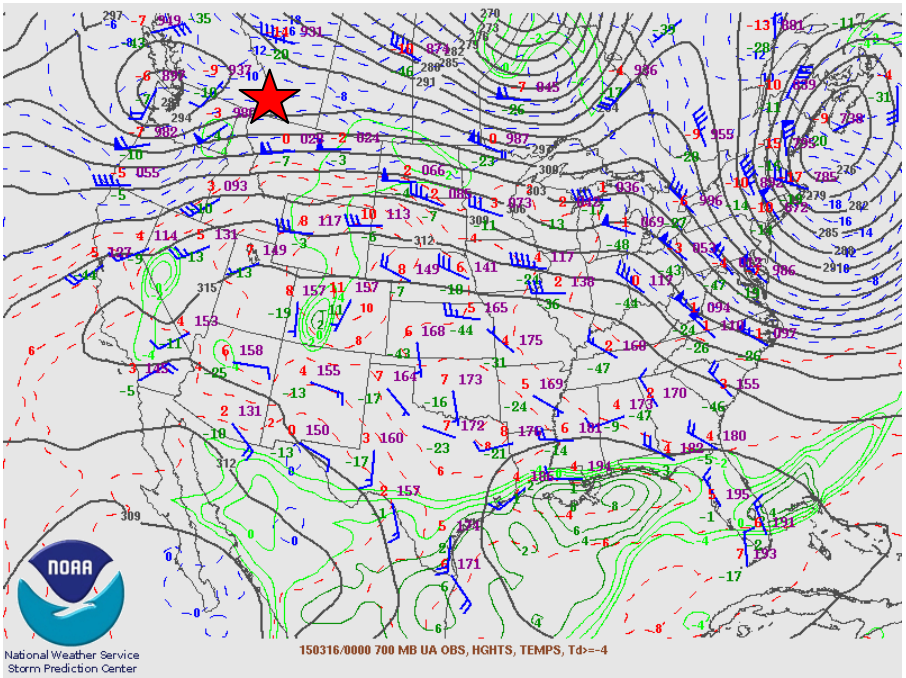


Figure 5.11: Upper analysis map of the 700 mb level on March 16, 2015 at 0000 UTC. The red star represents the location of KES. [Upper Analysis - 700 mb]. Retrieved April 26, 2016, from http://www.spc.noaa.gov/obswx/maps/

### 5.3.4.2 Case Study: April 4 - 5

Figure 5.12 to Figure 5.15 are the operational surface pressure analysis map, radar image, and upper analysis 850 and 700 mb levels during the event on April 4 – 5. The surface air was directed towards the west whereas the upper analysis levels (850 and 700 mb) and precipitation structures were both directed towards the east.

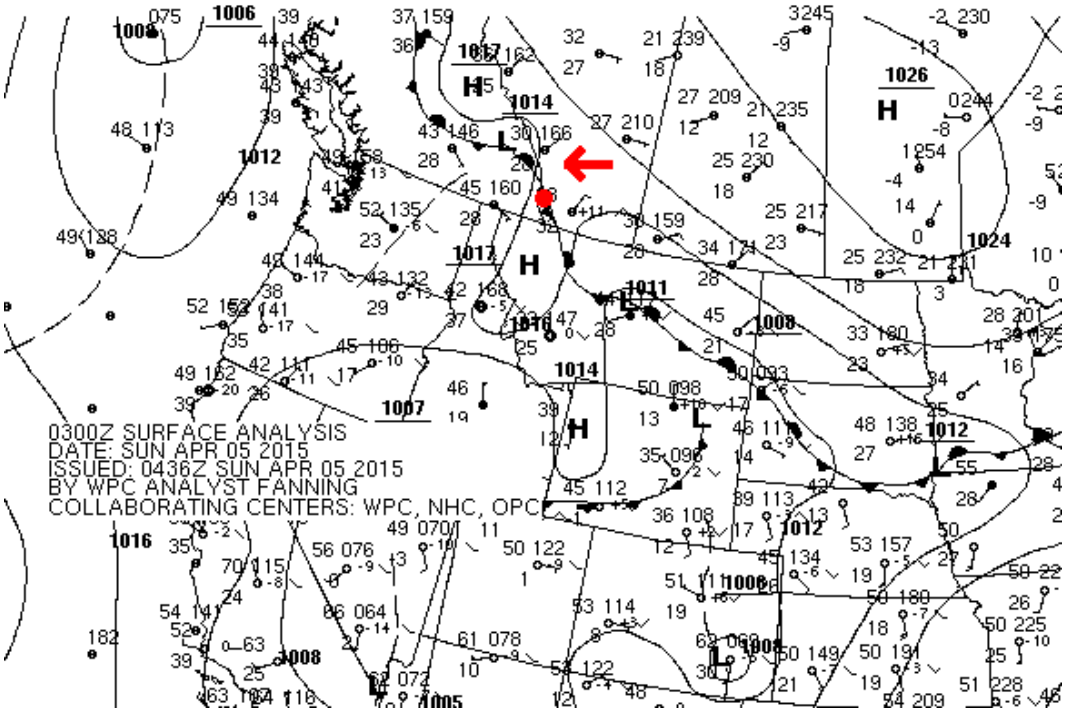


Figure 5.12: Surface analysis map of the air direction on April 5 at 0300 UTC. The red mark represents the location of KES and the red arrow represents the wind flow. [Surface Analysis]. Retrieved May 16, 2016, from http://www.wpc.ncep.noaa.gov/archives/web_pages/sfc/sfc_archive.php

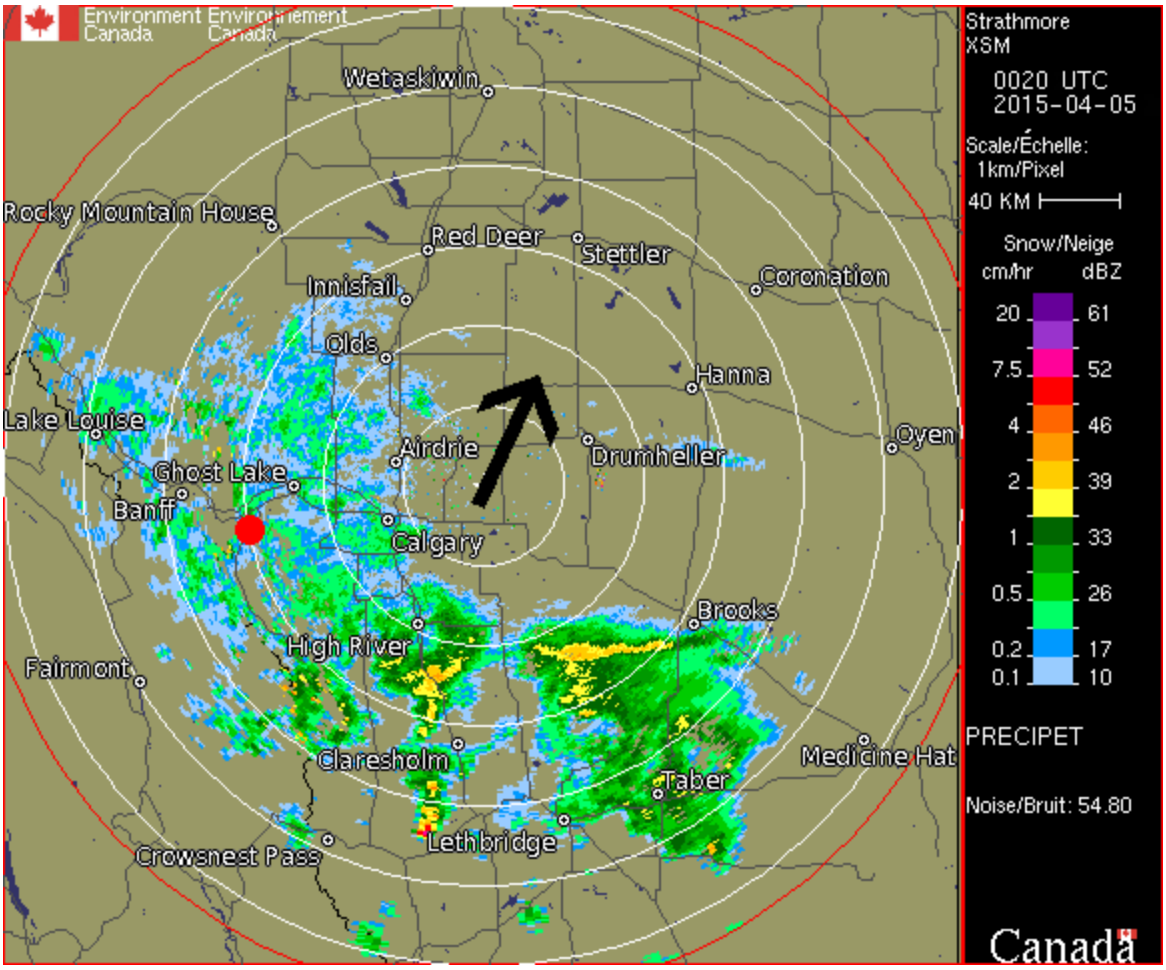


Figure 5.13: A regional view of the Strathmore, AB radar site on April 5, 2015 at 0020 UTC, as seen in the top right corner. The precipitation structures are represented by an intensity scale located on the right of the image. The scale represents the snowfall rate in cm/h and the reflectivity in dBz. The rings act as a scale guide and are each equally spaced 40 km apart. The red mark indicates the location of KES and the black arrows represents the direction of motion of the radar echo. [Strathmore Radar]. Retrieved March 8, 2016, from http://climate.weather.gc.ca/radar/index_e.html

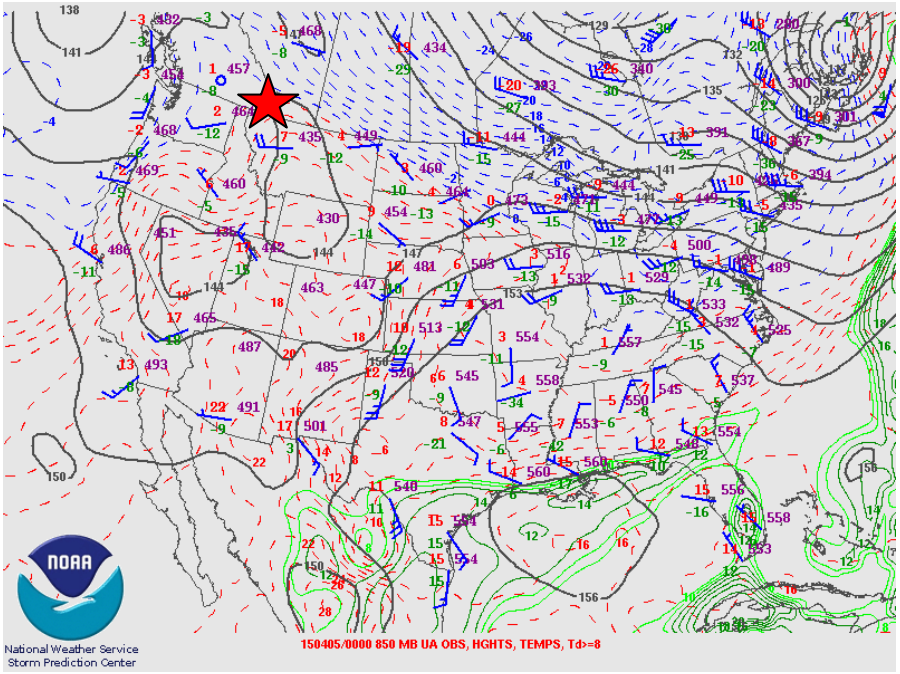


Figure 5.14: Upper analysis map of the 850 mb level on April 5, 2015 at 0000 UTC. The red star represents the location of KES. [Upper Analysis - 850 mb]. Retrieved April 26, 2016, from http://www.spc.noaa.gov/obswx/maps/

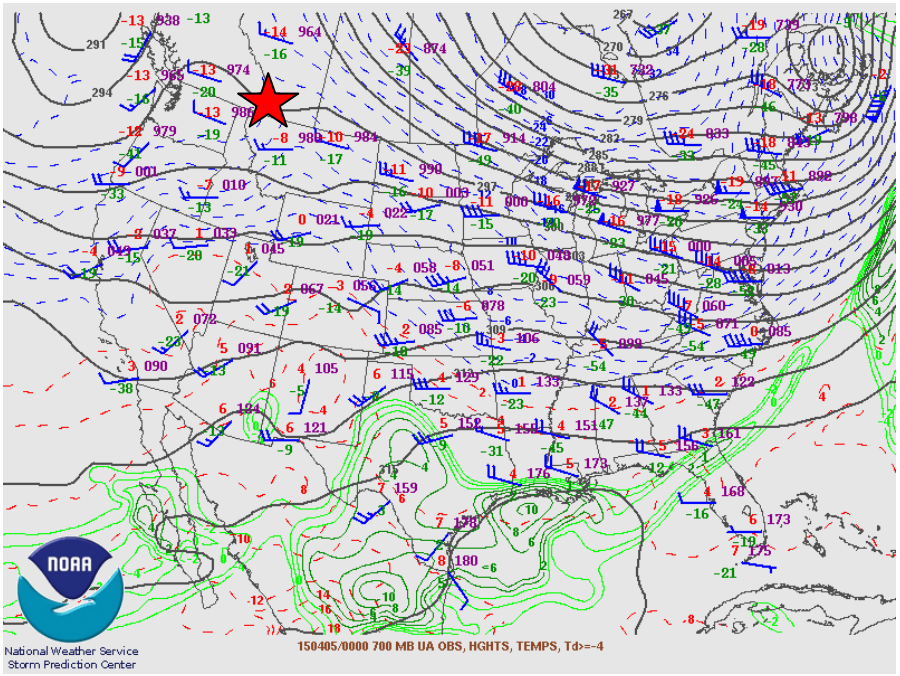


Figure 5.15: Upper analysis map of the 700 mb level on April 5, 2015 at 0000 UTC. The red star represents the location of KES. [Upper Analysis - 700 mb]. Retrieved April 26, 2016, from http://www.spc.noaa.gov/obswx/maps/

### 5.3.5. Summary of the Large and Local Scale Air Motion

Precipitation events containing microphotography observations were examined of its air motion. Table 5.3 summarizes the direction of motion for precipitation structures, surface air, and upper air levels.

Table 5.3: Summary of the precipitation events and the direction to which the air was directed towards.

| Event | Time (UTC) | Precipitation Structure Direction | Surface Air Direction | Upper Air 850 mb | Upper Air 700 mb |
|---|---|---|---|---|---|
| **Mar 15 – 16** | 0000 | Northeast | West | Northeast | East |
| **Mar 21 – 22** | 0000 | Northeast | East | East | East |
| **Apr 4 – 5** | 0000 | Northeast | West | East | East |
| **Apr 11 – 12** | 0000 | East | East | South-southeast | South-southeast |
| **Apr 14 – 15** | 0000 | East | East | South-southeast | South-southeast |
| **Apr 18** | 1200 | Southeast | South | South | Southeast |
| **Apr 25 – 26** | 0000 | West | West | West | South |

The results indicated that the surface air direction was less in agreement with the precipitation structures and the upper levels. For example, the March 15 – 16 and April 4 – 5 event indicated that the surface air was directed towards the west. The air motion was generally in agreement with the precipitation structures and the upper levels. This suggests that the driving

mechanisms for precipitation structures were mainly aloft and moved with the direction of the upper air.

Of the events examined, the air motion was generally directed towards the east, indicating that the events were downslope. However, the April 25 – 26 event indicated that the air motion was generally directed west, suggesting an upslope event.

### 5.4 Formation of Precipitation Particles

Many processes within the atmosphere influence the shape and formation of ice crystals and solid precipitation particles. The main processes include temperature and moisture, which were examined using radiosonde data.

A total of 38 radiosondes were launched from KES during precipitation events. Each sounding was approximately 90 min in duration. In total, 8 radiosondes were released during the occurrence of microphotography observations. These radiosondes were examined of its cloud temperature, moisture, and the conditions of the cloud layer during precipitation events. It is important to note that the soundings can flow several km away from the initial release location (KES) as it rises into the atmosphere.

#### 5.4.1 Event: April 4 – 5

Radiosondes were released on April 4 at 2014 UTC (Figure 5.16) and on April 5 at 0216 UTC (Figure 5.17), and 0514 UTC (Figure 5.18). The data were utilized and plotted on a skew-T diagram.

The sounding data indicated that the relative humidity did not reach saturation, with the average relative humidity between 76 and 78% for the 3 soundings. The 2014 UTC sounding of

a single cloud layer had the highest cloud base height of 2.4 km which had a cloud base temperature of -7.8°C.

The cloud tops ranged in height. The 0216 UTC sounding had the greatest cloud height of 7.8 km. The temperature at this height was -51.9°C.

The 0514 UTC sounding indicated that two cloud layers were present during the event. The first cloud layer was between 1.9 and 4.1 km (temperature ranged between -5.3 to -20.4°C), and the second cloud layer from 5.1 to 7.6 km (temperature ranged between -29.9 to -50.5°C).

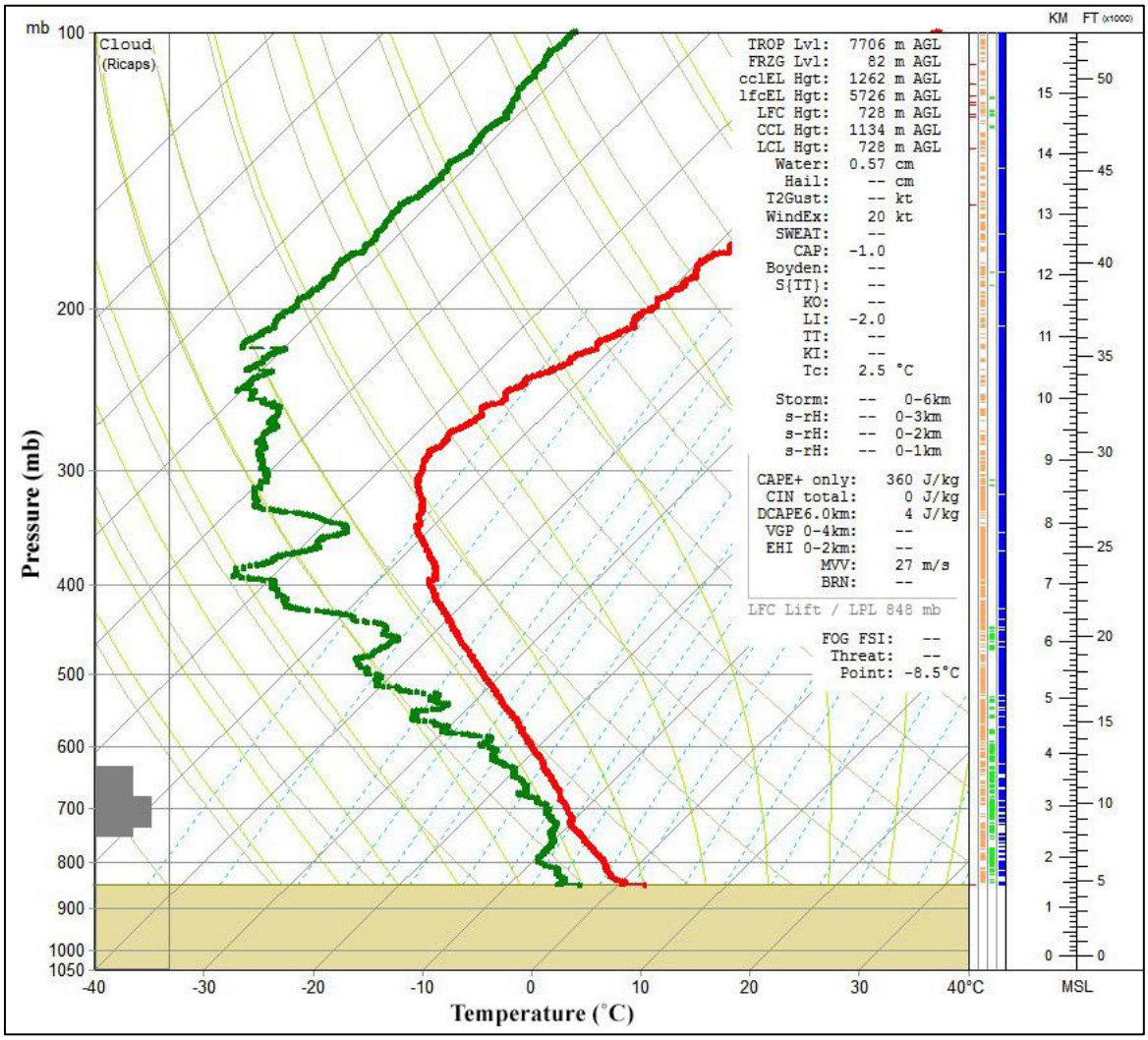


Figure 5.16: Skew-T diagram of the event on April 4 at 2014 UTC.

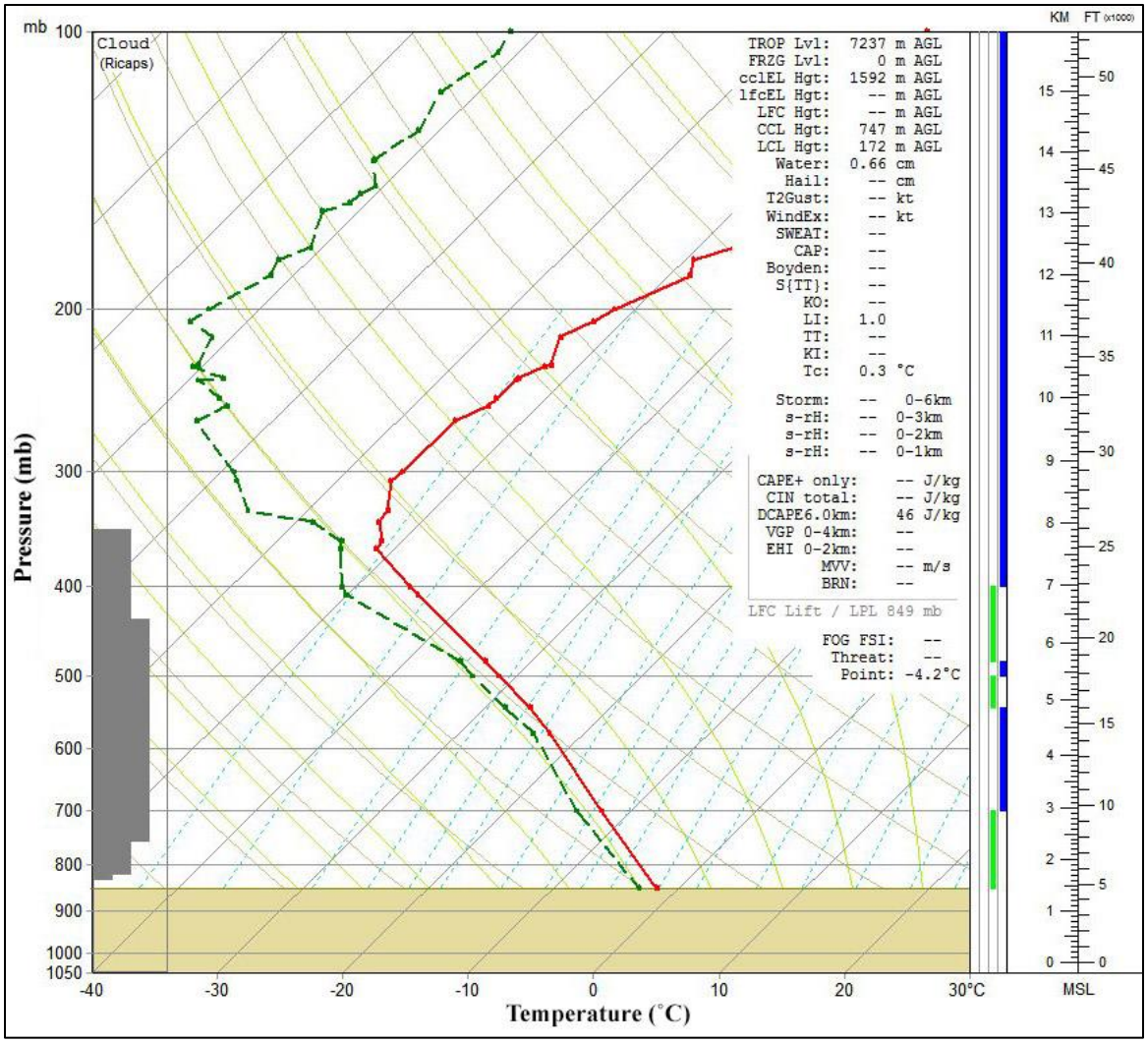


Figure 5.17: Skew-T diagram of the event on April 5 at 0216 UTC.

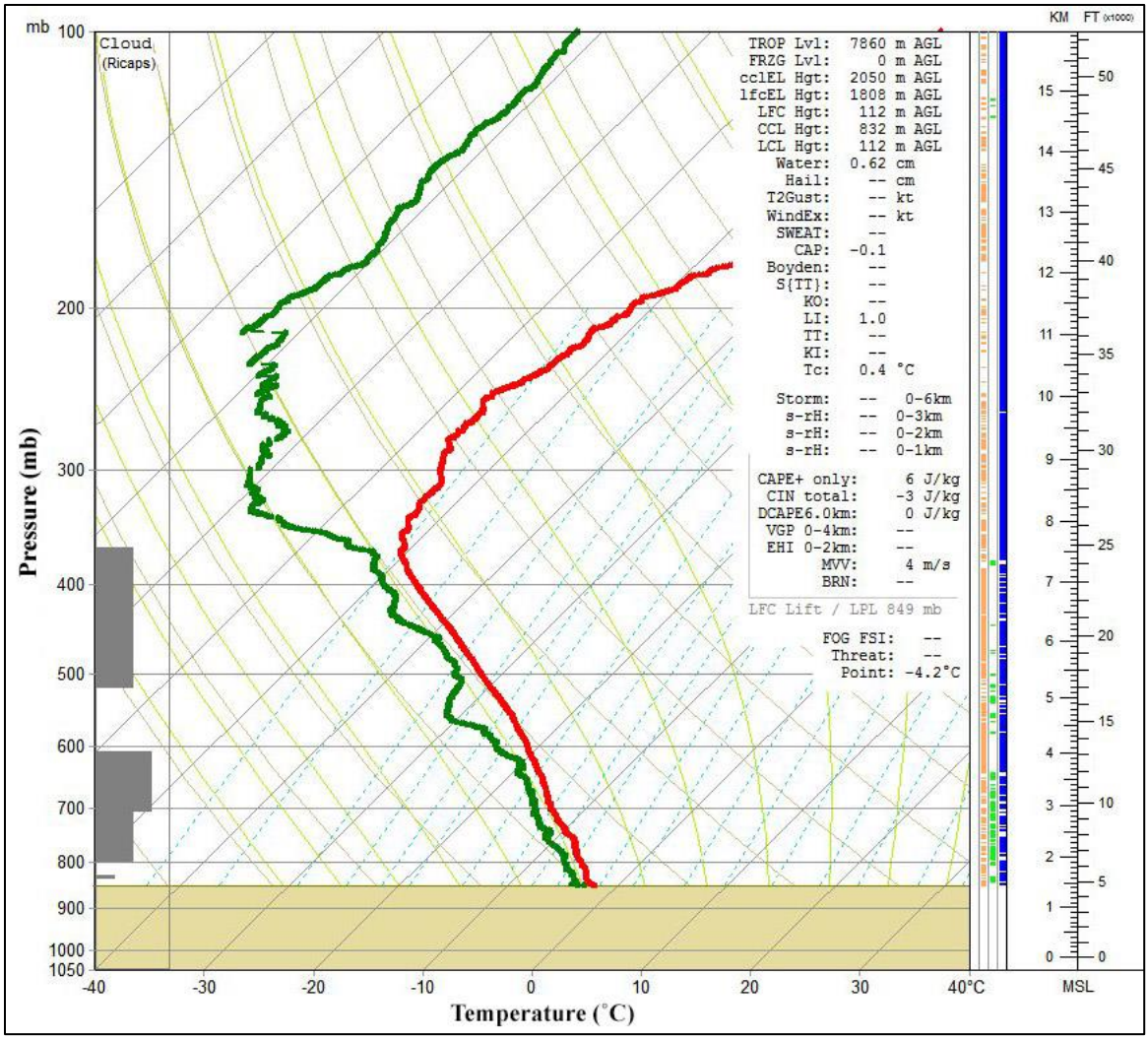


Figure 5.18: Skew-T diagram of the event on April 5 at 0514 UTC.

At the time of the 3 launches, microphotography observations identified plane crystals, rimed plane crystals, rimed column crystals, rimed irregular snow particles, rimed combination of column and plane, and rimed aggregates of snow crystals. The results suggest unrimed and rimed particles occurred simultaneously on the velvet pad. Overall, the crystal types observed at the surface and the sounding data agree with Figure 2.2 of the morphology diagram of the formation of ice crystals at different temperatures.

### 5.4.2 Event: April 11 – 12

Radiosondes were released on April 11 at 1355 UTC (Figure 5.19) and on April 12 at 0823 UTC (Figure 5.20). The sounding at 1355 UTC had a lower cloud base height of 1.8 km (with a temperature of -1.8°C) and a cloud top height of 3.6 km (with a temperature of -13.1°C).

Sounding data indicated that 2 cloud layers were present during the 0823 UTC sounding. The first cloud layer was from 2.6 to 2.9 km and the second cloud layer was from 4.6 to 4.7 km. The temperatures at the base of the clouds were cooler of -12.1°C (first cloud layer) and -27.4°C (second cloud layer). The cloud top temperatures were -13.7°C (first cloud layer) and -28.8°C (second cloud layer).

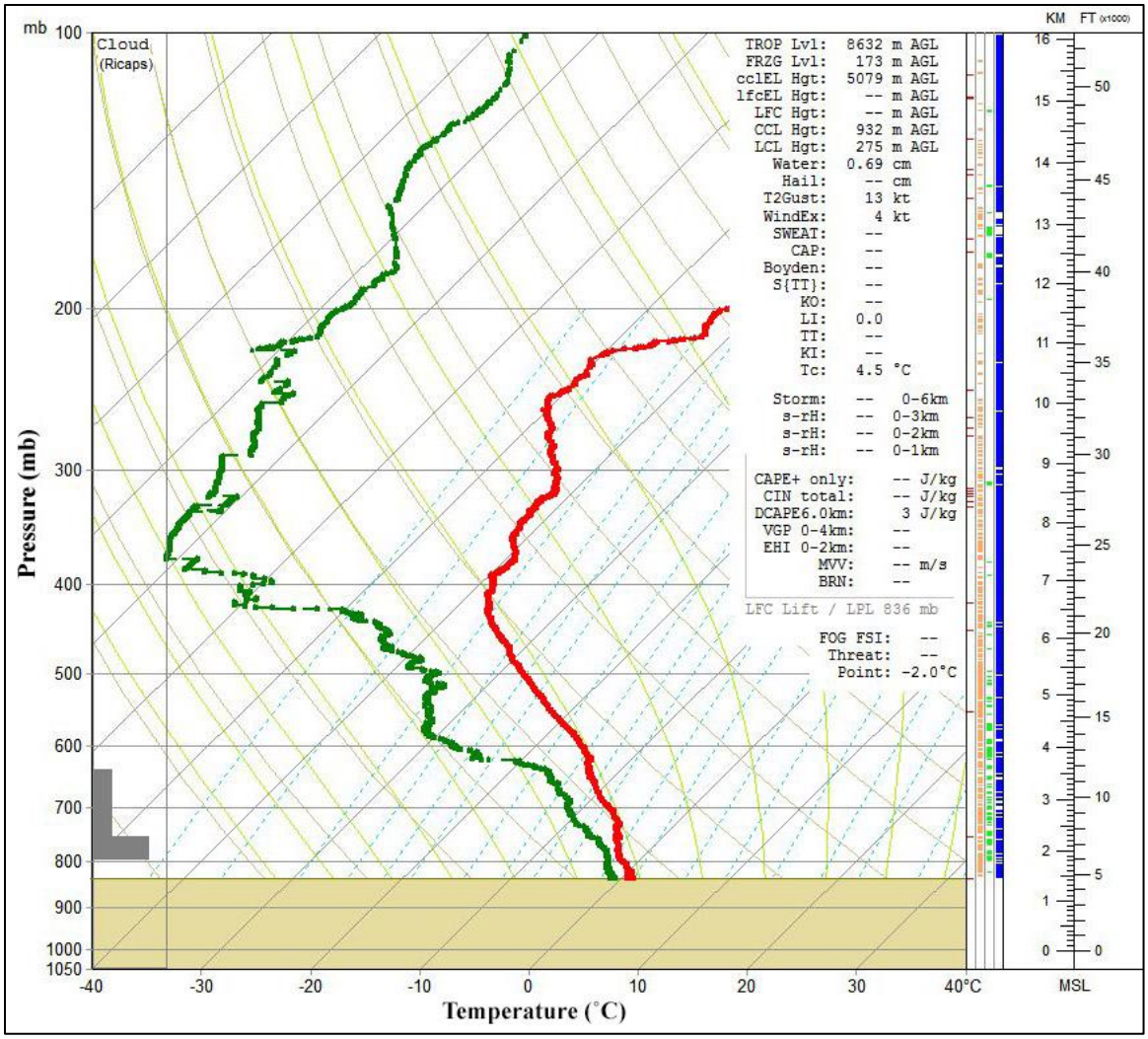


Figure 5.19: Skew-T diagram of the event on April 11 at 1355 UTC.

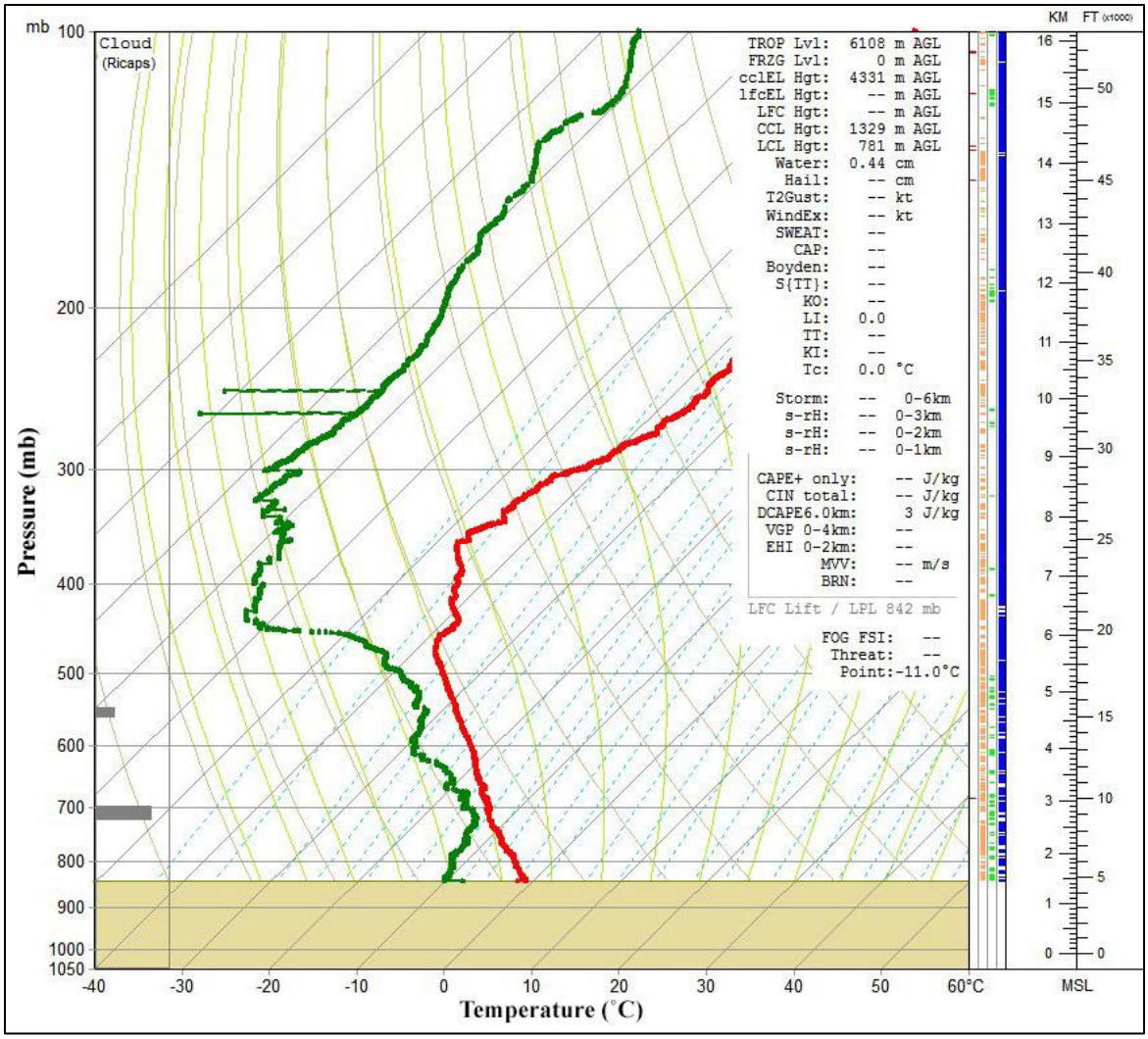


Figure 5.20: Skew-T diagram of the event on April 12 at 0823 UTC.

At the time of the 2 launches, microphotography observations identified rimed column crystals, rimed plane crystals, rimed irregular snow particles, snow pellets, rimed combination of column and plane, and rimed aggregates of snow crystals. Overall, the crystal types observed at the surface and the sounding data agree with Figure 2.2 of the morphology diagram of the formation of ice crystals at different temperatures.

### 5.4.3 Event: April 14 – 15

A radiosonde was released on April 14 at 2321 UTC (Figure 5.21). The sounding indicated that two cloud layers were present.

The first cloud layer was located at 2.3 to 5.0 km. The second cloud layer was located at 6.3 to 9.2 km. The base temperature was -5.0°C (first cloud layer) and -32.8°C (second cloud layer). The cloud top temperature was -21.9°C (first cloud layer) and -54.6°C (second cloud layer).

The layer near saturation had a temperature range from -4.6 to -10.8°C with a relative humidity range from 90 - 99%. These temperatures suggest that riming and aggregated snow crystal formation would be present.

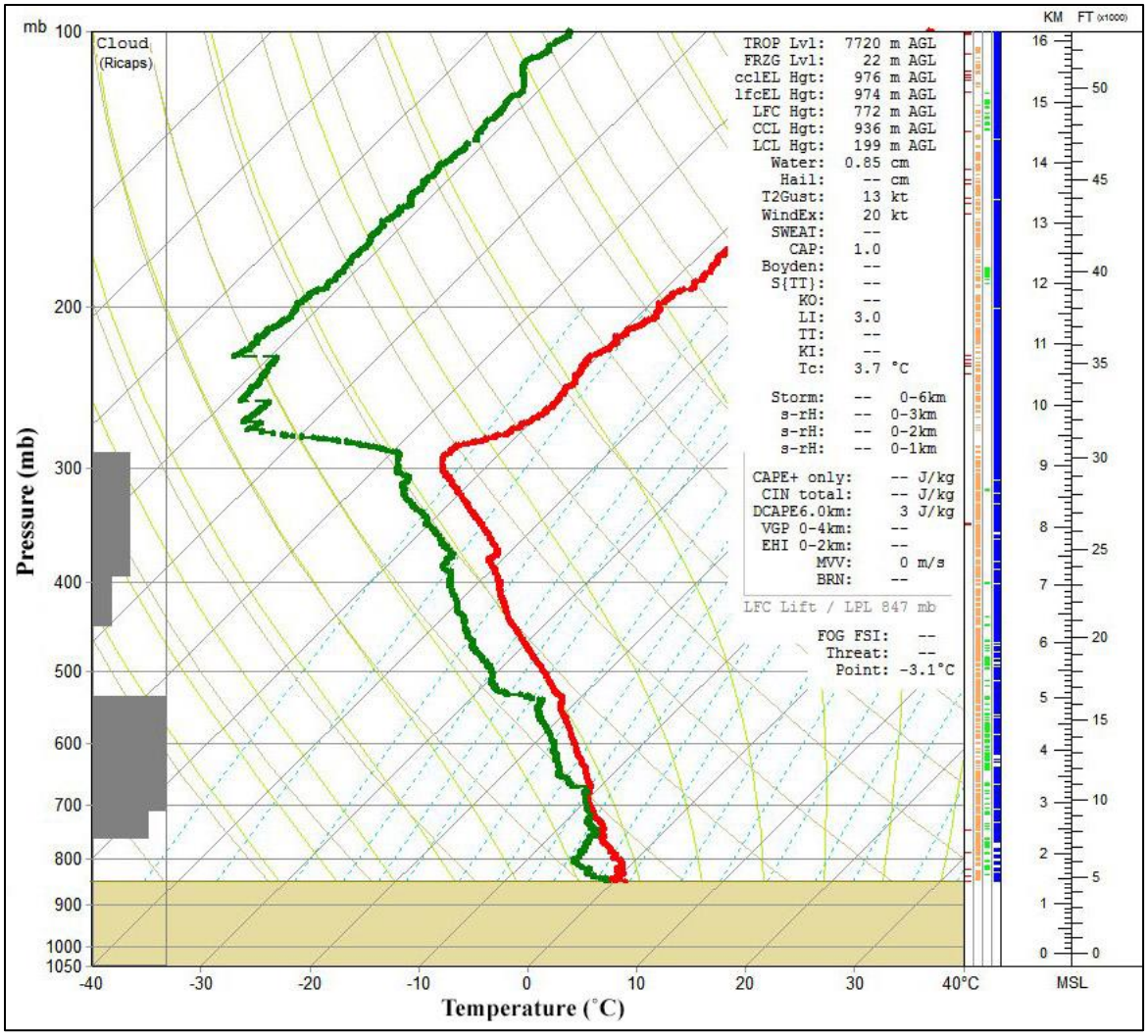


Figure 5.21: Skew-T diagram of the event on April 14 at 2321 UTC.

At the time of the launch, microphotography observations identified rimed plane crystal, rimed column crystal, rimed irregular snow particles, snow pellets, rimed combination of column and plane, and rimed aggregates of snow crystals. Overall, the crystal types observed at the surface and the sounding data agree with Figure 2.2 of the morphology diagram of the formation of ice crystals at different temperatures.

### 5.4.4 Event: April 18

A radiosonde was released on April 18 at 1132 UTC. The sounding indicated that two cloud layers were present as seen in Figure 5.22.

The first cloud layer, nearest to the surface, had a cloud base height of approximately 1.4 km and a cloud top height of approximately 3.5 km. The temperature at the base of the first cloud layer was -0.9°C and -14.0°C at the cloud top.

The second cloud layer had a base cloud height of approximately 4.2 km with a cloud height of approximately 4.3 km. The temperature at the base of the second cloud layer was -19.1°C and -23.2°C at the top.

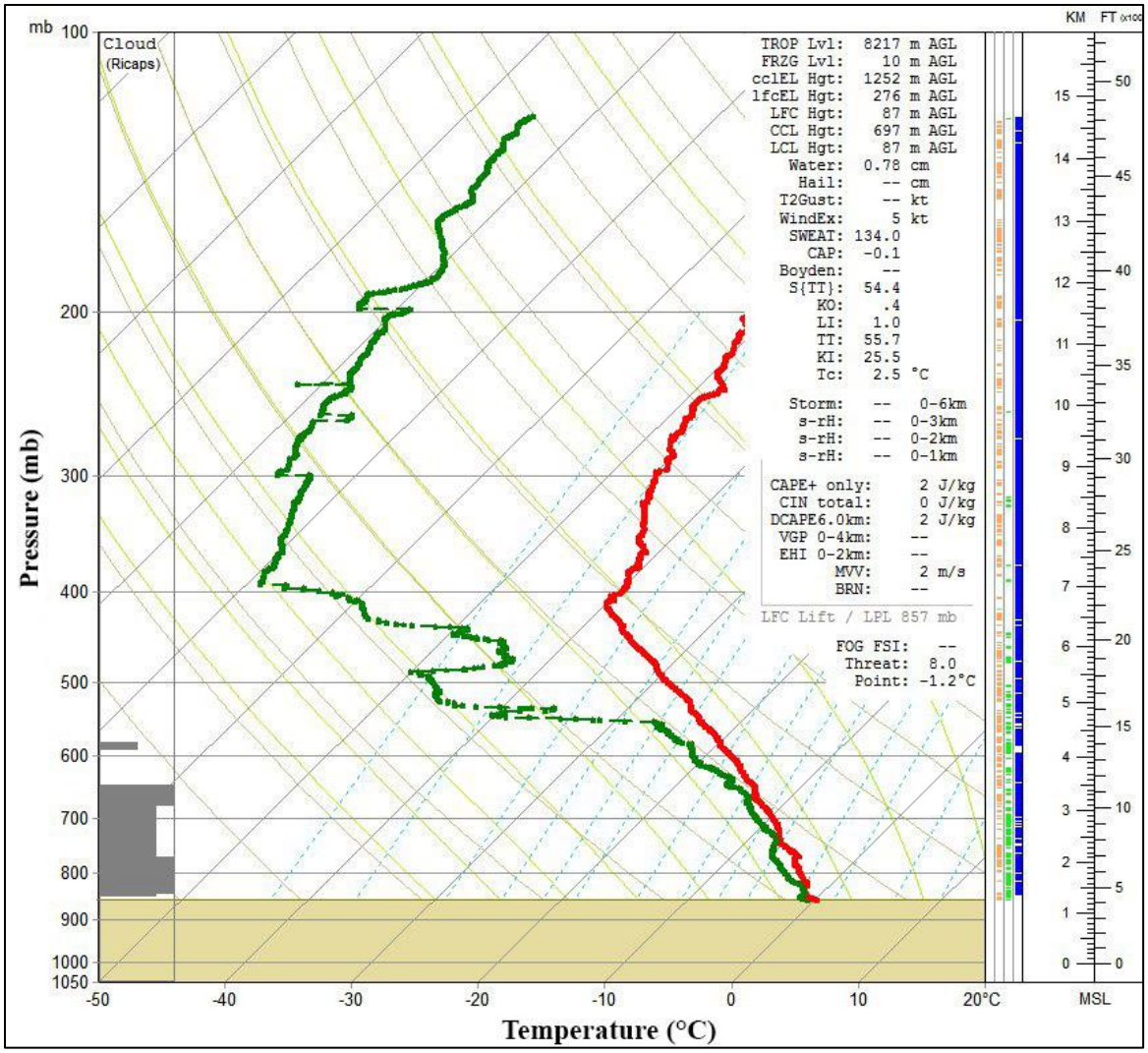


Figure 5.22: Skew-T diagram of the event on April 18 at 1132 UTC.

At the time of the release, microphotography observations identified rimed plane crystal, rimed column crystal, rimed irregular snow particles, snow pellets, rimed combination of column and plane, and rimed aggregates of snow crystals. Overall, the crystal types observed at the surface and the sounding data agree with Figure 2.2 of the morphology diagram of the formation of ice crystals at different temperatures.

### 5.4.5 Event: April 25 – 26

A radiosonde was released on April 25 at 2330 UTC (Figure 5.23). The cloud base of the first cloud layer nearest to the surface was located at 2.0 km with a temperature of -4.4°C. The cloud top height was 4.9 km with a temperature of -25.8°C.

The sounding indicated that a partial second cloud layer was present in the atmosphere with a cloud base height at 8.9 km. The temperature at the second cloud base was -54.3°C and the cloud top temperature was -55.1°C, at a height of 9.0 km. The sounding diagram indicated that the cloud layer was sub-saturated throughout.

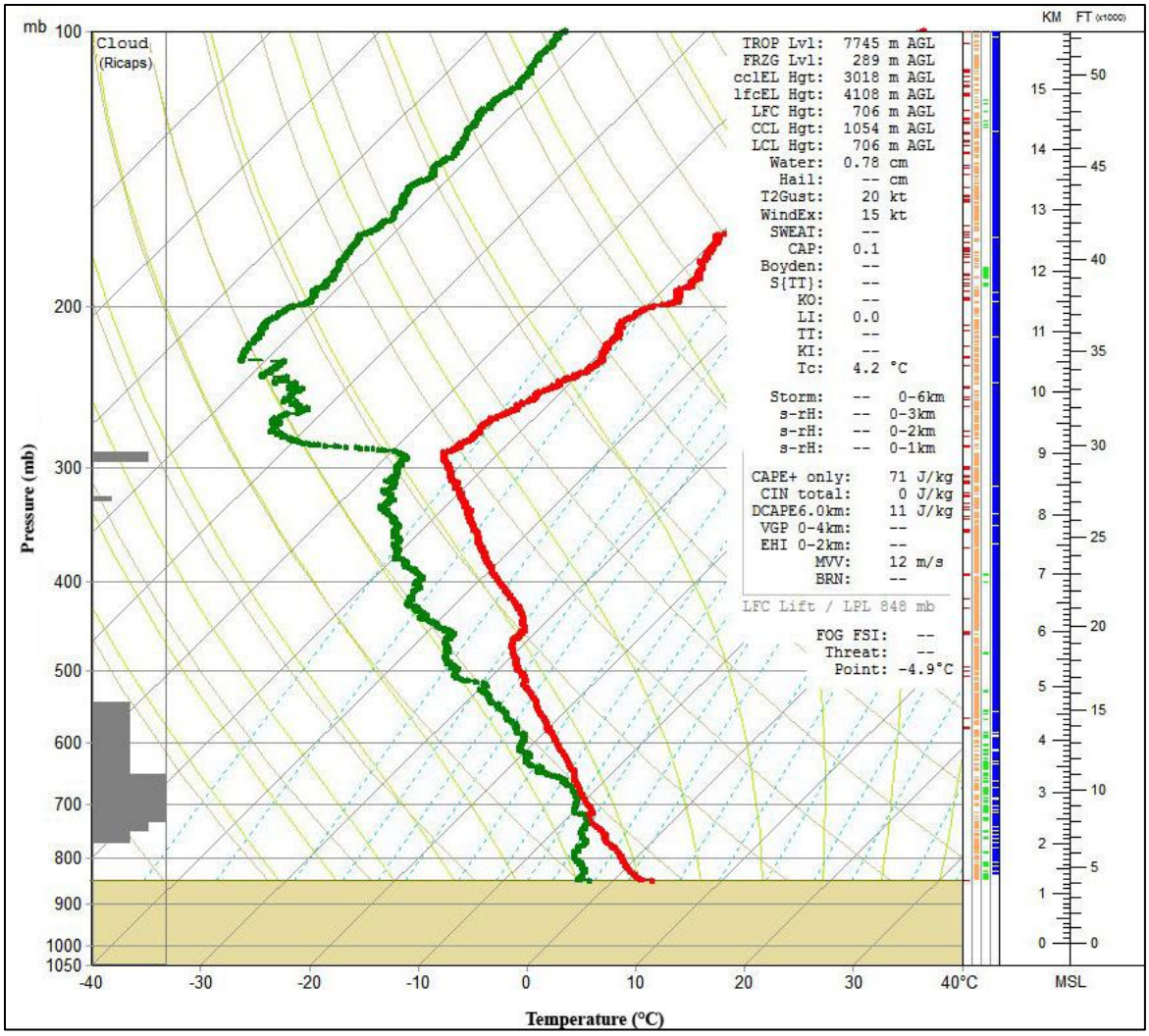


Figure 5.23: Skew-T diagram of the event on April 25 at 2330 UTC.

The average temperature and relative humidity within the first cloud layer nearest to the surface was -15.4°C and 81%. At the time of the release, microphotography observations identified rimed irregular snow particles and snow pellets. It is unclear whether the crystals observed at the surface and the sounding data agree with Figure 2.2 of the morphology diagram due to the heavy riming making it difficult to determine the type of crystal.

### 5.4.6 Summary of Radiosonde Data

The 8 soundings provided a view of the vertical atmospheric profile, cloud location, and cloud layer temperatures during precipitation events at KES. A summary of the 8 soundings can be viewed in Table 5.4. Overall, 5 soundings contained 2 cloud layers during the time of the release.

Table 5.4: Summary of the eight soundings released during microphotography observations. Events with 2 cloud layers present are listed with characteristics of the first cloud layer on the left of the slash and those of the second cloud layer on the right.

| Sounding (UTC) | Relative Humidity (water) below cloud (%) | Cloud Base Temperature (°C) | Cloud Base AGL Height (km) | Cloud Top Temperature (°C) | Cloud Top AGL Height (km) | Cloud Thickness (km) | CAPE (J/kg) |
|---|---|---|---|---|---|---|---|
| **Apr 4 - 2014** | 63 | -7.8/-- | 1.0/-- | -17.4/-- | 2.3/-- | 1.3/-- | 360 |
| **Apr 5 - 0216** | 89 | -6.8/-- | 0.3/-- | -51.9/-- | 6.4/-- | 6.1/-- | -- |
| **Apr 5 - 0514** | 87 | -5.3/-29.9 | 0.5/3.7 | -20.4/-50.5 | 2.7/6.2 | 2.2/2.5 | 6 |
| **Apr 11 - 1355** | 85 | -1.8/-- | 0.4/-- | -13.1/-- | 2.2/-- | 1.8/-- | -- |
| **Apr 12 - 0823** | 49 | -12.1/-27.4 | 1.2/3.2 | -13.7/-28.8 | 1.5/3.3 | 0.3/0.1 | -- |
| **Apr 14 - 2321** | 72 | -5/-32.8 | 0.9/4.9 | -21.9/-54.6 | 3.6/7.8 | 2.7/2.9 | -- |
| **Apr 18 - 1132** | 93 | -0.9/-19.1 | 0.1/2.8 | -14.0/-23.2 | 2.1/2.9 | 1.9/0.1 | 2 |
| **Apr 25 - 2330** | 66 | -4.4/-54.3 | 0.6/7.5 | -25.8/-55.1 | 3.5/7.6 | 2.9/0.1 | 71 |

The lowest relative humidity below the cloud was determined for the 8 soundings. Overall, the lowest relative humidity was identified during the April 12 sounding at 0823 UTC of 49%. The process of sublimation was favorable as conditions below the cloud were generally sub-saturated (76% average).

The cloud heights were generally low to the surface. The warmest cloud base temperature (-1.8°C) occurred on April 11 at 1355 UTC. As previously mentioned, the particles were heavily rimed which may have been due to the warm base temperature, enhancing the amount of riming. In contrast, the coldest cloud top temperature was -55.1°C on April 25 at 2330 UTC of the second cloud layer. The temperature of the lowest clouds ranged from -13.0 to -30.0°C as seen in Table 5.5.

Table 5.5: Summary of the average temperature, average relative humidity (water and ice), and maximum relative humidity (water and ice) of the cloud layers examined in the eight soundings. Events with 2 clouds present are listed with characteristics of the lower cloud on the left of the slash and those of the higher cloud on the right.

| Sounding (UTC) | Average Temperature (°C) | Average Relative Humidity (water) (%) | Average Relative Humidity (ice) (%) | Maximum Relative Humidity (water) (%) | Maximum Relative Humidity (ice) (%) |
|---|---|---|---|---|---|
| **Apr 4 – 2014** | -15/-- | 82/-- | 91/-- | 90/-- | 98/-- |
| **Apr 5 – 0216** | -28.7/-- | 76/-- | 95/-- | 92/-- | 110/-- |
| **Apr 5 – 0514** | -14.0/-40.0 | 86/75 | 97/104 | 92/85 | 106/117 |
| **Apr 11 – 1355** | -6.8/-- | 80/-- | 84/-- | 93/-- | 94/-- |
| **Apr 12 – 0823** | -13/-28.7 | 84/69 | 94/88 | 89/72 | 99/93 |
| **Apr 14 – 2321** | -13.1/-43.8 | 88/61 | 98/81 | 99/67 | 108/100 |
| **Apr 18 – 1132** | -7.6/-20.0 | 92/78 | 98/92 | 100/82 | 108/97 |
| **Apr 25 - 0013** | -15.4/-55.0 | 81/63 | 92/98 | 99/65 | 106/101 |

Sounding data provided insight on cloud thicknesses during precipitation events. The clouds containing greater thicknesses had lower temperatures. Therefore, optimal conditions were created for accretion.

#### 5.3.6.1 Convective Available Potential Energy (CAPE)

The soundings also revealed four events when convective available potential energy (CAPE) was present. Soundings containing CAPE were minimal in comparison to summer convective precipitation events, where values can exceed over 2,500 J/kg.

The particles observed during the release of the 8 soundings ranged from light to heavy riming. Therefore, rimed particles occurred alongside CAPE values, as well as when CAPE was not observed.

CAPE values ranged from 2 to 360 J/kg. Of the CAPE values recorded, rime intensity was examined. The sounding with the highest CAPE value of 360 J/kg was recorded on April 4 at 2014 UTC. The particles identified during the release of the sounding were rimed but of light intensity. The sounding with the lowest CAPE value of 2 J/kg was recorded on April 18 at 1132 UTC. The rimed particles identified at the surface during the release were moderate and heavy. Due to the variation in accretion, the results suggest CAPE does not influence or demonstrate any unique relationship with riming of precipitation particles. As well, it is unclear whether the low CAPE values would have any impact on accreted particles. It is important to note that CAPE may be released during the flight of soundings, making it difficult to identify any association with accretion.

#### 5.3.6.2 Cloud Thickness

Cloud thicknesses were examined in the soundings using RAOB. The thickness ranged from 0.1 to 6.1 km during precipitation events at KES as seen in Table 5.6. For this study, thin clouds referred to thicknesses of less than or equal to 2.5 km. Thick clouds referred to clouds with thicknesses greater than 2.5 km.

Relatively thin clouds were observed on the April 12 sounding at 0823 UTC. RAOB indicated two cloud layers in the sounding, with the top cloud layer having a 0.1 km thickness. A thickness of 0.1 km was also observed for the top cloud layer during the April 18 sounding at 1132 UTC and on April 25 at 2330 UTC. The soundings with 'thin clouds' were mainly of moderately rimed particles with varying precipitation intensity (light to heavy).

A thick cloud in the April 5 sounding at 0216 UTC had a thickness of 6.1 km with moderate precipitation intensity. As previously mentioned, the particles during the April 4 – 5 soundings were of a wide variety of particles. A closer examination of the particles after the sounding release revealed that unrimed and rimed particles occurred simultaneously. Many of the small particles were rimed aggregates of snow crystals, rimed columns, rimed irregular snow particles, and rimed combination of column and plates. Overall, riming intensity ranged from light to heavy for cases with thick clouds.

# Chapter 6 - Comparison with other Studies

In this section, a comparison with related studies is carried out. Several studies have examined cold season precipitation in several regions of northern Canada (Burford and Stewart, 1998; Stewart et al., 2004; Hudak et al., 2004; Henson et al., 2011; Fargey et al., 2013) and their findings need to be compared with those found at KES.

First, Burford and Stewart (1998) studied sublimation of falling snow over the Mackenzie River Basin as well as the Arctic during the autumn 1994 Beaufort and Arctic Storms Experiment (BASE). To approximate the mass loss caused by sublimation during the autumn season, models and results were compared to precipitation measurements at Inuvik, Tuktoyaktuk, and several sites in Northern Canada. Burford and Stewart (1998) stated that the density of the winter precipitation particle and its terminal velocity influences the rate of sublimation in addition to the cloud base height, relative humidity, and temperature. They found that precipitation was of light intensity and trace amounts. Particles during the BASE study were unrimed with rare occurrences of rimed particles. They found particle types ‘snow’ and ‘unrimed dendrites’ to sublimate most rapidly due to their lower density and lower terminal velocity. They also found that for a relative humidity of 70%, sublimation loss was 40 to 90% and increased to 100% for less heavily rimed particles. For a relative humidity of 90%, sublimation loss for particle type ‘snow’ was 18 to 70%. In addition, they identified that temperatures at 0°C had a sublimation loss of 70% or greater and at least a 20% loss at -20.0°C.

Burford and Stewart (1998) identified the process of sublimation to influence the amount of precipitation received at the surface during the BASE study. It was found that the probability of particles with a lower density and terminal velocity had a higher chance of sublimating.

However, unrimed particles (lower density and terminal velocity) were observed on site. In comparison to KES, several occurrences of light rime and light precipitation were observed. The majority of particles observed during the March 15 – 16 event were of unrimed particles. The results from Inuvik, Tuktoyaktuk, and KES indicate that unrimed particles can reach the surface before sublimating despite its lower density and terminal velocity in comparison to rimed particles.

Second, during the autumn and winter of 1998 and spring of 1999, precipitation events were examined at Fort Simpson, Northwest Territories (Stewart et al., 2004; Hudak et al., 2004). Data were collected during the Canadian Global Energy and Water Cycle Experiment (GEWEX) Enhanced Study. A two-part study utilized the data collected in which Stewart et al. (2004) studied the precipitation features and Hudak et al. (2004) studied the cloud features. A variety of observational tools were used to examine the precipitation events.

Stewart et al. (2004) stated that the precipitation at Fort Simpson was often influenced by sublimation. Photographed particles at Fort Simpson were largely unrimed single crystals with light intensity (Stewart et al., 2004). In addition, cloud features observed by Hudak et al. (2004) found the mean cloud thickness to be 2.3 km (spring of 1999) with several multilayer cloud systems. Stewart stated that cloud layers, along with sub-saturated conditions reduced the amount of precipitation reaching the surface.

Similarly at KES, cloud thickness observed using the sounding data indicated a mean of 2.4 km. Comparable to the location of KES, Fort Simpson is situated at the lee of the Rocky Mountains (Stewart et al., 2004). Despite the process of sublimation, unrimed particles were able to reach the surface before sublimating at Fort Simpson, similar to the study by Burford and Stewart (1998), and the results at KES.

Third, a similar study completed by Henson et al. (2011) as part of the Storms Studies in the Arctic (STAR) field campaign examined precipitation events in Iqaluit, Nunavut. Observations were collected during the autumn season between October 15, 2007 and December 5, 2007. Microphotography observations revealed rimed particles, aggregates, and snow pellets were common during light precipitation events (Henson et al., 2011). Henson et al. (2011) suggested that sublimation of particles occurred and as a result, affected the amount of precipitation received at the surface.

As stated by Burford and Stewart (1998) and Stewart et al. (2004), particles with a higher density and terminal velocity are more likely to reach the surface before sublimating. This was observed during STAR where heavily rimed particles were common. Similarly, several instances occurred when light precipitation and trace amounts were observed at KES during snow pellet observations (April 25 – 26 event). Due to a higher density and terminal velocity, it is likely that heavily rimed particles were able to reach the surface before sublimating at KES, as observed at Iqaluit, Nunavut.

Fourth, a study by Fargey et al. (2013) was carried out in the southeast Canadian Arctic over the orographic terrain of southern Baffin Island, Nunavut. The study utilized data collected from the Storm Studies in the Arctic (STAR) field campaign in autumn 2007 in relation to the study by Henson et al. (2011). The study analyzed notable differences between cloud and precipitation over orographic terrain in comparison to ocean regions. Fargey et al. (2013) stated that dynamic and thermodynamic factors would increase particle collision aloft, which may be why accretion and aggregation were more common over orographic terrain than the ocean regions. Fargey et al. (2013) also stated that accretion and aggregation increases a particles density and terminal velocity, wherein return, increases the probability of the particle reaching

the surface before sublimating. Data collected from the STAR field campaign indicated a lower concentration of small particles in the orographic region compared to the ocean region, suggesting that small particles are easily sublimated due to their lower density and terminal velocity (Fargey et al., 2013).

As mentioned by Fargey et al. (2013), accretion and aggregation were common over orographic terrain, including a lower concentration of small particles. These characteristics were similar over the orographic terrains of KES. In comparison to KES, accretion and aggregation were common in microphotography and manual observations. The heavily rimed particles at KES and southern Baffin Island likely reached the surface before sublimating due to their increased terminal velocity.

To summarize the comparison, the results at KES are somewhat similar to those found by Burford and Stewart (1998), Stewart et al. (2004), Hudak et al. (2004), Henson et al. (2011), and Fargey et al. (2013). The 5 studies identified sublimation as a critical factor for reducing the amount of precipitation observed at the surface, and they all typically found precipitation to occur during light intensity. Burford and Stewart (1998) and Stewart et al. (2004) identified unrimed particles as the dominant precipitation whereas accreted particles were dominant in Iqaluit (Henson et al., 2011; Fargey et al., 2013). The studies all suggested that heavily rimed particles would allow precipitation to reach the surface before sublimating due to a higher terminal velocity and generally a greater mass. Although the 5 studies were all completed in Northern Canada, the features and processes are comparable to the events observed at KES.

# Chapter 7 - Summary and Concluding Remarks

The Alberta field campaign was carried out during March and April 2015 in the Kananaskis Valley at the Kananaskis Emergency Site (KES) to improve our understanding of its precipitation and associated atmospheric conditions. A variety of instruments were deployed to collect precipitation and other observations. The overall goal of this thesis is to examine the characteristics and formation of precipitation during 11 events. The study focuses mainly on the analysis of microphotographic images taken during 7 precipitation events, manual observations of 4 events, as well as selected data from other instrumentation and observer notes. The results have led to several observations and conclusions as summarized below from small to large scale.

The microphotography images revealed a large range of particle types during the seven precipitation events. Unrimed and rimed particle types were placed into 12 categories of plane crystals, column crystals, irregular snow particles, other solid precipitation particles, snow pellets, combination of column and plane crystals, and aggregates of snow crystals. The most common category observed during the study was rimed irregular snow particles.

The images were used to identify the largest particle for each precipitation event where sizes ranged up to 24 mm. The largest particle type observed was an aggregate of snow crystal and the largest plane crystal examined ranged up to 5 mm in size.

Riming was common during the precipitation events. Microphotography results indicated 62% of the ice crystals and solid precipitation particles were rimed. Of the rimed particles, 59% were rimed irregular snow particles. Also, unrimed particles often occurred simultaneously with rimed particles on a single observing pad. Up to 21% of the images collected during a single event contained unrimed and rimed particles occurring simultaneously.

The intensity of riming was analyzed using microphotography observations. Each particle visible in the images was categorized as being unrimed, light, moderate, or heavily rimed. Of the rimed categories, the results indicated 26% of the particles were moderately rimed. However, 38% of the particles were unrimed where 98% were observed during the March 15 – 16 event.

Several frozen cloud droplets were examined on ice crystals and solid precipitation particles using the microphotography images. The liquid equivalent radii ranged up to 25 μm and the average liquid equivalent radius was 16 μm. Such sizes demonstrate characteristics of cloud droplets in continental air masses.

Ice crystals and solid precipitation particles were observed at the surface when temperatures were above 0°C, ranging up to 9.1°C (7.8°C at the KBA station) using manual observations. Observations indicated that rimed particles were most commonly observed in these instances although unrimed particles were also sometimes identified.

Sublimation aloft played a large role in determining the overall accumulated precipitation at the surface. Accretion was common as mentioned above and such denser, faster-moving particles are more readily able to reach the surface before sublimating in the generally dry atmospheric conditions. Similar results were seen in several past studies carried out in Northern Canada.

Surface winds were related to particle features. Of the 8 quadrants examined, 11 of the 12 particle categories were identified during northerly, southerly, southwesterly, and westerly winds. Rimed particles were present in almost all of the 8 quadrants in sub-saturated to near saturated conditions.

Precipitation structures, operational surface pressure analyses, and upper air analyses were used to examine the direction to which the air was directed. The radar-revealed

precipitation structures were mainly directed towards the east, and this was mainly consistent with upper levels (850 – 700 mb) which indicated that the overall air motion was generally 'downslope'. Surface pressure fields were not consistent with the precipitation structures and upper air analyses due to local topographic effects not directly linked with the storm conditions aloft that would initially produce the precipitation. Due to topographic influences and weather station citing, the KBA and ECCC wind data were not ideal for this analysis.

The soundings provided insight on the approximate heights and conditions aloft of crystal formation. Overall, the crystal types and sounding data were in agreement with the morphology diagram and temperature (Figure 2.2). Accretion on particles at the surface was associated with cloud thicknesses up to 6 km, cloud layer temperatures as low as -26˚C (first cloud layer above the surface), and in soundings with or without CAPE. However, no correlation was identified between accretion and CAPE values.

The study had several limitations. For instance, the location of KES is known to local residents as often being subjected to reduced precipitation due to topographic influences with little precipitation reaching KES but higher amounts nearby. No major precipitation event occurred during the field campaign, so results were limited to events producing modest precipitation. In comparison to archived temperature and precipitation data, the year 2015 was warm and dry, with March – April 2015 having above normal temperatures and substantially lower precipitation amounts. Issues involving the placement of the EC station near buildings or large objects may have also affected data quality. In addition, a few instruments were not delivered to the site before the field campaign commenced, which caused delays as well as missing data. Also, technical issues caused a few instruments to begin operating near the end of the month of March.

The project was also created as a pilot project for future research addressing mountain precipitation. Suggestions for future research include measurements at additional observational sites within the Kananaskis Valley that may be subjected to greater precipitation. Also, a longer duration experiment would be useful to examine seasonal variations. As well, it would be useful to photograph winter precipitation particles the moment they land on a surface, rather than placing the velvet pad inside a ventilated tent since the temperatures inside can be warmer and would undoubtedly increase the rate of melting.

In summary, the cold season precipitation identified at KES varies considerably in its characteristic and form. Observations of unrimed and rimed particles occurring simultaneously were not uncommon and solid precipitation particles were able to reach the surface with temperatures above 0˚C with low relative humidities. Events examined were generally sub-saturated aloft, producing precipitation commonly observed with light intensity. The results were similar to precipitation features and formation processes inferred in northern Canada which highlights how the process of sublimation can negatively affect the amount of precipitation reaching the surface. This was at least partially a result of the air aloft being mainly directed towards the east and generally ‘downslope’.

**Bibliography**


Alberta Agriculture and Forestry, n.d.: AgroClimatic Information Service (ACIS) Definitions. Retrieved from http://agriculture.alberta.ca/acis/docs/station-viewer-explained-y2015_m04_d21.pdf

Alberta Agriculture and Forestry, 2016: Alberta Climate Information Service (ACIS) – Kananaskis Boundary Auto station [Data file]. Retrieved May 25, 2016 from http://agriculture.alberta.ca/acis/.

Barthazy, E. and R. Schefold, 2006: Fall velocity of snowflakes of different riming degree and crystal types. *Atmos. Res.,* **82**, 391-398.

Burford, J. E., and R. E. Stewart, 1998: The sublimation of falling snow over the Mackenzie River Basin. *Atmos. Res.*, **49**, 289-313.

DeBeer, C. M., H. S. Wheater, W. L. Quinton, S. K. Carey, R. E. Stewart, M. D. Mackay, and P. Marsh, 2014: The Changing Cold Regions Network: Observation, diagnosis and prediction of environmental change in the Saskatchewan and Mackenzie River Basin, Canada. *Earth Sci.,* **58**, 46-60.

Dingman, S. L., 1994: *Physical Hydrology.* Prentice Hall, Upper Saddle River: New Jersey.

Fargey, S., J. Hanesiak, R. Stewart, and M. Wolde, 2013: Aircraft observations of orographic cloud and precipitation features over southern Baffin Island, Nunavut, Canada. *Atmos.-Ocean,* **52 (1)**, 54-76.

Fleagle, R. G., and J. A. Businger, 1980: *An Introduction to Atmospheric Physics.* New York: Academic Press.

Furukawa, Y., and J. S. Wettlaufer, 2007: Snow and ice crystals. *Phys. Today*, **60**, 70-71.

Gibson, S. R., and R. E. Stewart, 2007: Observations of ice pellets during a winter storm. *Atmos. Res.,* **85**, 64-76.

Gibson, S. R., R. E. Stewart, and W. Henson, 2009: On the variation of ice pellet characteristics. *J. Geophys. Res.* D09207, doi:10.1029/2008JD011260.

Hanesiak, J., R.E. Stewart, P. Taylor, K. Moore, D. Barber, G. McBean, W. Strapp, M. Wolde, D. Hudak, J. Scott, G. Liu, J. Gilligan, S. Biswas, R. Dyck, S. Fargey, R. Field, G. Gascon, M. Gordon, H. Greene, C. Hay, W.Henson, K. Hochheim, A. Laplante, M. Albarran Melzer, and S. Zhang, 2010: Storm Studies in the Arctic: the meteorological field project. Bull. Amer. Meteor. Soc., 91, 47-68.

Harder, P., 2008: *Hydroclimatological trends in the Kananaskis Valley* (Unpublished masters thesis). University of Saskatchewan, Saskatoon, Saskatchewan.

Henson, W., R. E. Stewart, R. E., and D. Hudak, 2011: Vertical reflectivity of precipitation over Iqaluit, Nunavut during autumn 2007. *Atmos. Res.,* **99**, 217-229.

Hudak, D., B. Currie, R. E. Stewart, P. Rodriguez, J. Burford, N. Bussieres, and B. Kochtubajda, 2004: Weather systems occurring over Fort Simpson, Northwest Territories, Canada, during three seasons of 1998-1999: 1. Cloud features. *J. Geophys. Res.,* **109**, D22108, doi:10.1029/2004JD004876.

Kikuchi, K., T. Kameda, K. Higuchi, and A. Yamashita, 2013: A global classification of snow crystals, ice crystals, and solid precipitation based on observations from middle latitudes to polar regions. *Atmos. Res.,* **132-133**, 460-472.

Kobayashi, T. and Y. Furukawa, 1974: On twelve-branched snow crystals. *J. Crystal Growth,* **28,** 21-28.

Libbrecht, K., 2001: Morphogenesis on ice: The physics of snow crystals. *Eng. Sci.,* **64,** 10-19.

Magono, C. and C. W. Lee, 1966: Meteorological classification of natural snow crystals. *J. Fac. Sci.,* Hokkaido Univ., Ser. 7, **5**, 321-335

Maidment, D. R.,1993: *Handbook of Hydrology*. McGraw-Hill, Michigan: University of Michigan.

Matsuo, T., Y. S. Sasyo, and Y. Sato, 1981: Relationship between types of precipitation on the ground and surface meteorological elements. *J. Meteor. Soc. Jpn.,* **59**, 462-476.

Nakaya, U., 1954: *Snow Crystals, Natural and Artificial.* Harvard University Press, 510 pp.

Rogers, R. R., 1978: A Short Course in Cloud Physics 2nd Edition. Willowdale, Ontario: Pergamon Press.

Stewart, R. E., J. D. Marwitz, J. C. Pace, and R. E. Carbone, 1984: Characteristics through the melting layer of stratiform clouds. *J. Atmos. Sci.,* **41**, 3227-3237.

Stewart, R. E., J. E. Burford, D. R. Hudak, B. Currie, B. Kochtubajda, P. Rodriguez, and J. Liu, 2004: Weather systems occurring over Fort Simpson, Northwest Territories, Canada, during three seasons of 1998-1999: 2. Precipitation features. *J. Geophys. Res.,* **109**, D22109, doi:10.1029/2004JD004929.

Stewart, R. E., J. Thériault, and W. Henson, 2015: On the characteristics of and processes producing winter precipitation types near 0˚C. *Bull. Amer. Meteor. Soc.,* **96**, 623-639.

Stoelinga, M. T., R. E. Stewart, G. Thompson, and J. M. Theriault, 2013: Microphysical processes within winter orographic cloud and precipitation systems. *Mountain Weather Research and Forecasting: Recent Progress and Current Challenges,* F. K. Chow, S. F. J. De Wekker, and J. B. Snyder, Eds., Springer, 345-408.

Theriault, J. M., K. L. Rasmussen, T. Fisico, R. E. Stewart. P. Joe, I. Gultepe, M. Clement, and G. A. Issac, 2014: Weather observation on Whistler Mountain during five storms. *Pure Appl. Geophys.,* **171**, 129-155.

Travel Alberta, 2016: Kananaskis Country. Retrieved November 2, 2016 from https://www.travelalberta.com/ca/places-to-go/provincial-parks/kananaskis-country/

Universal Rawinsonde Observation Program, 2016: RAOB Integrated Cloud and Precipitation System (RICAPS). Retrieved November 7, 2016 from http://www.raob.com/ricaps.php

Whitfield, P. H., 2014: Climate station analysis and fitness for purpose assessment of 3053600 Kananaskis, Alberta. *Atmos. Ocean,* **52**, 363-383.

# Appendix A: Instruments at the Kananaskis Emergency Site

Figure A.1. Left to right: Precipitation accumulation, sounding instruments1 and 2, particle size velocity disdrometer (PARSIVEL) (not used in this thesis). (Almonte, 2015).

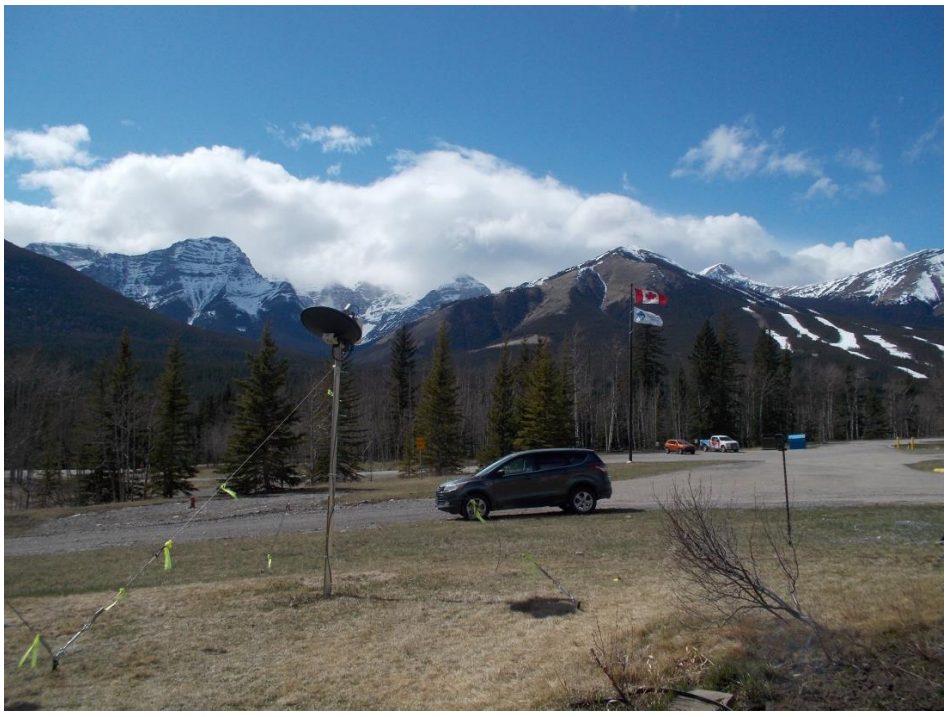

Figure A.2. Micro Rain Radar (MRR) (not used in this thesis). (Almonte, 2015).

Figure A.3. Kananaskis Boundary Auto station. (Porier, 2015).


Figure A.4. Environment and Climate Change Canada station. (Almonte, 2015).

# Appendix B: Global Classification of Ice Crystals and Solid Precipitation Particles

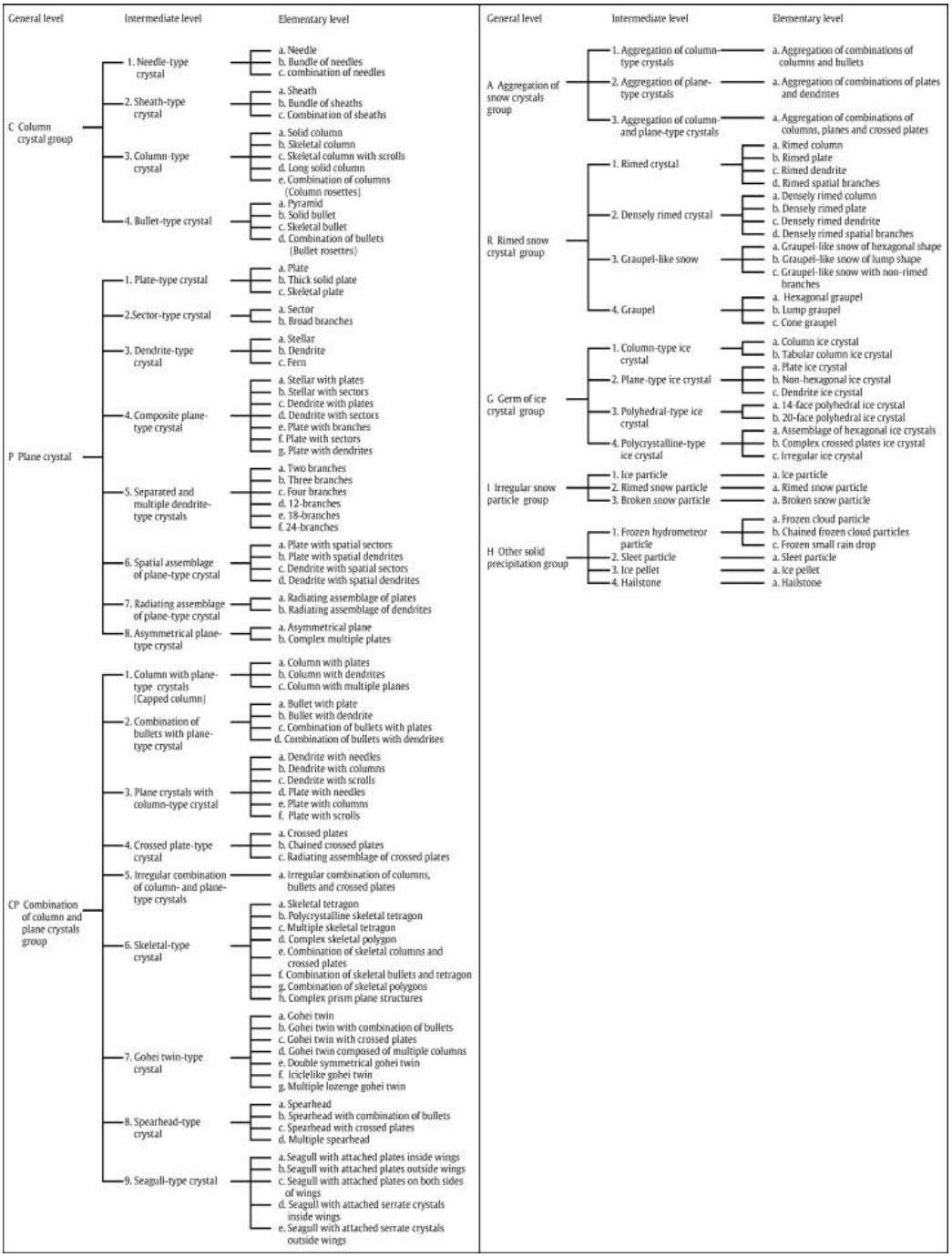


Figure B.1. The global classification table of snow crystals, ice crystals, and other solid precipitation that has been identified (Kikuchi et al., 2013).

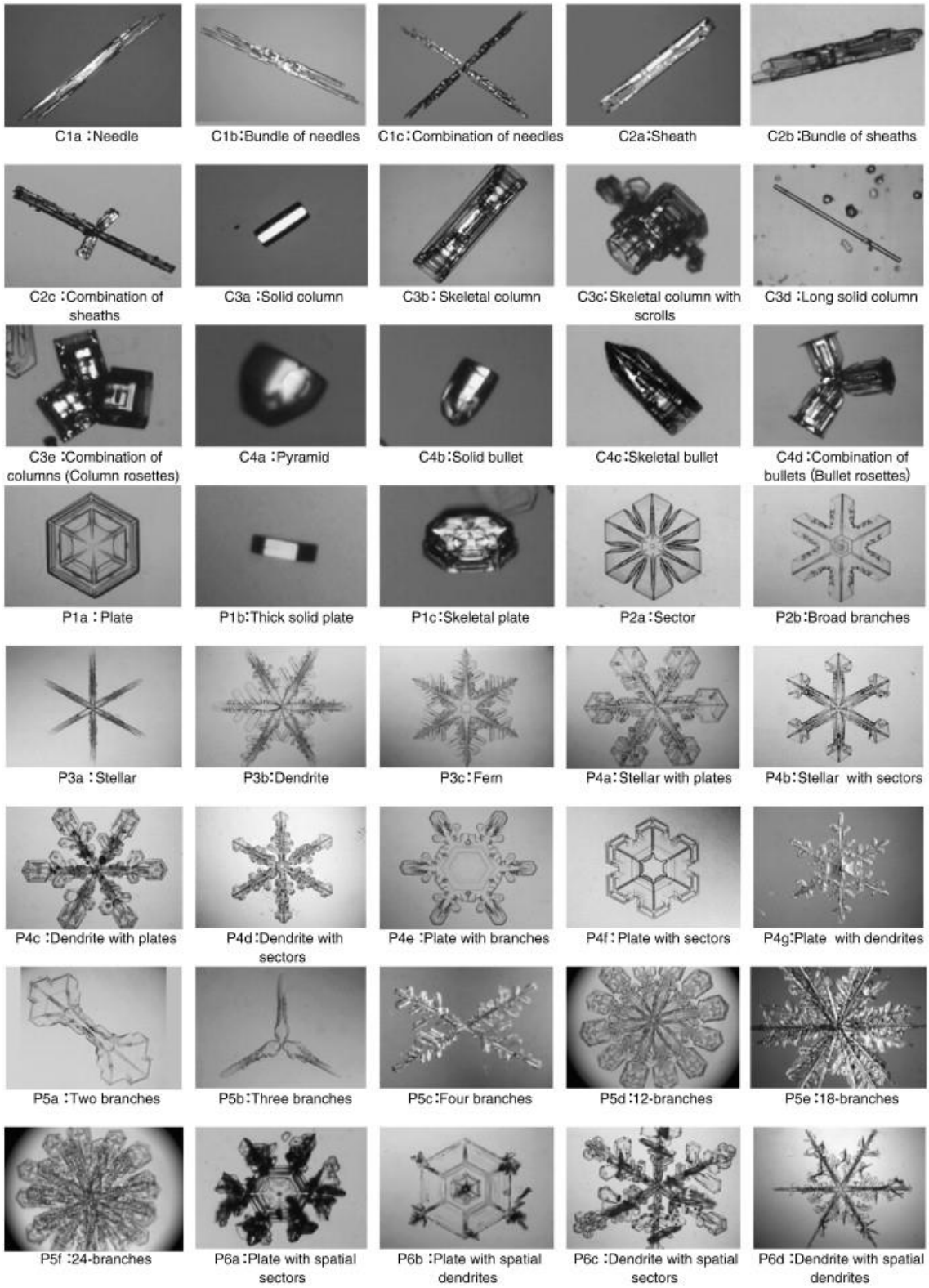


Figure B.2. Microscopic images of snow crystals from C1a to P6d (Kikuchi et al., 2013).

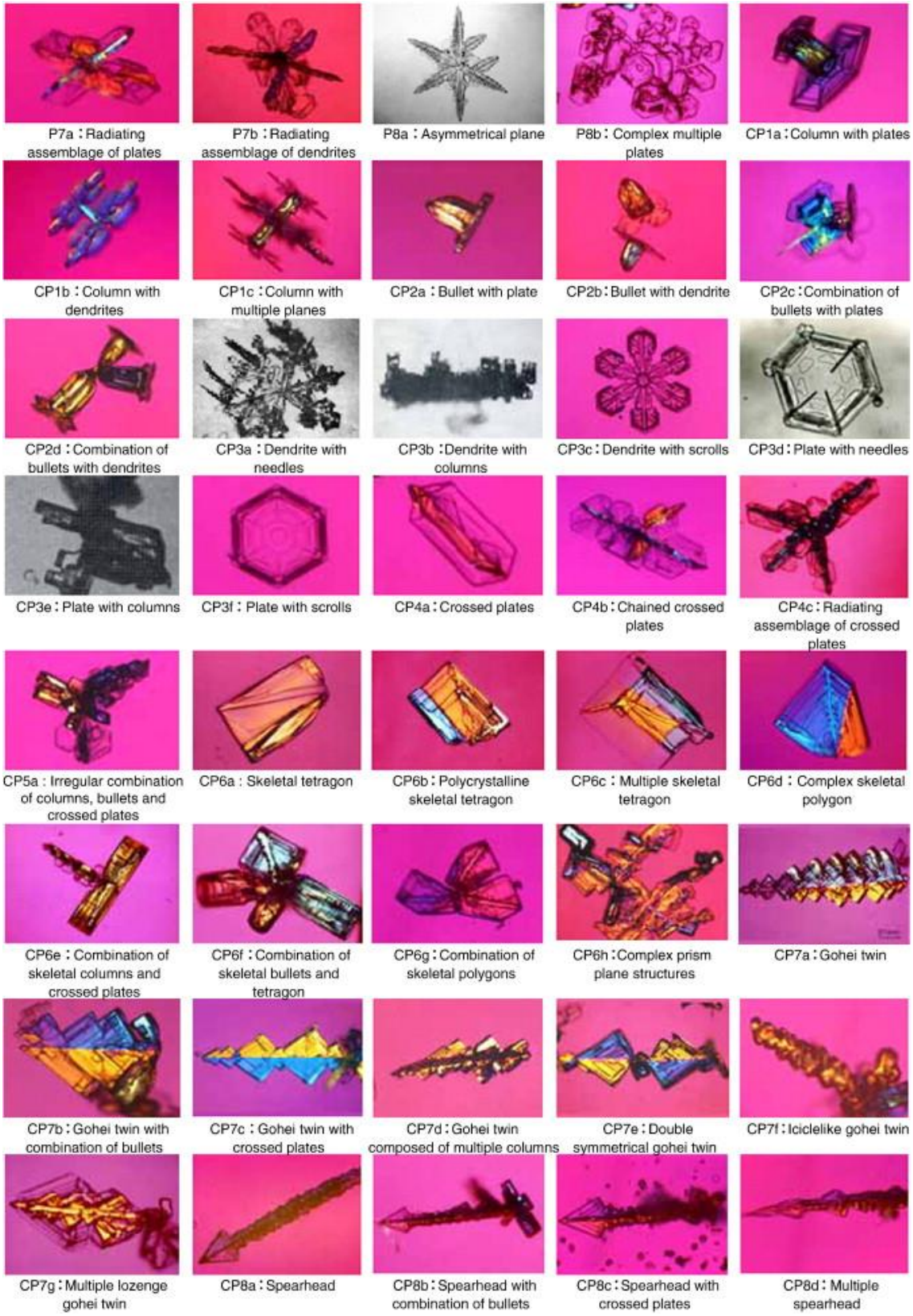


Figure B.3. Microscopic images of snow crystals from P7a to CP8d (Kikuchi et al., 2013).

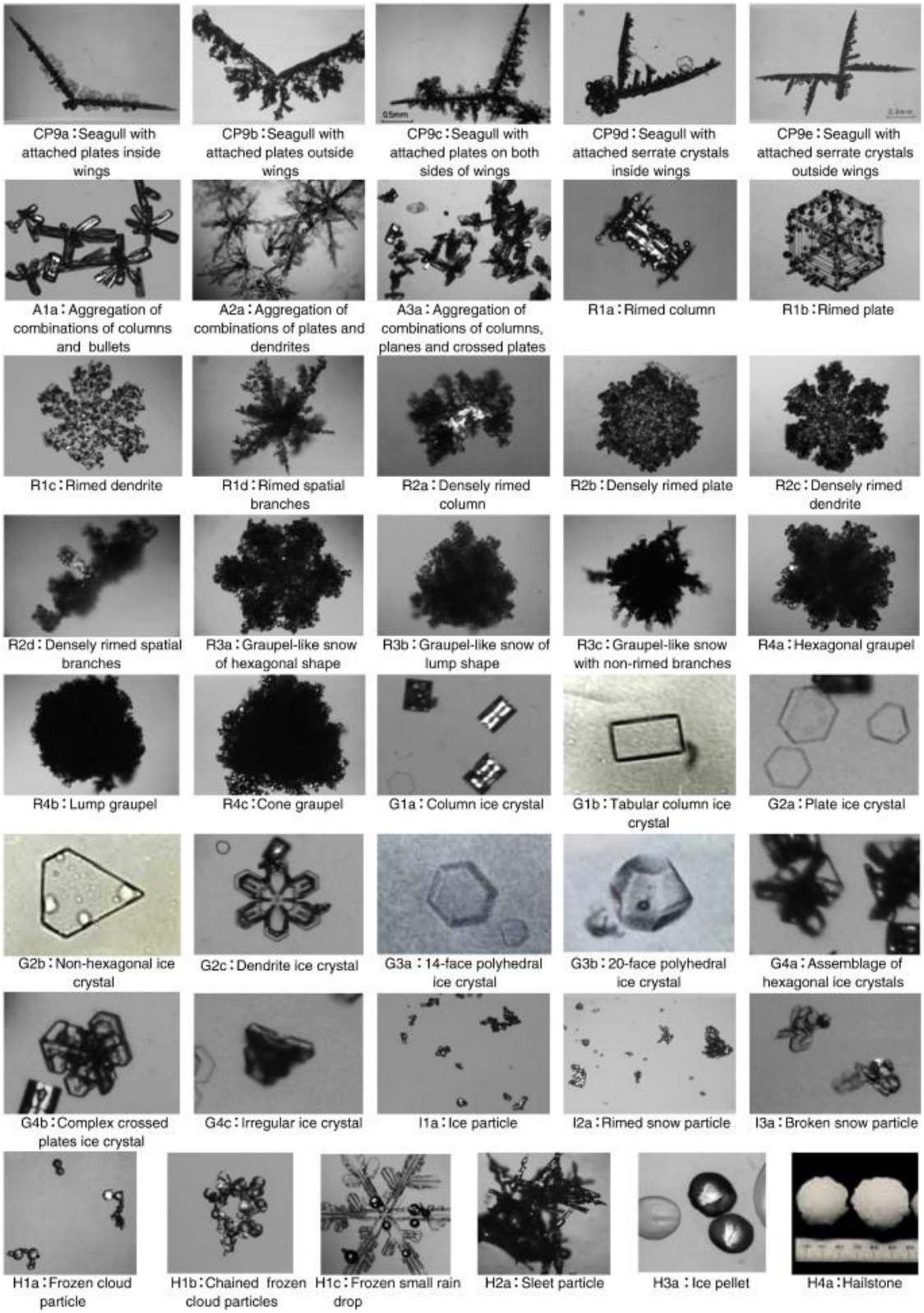


Figure B.4. Microscopic images of snow crystals, ice crystals, and solid precipitation from CP9a to H4a. (Kikuchi et al., 2013).

## Appendix C: Ice Crystals and Solid Precipitation Groups and the Elementary Names

The list of the precipitation names and elementary names were adapted from Kikuchi et al. (2013).

Column crystal group is stated to include snow crystals with characteristics similar to columns. Elementary level types in this category include needle-type crystal, sheath-type crystal, column-type crystal, and bullet-type crystal.

Plane crystal group identifies snow crystals that are planar shaped. Elementary levels in the plane crystal group include plane-type crystal, sector-type crystal, dendrite-type crystal, composite plane-type crystal, separated and multiple dendrite-type crystals, spatial assemblage of plane-type crystal, radiating assemblage of plane-type crystal, and asymmetrical plane-type crystal.

Irregular snow particles group are identified as particles raised from a snow cover by strong winds. Elementary levels include ice particle, rimed snow particle, broken snow particle, other solid precipitation group, frozen hydrometeor particle, sleet particle, ice pellet, and hailstone.

Combination of column and plane crystals group describes snow crystals that are composed of columns and planes. Elementary levels include column with plane-type crystals, combination of bullets with plane-type crystal, plane crystals with column-type crystal, crossed plate-type crystal, irregular combination of column-and plane-type crystals, skeletal-type crystal, gohei twin-type crystal, spearhead-type crystal, seagull-type crystal.

Aggregation of snow crystals group describes snow crystals that combine together to form a larger particle. Elementary level particles include aggregation of column-type crystals, aggregation of plane-type crystals, and aggregation of column-and plane-type crystals.

# Appendix D: Temperature and Relative Humidity Difference (Environment and Climate Change Canada Station and Kananaskis Boundary Auto Station)

## D.1 March 21 – 22

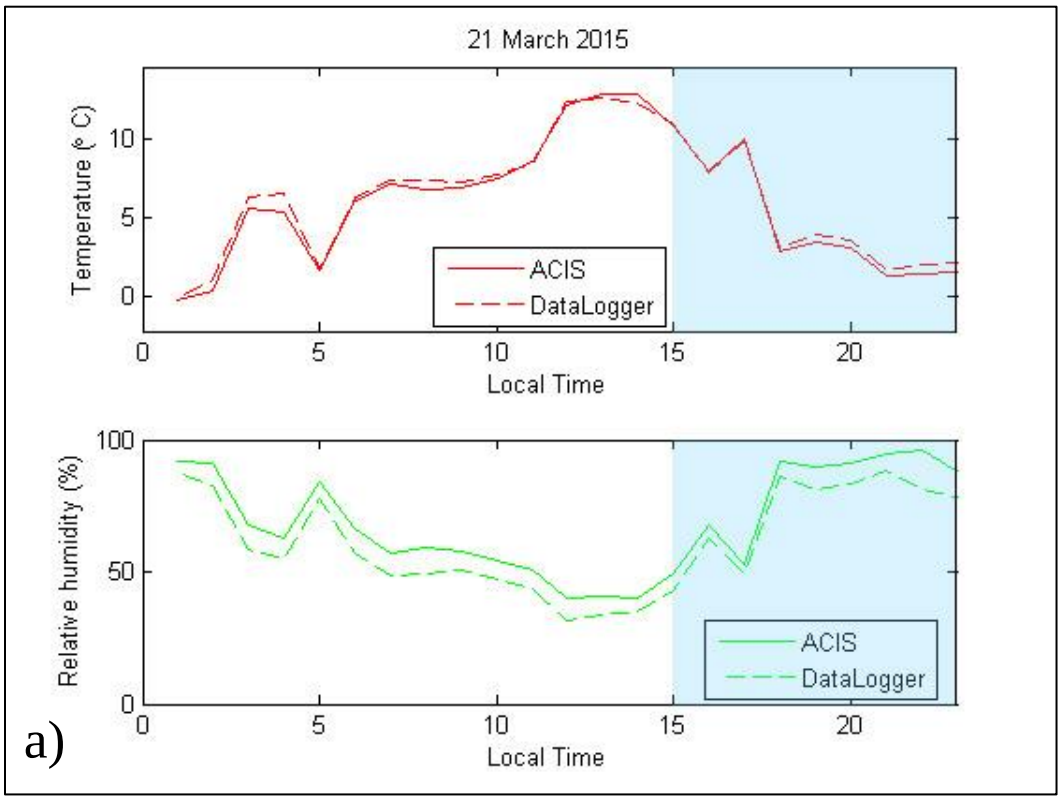

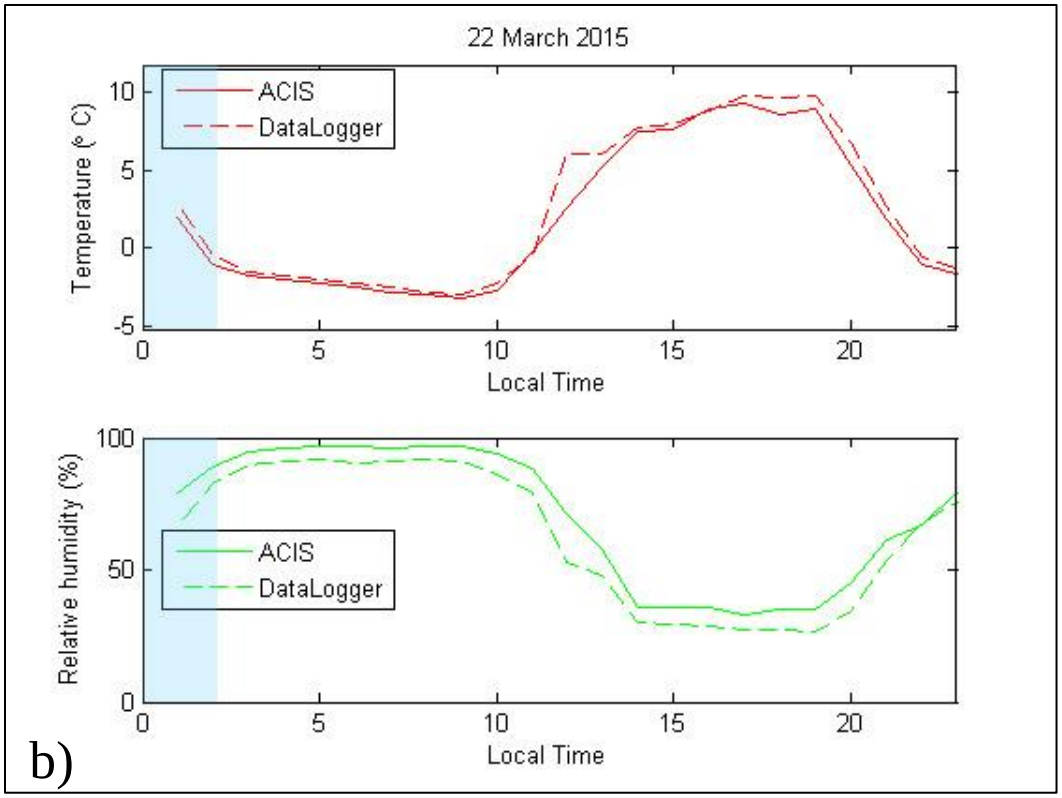


Figure D.1: Temperature (red) and relative humidity (green) difference on a) March 21 and b) Match 22 (LST) between the ECCC station (datalogger) and KBA station (ACIS). The blue shading represents the time of the precipitation event. The image was adapted from Vaquer (2016).

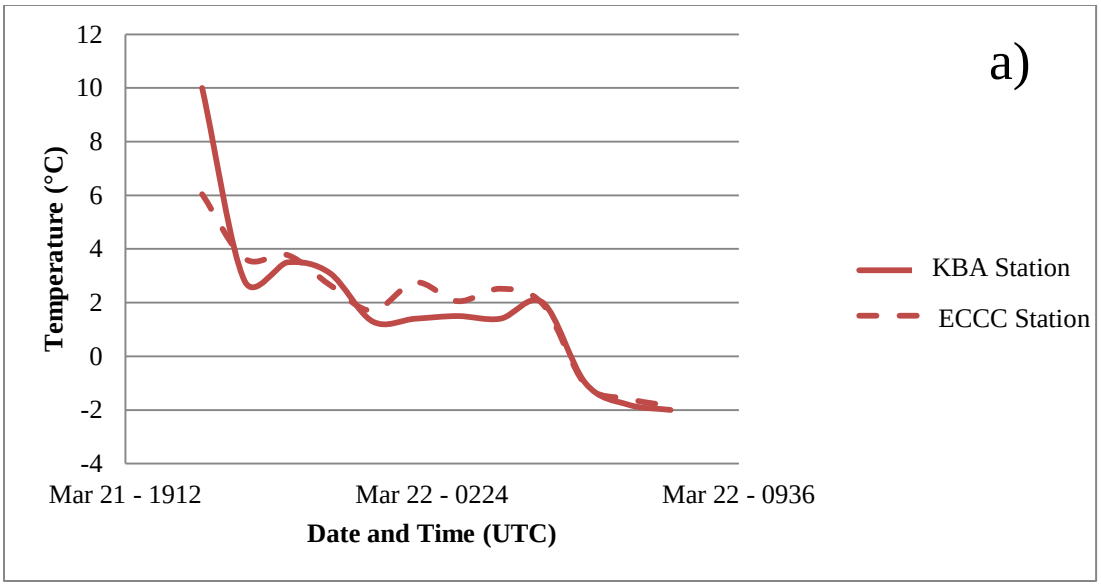


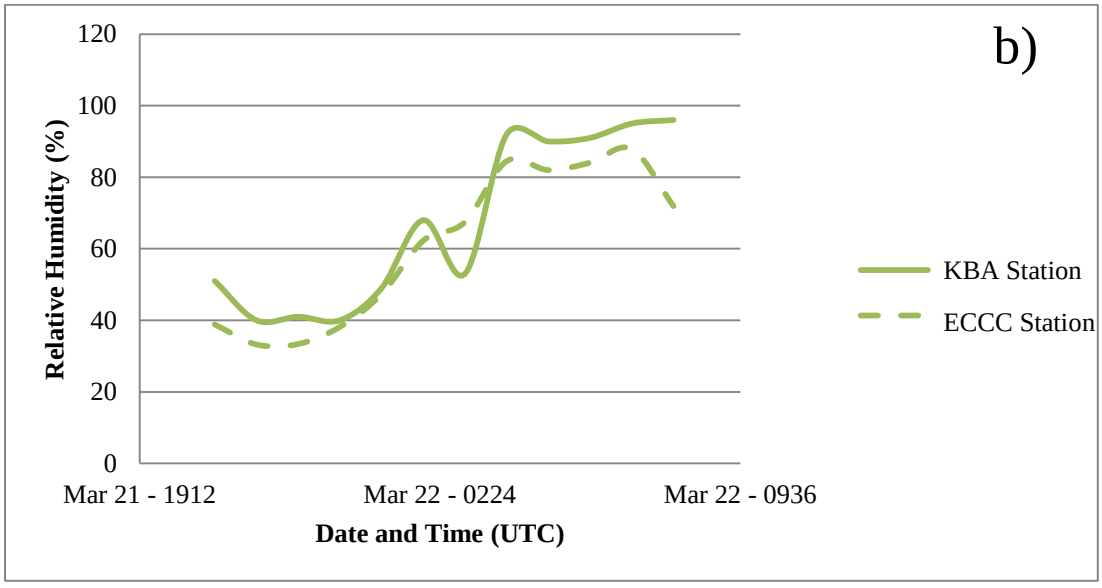


Figure D.2: a) Temperature (red) and b) relative humidity (green) difference on March 21 – 22 between the ECCC station and KBA station when observations commenced on site.

**D.2 April 4 – 5**

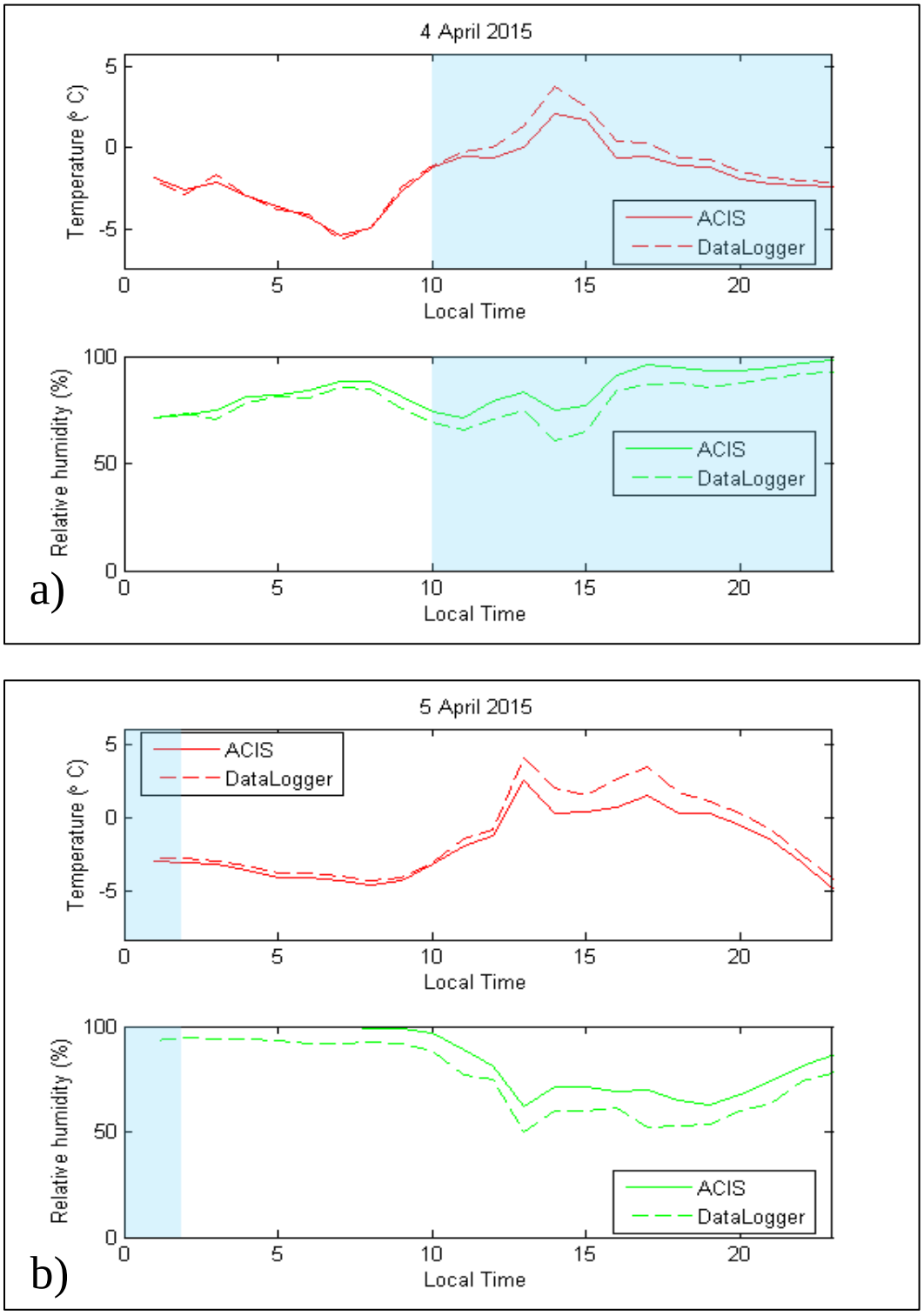


Figure D.3: Temperature (red) and relative humidity (green) difference on a) April 4 and b) April 5 between the ECCC station (datalogger) and KBA station (ACIS). The blue shading represents the time of the precipitation event. The image was adapted from Vaquer (2016).

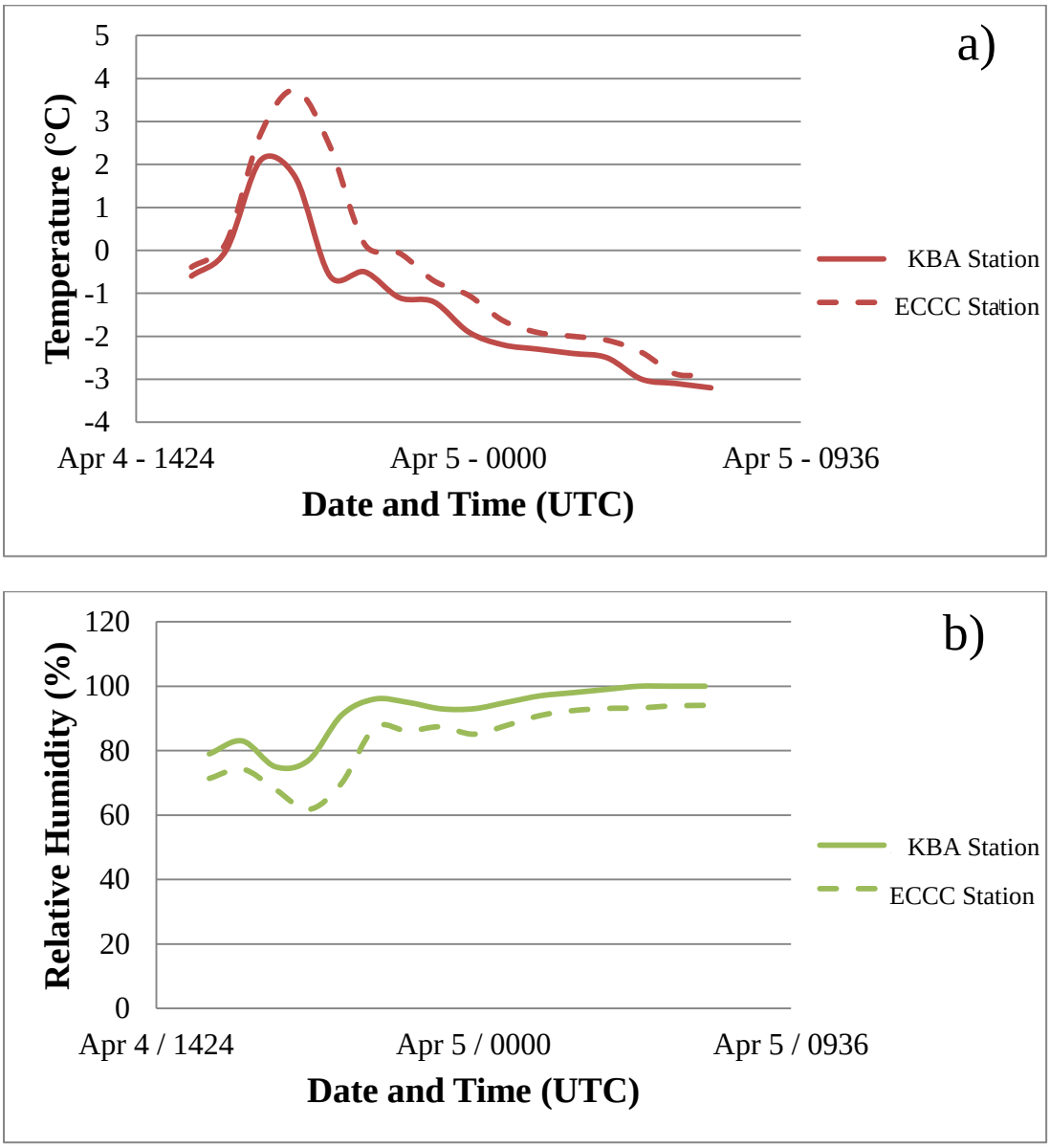


Figure D.4: a) Temperature (red) and b) relative humidity (green) difference on April 4 – 5 between the ECCC station and KBA station when observations commenced on site.

### D.3 April 6

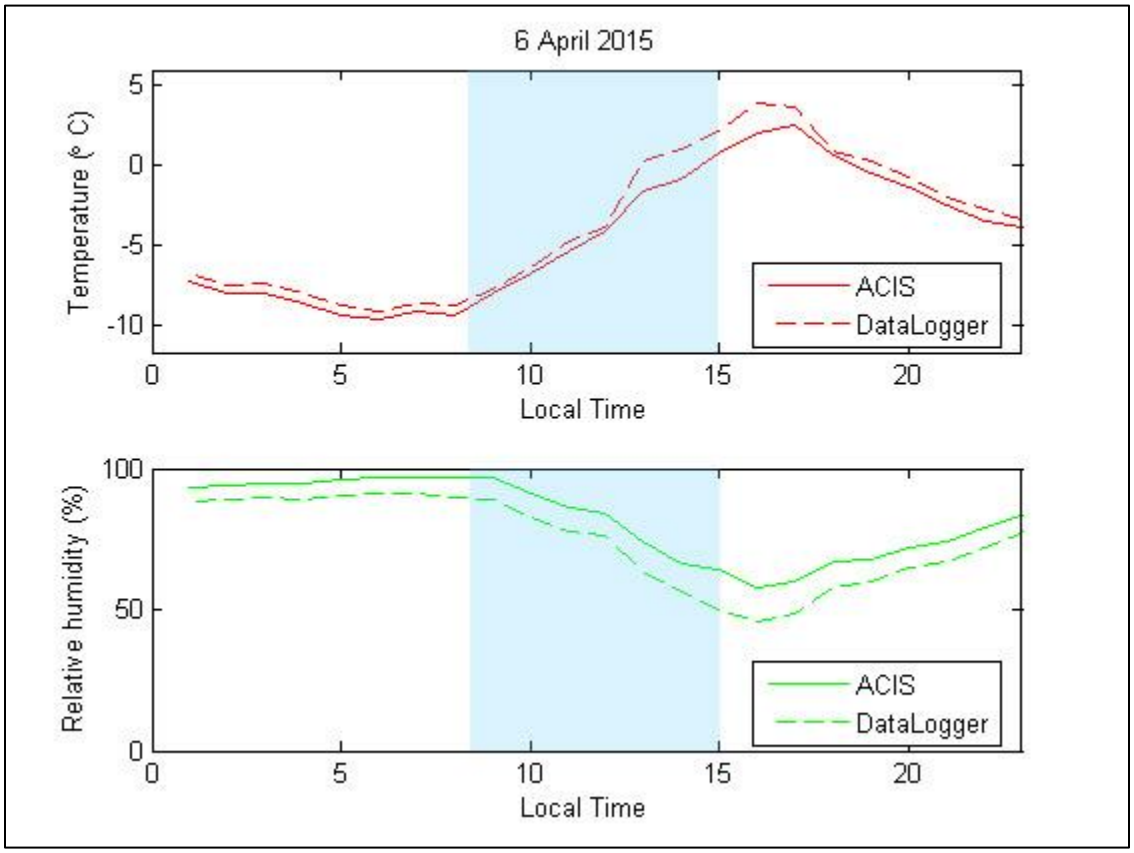


Figure D.5: Temperature (red) and relative humidity (green) difference on April 6 between the ECCC station (datalogger) and KBA station (ACIS). The blue shading represents the time of the precipitation event. The image was adapted from Vaquer (2016).

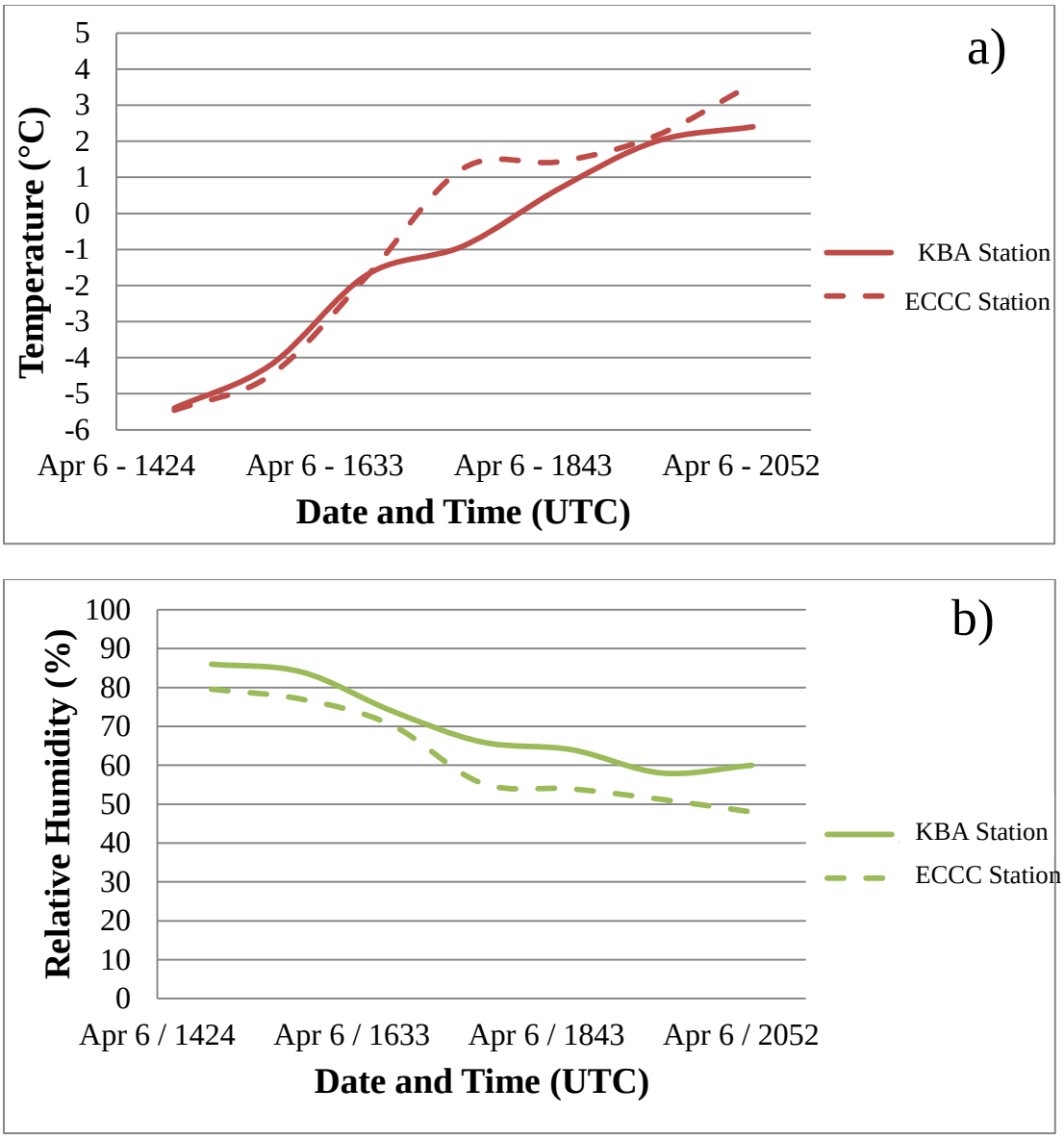


Figure D.6: a) Temperature (red) and b) relative humidity (green) difference on April 6 between the ECCC station and KBA station when observations commenced on site.

**D.4 April 14 – 15**

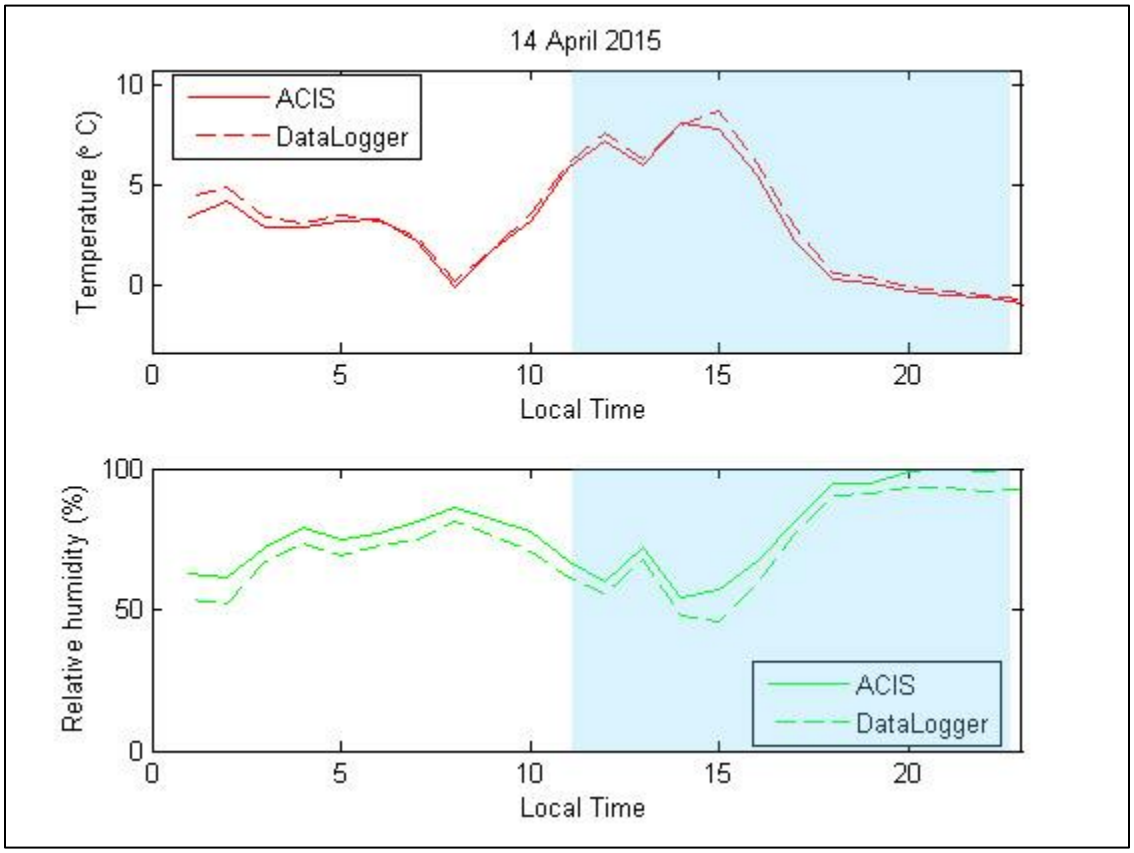


Figure D.7: Temperature (red) and relative humidity (green) difference on April 14 between the ECCC station (datalogger) and KBA station (ACIS). The blue shading represents the time of the precipitation event. The image was adapted from Vaquer (2016).

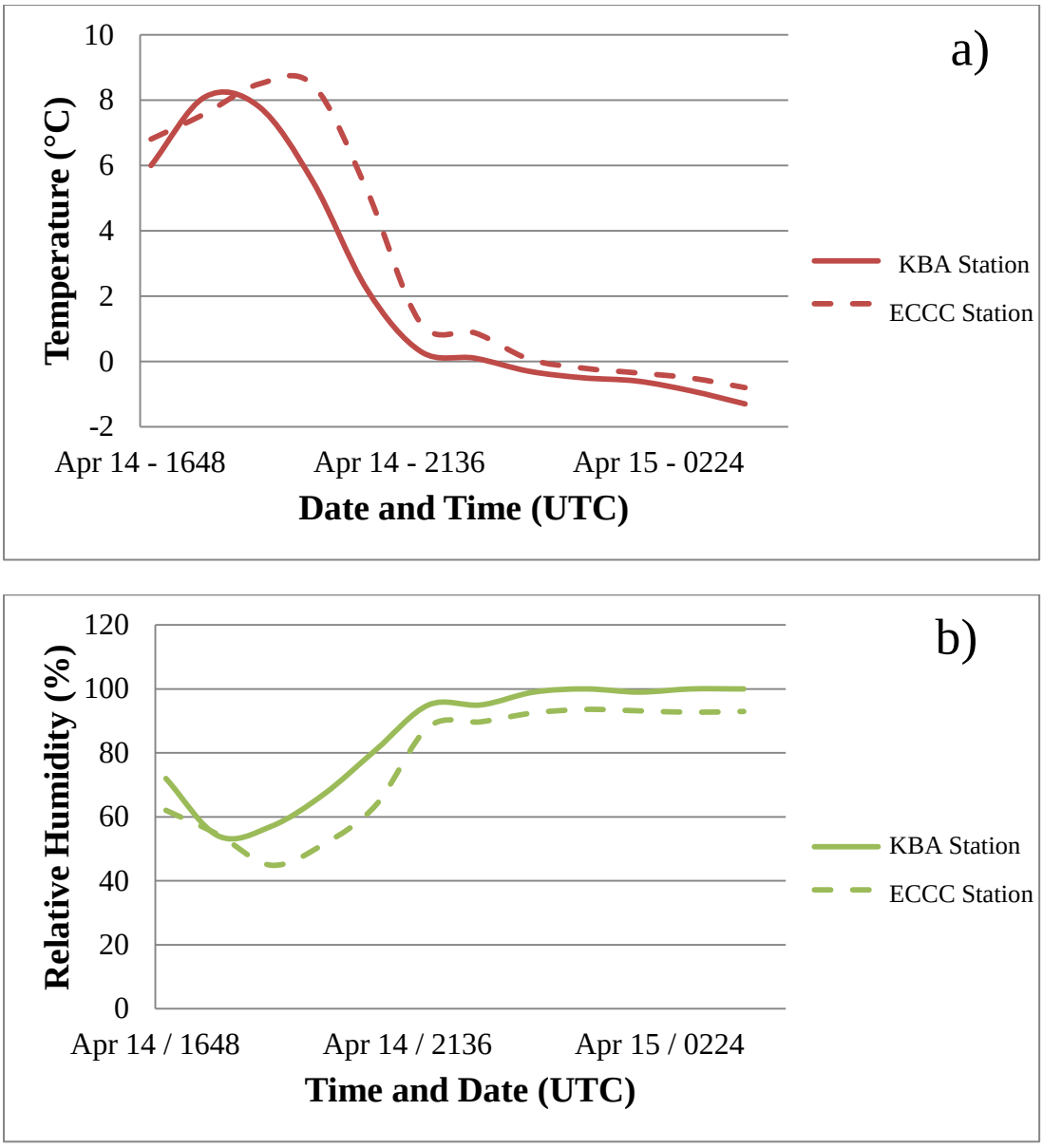


Figure D.8: a) Temperature (red) and b) relative humidity (green) difference on April 14 - 15 between the ECCC station and KBA station when observations commenced on site.

## D.5 April 18

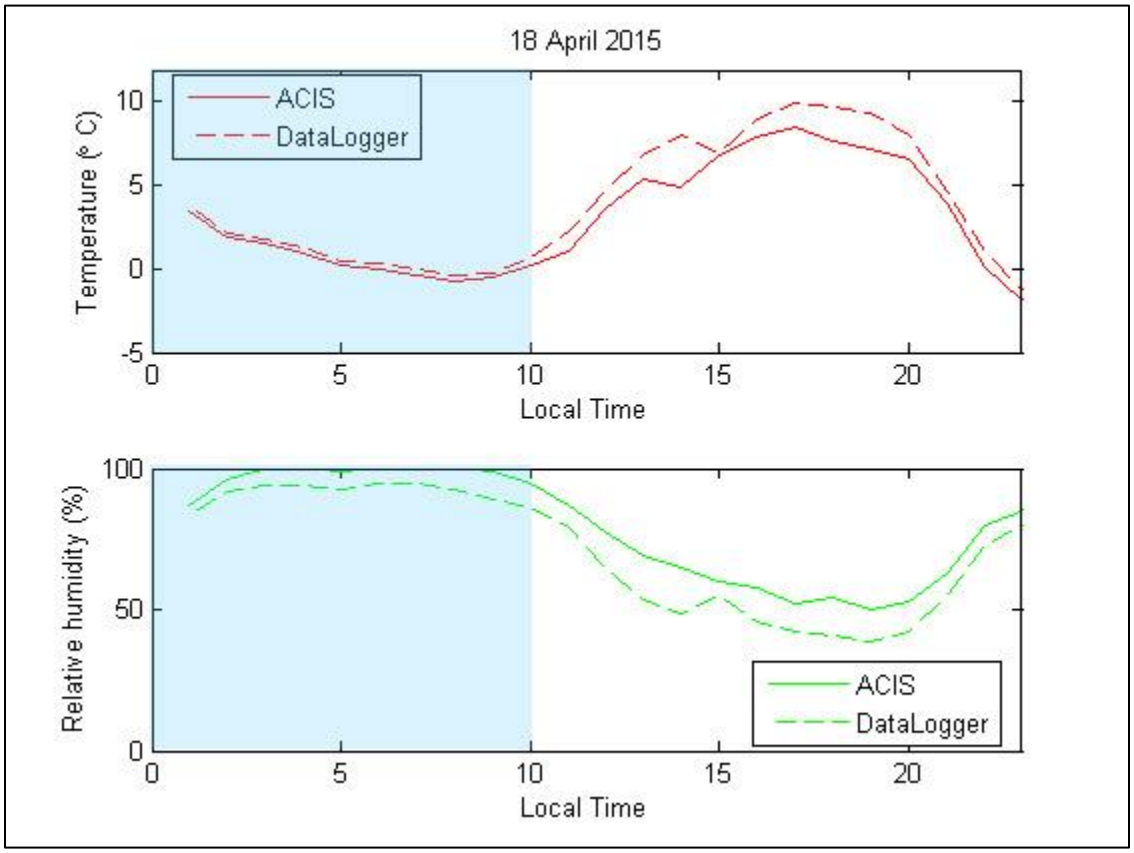


Figure D.9: Temperature (red) and relative humidity (green) difference on April 18 between the ECCC station (datalogger) and KBA station (ACIS). The blue shading represents the time of the precipitation event. The image was adapted from Vaquer (2016).

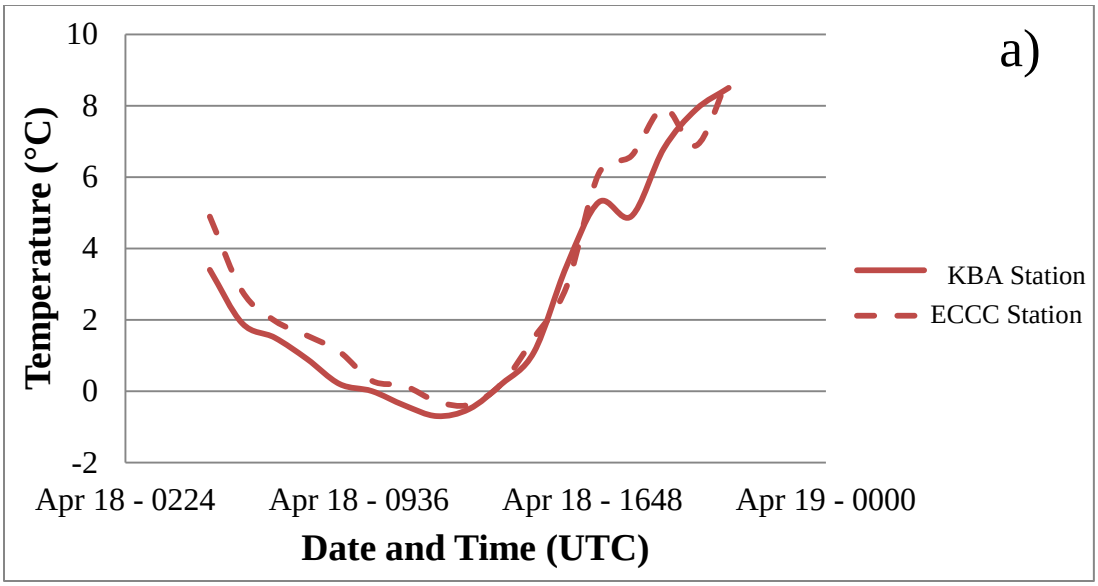


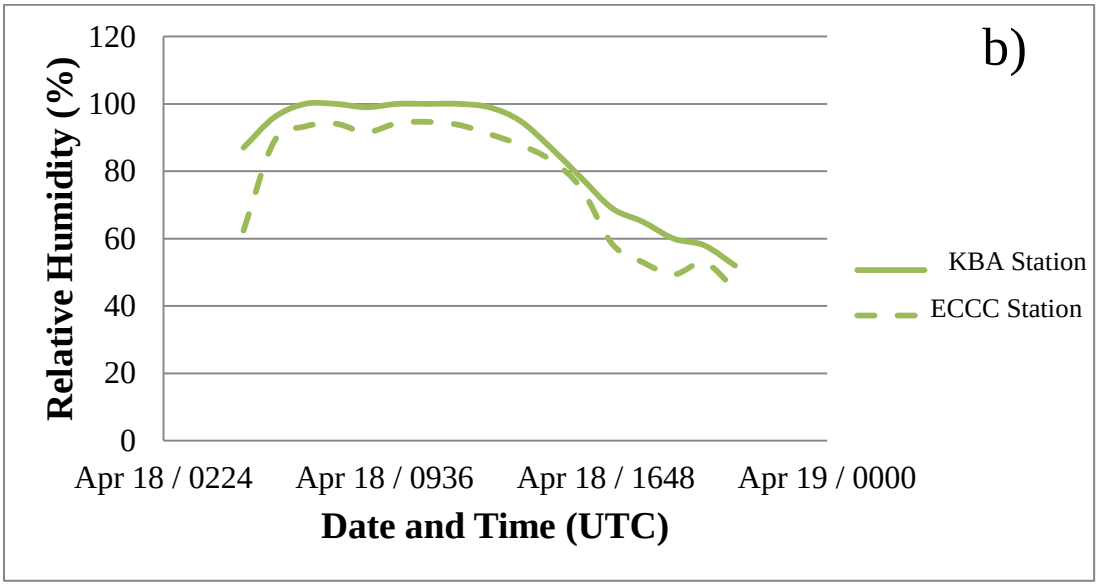


Figure D.10: a) Temperature (red) and b) relative humidity (green) difference on April 18 between the ECCC station and KBA station when observations commenced on site.

**D.6 April 22 – 23**

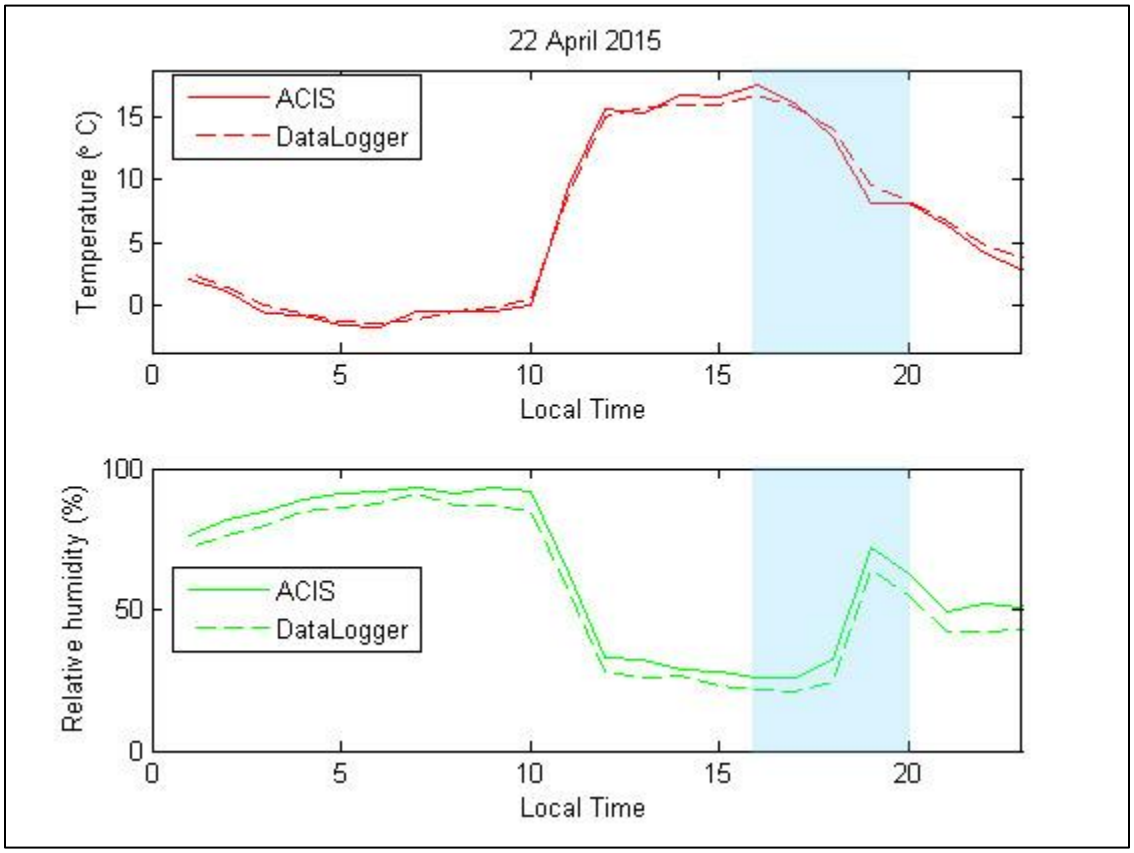


Figure D.11: Temperature (red) and relative humidity (green) difference on April 22 between the ECCC station (datalogger) and KBA station (ACIS). The blue shading represents the time of the precipitation event. The image was adapted from Vaquer (2016).

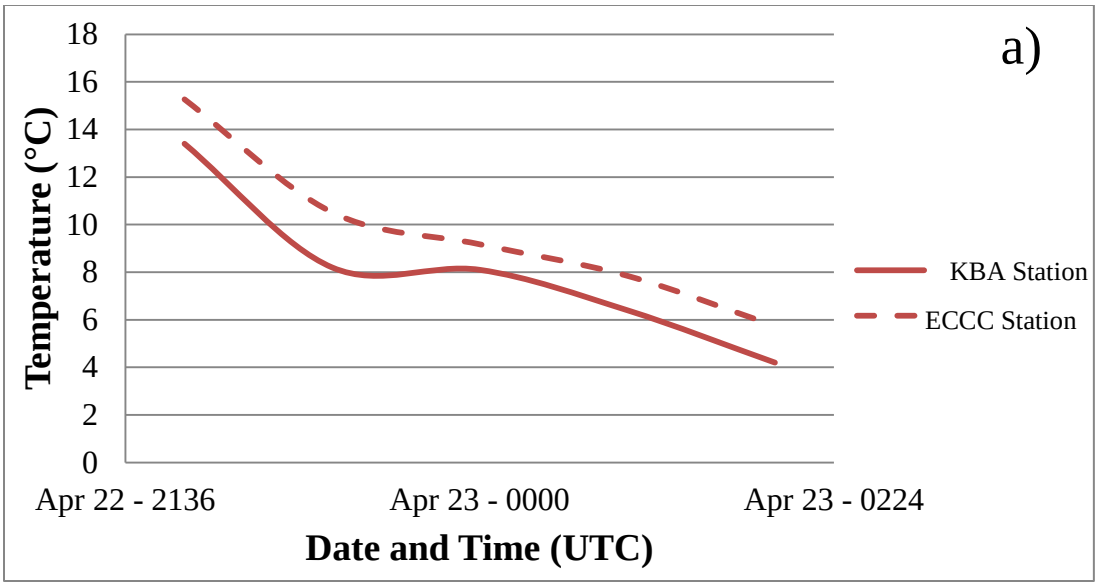


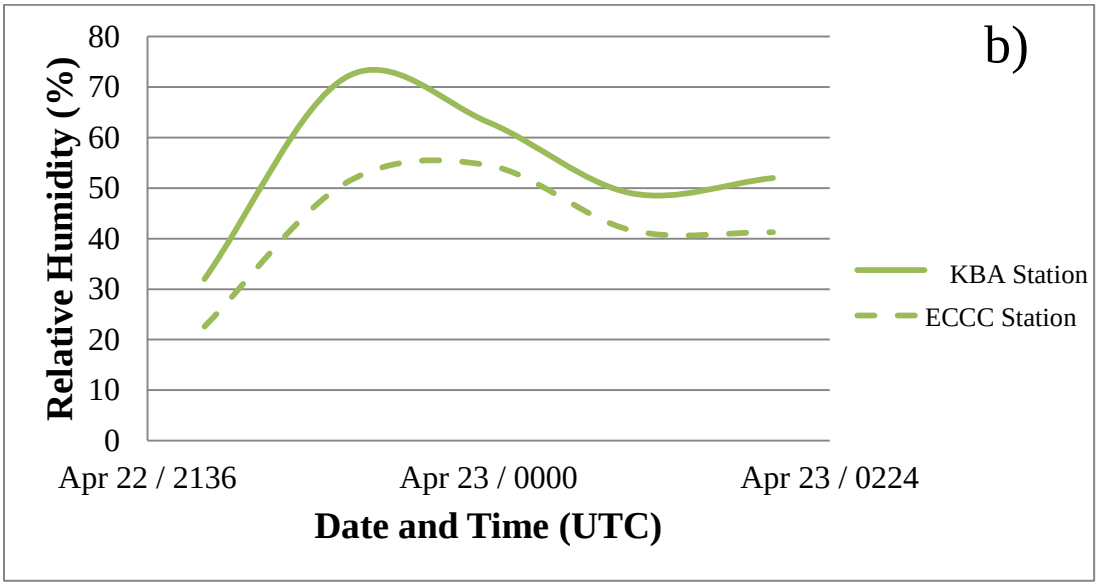


Figure D.12: a) Temperature (red) and b) relative humidity (green) difference on April 22 - 23 between the ECCC station and KBA station when observations commenced on site.

**D.7 April 24 – 25**

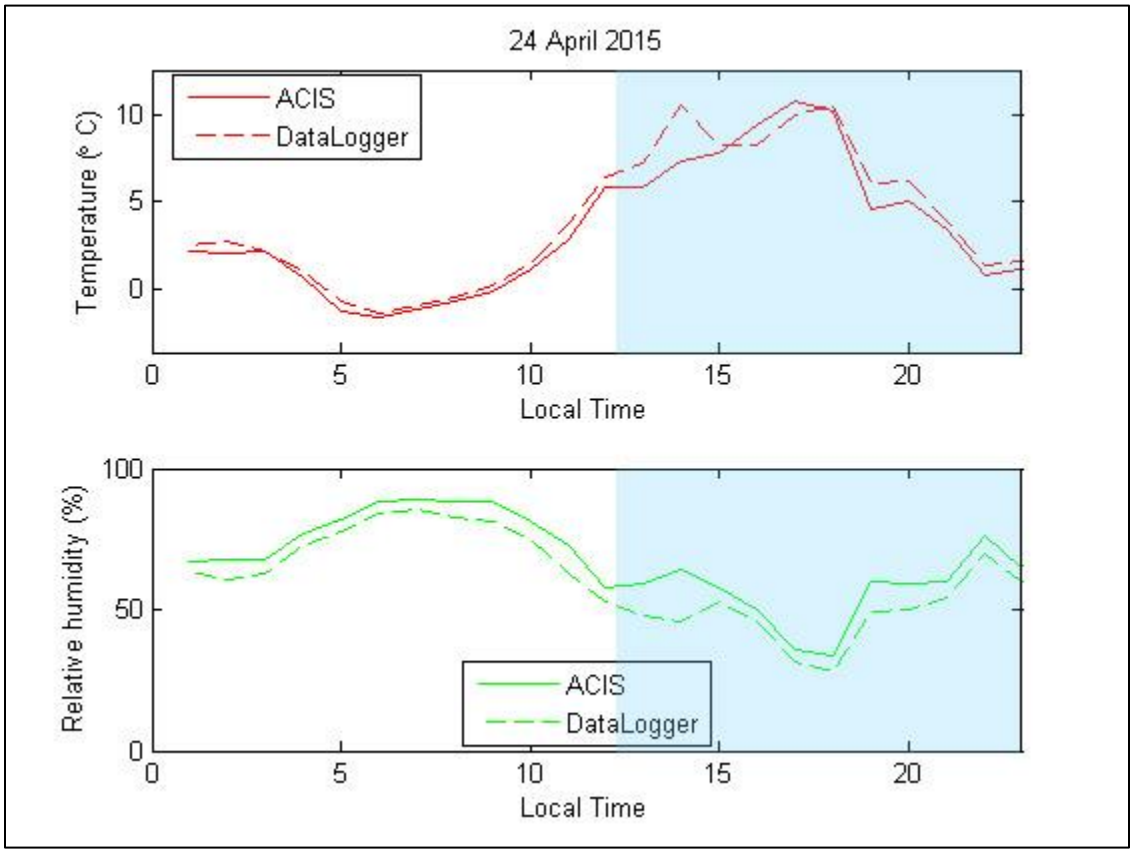


Figure D.13: Temperature (red) and relative humidity (green) difference on April 24 – 25 between the ECCC station (datalogger) and KBA station (ACIS). The blue shading represents the time of the precipitation event. The image was adapted from Vaquer (2016).

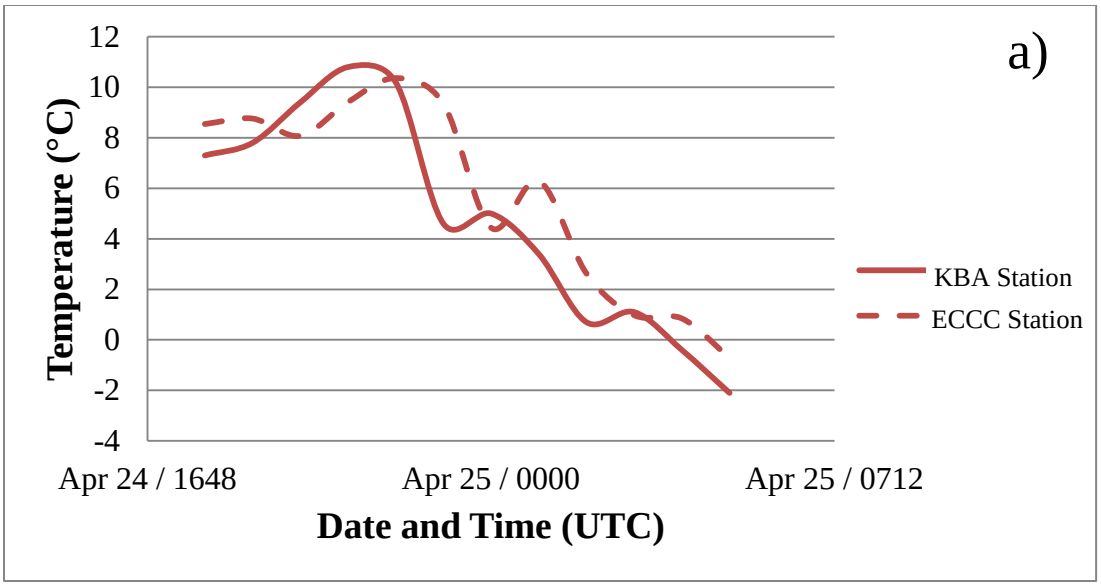


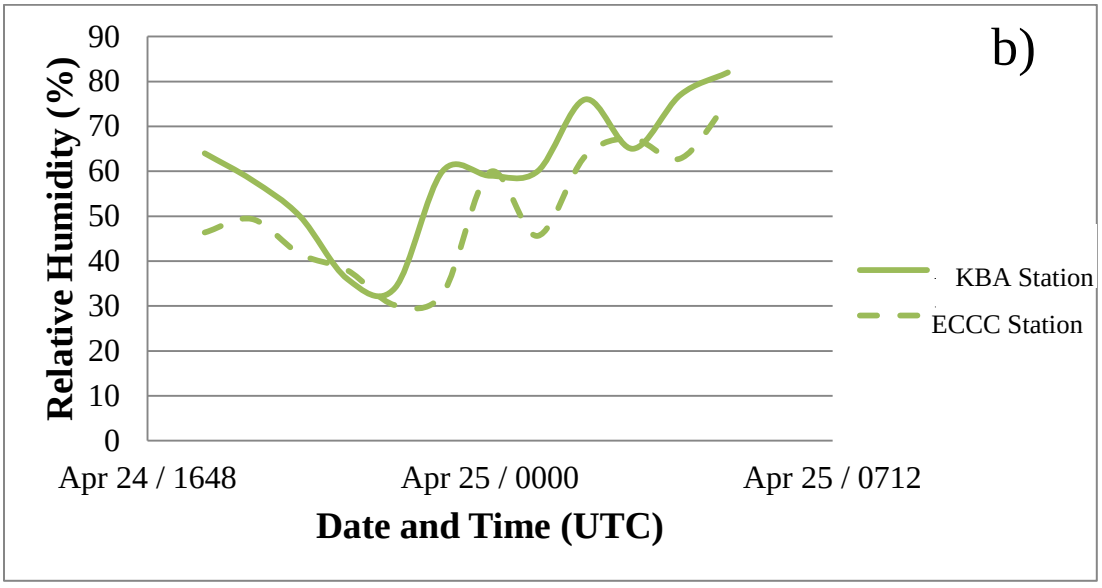


Figure D.14: a) Temperature (red) and b) relative humidity (green) difference on April 24 - 25 between the ECCC station and KBA station when observations commenced on site.

**D.8 April 25 – 26**

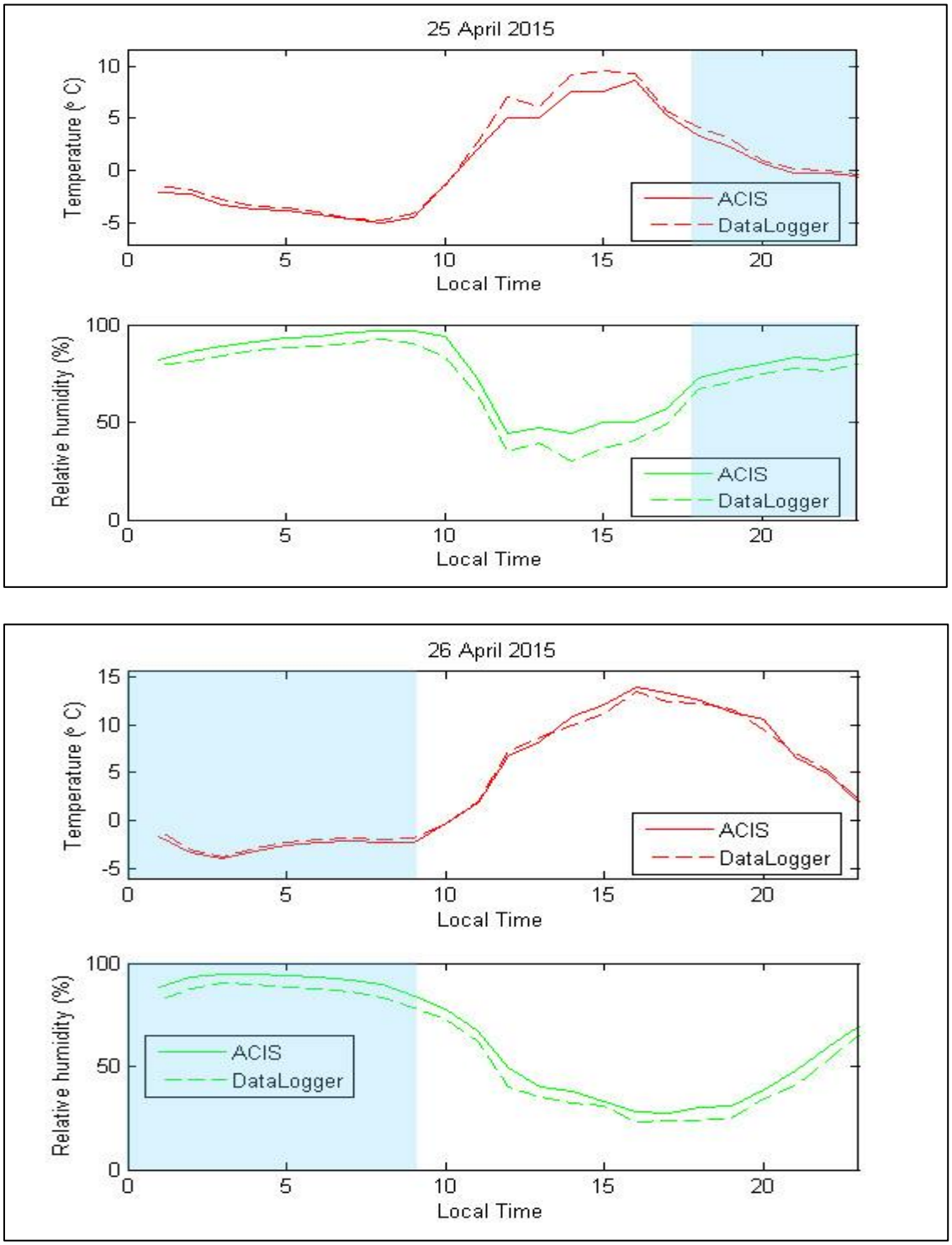


Figure D.15: Temperature (red) and relative humidity (green) difference on a) April 25 and b) April 26 between the ECCC station (datalogger) and KBA station (ACIS). The blue shading represents the time of the precipitation event. The image was adapted from Vaquer (2016).

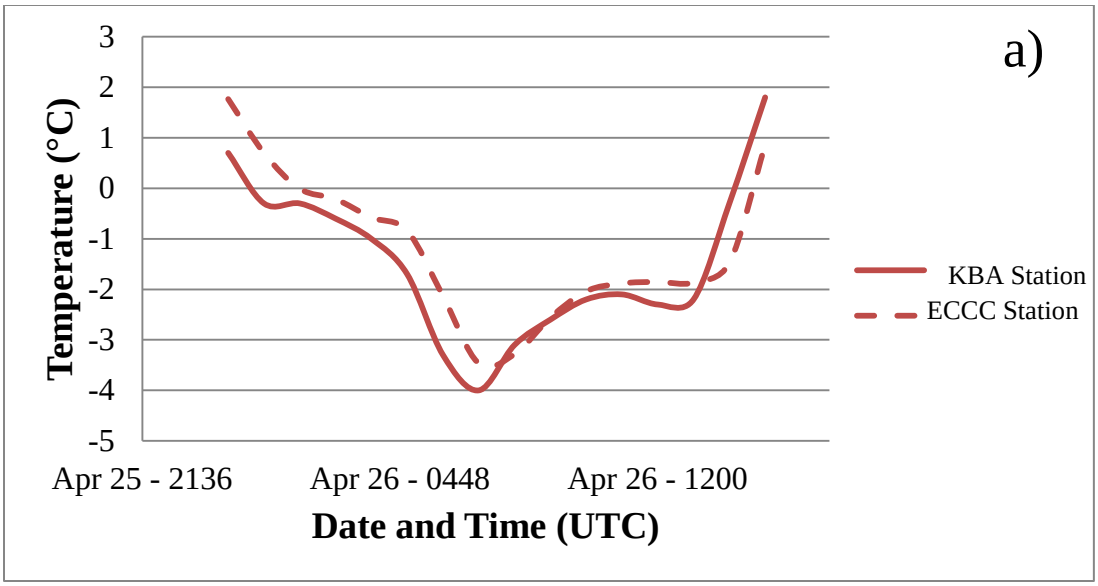


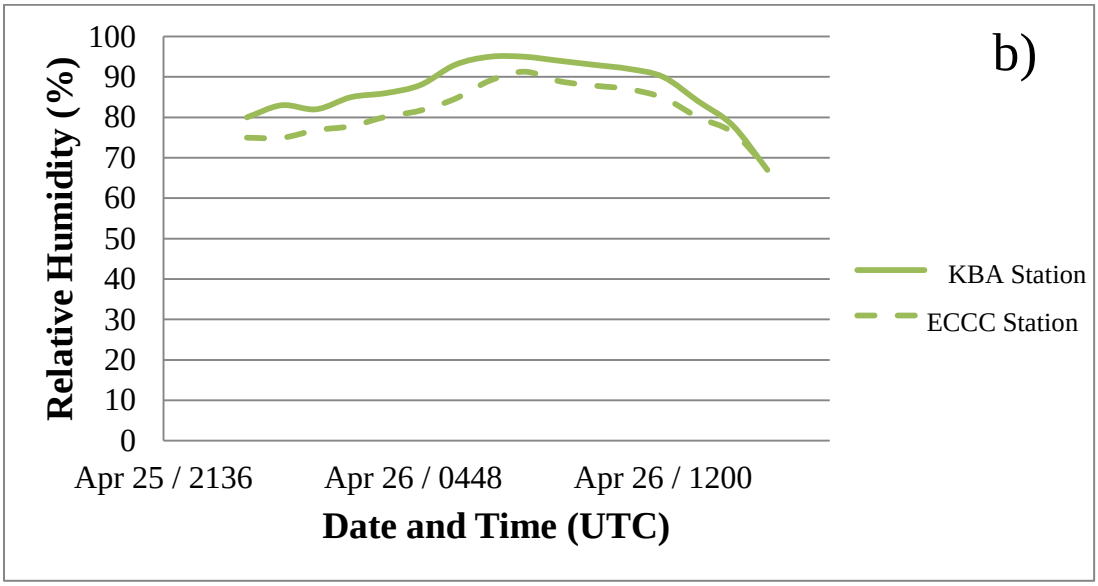


Figure D.16: a) Temperature (red) and b) relative humidity (green) difference on April 25 - 26 between the ECCC station and KBA station when observations commenced on site.

## D.9 April 29

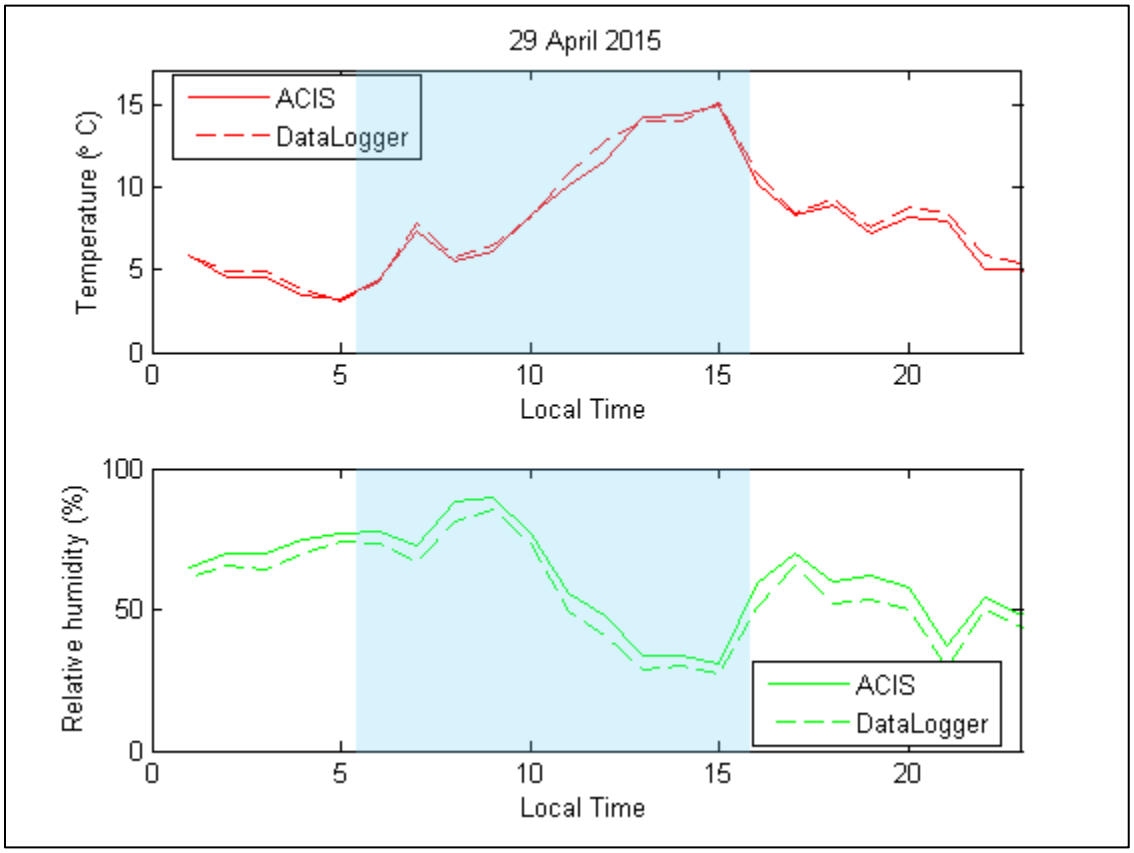


Figure D.17: Temperature (red) and relative humidity (green) difference on April 29 between the ECCC station (datalogger) and KBA station (ACIS). The blue shading represents the time of the precipitation event. The image was adapted from Vaquer (2016).

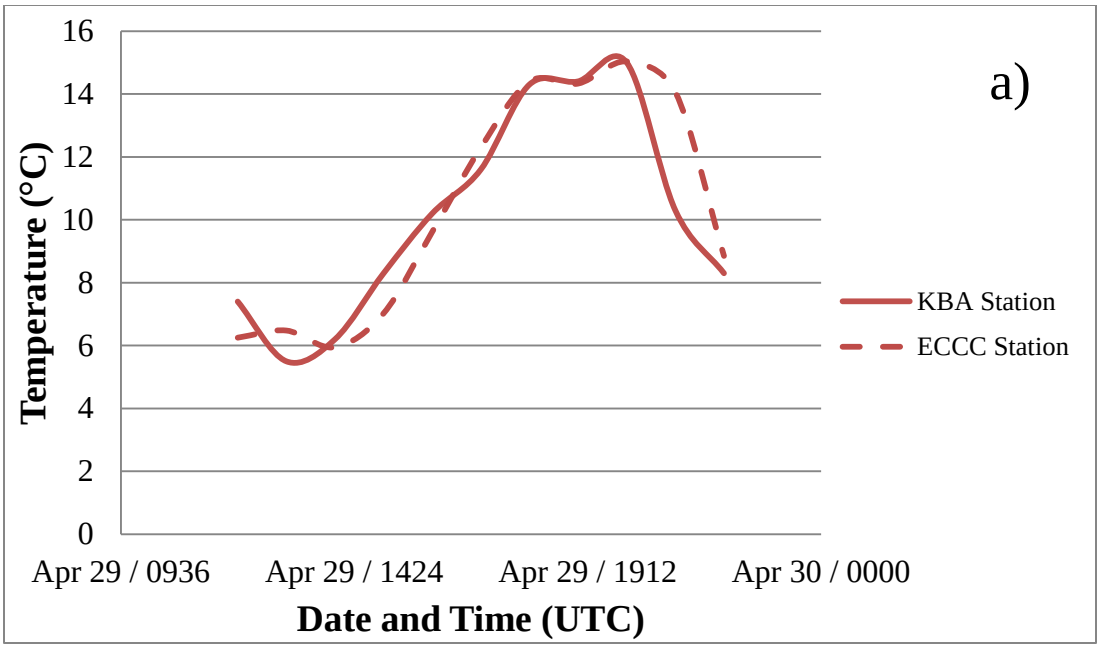


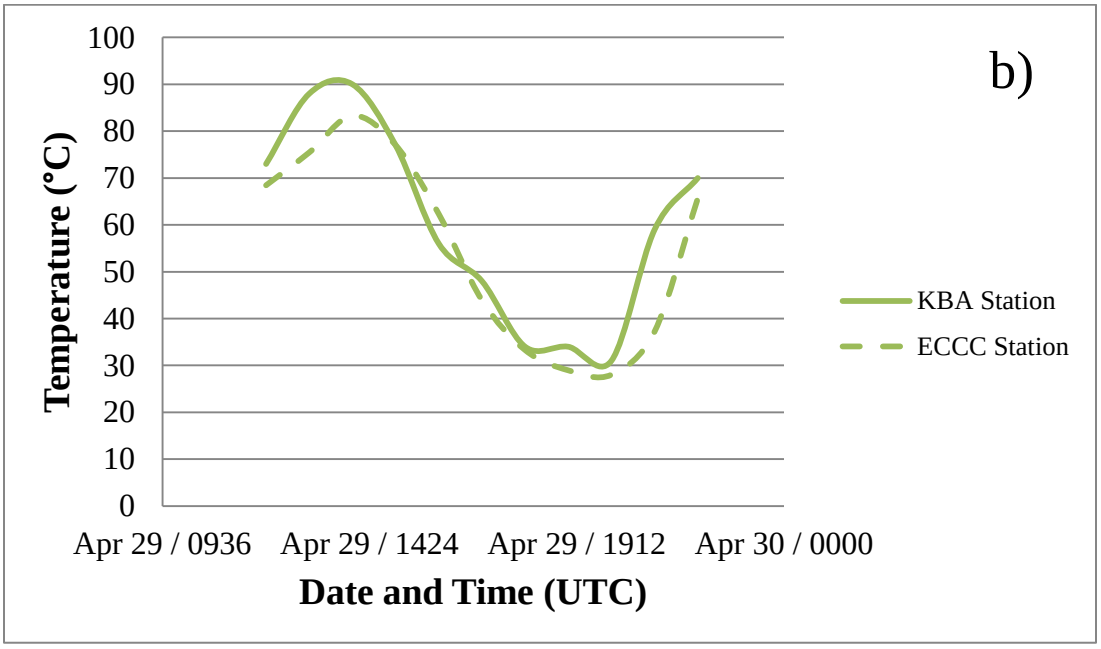


Figure D.18: a) Temperature (red) and b) relative humidity (green) difference on April 29 between the ECCC station and KBA station when observations commenced on site.

## Appendix E: Wind Rose Plots

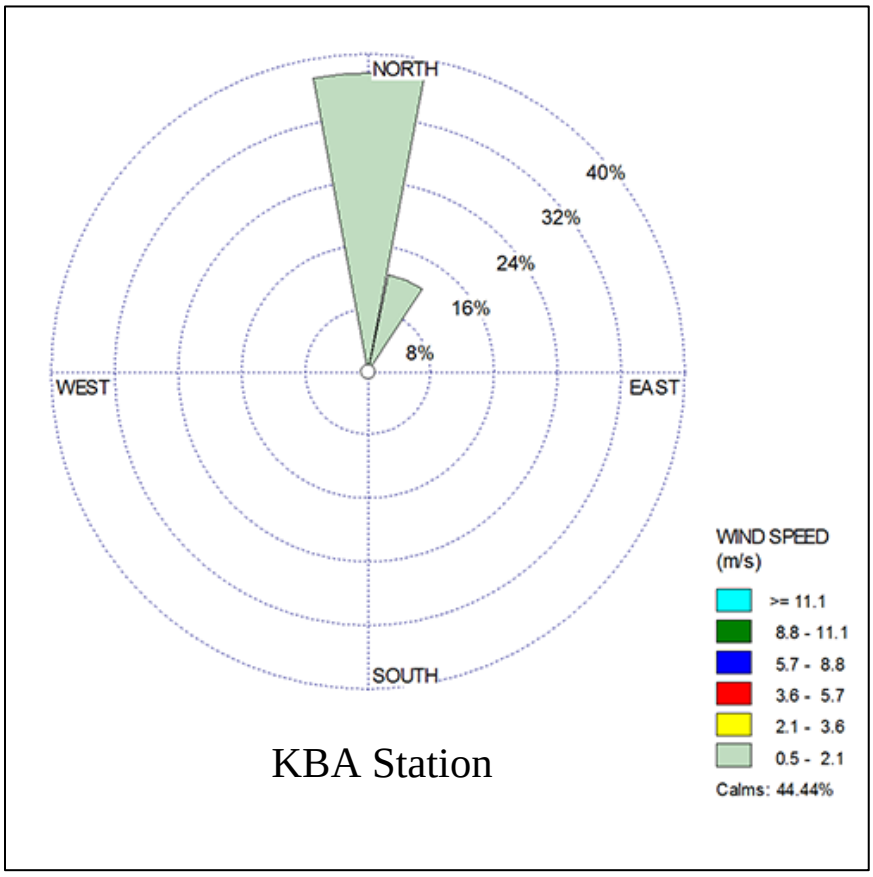


Figure E.1: A wind rose plot during the precipitation event on March 15 – 16.

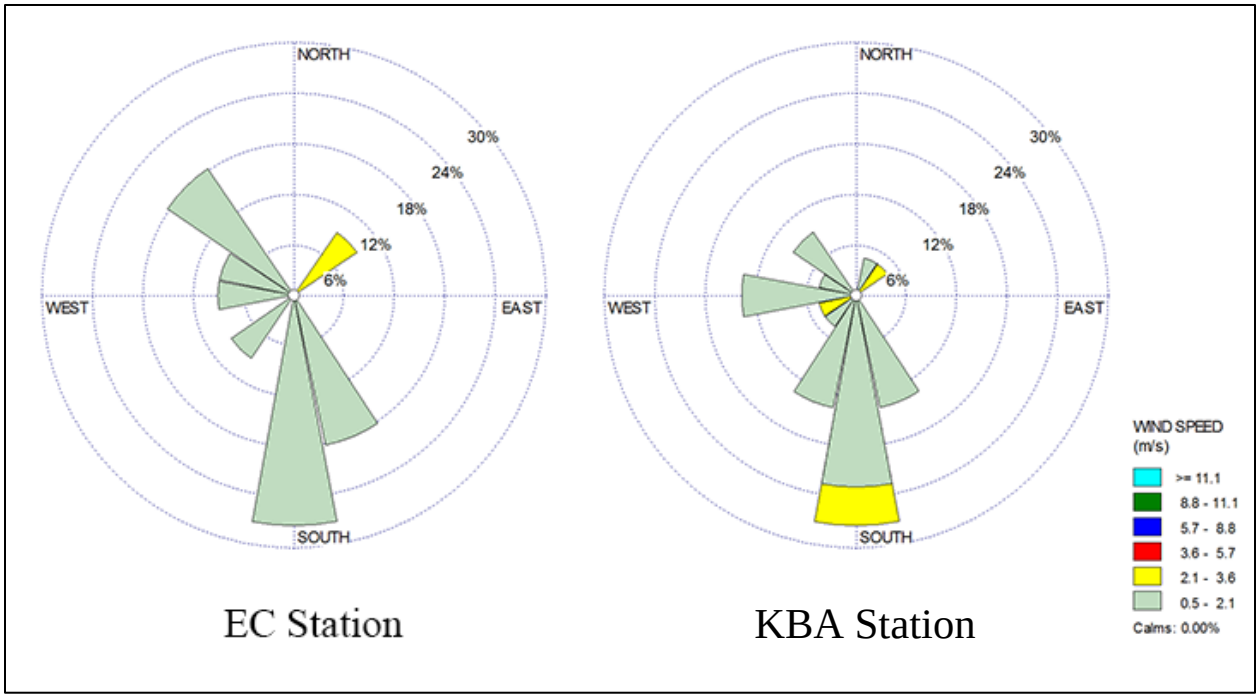


Figure E.2: A wind rose plot during the precipitation event on March 21 – 22. The left plot is of the EC Station and the right is of the KBA station.

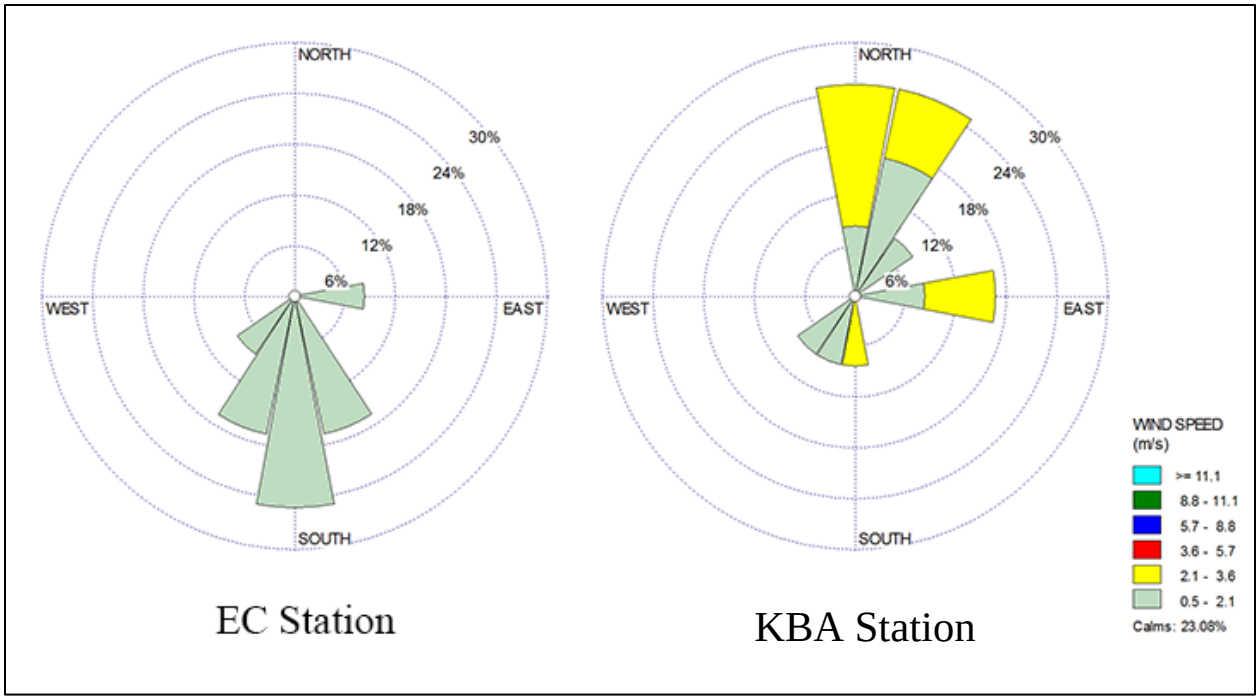


Figure E.3: A wind rose plot during the precipitation event on April 14 – 15. The left plot is of the EC Station and the right is of the KBA station.

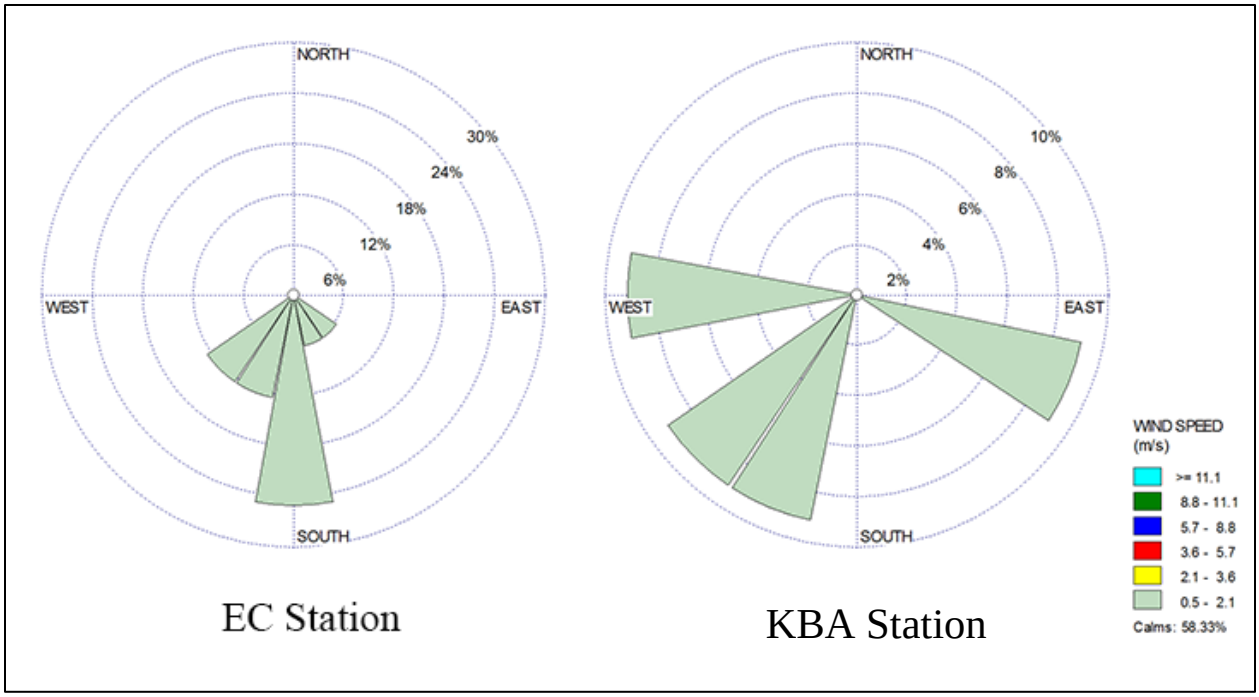


Figure E.4: A wind rose plot during the precipitation event on April 18. The left plot is of the EC Station and the right is of the KBA station.

## Appendix F: Particles of the Categories of Unrimed Ice Crystals and Solid Precipitation

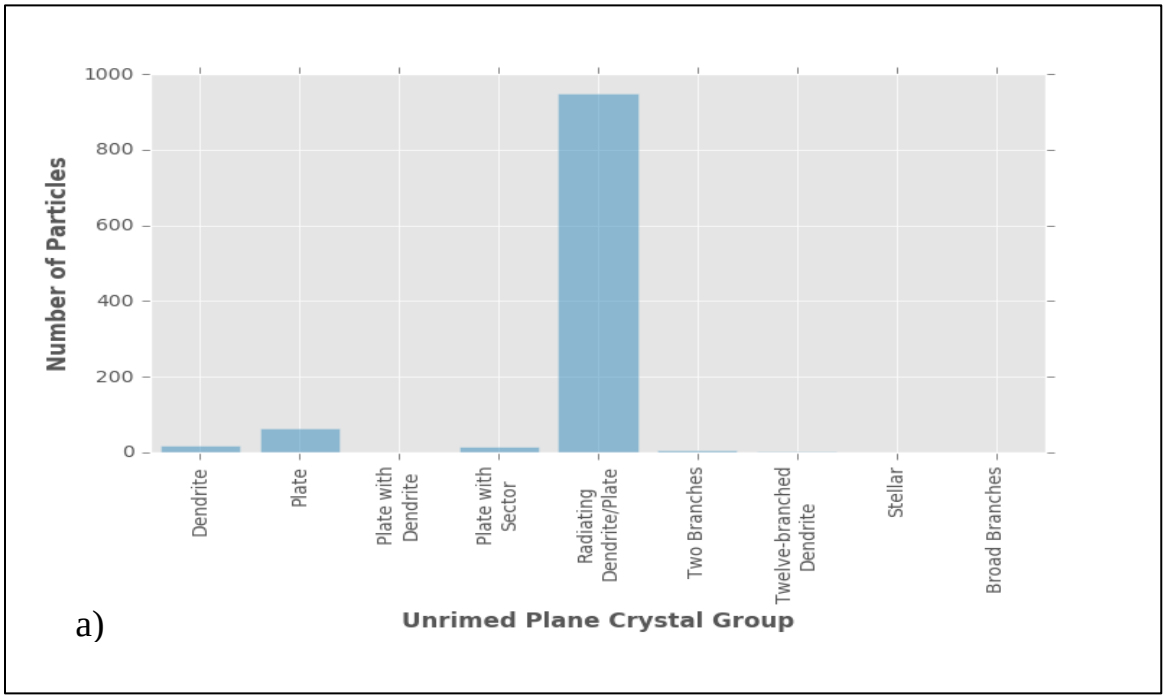


a)

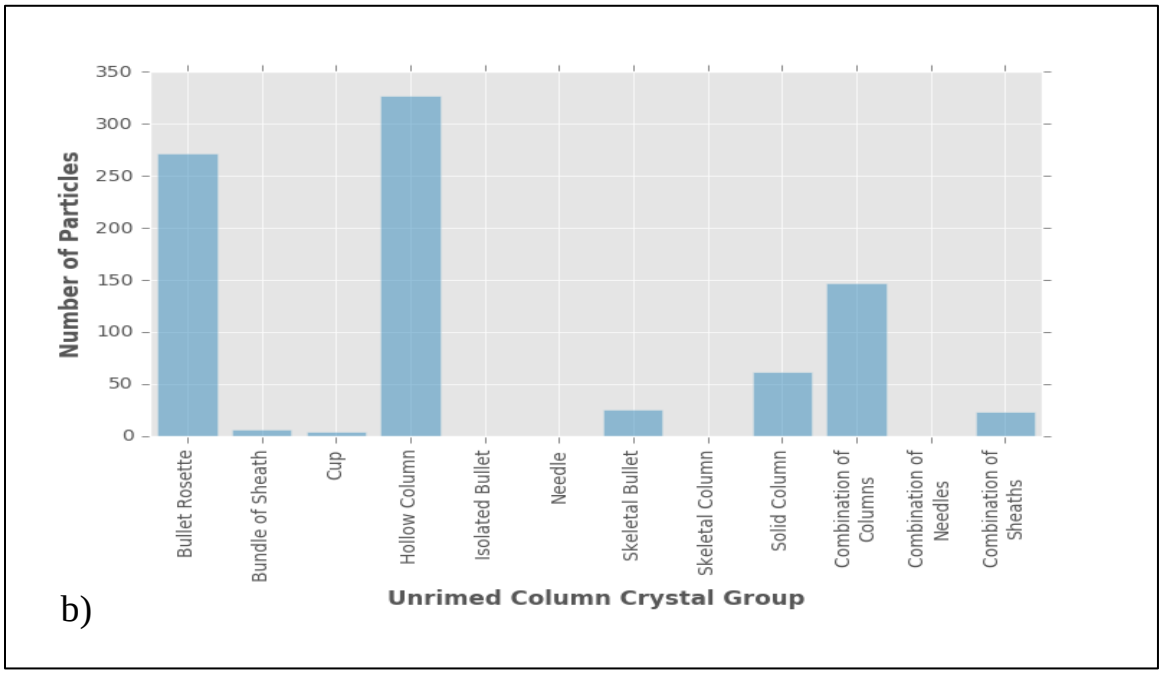


b)

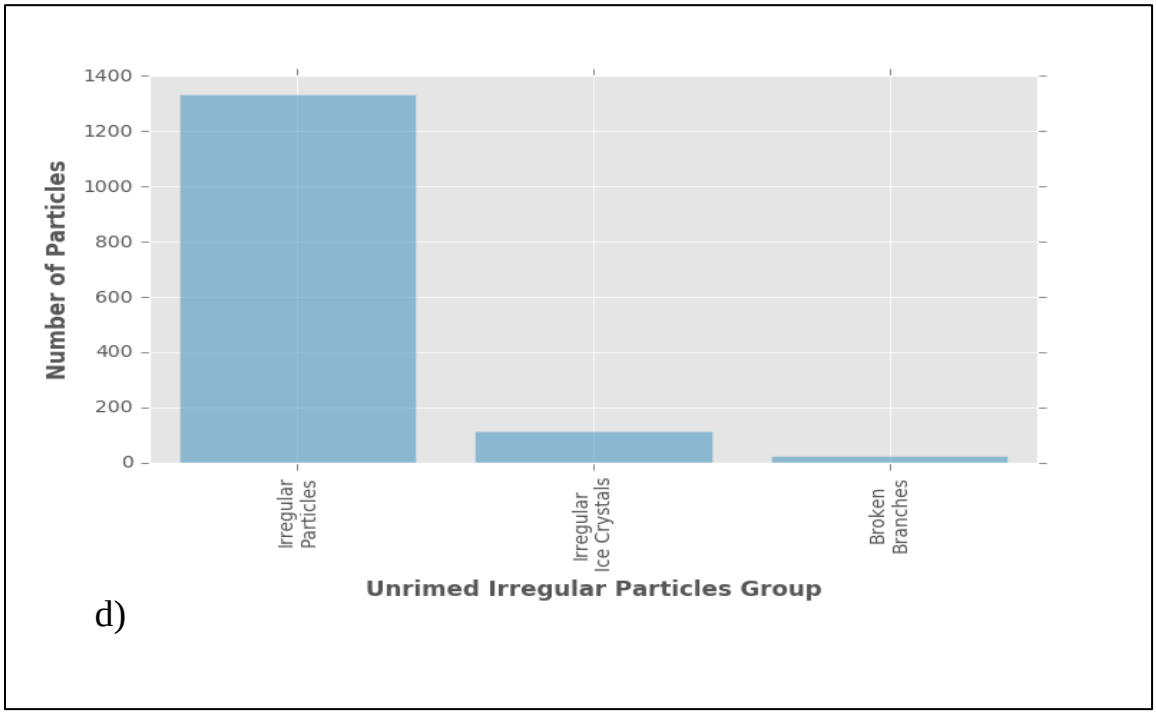
1400
1200
1000
800
600
400
200
0
Number of Particles
Irregular Particles
Irregular Ice Crystals
Broken Branches
Unrimed Irregular Particles Group

d)

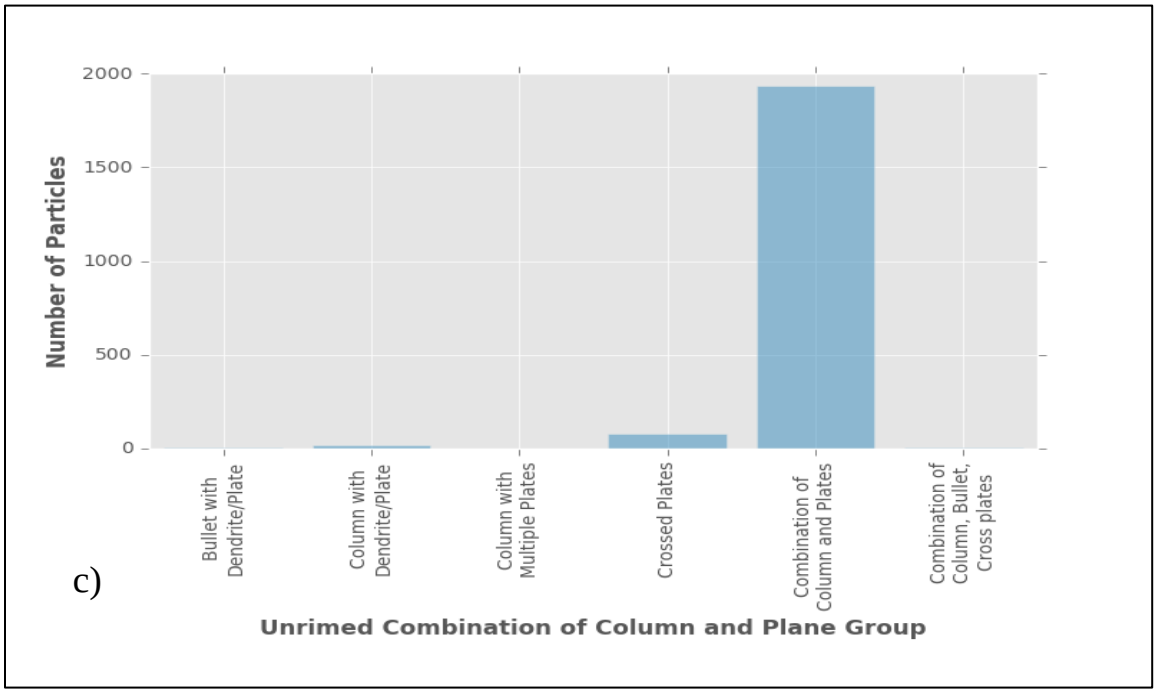
2000
1500
1000
500
0
Number of Particles
Bullet with Dendrite/Plate
Column with Dendrite/Plate
Column with Multiple Plates
Crossed Plates
Combination of Column and Plates
Combination of Column, Bullet, Cross plates
Unrimed Combination of Column and Plane Group

c)

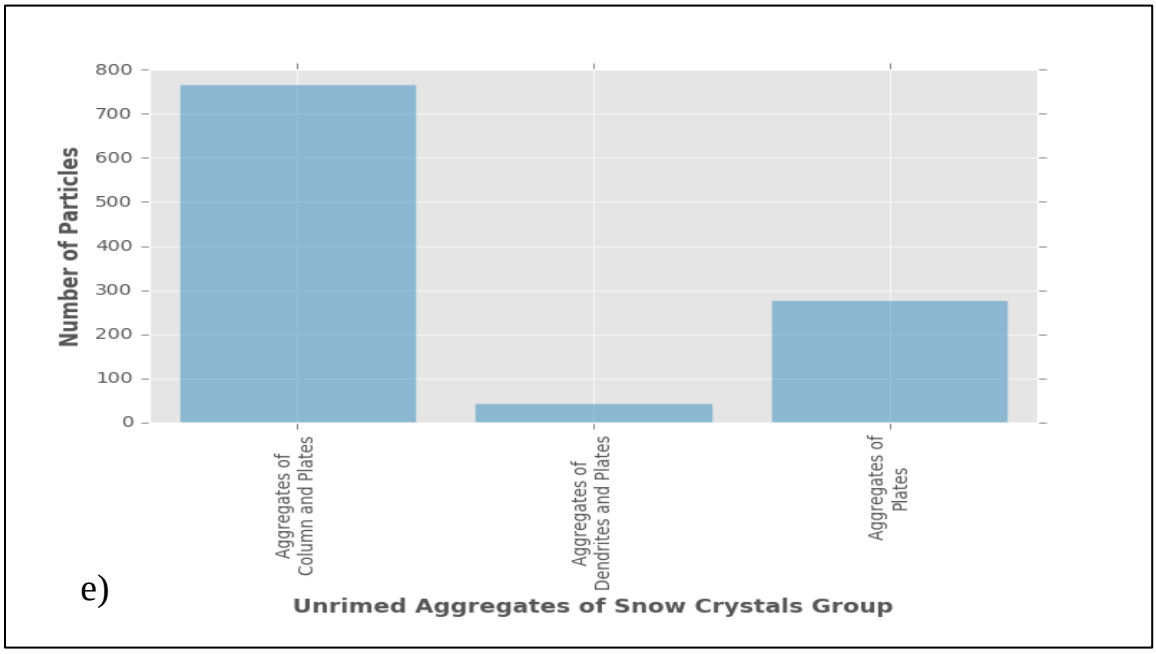


Figure F.1: Number of unrimed particles found in the ice crystal and solid precipitation particle categories. Categories include a) plane crystal, b) column crystal, c) irregular snow particles, d) combination of column and plane crystals, and e) aggregates of snow crystals.

## Appendix G: Particles of the Categories of Rimed Ice Crystals and Solid Precipitation

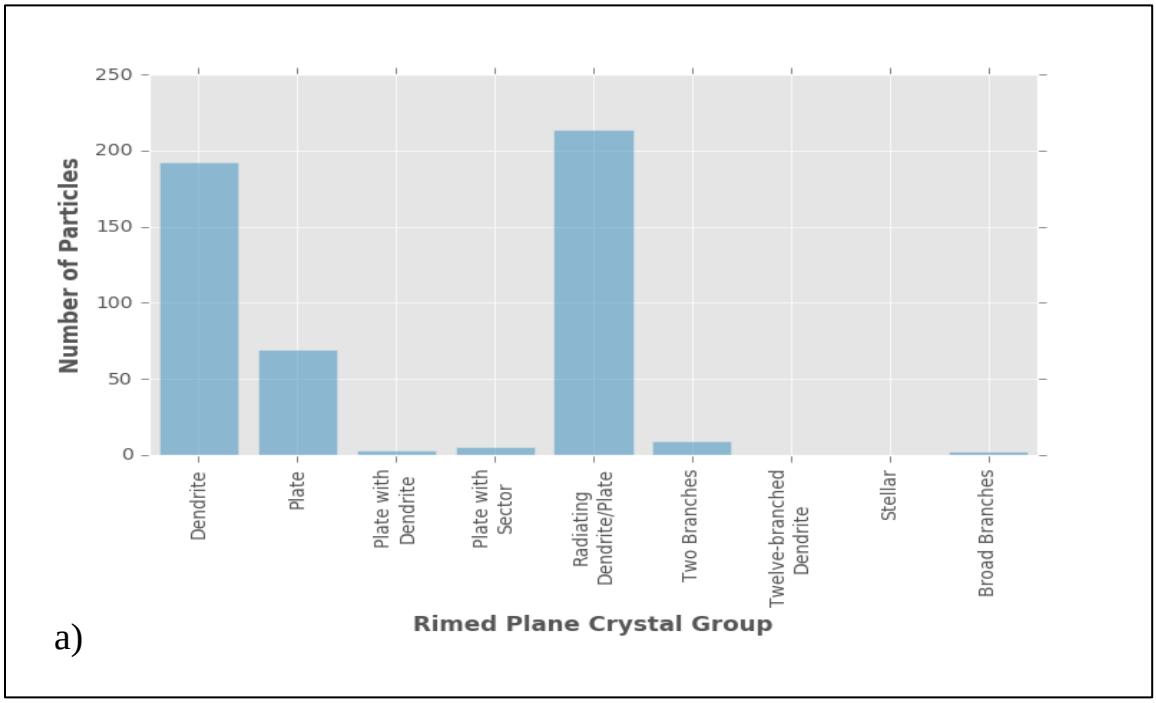


a)

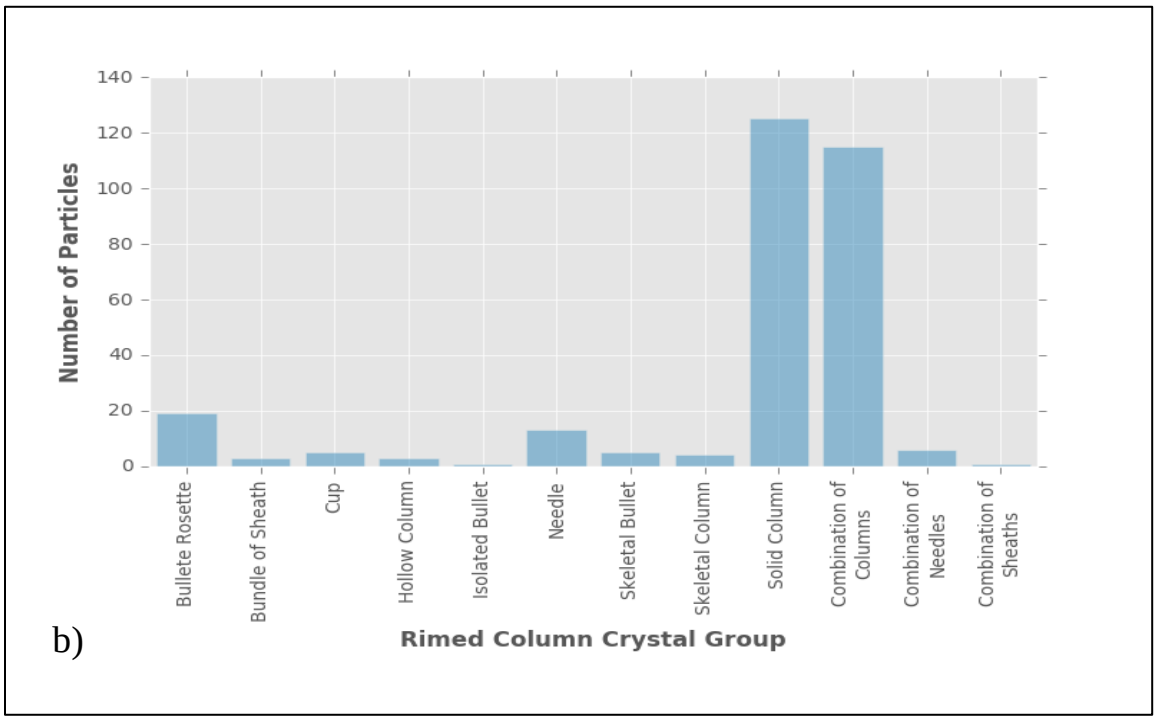


b)

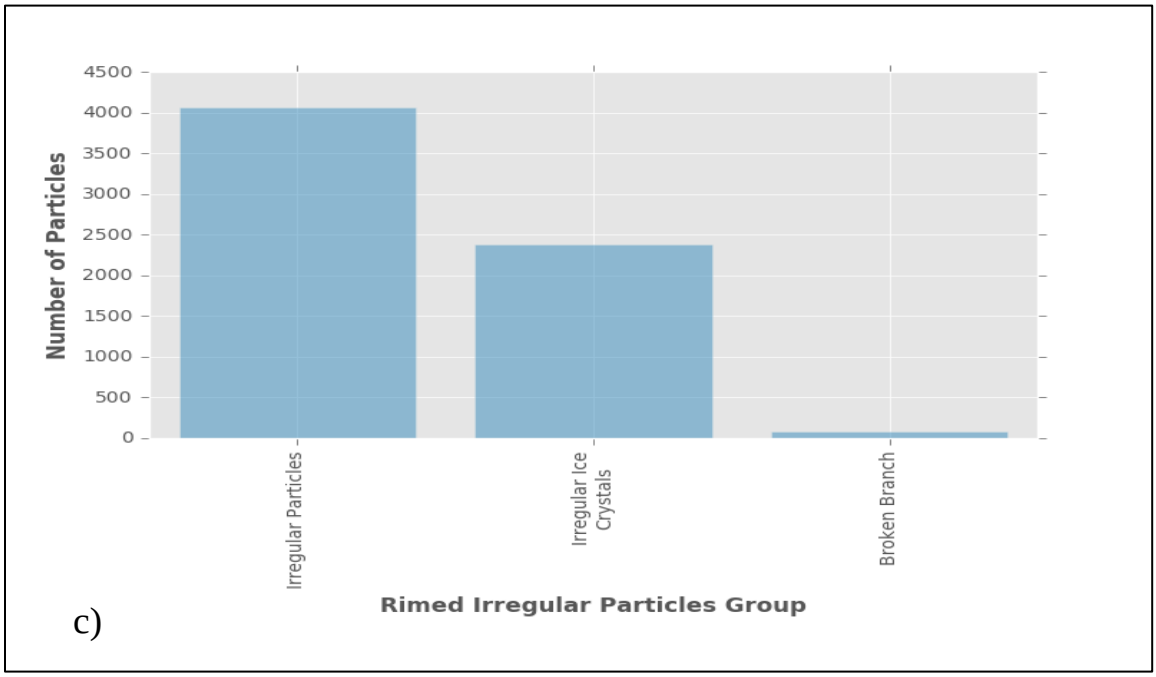
Number of Particles
4500
4000
3500
3000
2500
2000
1500
1000
500
0
Irregular Particles
Irregular Ice Crystals
Broken Branch
Rimed Irregular Particles Group

c)

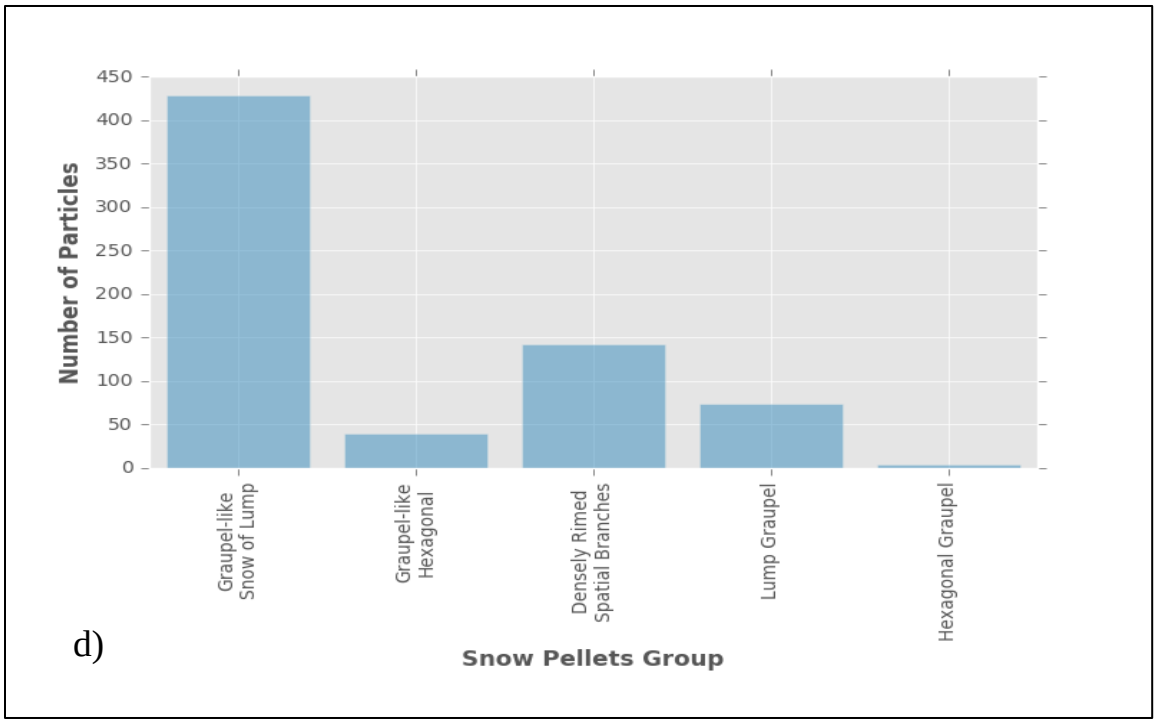
Number of Particles
450
400
350
300
250
200
150
100
50
0
Graupel-like Snow of Lump
Graupel-like Hexagonal
Densely Rimed Spatial Branches
Lump Graupel
Hexagonal Graupel
Snow Pellets Group

d)

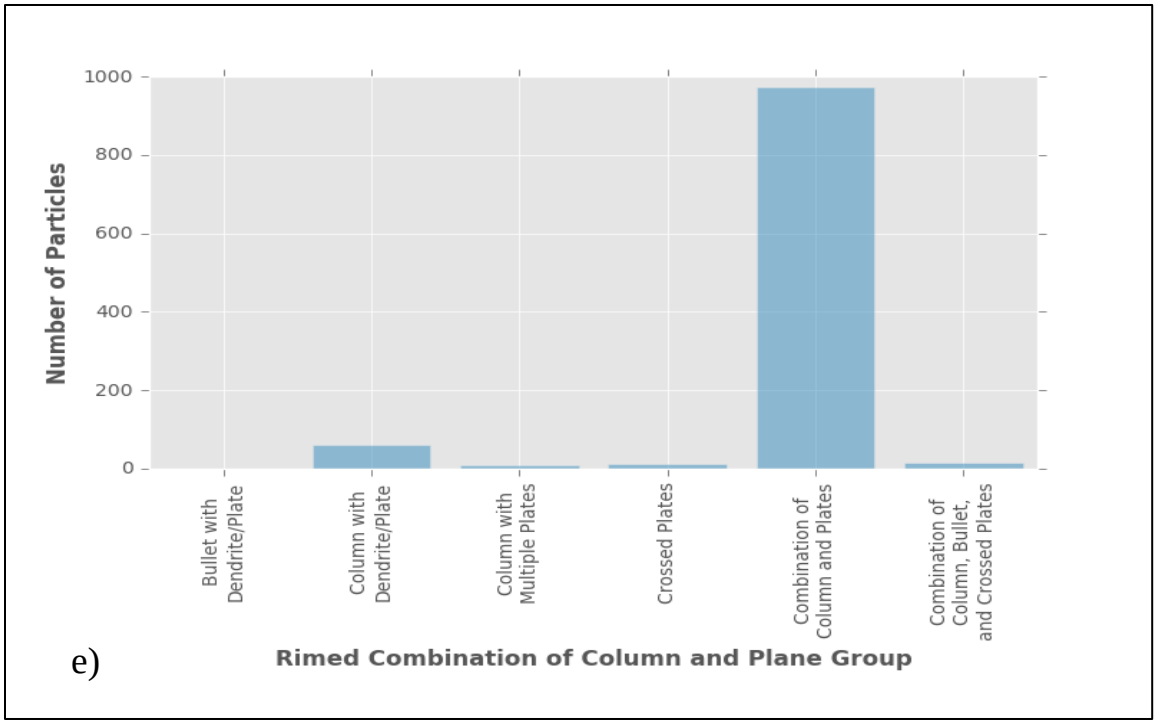


e)

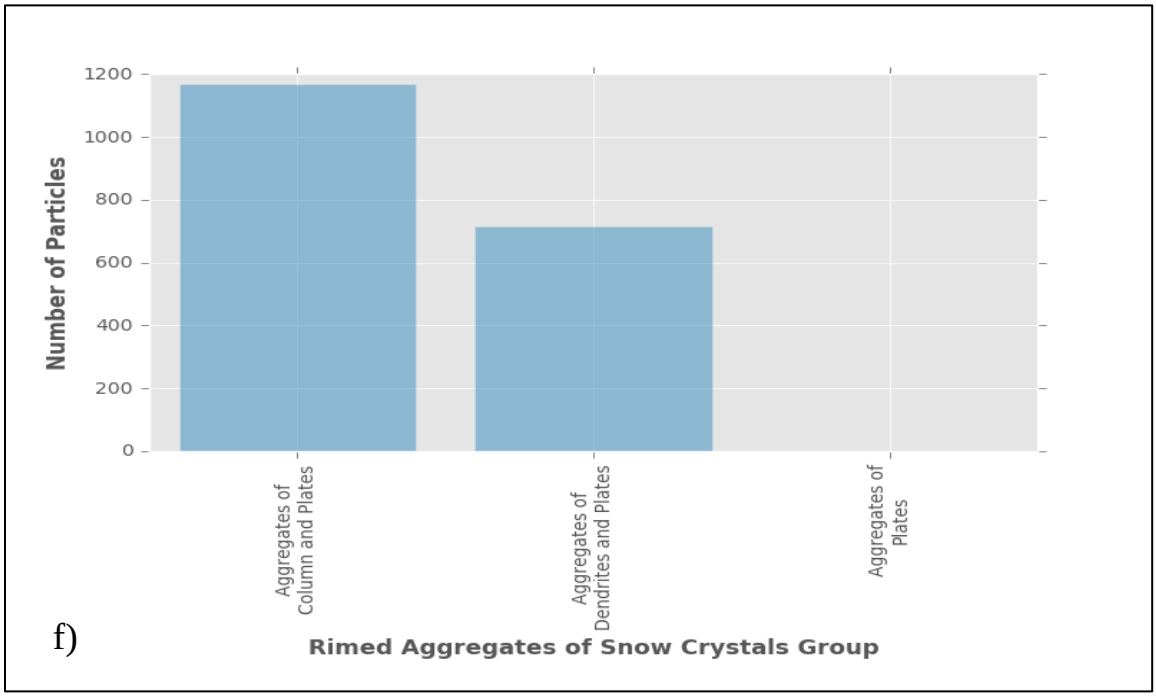


f)

Figure G.1: Number of rimed particles found in the ice crystal and solid precipitation particle categories. Categories include a) plane crystal, b) column crystal, c) irregular snow particles, d) snow pellets, e) combination of column and plane crystals, and f) aggregates of snow crystals.

# Appendix H: Time of Occurrence of Ice Crystals and Solid Precipitation Particles

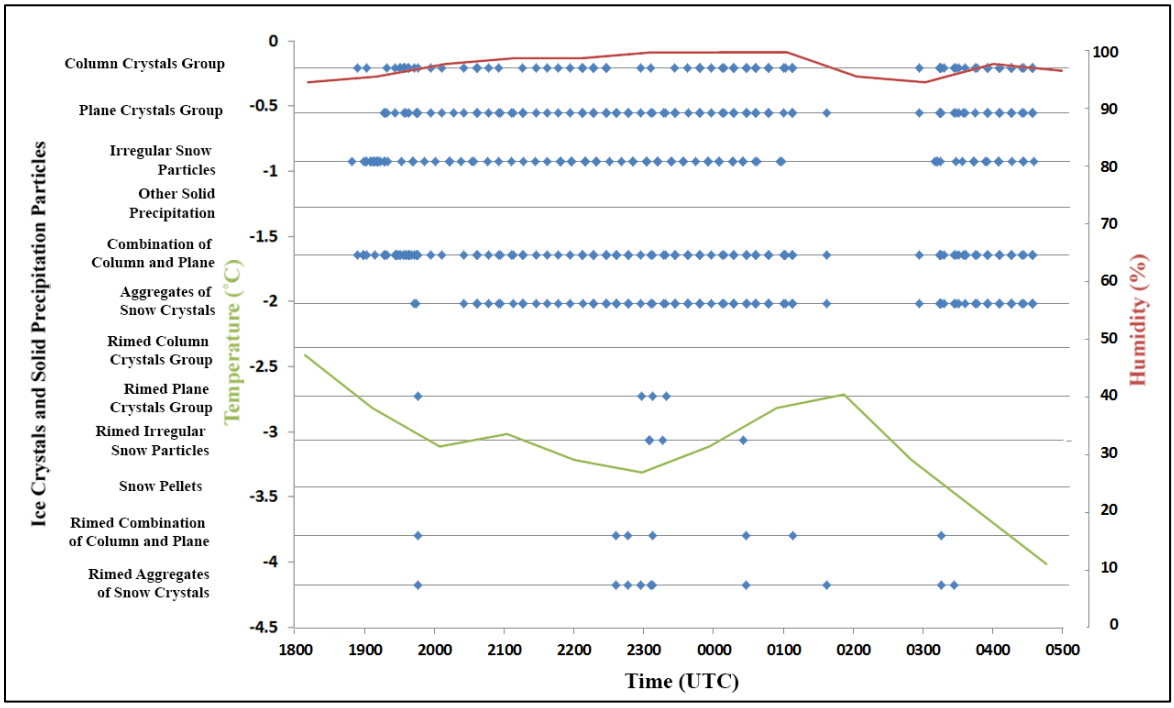


Figure H.1: The time of occurrence of precipitation particles photographed during the March 15 – 16 event. Each point indicates the occurrence of a category.

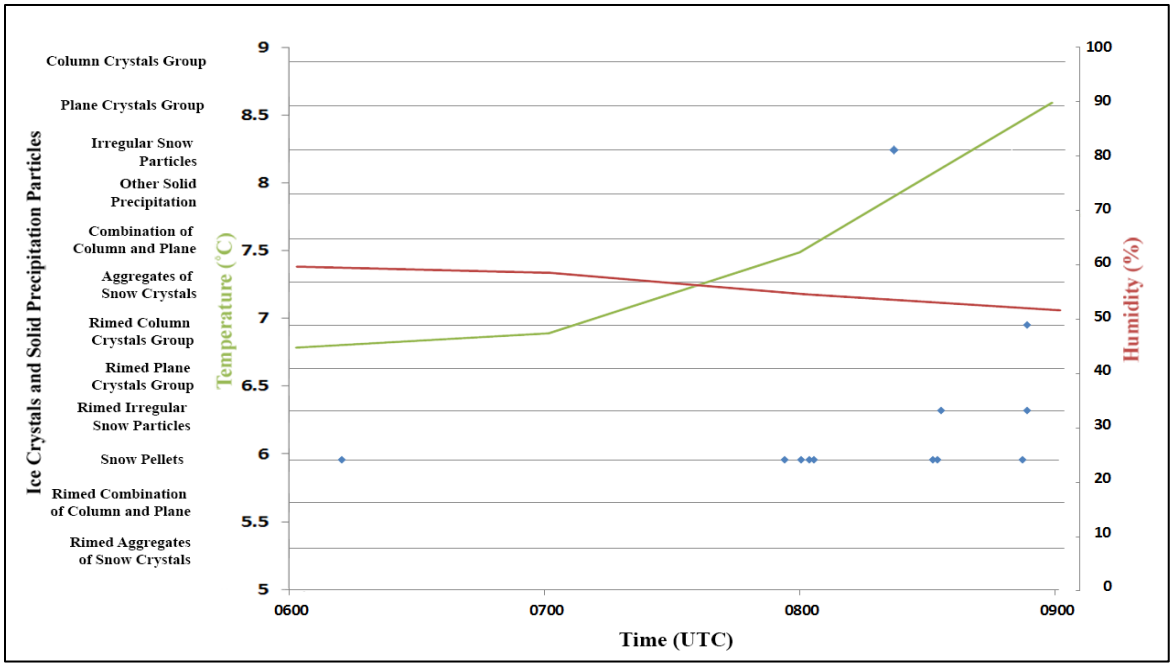


Figure H.2: The time of occurrence of precipitation particles photographed during the March 21 event. Each point indicates the occurrence of a category.

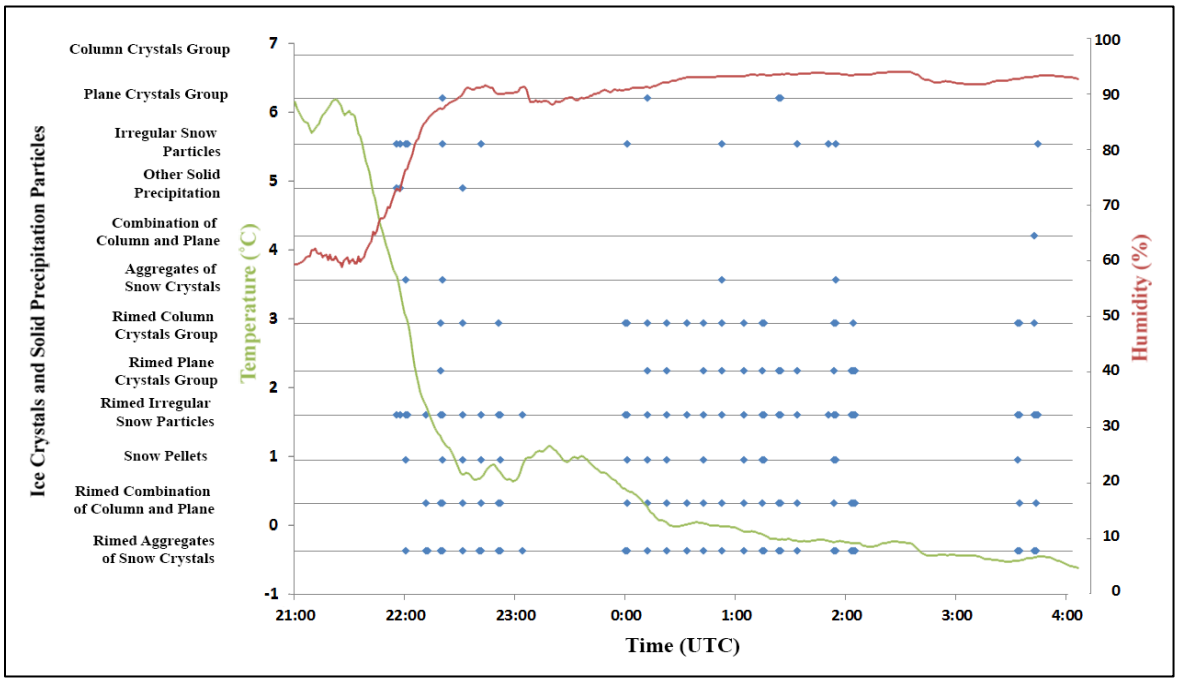


Figure H.3: The time of occurrence of precipitation particles photographed during the April 14 – 15 event. Each point indicates the occurrence of a category.

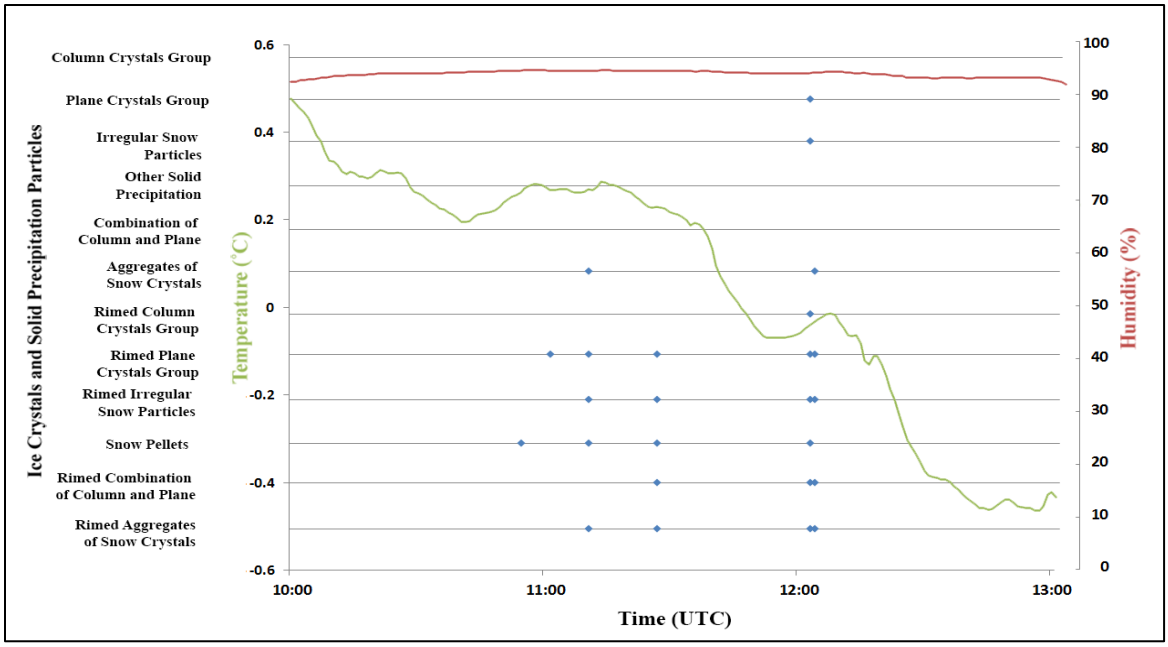


Figure H.4: The time of occurrence of precipitation particles photographed during the April 18 event. Each point indicates the occurrence of a category.

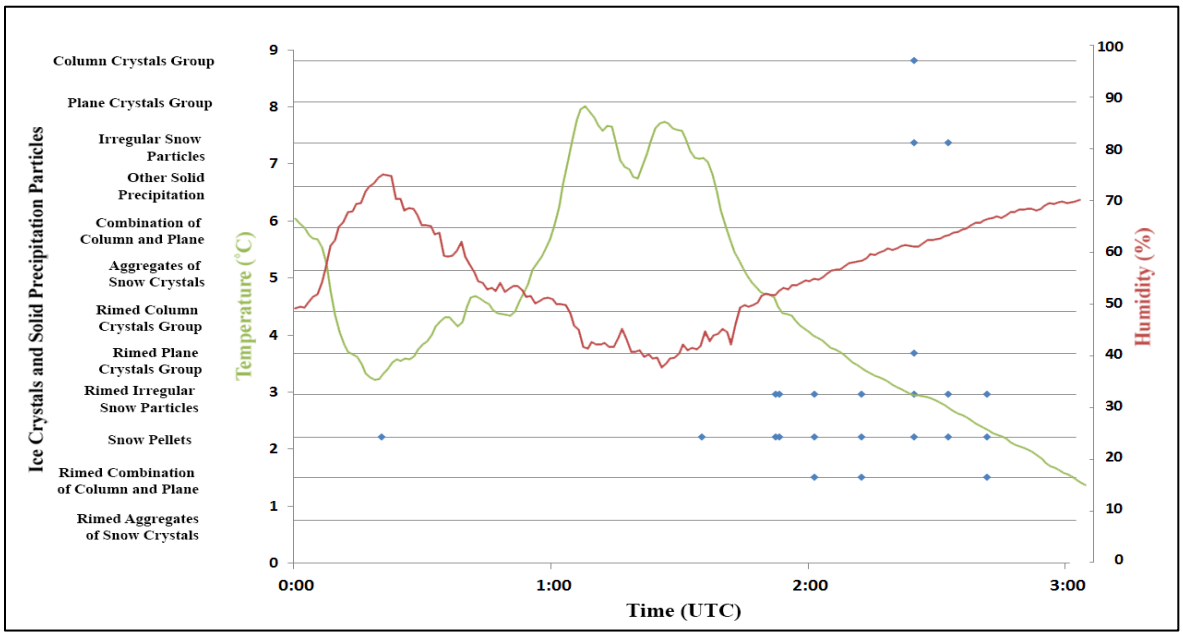


Figure H.5: The time of occurrence of precipitation particles photographed during the April 25 – 26 event. Each point indicates the occurrence of a category.

# Appendix I: Photographed Ice Crystals and Solid Precipitation Particles above 0°C at the Surface

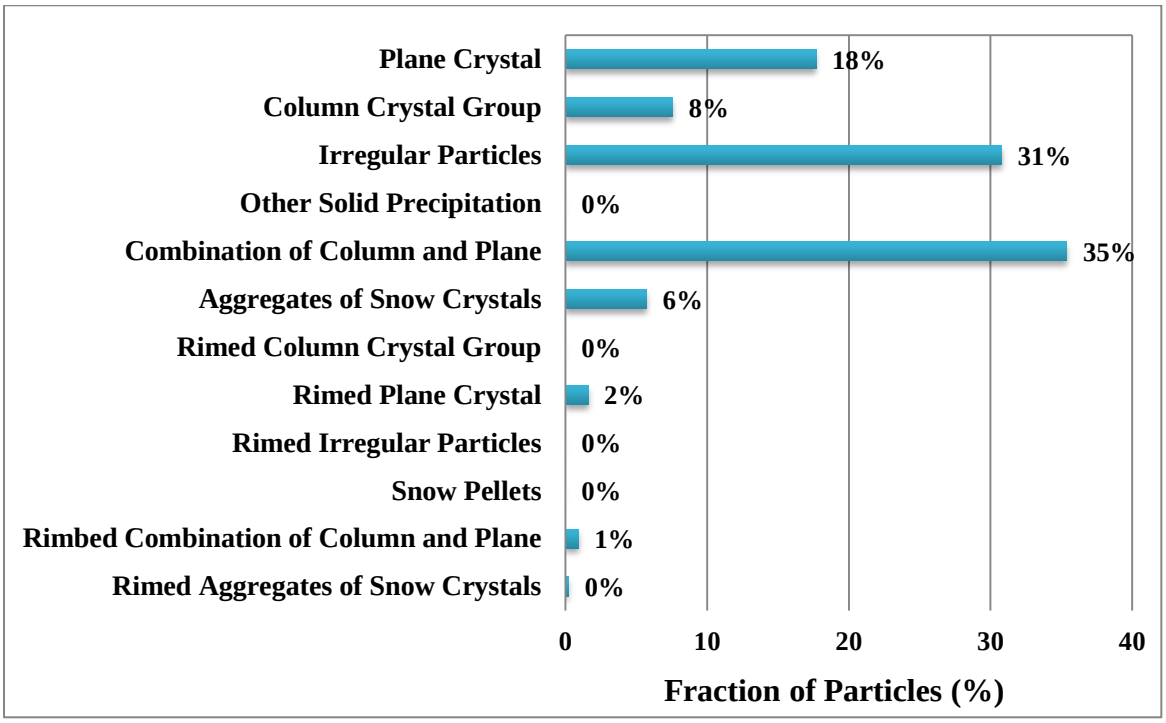


Figure I.1: The percentage of ice crystals and solid precipitation particles photographed on March 15 at 1800 UTC – 2000 UTC when temperatures were above 0°C based on the KBA station hourly data.

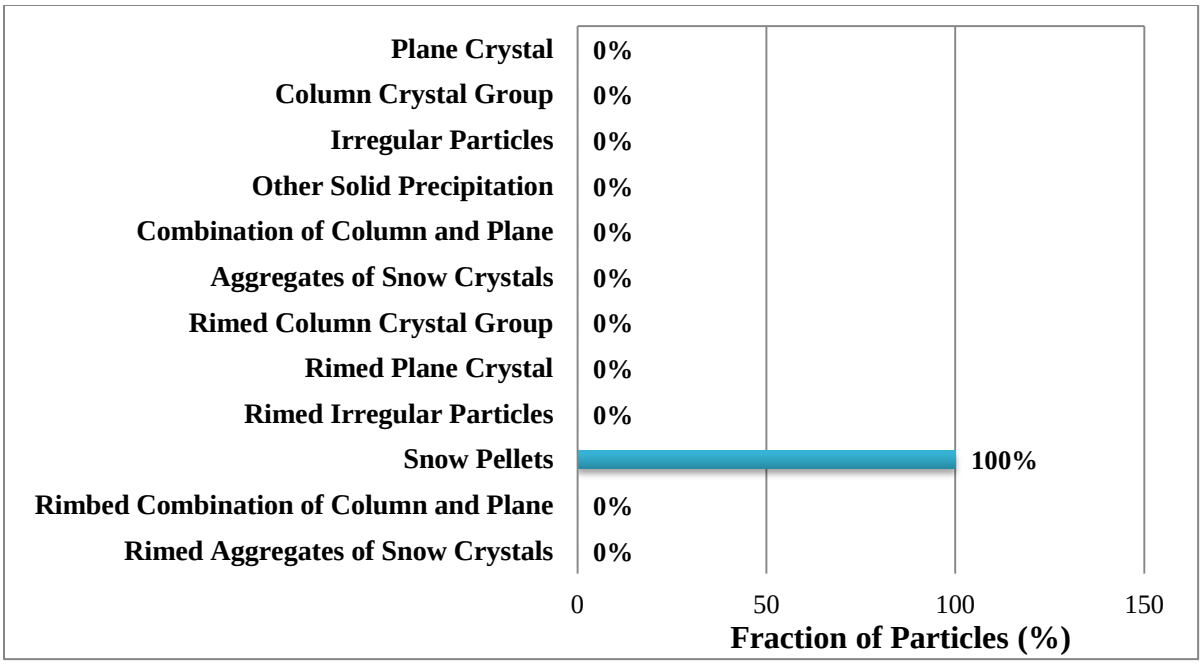


Figure I.2: The percentage of ice crystals and solid precipitation particles photographed on March 22 at 0612 UTC when temperatures were above 0°C based on the EC station 5 min data.

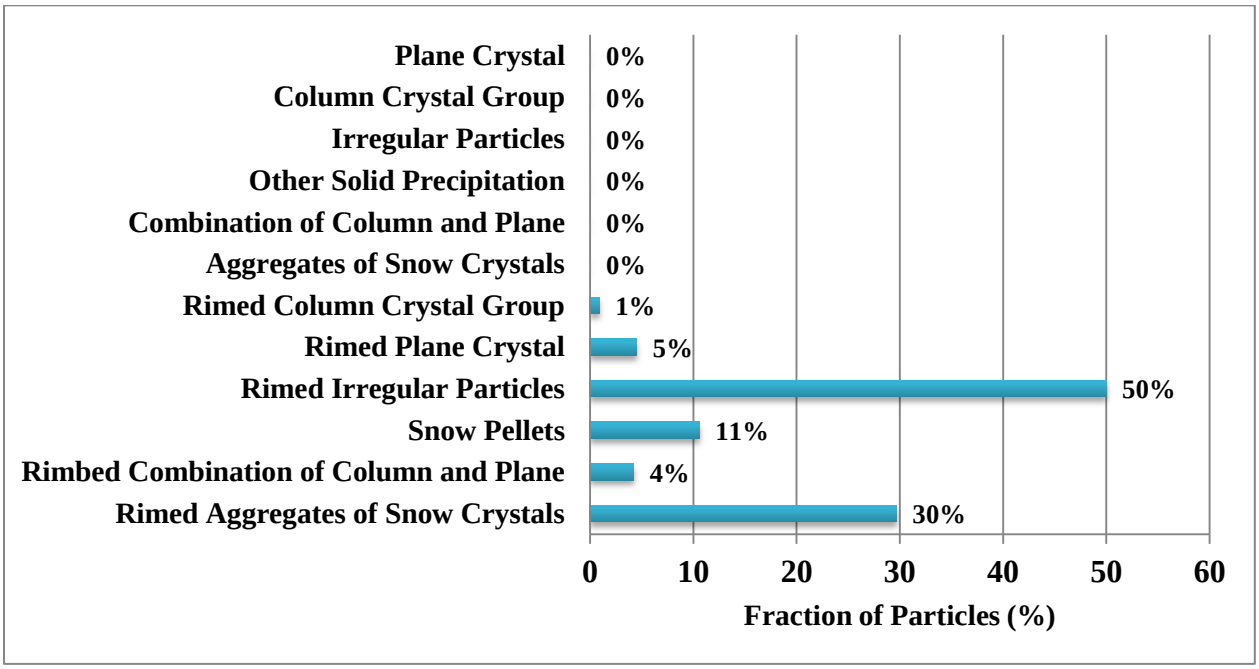


Figure I.3: The percentage of ice crystals and solid precipitation particles photographed on April 11 at 1330 UTC – 1431 UTC when temperatures were above 0°C based on the ECCC station 1 min data.

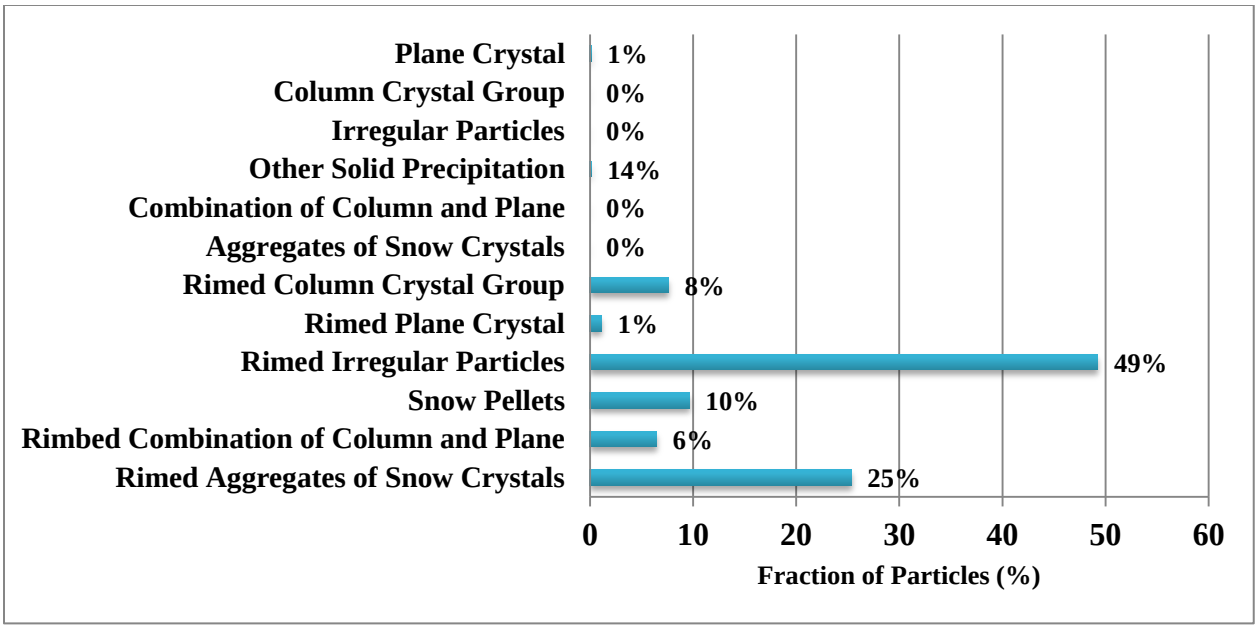


Figure I.4: The percentage of ice crystals and solid precipitation particles photographed on April 14 at 2155 UTC – 0011 UTC when temperatures were above 0°C based on the ECCC station 1 min data.

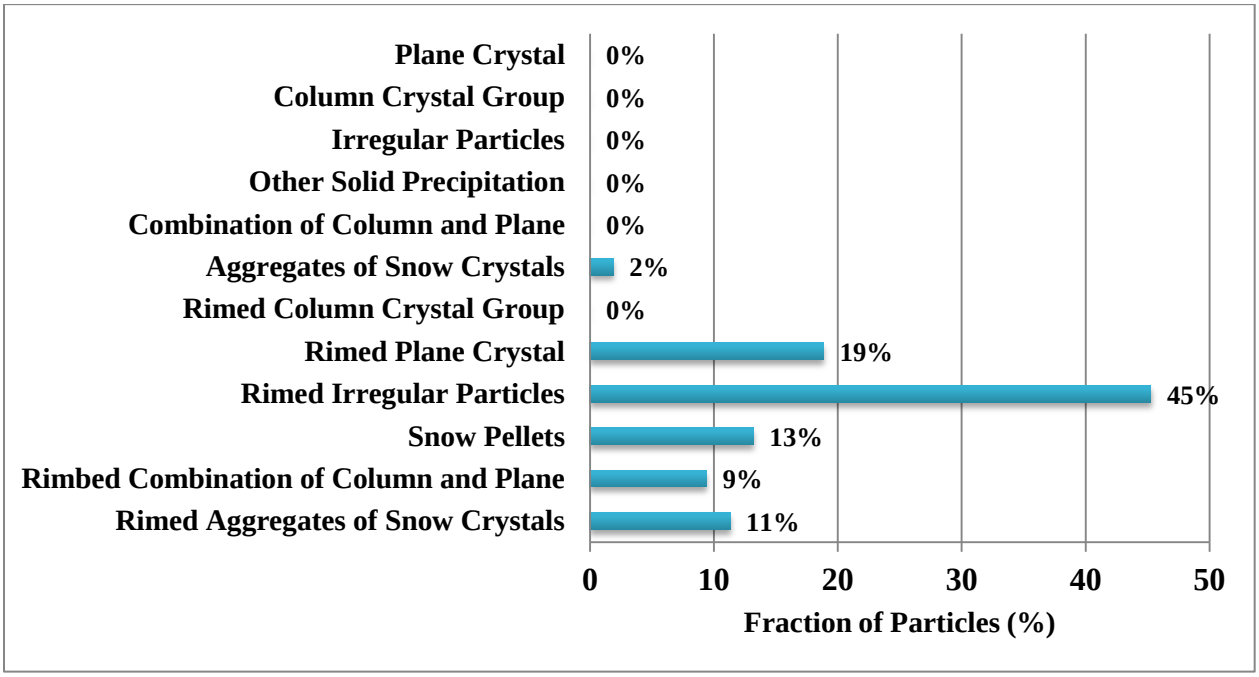


Figure I.5: The percentage of ice crystals and solid precipitation particles photographed on April 18 at 1054 UTC – 1126 UTC when temperatures were above 0°C based on the ECCC station 1 min data.

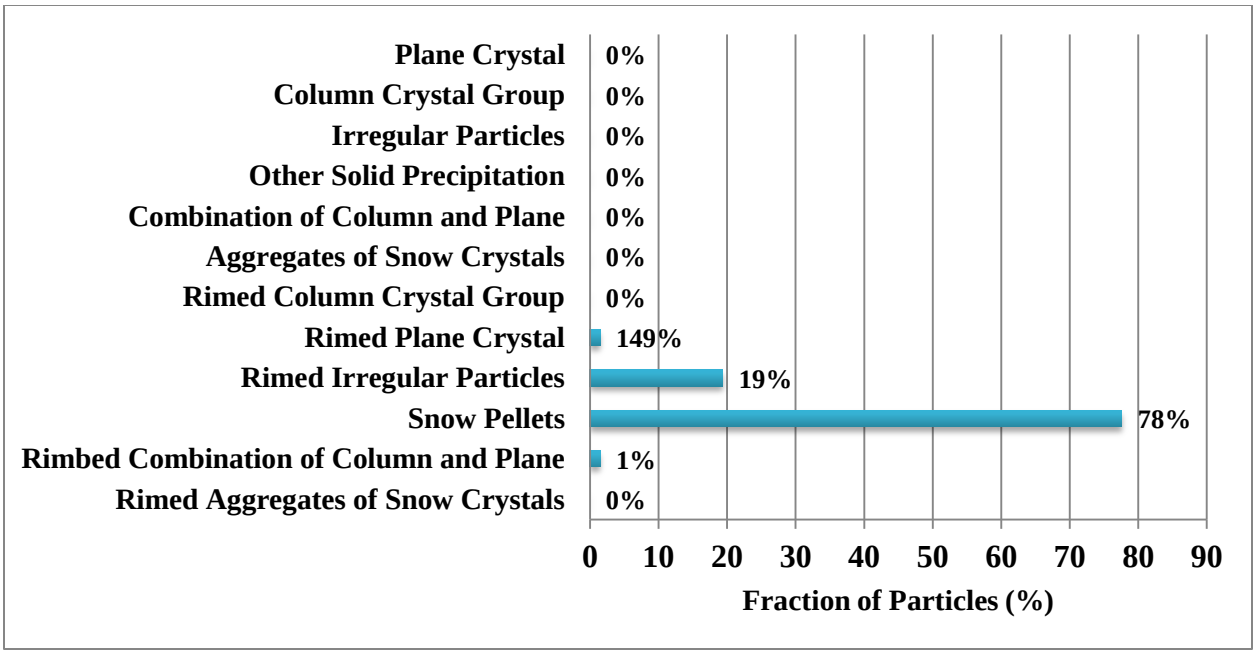


Figure I.6: The percentage of ice crystals and solid precipitation particles photographed on April 26 at 0020 UTC – 0200 UTC when temperatures were above 0°C based on the ECCC station 1 min data.

## Appendix J: Strathmore Radar Images

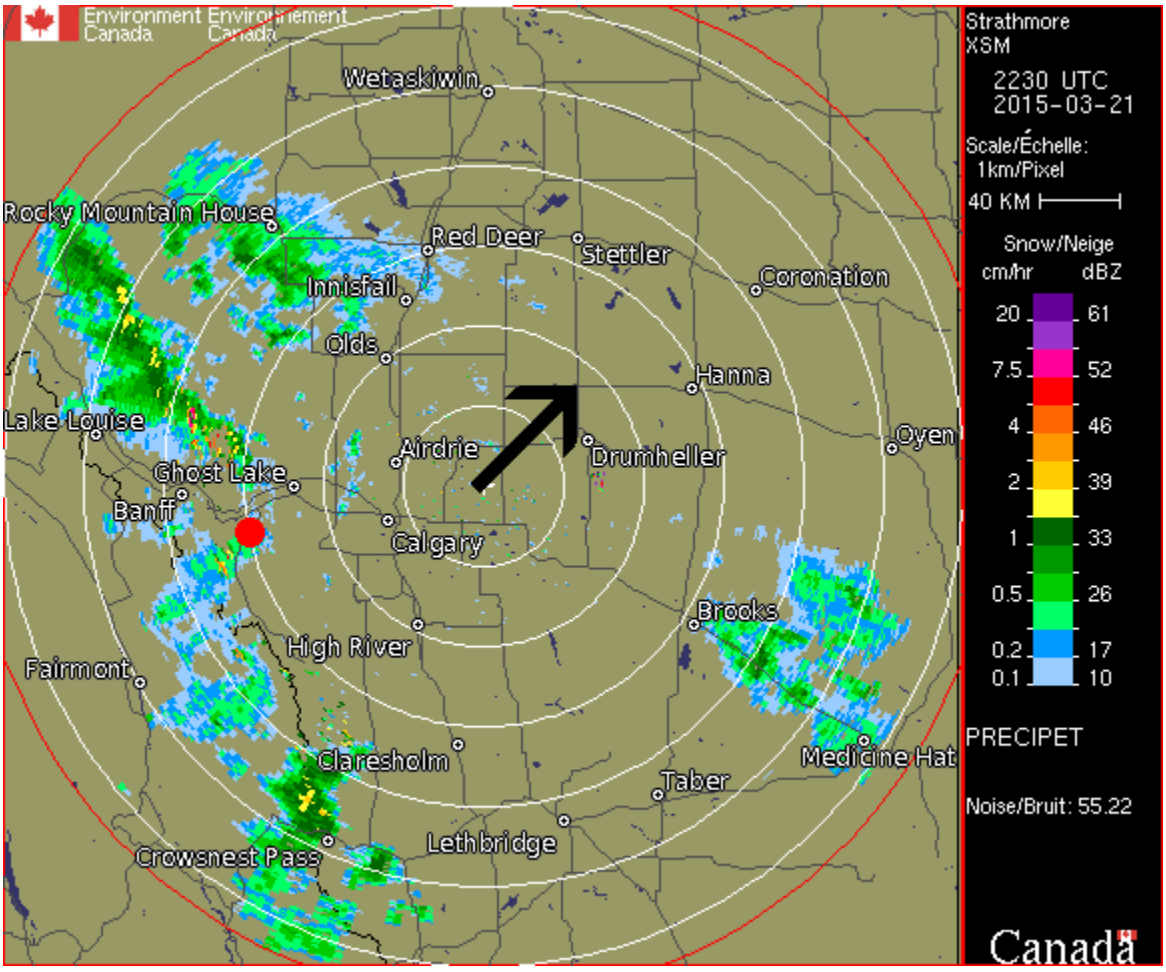


Figure J.1: A regional view of the Strathmore, AB, radar site on March 21, 2015 at 2230 UTC, as seen in the top right corner. The precipitation structures are represented by an intensity scale located on the right of the image. The scale represents the snowfall rate in cm/h and the reflectivity in dBz. The rings act as a scale guide and are each equally spaced 40 km apart. The red mark indicates the location of KES and the black arrows represents the direction of motion of the radar echo. [Strathmore Radar]. Retrieved March 8, 2016, from http://climate.weather.gc.ca/radar/index_e.html

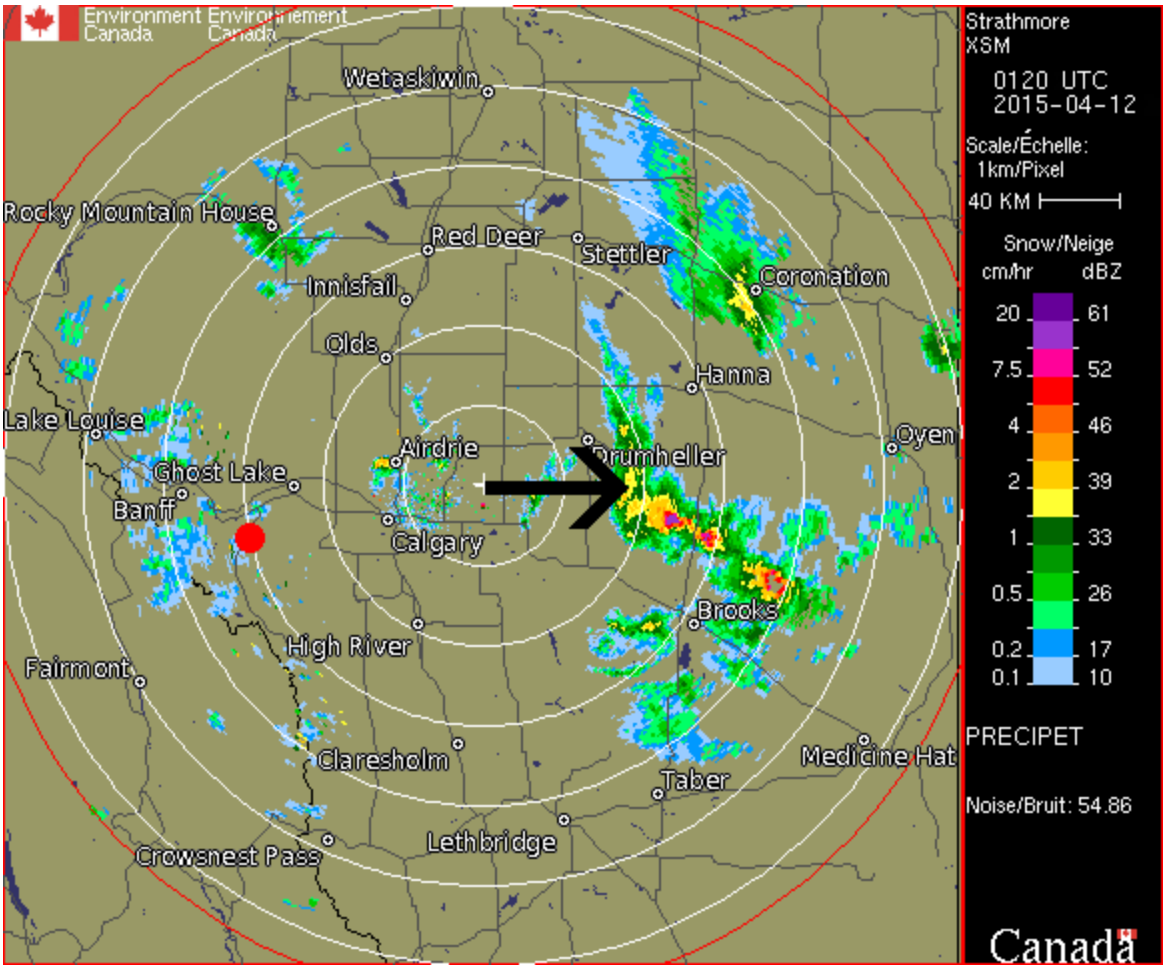


Figure J.2: A regional view of the Strathmore, AB, radar site on April 12, 2015 at 0120 UTC, as seen in the top right corner. The precipitation structures are represented by an intensity scale located on the right of the image. The scale represents the snowfall rate in cm/h and the reflectivity in dBz. The rings act as a scale guide and are each equally spaced 40 km apart. The red mark indicates the location of KES and the black arrows represents the direction of motion of the radar echo. [Strathmore Radar]. Retrieved March 8, 2016, from http://climate.weather.gc.ca/radar/index_e.html

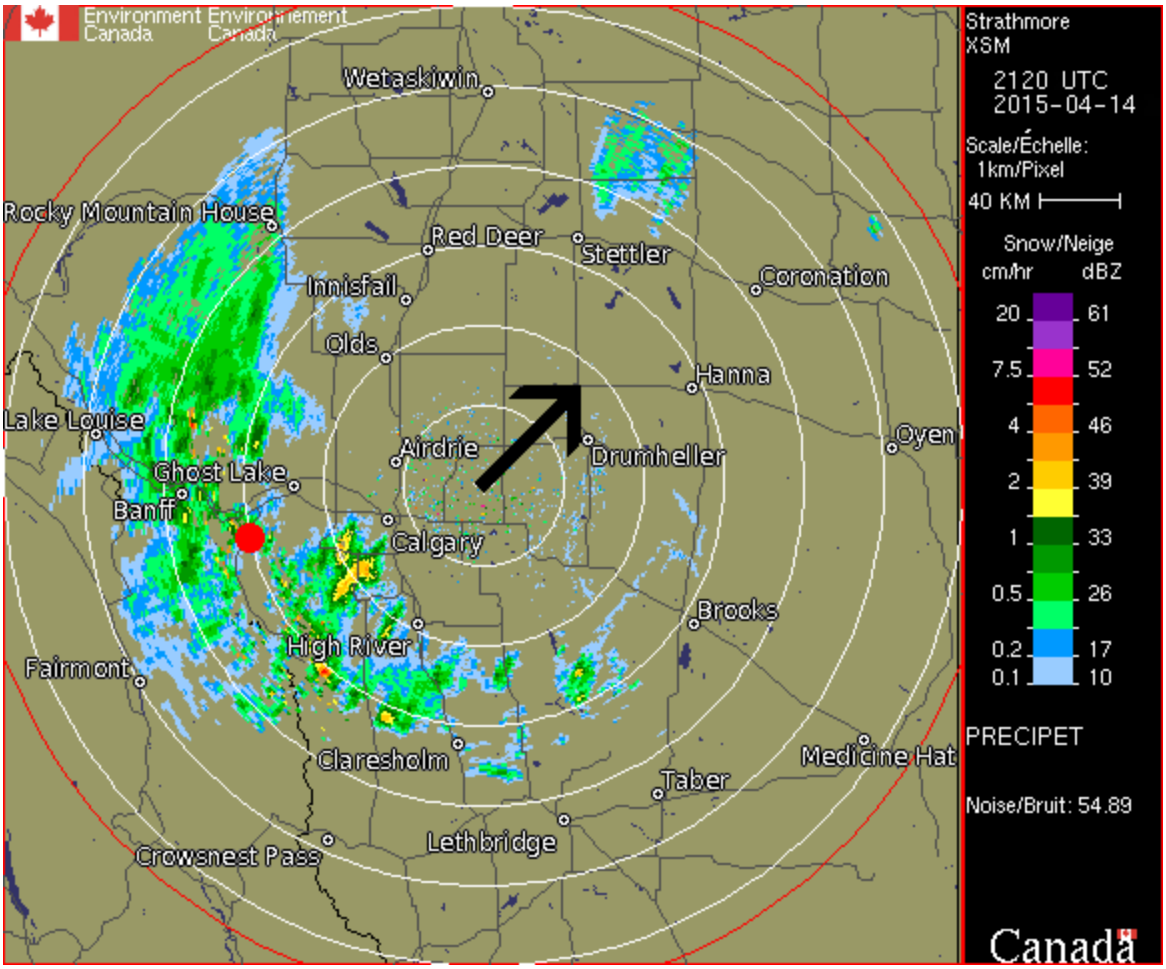


Figure J.3: A regional view of the Strathmore, AB, radar site on April 14, 2015 at 2120 UTC, as seen in the top right corner. The precipitation structures are represented by an intensity scale located on the right of the image. The scale represents the snowfall rate in cm/h and the reflectivity in dBz. The rings act as a scale guide and are each equally spaced 40 km apart. The red mark indicates the location of KES and the black arrows represents the direction of motion of the radar echo. [Strathmore Radar]. Retrieved March 8, 2016, from http://climate.weather.gc.ca/radar/index_e.html

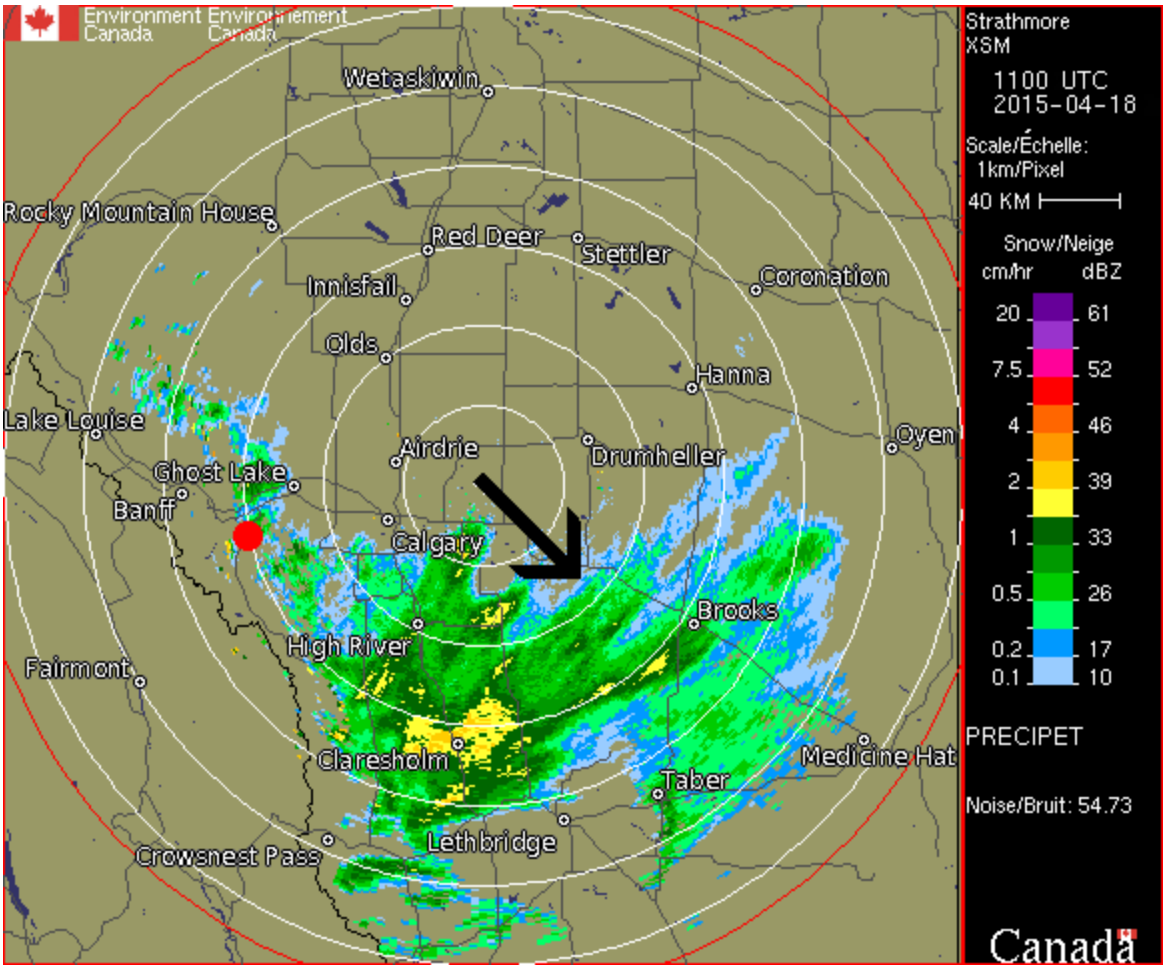


Figure J.4: A regional view of the Strathmore, AB, radar site on April 18, 2015 at 1100 UTC, as seen in the top right corner. The precipitation structures are represented by an intensity scale located on the right of the image. The scale represents the snowfall rate in cm/h and the reflectivity in dBz. The rings act as a scale guide and are each equally spaced 40 km apart. The red mark indicates the location of KES and the black arrows represents the direction of motion of the radar echo. [Strathmore Radar]. Retrieved March 8, 2016, from http://climate.weather.gc.ca/radar/index_e.html

## Appendix K: Surface Pressure Analysis Maps

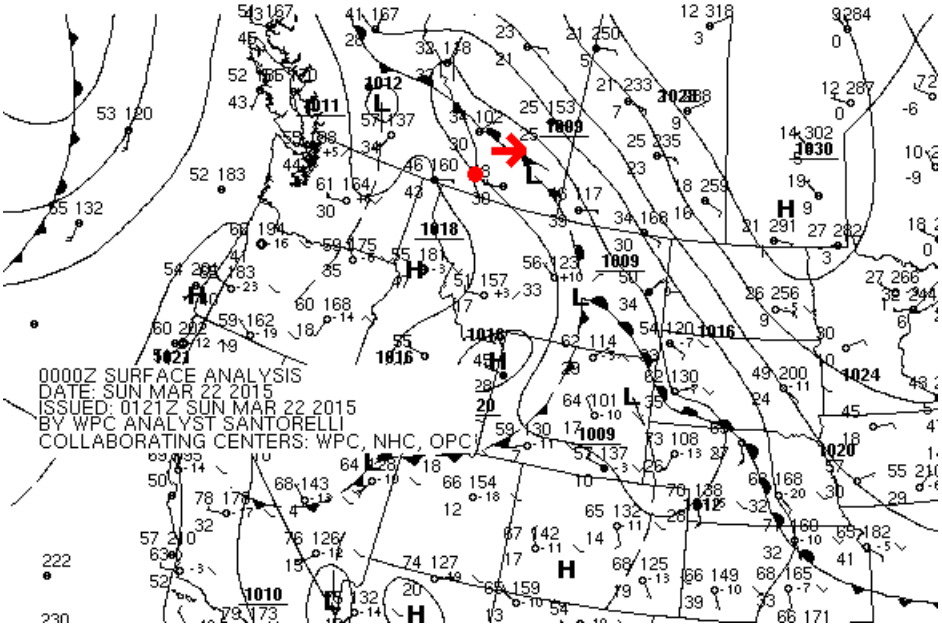


Figure K.1: Surface analysis map of the wind direction on March 22 at 0000 UTC. The red mark represents the location of KES and the red arrow represents the wind flow. [Surface Analysis]. Retrieved May 16, 2016, from http://www.wpc.ncep.noaa.gov/archives/web_pages/sfc/sfc_archive.php

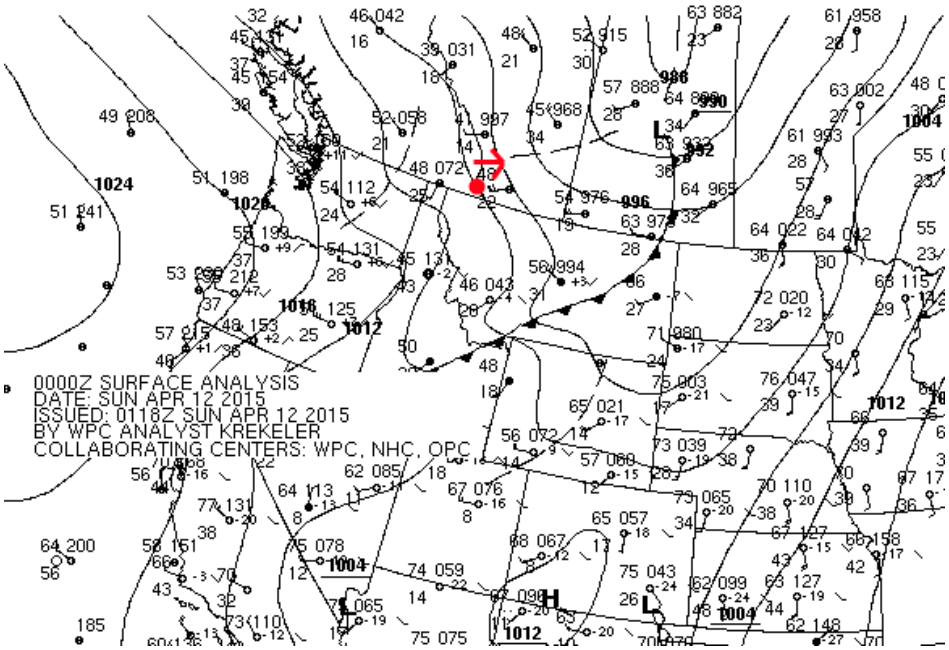


Figure K.2: Surface analysis map of the wind direction on April 12 at 0000 UTC. The red mark represents the location of KES and the red arrow represents the wind flow. [Surface Analysis]. Retrieved May 16, 2016, from http://www.wpc.ncep.noaa.gov/archives/web_pages/sfc/sfc_archive.php

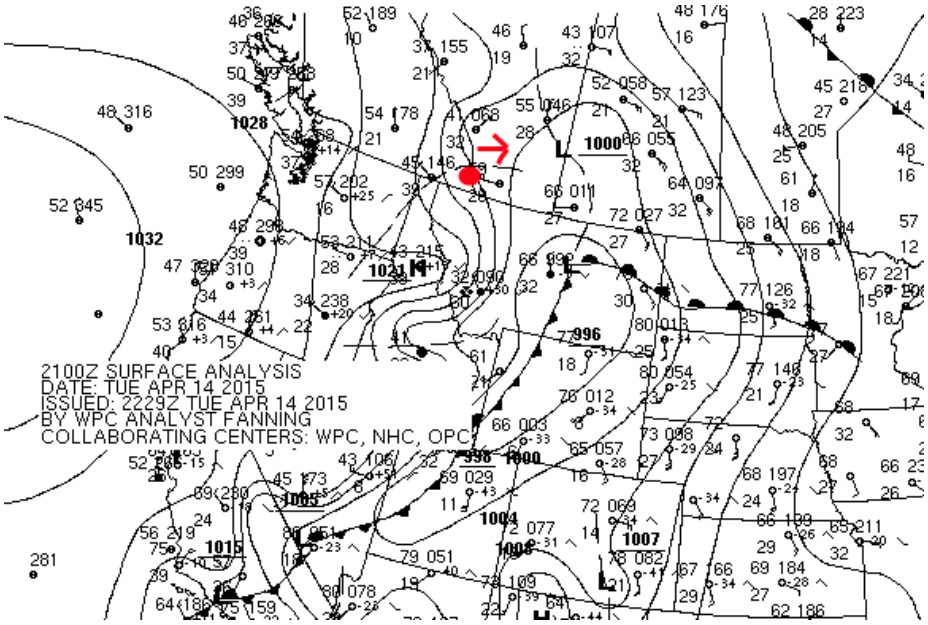


Figure K.3: Surface analysis map of the wind direction on April 14 at 2100 UTC. The red mark represents the location of KES and the red arrow represents the wind flow. [Surface Analysis]. Retrieved May 16, 2016, from http://www.wpc.ncep.noaa.gov/archives/web_pages/sfc/sfc_archive.php

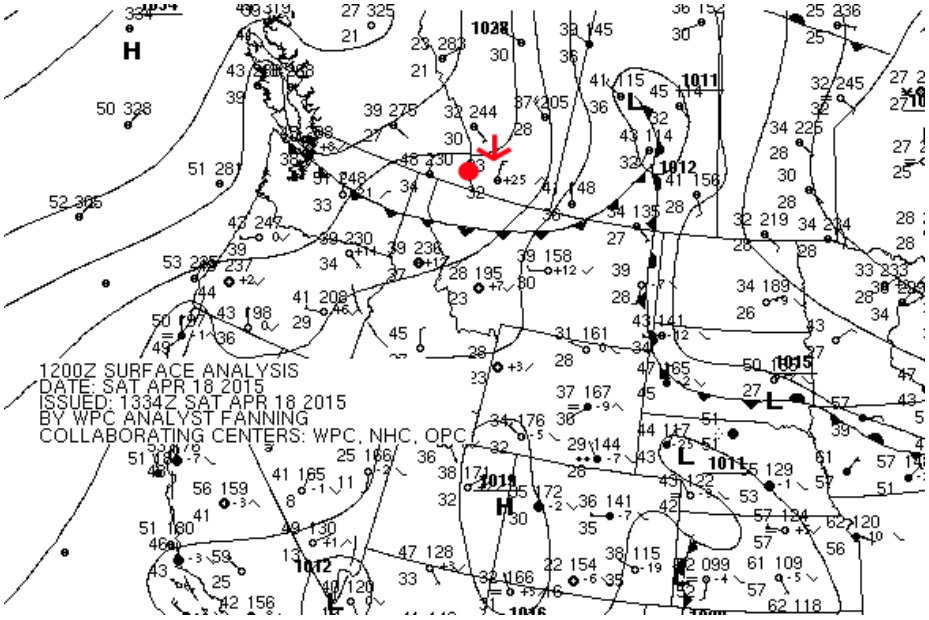


Figure K.4: Surface analysis map of the wind direction on April 18 at 1200 UTC. The red mark represents the location of KES and the red arrow represents the wind flow. [Surface Analysis]. Retrieved May 16, 2016, from http://www.wpc.ncep.noaa.gov/archives/web_pages/sfc/sfc_archive.php

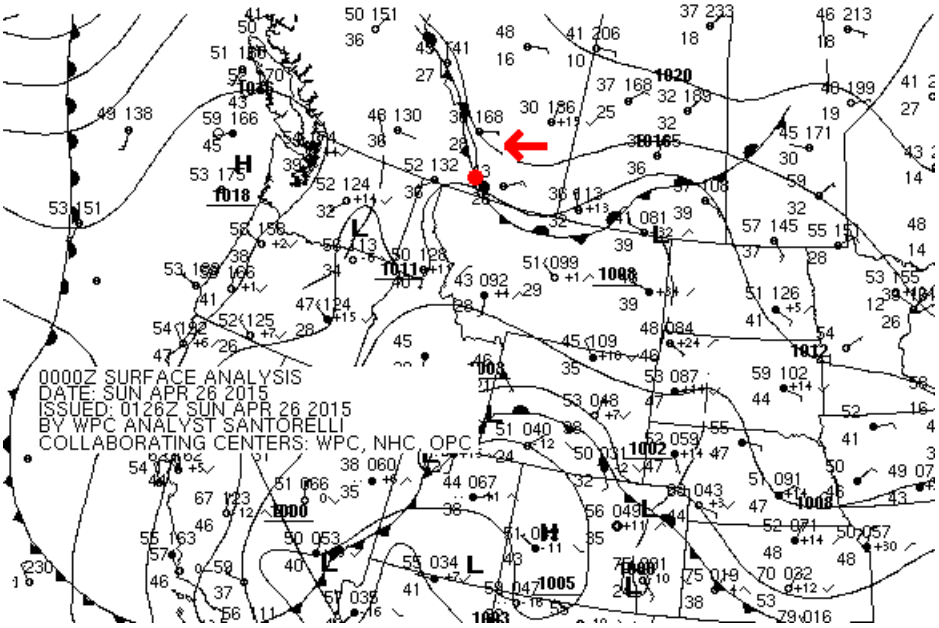


Figure K.5: Surface analysis map of the wind direction on April 26 at 0000 UTC. The red mark represents the location of KES and the red arrow represents the wind flow. [Surface Analysis]. Retrieved May 16, 2016, from http://www.wpc.ncep.noaa.gov/archives/web_pages/sfc/sfc_archive.php